Fakultät für Mathematik, Informatik und Naturwissenschaften | RWTH AACHEN UNIVERSITY

Spin- und Ladungsordnung in dem neu bewerteten Antiferromagneten $YbFe_2O_4$

Von der Fakultät für Mathematik, Informatik und Naturwissenschaften der RWTH Aachen University zur Erlangung des akademischen Grades einer Doktorin der Naturwissenschaften genehmigte Dissertation.

vorgelegt von

Hailey L. Williamson, Masters of Science

aus

Derby, England

Berichter: Dr. M. Angst
Universitätprofessor Dr. U. Klemradt
Universitätsprofessor Dr. C. Honerkamp

Tag der mündlichen Prüfung: 18. September 2019

Eidesstattliche Erklärung

I, *Hailey Louise Williamson*

erklärt hiermit, dass diese Dissertation und die darin dargelegten Inhalte die eigenen sind und selbstständig, als Ergebnis der eigenen originären Forschung, generiert wurden.

Hiermit erkläre ich an Eides statt

1. Diese Arbeit wurde vollständig oder größtenteils in der Phase als Doktorand dieser Fakultät und Universität angefertigt;

2. Sofern irgendein Bestandteil dieser Dissertation zuvor für einen akademischen Abschluss oder eine andere Qualifikation an dieser oder einer anderen Institution verwendet wurde, wurde dies klar angezeigt;

3. Wenn immer andere eigene- oder Veröffentlichungen Dritter herangezogen wurden, wurden diese klar benannt;

4. Wenn aus anderen eigenen- oder Veröffentlichungen Dritter zitiert wurde, wurde stets die Quelle hierfür angegeben. Diese Dissertation ist vollständig meine eigene Arbeit, mit der Ausnahme solcher Zitate;

5. Alle wesentlichen Quellen von Unterstützung wurden benannt;

6. Wenn immer ein Teil dieser Dissertation auf der Zusammenarbeit mit anderen basiert, wurde von mir klar gekennzeichnet, was von anderen und was von mir selbst erarbeitet wurde;

7. Kein Teil dieser Arbeit wurde vor deren Einreichung veröffentlicht. *oder* Ein Teil oder Teile dieser Arbeit wurden zuvor veröffentlicht und zwar in: *Auflistung*

H. L. Williamson, T Mueller, M Angst, and G Balakrishnan, Growth of $YbFe_2O_4$ single crystals exhibiting long-range charge order via the optical floating zone method. J. Cryst. Growth, 2017.

Datum 3/18/2020

Unterschrift H.williamson

Abstract

The main focus of this thesis was dedicated to uncovering the true intrinsic magnetic and charge order properties of $YbFe_2O_4$, with a large emphasis on the crystal structure determination at 200 and 90 K. Previous research on its isostructural neighbor $LuFe_2O_4$, uncovered what was thought to initially be; "ferroelectricity through valence ordering". The high temperature RFe_2O_4 structure (space group $R\bar{3}m$) can be described as Fe^{2+} and Fe^{3+} valence mixed bilayers, separated by R^{3+}-O mono-layers. The concept of ferroelectricity through valence ordering was later suspended after the refinement on a highly stoichiometric $LuFe_2O_4$ single crystal, which resulted in a lower symmetry $C2/m$ space group, and charged rather than polar bilayers. This sparked new interest in this series of compounds and provided the inspiration for this thesis; to determine if highly stoichiometric $YbFe_2O_4$ exhibits ferroelectricity through charge ordering. The charge order investigated in this thesis exhibits the same incommensurate phase at room temperature, but in contrast to $LuFe_2O_4$, a second phase transition to a commensurate charge order was also observed. This commensurate charge order was refined in the $P\bar{1}$ space group using single crystal x-ray diffraction data measured at 200 and 90 K. This space group is representative of all temperatures until above the 3D charge order phase, at which point the charge order becomes diffuse and the structure can be refined in the $R\bar{3}m$ space group. For the first time, the magnetic phase diagram for highly stoichiometric $YbFe_2O_4$ has been established, and shows a ferrimagnetic state even in zero field, in the temperature range 240-260 K, which was not observed in $LuFe_2O_4$. From the analysis of neutron diffraction data measured on $YbFe_2O_4$, the same ferri (fM) and antiferromagnetic (AFM) spin structures intrinsic to $LuFe_2O_4$ are present in $YbFe_2O_4$, and deduced from almost identical intensity ratios of reflections measured along $(\frac{1}{3}, \frac{1}{3}, \ell)$, for the three magnetic domain populations. The two magnetic phases are newly described in the proper magnetic space groups; $P\bar{1}$ (fM phase) and $P\bar{1}'$ (AFM phase) in contrast to the previous refinement of $LuFe_2O_4$, where the observed reflections could not be refined in a proper monoclinic magnetic space group. The final charge order structure, determined through bond valence sum analysis, provides polar bilayers with an anti-polar stacking in the $P\bar{1}$ space group. This charge order is characterized by three modes; Y1, Y2 and T1+, and results from a combination of 2 irreducible representations, namely a Y1 and Y2 propagation vector. This was not considered before, as it is very unlikely for a first order charge order phase transition to be described by 2 irreducible representations. It was the successful refinement in the $P\bar{1}$ space group, which led to the understanding that a combination of 2 irreducible representations is required, as it is this that reduces the space group symmetry. The final correct spin-charge structure was determined through x-ray magnetic circular dichroism measurements, which yielded the same spin arrangement as that observed for $LuFe_2O_4$, except it is described in the lower symmetry $P\bar{1}$ space group, in contrast to the original refinement in the $C2/m$ symmetry.

Dedicated to Mum, Dad and my best friend's Shirin and Jess....

Took longer than I would have liked but... a Hobbit's tale by Hailey L. Williamson

Contents

1 | Complex ordering in correlated electron systems

Strongly correlated electron systems [1] offer a wide range of interesting phenomena. Some examples for these types of properties are colossal magnetoresistance (CMR); extremely large variations in resistance, induced by small magnetic field changes [2–4], and high temperature superconductivity [5, 6]; the resistance of the material drops abruptly to zero at a critical temperature. Another example of complex behavior researched primarily in this thesis is that of multiferroicity [7–15], where the coexistence of two specific ferroic orders occurs at a critical temperature. These types of intrinsic behavior all provide solid grounds for novel functionalities in the future technological advancement of electronics [15, 16]. The following sections offer a brief description of the types of magnetic order present in the compounds discussed in this thesis. The final parts of this chapter lead to the different types of multiferroic behaviors discovered to date, with primary focus on ferroelectricity by charge ordering.

1.1 Phase transitions and ordering phenomena

What is a phase transition? In common terms a phase transition is when a substance changes from a solid, liquid or gas state to a different state. A prime example more specific to this work would be a paramagnetic disordered phase ordering ferrimagnetically, below the Curie point (critical temperature) of a system [17]. Another example, although more complex is that of a charge ordering transition, in this case due to a strong interaction between electrons, the charges are localized on different sites leading to a disproportionation and an ordered super lattice [18]. When describing such phase transitions in a system, two types of classification are used; a first or a second order transition. The Landau theory [19] of phase transitions developed two criteria to describe the observation of subtle changes in physical properties of a material. The distinction between the two types of phase transitions is based on the derivatives of the free energy F and how they behave.

- First order phase transitions: this type of transition involves an abrupt (discontinuous) change in symmetry [20] which, is accompanied by a release of latent heat. In addition to latent heat, other thermodynamic variables are; internal energy, entropy, enthalpy and volume... etc. A discontinuous jump at the transition point is seen here in the first derivative of the free energy F, for

example with respect to the temperature T:

$$S = -\frac{\partial F}{\partial T} \tag{1.1}$$

- Second order phase transitions: in this case, the phase transition is continuous across the transition temperature. The first derivatives of the free energy are continuous but the second derivatives from the free energy are discontinuous, this is commonly seen as a pronounced anomaly in the specific heat, c;

$$c = \frac{T\partial S}{\partial T} = \frac{-T\partial^2 F}{\partial T^2} \tag{1.2}$$

The Landau theory, describes the energetics of a system in the vicinity of a phase transition, by expressing the relevant part of the free energy in terms of one or several order parameters. More crucially, the Landau free energy also depends on the order parameters of all relevant modes of the system [21,22]. The basic assumption starts when one considers that a system will be in a high symmetry state, usually at higher temperatures, which gives the free energy as:

$$F = F_0 + \Delta F(\eta^i) \tag{1.3}$$

Here, it assumes no lowering of symmetry due to a phase transition and therefore all order parameters are zero. The term F_0 is an analytical (smooth) function of temperature and $\Delta F(\eta^i)$ contains all the information regarding the dependence of the order parameter η, which is small in the vicinity of a phase transition T_c. The appropriate order parameter is zero in a disordered phase and non-zero in an ordered phase, where particular examples of types of order parameters are magnetization in a ferromagnet, amplitudes of the Fourier modes in a crystal or the degree of orientation of a nematic liquid crystal [17,23]. The development of this theory to include the order of a phase transition, by Landau's interpretation [19] could be theoretically described by the degree of the derivatives from the free energy of the system. The free energy can therefore be expanded in a Taylor series:

$$F(P,T,\eta) = F_0 + \alpha\eta + A\eta^2 + C\eta^3 + B\eta^4 + ... \tag{1.4}$$

The coefficients given in Eqn. 1.4 are functions of pressure, P, and temperature, T. As already mentioned, when there is a phase transition the order parameter $\eta \neq 0$ and in the case where $\eta = 0$ due to underlying symmetry differences, i.e the example given in the following for magnetic order and time reversal symmetry, the linear term of the order parameter vanishes. This means that only powers which are invariant with respect to the symmetry are allowed to be present in the polynomial $F_0(\eta)$ [24]. The well know case of magnetic order in a system, in which by time reversal symmetry all the spins will at the phase transition change their direction $\overrightarrow{S_i} \rightarrow -\overrightarrow{S_i}$, as a result leaves the free energy of the system unchanged. Due to the effect of time reversal, the symmetry is preserved leaving only even powers of the Taylor expansion shown Eqn. 1.5, and the expansion given for a second order phase transition is:

$$F(P,T,\eta) = F_0 + A\eta^2 + C\eta^4 + ... \tag{1.5}$$

The simplest interpretation to describe the phase change where $T = T_c$ can be achieved with the temperature dependence of the first coefficient A:

$$A(P,T) = a(T - T_c) \tag{1.6}$$

Given that $\eta \neq 0$ below the transition T_c and 0 for all temperatures above, the coefficient of the quartic term is $B(P) > 0$. Based on these conditions the Fourier approximation is then written as:

$$F(P,T,\eta) = F_0 + a(P)(T - T_c)\eta^2 + b(P)\eta^4 + ... \tag{1.7}$$

Solving Eqn. 1.7 by minimizing the free energy $\partial F/\partial\eta = 0$ and using the boundary condition of the order parameter $\eta = 0$ and $\eta \neq 0$ (above and below the phase transition), the solution to the minimized free energy is:

$$\eta^2 = \frac{a(T_c - T)}{2B} \quad \text{for} \quad (T < T_c) \quad \text{and} \quad \eta = 0 \quad \text{for} \quad (T > T_c) \tag{1.8}$$

For a second order phase transition, the order parameter η is proportional to the critical temperature T_c; $\eta \propto \sqrt{(T_c - T)}$ with the conditions assumed above.

1.2 Magnetic exchange interaction

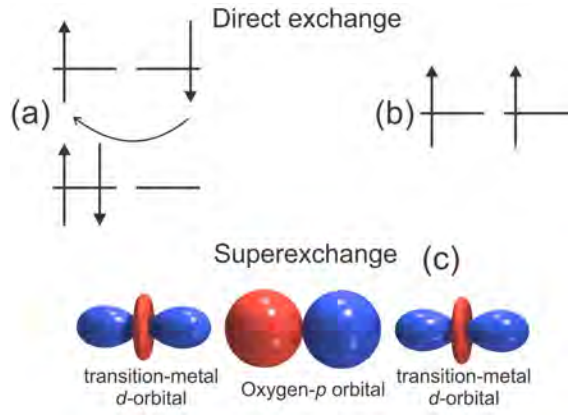

Figure 1.1: : Direct exchange interactions (a) A favored antiparallel alignment of spins, as it allows electrons to hop to neighbouring site. (b) the case for nearest neighbour parallel spins, hopping in this case is suppressed by the Pauli principle. Super exchange interaction (c), in this case two transition-metal d-orbitals are mediated by an oxygen p-orbital. Superexchange is far more common than direct exchange in complex oxides.

The magnetic ordering in complex correlated electron systems are governed by exchange interactions. In terms of the rare earth ferrite compounds investigated in this thesis both direct and indirect interactions need to be considered. The simplest type of interaction in a system is that of direct exchange. This mechanism only works when the electron orbitals of neighbouring atoms are wide enough to allow exchange and the hopping of free electrons. Two basic examples of direct exchange is given in Fig. 1.1, in (a) the neighbouring spins are antiparallel, in (b) they are parallel. In this case the antiparallel alignment and exchange interaction is preferred, as the hopping of the parallel spins is suppressed due to the Pauli principle [1]. Interestingly, much of the phenomena mentioned earlier in this chapter, can not solely be described by this type of interaction. The rare earth's have strongly localized $4f$ electrons, meaning they lie very close to the nucleus and direct exchange is unlikely to be effective in this case [17]. Another well known example of direct

[1]The Pauli principle: a fundamental rule in quantum physics which states that two or more identical fermions (particles with half integer spin) cannot occupy the same quantum state within a quantum system at the same time.

exchange not providing a solution for complex electron behavior is in antiferromagnetism in transition metal oxides (see Sec. 1.3). In this case, the antiferromagnetism of most transition metal oxides have very localized d-orbitals, which means hopping of electrons can only occur between orbitals on different atoms that are very close to each other. But as most antiferromagnetic insulators are transition metal oxides, the transition metal cations are separated by large oxygen anions. Therefore, one needs to consider the concept of in-direct interaction, also known as superexchange. This type of mechanism mediates the exchange interaction between two transition metal oxides via an oxygen p-orbital as depicted in Fig. 1.1 (c). Since superexchange involves an oxygen orbital as well as a metal atom it is a second order process and as a result derived from second order perturbation theory [17]. In the rare earth ferrites, superexchange is a primary mechanism that describes the magnetic interactions [3, 25]

1.2.1 Heisenberg and Ising spin model

The types of exchange interactions that occur in electronic systems can be described by various toy models. For (anti)ferromagnetic spin arrangements on a lattice, the initial starting point and basic Heisenberg model is given by the following Hamiltonian:

$$\hat{H} = -\frac{1}{2}\sum_{\langle ij \rangle} J_{ij}\mathbf{S}_i \cdot \mathbf{S}_j \tag{1.9}$$

Here, the constant J_{ij} is the exchange integral, the symbol $\langle ij \rangle$ below the $\sum$ denotes the sum over neighbouring spins and the -$\frac{1}{2}$ denotes the spin of an electron. The spins $\mathbf{S}_i$ and $\mathbf{S}_j$ are representative of three dimensional vectors that can point in any direction in space [17]. This is however a simplified case, in more complex systems; in particular transition metal oxides and rare earth ferrites [25], this basic model will often not support the magnetic behavior observed in experiments. As already mentioned, the orbitals of transition metal oxides do not extend far from the nucleus, therefore mediation via neighbouring oxygen anions are required. A more involved and applicable Heisenberg Hamiltonian with additional terms is given as:

$$\hat{H} = -\sum_{ij} J_{ij}\mathbf{S}_i \cdot \mathbf{S}_j + g\mu_B \sum_j \mathbf{S}_j \cdot \mathbf{B} - D\sum_{\langle i \rangle}^{N} (\mathbf{S}_i^z)^2 \tag{1.10}$$

The first term in Eqn. 1.10 is the Heisenberg exchange energy already provided in Eqn. 1.9. The first added term on the right is the Zeeman energy including the Landé g factor. The Zeeman energy describes the potential energy of a magnetized body in an external magnetic field, the Landé g factor incorporates the two spins of the electron (up and down) considering the electrons orbital and angular momentum. The addition of the Zeeman term is necessary to describe the order in the system with an external field applied (fM or AFM). In antiferromagnets the Zeeman term is always required as the net moment is zero, due to the antiparallel arrangement of spins. A ferrimagnet which, also intrinsically has two magnetic sub-lattices of anti-parallel spins, has inequivalent moments and will lead to a net magnetization. There are however fM systems with only antiferromagnetic interactions, this

was observed for example in the $R\mathrm{Fe_2O_4}$ series for a single Fe-O bilayer [25]. The only differences between fM and AFM orders are the exchange interaction i and j, which for an ferromagnet $J_{ij}>0$ and for an antiferromagnet $J_{ij}<0$. The last term $D\sum_{\langle i\rangle}^{N}(\mathbf{S}_i^z)^2$ represents single ion anisotropy (D= anisotropy constant). In crystal fields, this effect is commonly seen for example in magnetization experiments, for a system with sufficiently high magnetic anisotropy the spins prefer to align along a particular direction, commonly named the easy axis. Along this easy axis the magnetization is much higher than that along the other crystallographic directions and this is a common feature in the rare earth ferrite's [26, 27].

The spin model which is representative of the compounds investigated in this thesis is the Ising spin model. The selection of the Ising model stems from the large magnetic anisotropy of the Fe^{2+} and Fe^{3+} spins observed in magnetization measurements, where the moments prefer to align $||c$. A theoretical study by [25] on the Ising ferrimagnetism of $\mathrm{LuFe_2O_4}$, using density functional calculations further solidified this assertion at least in terms of interlayer interaction. In this simulation spins in a bilayer of the unit cell were allowed to point along several directions; the calculation supported the experimentally observed c-axis crystalline anisotropy. In contrast to the Heisenberg model, the spins are thus restricted to up and down, and considers only the z component of the spin. The basic Hamiltonian of the Ising model (when the limit of $D\rightarrow\infty$) is written as:

$$\hat{H}=-\frac{1}{2}\sum_{\langle ij\rangle}JS_i^z\cdot S_j^z \tag{1.11}$$

Identical to the Heisenberg Hamiltonian, the Ising model contains the Zeeman term, but for the more complex magnetism and intralayer interactions, concurrent in $\mathrm{LuFe_2O_4}$ an additional term is also required, namely the demagnetizing field, the latter also present in ferromagnets. For example, when a ferromagnetic material is magnetized by an applied field, magnetic poles are formed at the opposite ends of the specimen. These poles cause, within the sample magnetic fields in the opposite direction to the applied field. The demagnetizing field is given by $H_d{=}NM$. The demagnetizing factor N is representative of the shape of the sample, this is often a complex correction, and in most simplified cases is calculated in terms of a sphere or ellipsoid. These combined with the Zeeman term allows one to view not only superexchange interaction in one bilayer, but also the interactions to that of neighbouring bilayers. The final Ising Hamiltonian can be given as:

$$\hat{H}=-\frac{1}{2}\sum_{\langle ij\rangle}JS_i^z\cdot S_j^z+g\mu_B\sum_j\mathbf{S}_j\cdot H_d\mathbf{B}-D\sum_{\langle i\rangle}^{N}(\mathbf{S}_i^z)^2 \tag{1.12}$$

The following section describes the main types of magnetic orders based on spin interactions discussed in this section.

1.3 Types of magnetic ordering

The four main types of collinear magnetism are sketched in Fig. 1.2. For the rare earth ferrite compounds of concern in this thesis, both antiferromagnetic and ferrimagnetic collinear orderings occur. However, there are a number of additional

magnetic phenomena [17] which can reside in complex correlated electron systems such as; helical magnetic order [28, 29], superparamagnetism [30], itinerant magnetism and Pauli paramagnetism [31] to name a few, but these are not relevant for this thesis and therefore omitted from discussion.

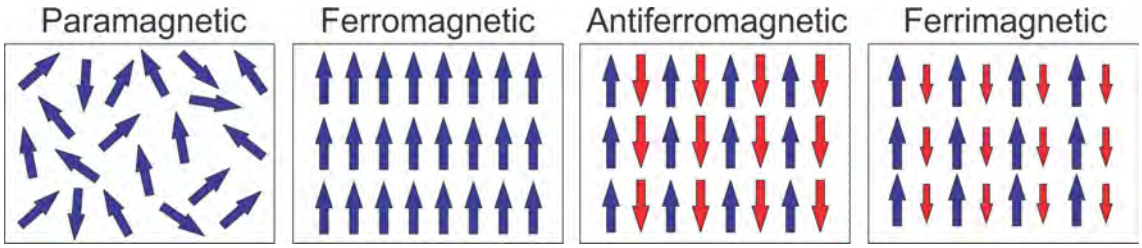

Figure 1.2: A basic set of diagrams including the four main types of magnetism: (a) paramagnetism, (b) ferromagnetism, (c) antiferromagnetism and lastly (d) ferrimagnetism

- **Paramagnetism**: at sufficiently high temperature materials containing ions with partially filled d or f shells, exhibit a paramagnetic state (see Fig. 1.2 (a)). The individual atoms or ions have magnetic moments but these are fluctuating and the arrangement is one of complete disorder in zero magnetic field. However, upon cooling to a critical temperature an ordering of the spins can develop.

- **Ferromagnetism**: this type magnetic ordering shown in (b) of Fig. 1.2 favours a parallel alignment of spins since the exchange interaction between neighbouring spins is $S_{ij}>0$ (see Sec. 1.2.1), and as a result yields a very high net magnetization [8]. A ferromagnet also has a spontaneous magnetization, which occurs without the need of an externally applied magnetic field, making ferromagnetic materials prime candidates for use in future electronic devices. The temperature at which a ferromagnetic material ceases to exhibit a spontaneous magnetization is called the Curie temperature T_{C}.

- **Antiferromagnetism**: in the case of an antiferromagnetic material, adjacent spins lie antiparallel as depicted in Fig. 1.2 (c). Contrary to ferromagnetism, the exchange interaction between the neighbouring spins is negative with $S_{ij}<0$, and the resulting arrangement can be considered as two interpenetrating sub-lattices, one with the spins pointing up and the other the spins point down. Ordering of this type of magnetism occurs below a critical Néel temperature T_{N}, where one set of spins will order spontaneously at this temperature the other sub-lattice is magnetized in the same way but with the spins pointing in the opposite direction. Heating above this temperature will lead to a paramagnetic state. These features make this type of magnetic ordering in some systems very complex.

- **Ferrimagnetism**: this type of magnetic ordering is a special case of antiferromagnetic ordering, the spins also prefer an anti-parallel alignment, with a negative exchange interaction $S_{ij}<0$. The primary difference is the existence of a net moment, which for example could be due to inequivalent spins e.g. on different elements or valence states, a simplified model is given in Fig. 1.2 (d). However, in more complex structures, such as $R\mathrm{Fe_2O_4}$ (R=rare earth) the net magnetization is determined by the different number of spins pointing in the same direction, arising from spin frustration [25, 32, 33] (see Chapter. 7).

1.3.1 Spin frustration and spin glass states

Spin frustration and the occurrence of spin glass states in materials often come hand in hand. The term spin frustration comes originally from the work by [34, 35] and exists when spin interactions are not fulfilled. The typical example of geometric frustration resides on a 2D triangular lattice, where the neighbouring atoms have an antiferromagnetic exchange interaction and presents three spins at each apex of the triangle [36], graphically shown for an Ising system in Fig. 1.3 (left).

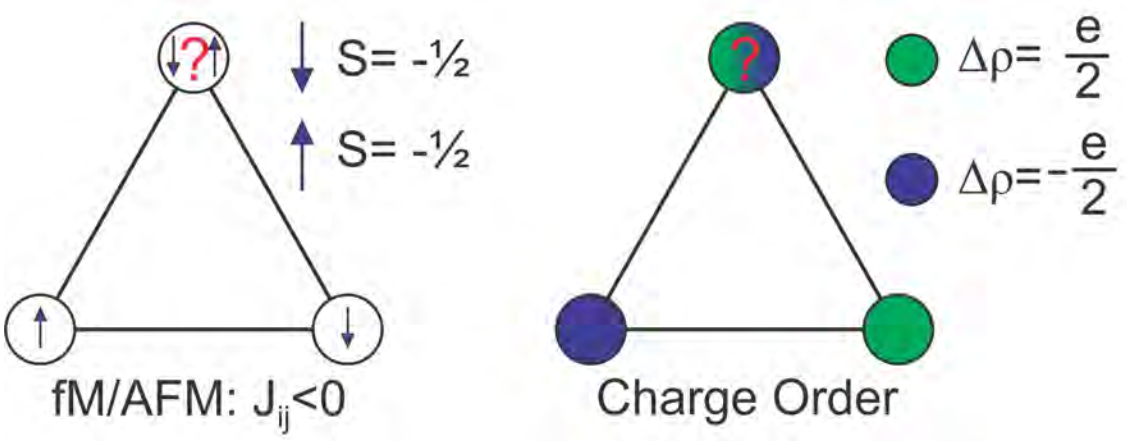

Figure 1.3: The concept of spin frustration vs charge frustration on a 2D triangular lattice. Left: Ising spins in an anti/ferrimagnetic configuration, 2 spins ↑ and ↓ with third site unfulfilled due to spin ordering. Right: the same situation but in the case of ion/valence charge distribution of an anti/ferrimagnet. Taken from [36] and adapted.

In this particular case only two of the three spins in this configuration can be simultaneously aligned anti-parallel, according to the antiferromagnetic spin exchange interaction. The third spin, by taking either and up or a down configuration when considering an Ising spin model is not permitted. This can cause a 'spin freezing' from geometric frustration leading to exotic ground states, in particular spin glasses [37, 38], where the spins freeze in unusual patterns [39, 40] preventing long-range order. The mixed interaction of spins are often characterized by random, but cooperative, freezing of spins at a well defined temperature (T_f). Below this transition a metastable frozen state appears without the typical long-range order [17, 41]. This phenomena occurs in systems with frustrated interactions, a prime example being oxygen vacancies in transition metal oxides. This particular feature is of great importance within the context of $YbFe_2O_4$ (see Sec. 4.2.1) and the other rare earths in this series, which exhibits spin freezing and competition between ferri and antiferromagnetic orders [32, 33, 42, 43]. The same consideration can also be made for the relative charge arrangements of the individual ions on a triangular lattice, depicted in Fig. 1.3 (right).

1.4 Charge ordering

We have now discussed the ordering phenomena of spins and the different types of magnetic order which arises from this. One may have to consider also in many

complex correlated electron systems that charge ordering as well as magnetic ordering may take place. A prime example and the main focus of this thesis is that of charge ordering through valence electrons in compounds with the chemical formula $R\mathrm{Fe_2O_4}$, where R^{3+} is a candidate rare earth material. However, for it to follow suit and provide overall chemical neutrality, the iron atoms in the system would theoretically take $\mathrm{Fe}^{2.5+}$ valence, which supports the $\mathrm{Lu/Yb}^{3+}$ and O^{2-}. Therefore the localized electrons in the system form a mixed valency of Fe^{2+} and Fe^{3+}. It is this mixed valency that gives rise to both fM and AFM order, via intricate superexchange interaction and complex coordination of the $3d$ orbitals (and how the orbitals are filled) in this series of multiferroic compounds. The mixed valency not only leads to complex magnetic orders but simultaneously produces charge ordering in the system. Charge ordering, often classified by a first or second order phase transition and largely inherent in transition metal oxides or organic molecular solids [44], develops in part from the strong interaction between electrons, which can in special cases localize the charges on different sites leading to a disproportionation and ordered sub-lattice [18, 45, 46].

There are special conditions in which ferroelectricity from charge ordering can arise, i.e CO is non-centrosymmetric. One example of CO is site centered charge ordering, in this case the sites become inequivalent but do not break spatial inversion symmetry, as there has been no shift of the site charges forming a net dipole moment [18]. A second type of charge ordering is bond centered, also known as dimerization, for this case the sites are equivalent but the bonds between the sites are not and thus the strong and weak bonds alternate. The third case of charge ordering is one that combines the first two types of charge order; site centered and bond-centered. The situation with simultaneous site and bond-centered charge ordering breaks spatial inversion symmetry, and as a result each molecule develops a net dipole moment sometimes resulting in a ferroelectric state, when all dipoles point in the same direction. However, in more complex electronic systems, the polarized state does not always result in ferroelectricity, in fact there are a number of systems which exhibit antiferroelectricity. This type of mechanism, in terms of charge ordering is the opposite to ferroelectricity, in which one set of electric dipoles will constitute in a net polarization in one direction to an adjacent set of dipoles that are oriented in the opposite direction (antiparallel), resulting in no net polarization. (see Sec. 1.8 and Chapter 6 of this thesis). In this case, antiferroelectric materials could potentially be tuned via the application of an external electric field to a ferroelectric state [47], or by other mechanisms like strain [11]. The localization of charges which were once on an equivalent site through charge ordering will lead to a disproportionation and super lattice due to the lowering of symmetry. This type of CO has been observed in $\mathrm{LuFe_2O_4}$ where the CO super-structure reduces the symmetry from $\mathrm{R}\bar{3}m$ to at least $C2/m$ [48]. In systems which exhibit CO it is likely that there is also a coupled magnetic order. For ferroelectricity to arise in such materials both spatial and time inversion symmetry must be broken, this in some cases can lead to a coupling between each order. These are known today as multiferroics.

1.5 Orbital ordering

We have discussed magnetic ordering and charge ordering, but one final consideration is that of orbital ordering. This particular degree of freedom indicates the

emergence of a broken symmetry state in which localized orbitals form a regular pattern, in a similar way as spins do in magnetically ordered structures. A clear example of this is shown in Fig. 1.4, on $La_{0.5}Sr_{1.5}MnO_4$ [49], more specifically the MnO_2 planes. In this projection, one can see spin, charge and orbital ordering. The solid line is representative of the $I4/mmm$ unit cell. The red dotted line represents the CO superstructure cell and the largest cell (blue dotted line) presents the Jahn-Teller[2] [50] orbital order unit cell. This is quite a complex system, but can be compared in terms of $LuFe_2O_4$ and $YbFe_2O_4$, as both exhibit a CO superstructure cell and complex magnetic ordering. The CO in this case is based of the $Fe^{2+/3+}$ valence, for the example provided here the CO stems from the $Mn^{3+/4+}$ valencies. To observe orbital order directly, the most common method is the use of soft resonant x-ray diffraction, and for this case, probing the manganese L_{III} and L_{II} edges [51].

The difficulty in understanding orbital order arises from the prerequisite information of the structure, so depending on what environment a transition metal forms with neighbouring oxygen atoms will dictate the type of crystal field splitting. For example a paper by [52], considers a transition metal oxide in a perovskite structure, surrounded by 6 O^{-2} atoms. The arrangement of oxygen atoms alone will create a crystal field splitting of the d-orbitals and as a result hinder the free rotation of the electrons, quenching the orbital angular momentum. These factors alone, can make determination of how the orbital order effects the system complex, but necessary as it allows one to better understand metal-insulator transitions as well as; high temperature superconductivity and colossal magnetoresistance [52]. For the rare earth ferrites, the orbitals of main concern are those given in Fig. 1.5 (left). For a $3d$ transition metal there are 5 possible orbitals, which can be sub-categorized into 2 e_g orbitals; $3z^2-r^2, x^2-y^2$ and 3 t_2g orbitals; zx, yz, and xy. These two classes of orbitals are better known as crystal field splitting and differ strongly depending on the environment the orbitals occupy; octahedral, tetragonal or pyramidal. For the case of an Fe^{2+} atom, which has the electronic configuration $^3d_6$, in general, the lowest t_{2g} levels will be filled before the higher energy e_g orbitals. However, the order to which the orbitals are filled can be far more complex and depends on; the competition between crystal field energy, Coulomb energy and the pairing energy P, which is the energy required to place two electrons in the same

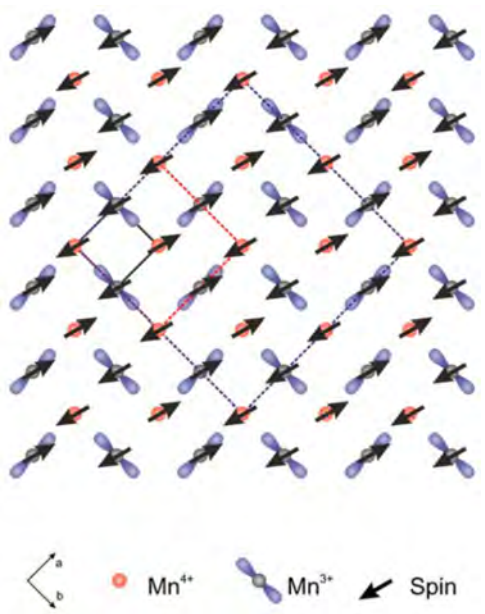

Figure 1.4: The MnO_2 plane of $La_{0.5}Sr_{1.5}MnO_4$ showing charge, orbital and spin ordering. The black solid line represents $I4/mmm$ original unit cell. The unit cell describing the CO superstructure is marked by the red dotted line. The larger orbitally ordered cell is given by blue dotted line. Adapted from [49].

[2]Jahn-Teller theorem: whenever there is a non-linear molecule with a spatially degenerate electronic ground state, it will undergo a geometrical distortion that removes the degeneracy, because the distortion lowers the overall energy of the species.

orbital. If the crystal field energy is lower than the pairing energy, each electron will fill each orbital singly before any orbital becomes doubly occupied. This is known as the weak field case and shown in Fig. 1.5 (right, (a)). The second possibility is when the crystal field energy is higher than the pairing energy, the electrons will doubly occupy the lower energy orbitals before attempting to fill the higher energy level orbitals (e_g), and known as the high field case Fig. 1.5 (right, (b)). This is of course a more simplistic example of crystal field splitting, more complicated orbital environments can occur e.g phenomena such as Jahn-Teller distortions [50,53]. This degree of freedom has been pondered for $LuFe_2O_4$ theoretically [54–56], which in this case has a trigonal-bipyramidal rather than a octahedral crystal field environment, and suggests a strong likelihood for orbital order. However, as there have been large discrepancies in the suggested and refined CO structures from experimental data, it is difficult to say if the predicted and theorized orbital order is correct, outside the low temperature phase. X-ray Magnetic circular Dichroism (XMCD) data shows there is no orbital order [48], but below this phase it is yet to be elucidated experimentally.

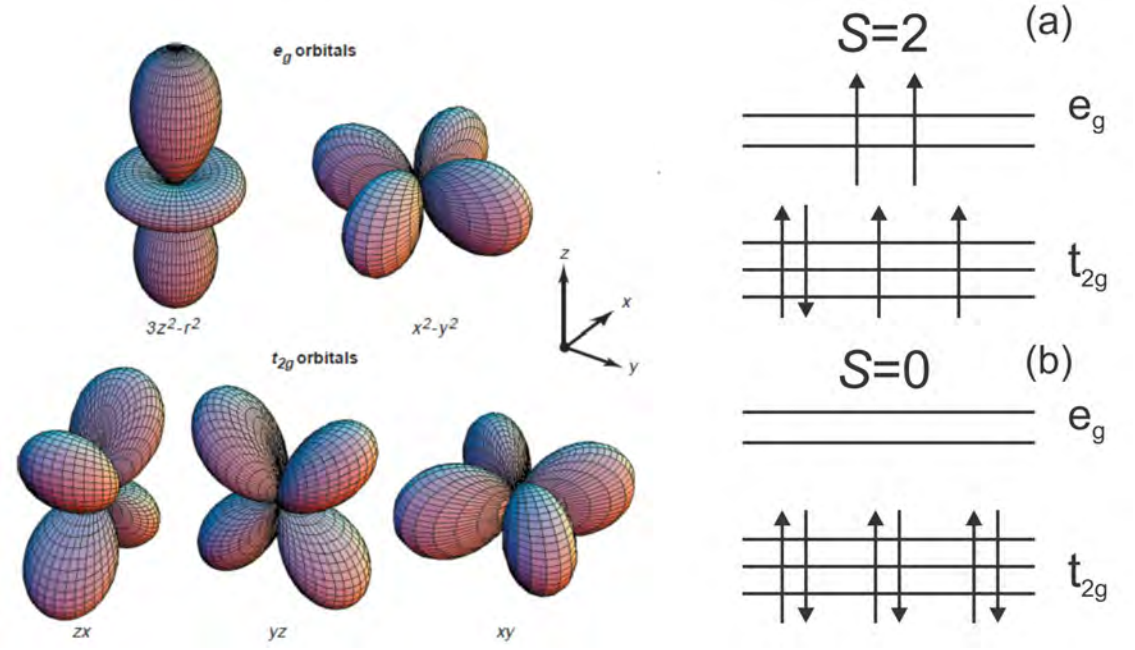

Figure 1.5: 3d transition metal orbitals and spin configuration. Left: the shapes of the 5 possible $3d$ orbitals, Image adapted from [52]. Right: an example of (a) high-spin (S=2, weak-field) and (b) low-spin (S=0, strong field) electronic configurations for a $3d^6$ ion (e.g Fe^{2+}). Image adapted from [17].

1.6 Multiferroics

The term multiferroic, describes the coexistence of more than one ferroic order for example; ferroelectricity and ferromagnetism, if these are coupled, the magnetism is switchable with an externally applied electric field and vice versa. For a much more detailed view of the types of multiferroics, and what classifies them as proper and improper please refer to [9, 12, 26, 57]. However, the basics will be briefly outlined in the following subsections. The general difficulty with this class of materials is the coupling of a magnetic order and ferroelectricity. Magnetic materials require a

partially filled outer electron shell to allow for electron transfer and exchange seen in metallics and semi-conducting compounds. Materials that exhibit ferroelectricity are commonly ceramic materials, and transition metal oxides but in this case require an empty d orbital. The traditional mechanism of ferroelectricity sees a collective shift of cations and anions inside a periodic crystal induce a bulk electric polarization, in which the mechanism of covalent bonding or electron pairing provides a virtual hopping of electrons, from one filled oxygen shell to and empty d shell of a transition metal ion. In this process the material as a result is typically insulating [58]. From these two very opposite classes of material, how can a coupling occur between these two ferroic orders?.

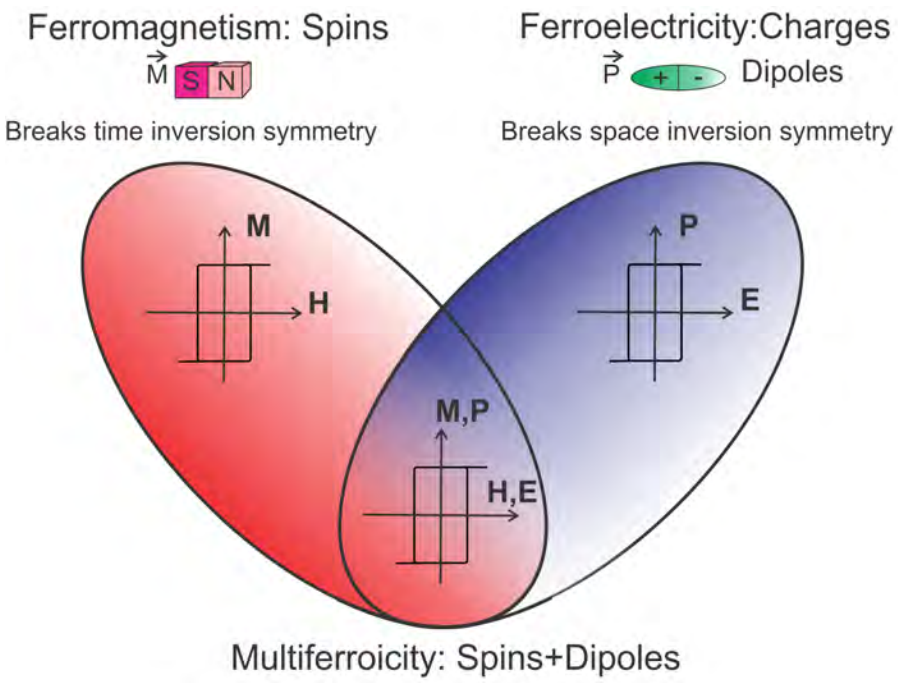

Figure 1.6: Multiferroic overlap. The diagram shows the two main types of ferroic order. Left: Ferromagnetism, the control of sample magnetization M which occurs spontaneously and of course with an externally applied field H. Right: Ferroelectricity where the polarization P is controlled with an externally applied electric field. The overlapped section shows the coexistence of both ferroic orders, and in particular a magnetoelectric material which can use an external magnetic field to electrically polarize the sample and vice versa. Concepts taken from [7, 26] and adapted.

In the well known case of magnetoelectric materials, which allows one to use an externally applied magnetic field to electrically polarize a sample and vice versa (illustrated in Fig. 1.6), the symmetry of spatial inversion is broken when ferroelectrics develop their electric dipole moment, and time reversal is broken when ferromagnets become magnetic. The are a number of different mechanisms that allow for this required symmetry breaking, the main examples are covered in the following section.

1.7 Classes of multiferroics

There are four types of ferroic order, ferromagnetism, ferroelectricity, ferroelasticity and ferrotoroidicity and of these mechanisms their exist two classes of multiferroics:

proper and improper which, form Type I and Type II multiferroics. The question then is, what are the definitions of these different classes? the answer lies in the driving force (the primary order parameters) that lead to ferroelectricity. The general definition of a proper mulitferroic is one who's primary order parameter is ferroelectric distortion. The classification of improper multiferroic materials stem from non-conventional ferroelectric induction in which electron pairing is the main driving force of the transition. Improper multiferroic materials induce ferroelectricity from some complex structural change or magnetic ordering. These days, it is common to include all types of magnetism in to the definition of multiferroic. It was, for some time more limited to ferromagnetism (with spontaneous magnetism) which is the best primary order candidate. However, a large majority of compounds which exhibit a coupling of more than one ferroic order are not ferromagnetic but rather antiferromagnetic (not classed as a ferroic order), but the definition has been expanded to include non-primary order parameters.

1.7.1 Proper Multiferroics (Type I)

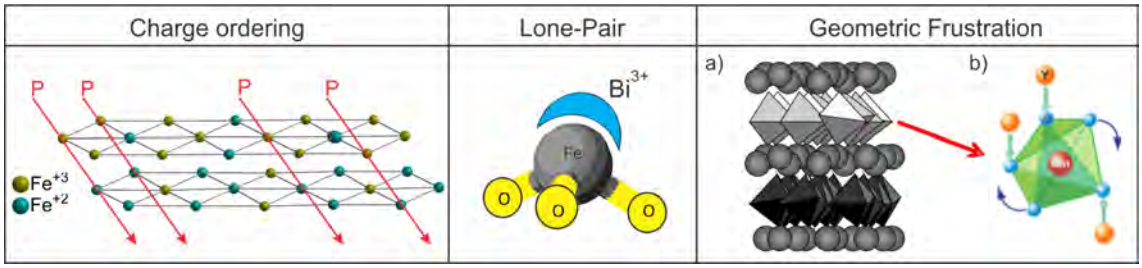

Figure 1.7: Schematic view of each Type I multiferroic mechanism: charge ordering showing two bilayers of $LuFe_2O_4$ with driven polarization for Fe^{3+} to Fe^{2+}. Design concept taken from [18]. Lone-pairs: example of $BiFeO_3$ stereo-chemically active Bi^{3+} lone pair (blue) and Fe-O environment (grey/yellow) where a resultant hybridization of the Bi and O ultimately results in ferroelectricity, concept taken from [57, 59]. Geometric frustration in the case of $YMnO_3$, which stems from close packing of MnO_5 polyhedra (grey (a)) that lie between the Y layers. The bucking of the polyhedra influences long-range dipole-dipole interaction, causing the oxygen atoms to generate a stable ferroelectric state (b). Taken from [57, 60] and adapted.

Charge ordering

At a charge ordering transition T_{CO}, the system undergoes a symmetry breaking process, where a single crystallographic metal site above this transition has an average charge (valence state), below this critical temperature, two or more inequivalent sites with different charges are observed. Furthermore, the distinction of the different charge sites can be obtained through bond valence sum (BVS) analysis [61]. As described earlier in Sec. 1.4, there are different types of charge ordering a system can exhibit, for example site centered or bond centered charge ordering, the former in some complex crystal structures can lead to a ferroelectric state, but it is usually a combination of these two mechanisms which results in ferroelectricity. There are a number of systems that exhibit charge ordering for example: half doped manganites $A_xB_{1-x}MnO_3$ [49] where A is a trivalent ion (Bi, La, Pr, Sm, Y) and B is a divalent alkaline rare-earth element, and Fe_2OBO_3 [62]. Unfortunately none have currently lead to the desired result of ferroelectricity, at least in terms of experimental observation. Another, but rather prime example is that of multiferroic $LuFe_2O_4$. Once

considered to be the first compound to exhibit ferroelectricity through charge ordering [63], it was suspected that based on the mixed Fe valency of the bilayers would drive a net polarization. For this to occur, each identical bilayer would consist of one layer with majority Fe^{2+} and the other Fe^{3+}, this charge coordination would of course result in a net polarization inducing ferroelectricity. A sketch of this is shown in Fig. 1.7 (left panel). However, as with many transition metal oxides, stoichiometry is a key factor and by itself strongly dictates the intrinsic properties of the system.

Lone-pair Multiferroics

A good example of a lone-pair multiferroic compound is the very well knows $BiFeO_3$ [64] which remarkably is ferroelectric, ferroelastic and weakly ferromagnetic [11]. In this particular mechanism, the Bi^{3+} (A-cation) has a stereochemically active $6s^2$ lone pair (a local electronic dipole). The A-cation drives a displacement of the B-anion site, which in this case is Fe^{3+}, and contributes to the magnetism in the system (see Fig. 1.7 middle panel). The ferroelectricity in the system stems from the active $6s^2$ lone pair that causes the Bi 6p (empty) orbital to come much closer in energy to the oxygen O 2p orbitals. In the process a resultant hybridization of the Bi and O orbitals drives an off-centering of the cations towards neighbouring anions thus carrying an electric dipole moment driving a net polarization that induces ferroelectricity [11].

Geometrically frustrated Multiferroics

Materials which possess ferroelectricity from geometric frustration through various atomic positioning is still largely under investigation. The candidate compound, hexagonal-type $YMnO_3$ has been well studied over the years [65, 66] and its complex structure provides a basis for the onset of ferroelectricity through net electric polarization. Its hexagonal structure consists of MnO_5 trigonal bipyramids which are separated by monolayers of Y^{3+} (see Fig. 1.7 right panel (a)). For this system to form an energy favorable state, a distinct close-packing of the MnO_5 polyhedra between the Y^{3+} layers occur. This close-packing results in a structural distortion or rather buckling of the polyhedra and as a result influences long-range dipole-dipole interaction, where rotation of the oxygen atoms generate a stable ferroelectric state (shown in 1.7 right panel (b)).

1.7.2 Improper Multiferroics (Type II)

Spiral magnetic structures

The first common case of this type of ferroelectricity (which is a non-conventional) is spin-spiral magnetic structures, and a solid example of this is seen in the perovskite-type $R\mathrm{MnO}_3$ series [9]. The effect of spiral magnetic ordering originates from exchange-striction, described as lattice relaxation in a magnetically ordered state. A typical mechanism which promotes the ferroelectricity in such systems is the Dzyaloshinskii-Moriya (DM) interaction [67] shown in Fig. 1.8 (left panel (a)), where the exchange between the spins of a transition metal ion, is in the majority of cases

mediated by the surrounding ligands (typically oxygen atoms). In a chain of spiral spins, depending on the exchange-striction between each DM interaction, the negative oxygen ions form in one specific direction, perpendicular to the positively charged magnetic spin-chain and a result induces ferroelectricity shown in Fig. 1.8 (left panel (b)).

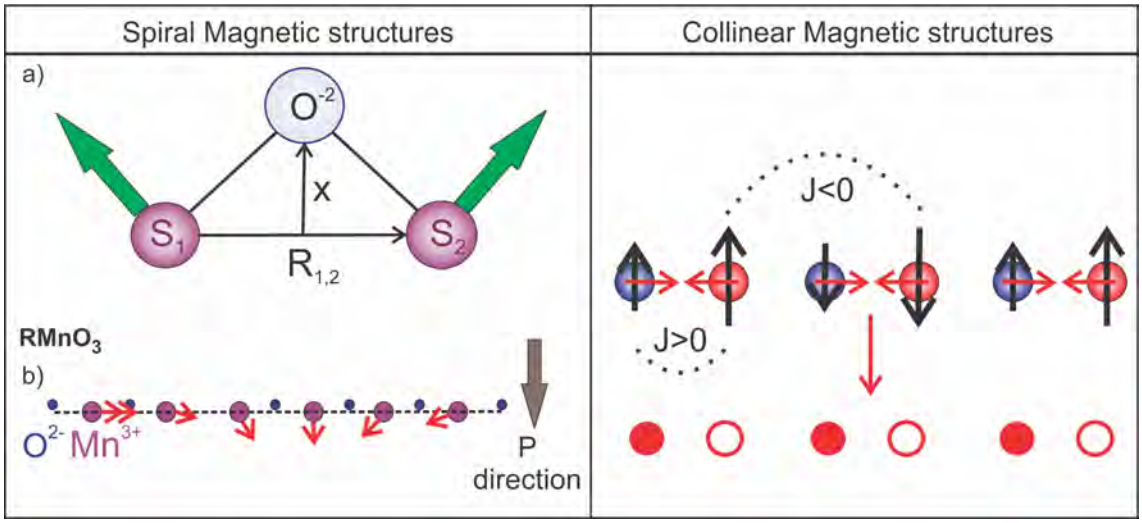

Figure 1.8: Schematic view of each Type 2 multiferroic mechanism: spiral magnetic order (left panel) in (a) the Dzyaloshinskii-Moriya interaction between two spins in a chain and oxygen ligand. The shift in x forms the exchange-striction between S_1 and S_2. In (b) this effect is shown for a set of spins in a chain, for the compound $R\mathrm{Mn_2O_5}$ [9] where the exchange-striction due to the DM effect induces a net ferroelectric polarization, **P**. Collinear magnetic order: (right panel), in this diagram a set of collinear spins that exhibit nearest neighbour ferromagnetic exchange (j>0) and next-nearest neighbour antiferromagnetic exchange (j<0).

Collinear magnetic structures

Another type of improper muliferroic, is one where the ferroelectricity originates from a collinear magnetic structure. This type of magnetic ordering may for example originate from highly frustrated Ising spins with a ground state co-ordination ↑↑↓↓ on alternating ions [9], see Fig. 1.8 (right panel). As a result of this spin ordering, there is nearest neighbour ferromagnetic ordering and next-nearest neighbour antiferromagnetic interaction, which leads to a net dipole moment (depicted in red of Fig. 1.8, right panel). This is a prime example of polarization induced by site centered charge and spin orders, where the ions are shifted away from centrosymmetric positions by exchange-striction, breaking spatial inversion symmetry and inducing a ferroelectric polarization, an example can be seen in $\mathrm{YMnO_5}$ [68].

1.8 Antiferroelectrics

The topic of antiferroelectrics [3, 69–71] is sometimes dismissed, when a compound deemed multiferroic does not turn out to exhibit ferromagnetism coupled with ferroelectricity. However, as it happens there are substantially more cases of antiferroelectricity, often due to the complex nature of the magnetism and charge distributions. An antiferroelectric material consists of an ordered array of electric dipoles but with adjacent dipoles oriented in the opposite direction, zero net polarization. This is the

opposite to ferroelectricity, where all dipoles align along the same direction. There may be ways to tune an antiferroelectric state to a ferroelectric state via strain induced engineering in thin films [11], or by electric-field induced switching [72]. These mechanisms provide a positive outlook for non-conventional multiferroics, as so few materials exhibit the desired ferromagnetism and ferroelectricity as primary order. The possibility of being able to switch part of the sample polarization with the application of a steady electric field, expands the potential for future use in electronics.

2 | The $R\mathrm{Fe_2O_4}$ family

2.1 A short timeline of events

The compounds of the $R\mathrm{Fe_2O_4}$ family each contain a rare earth ion, R^{3+} with possible candidates: Y, Ho, Er, Yb, Lu, and In. The initial synthesis and structural clarification of Ho, Er, Tm, Yb and $\mathrm{LuFe_2O_4}$ in the $R\bar{3}m$ space group was successfully achieved in 1974 by Kimizuka *et al.* [73] (later again by [74]), with more detailed crystal growth studies on $\mathrm{YbFe_2O_4}$ [75] and $\mathrm{YFe_2O_4}$ [76] published soon after.

The oxygen content in these systems is variable, and synthesis was performed using a mixed $\mathrm{CO_2/H_2}$ partial pressure atmosphere to control the stoichiometry, using an optimum temperature 1200°C. Several years after the discovery of this perplexing series, focus was then placed on $\mathrm{LuFe_2O_4}$, $\mathrm{YbFe_2O_4}$ and $\mathrm{YFe_2O_4}$, most likely due to the easier stabilization of synthesis. For example $\mathrm{InFe_2O_4}$ to date has reports only on powder samples, which often have large $\mathrm{Fe_3O_4}$ impurities, greatly obscuring the intrinsic properties [77]. Efforts were then made to fine tune the synthesis and crystal growth of Y, Yb and $\mathrm{LuFe_2O_4}$ and thus establishing accurate phase equilibria diagrams [76, 78, 79]. This was followed shortly by publications of the first macroscopic measurements investigating the magnetic properties of the systems [80–84] and the first successful structural refinement of $\mathrm{LuFe_2O_4}$ by [85]. The compounded interest in $\mathrm{LuFe_2O_4}$ and establishment of the phase equilibria diagrams opened up the idea that oxygen stoichiometry plays a large role in the properties of the system. Experimentation with synthesis conditions as a result, provided a number of magnetization curves indicating variations in transitions and temperature onset [82–84]. Different forms of scattering techniques [86, 87], which uncovered strong Bragg peaks along $(\frac{1}{3}, \frac{1}{3}, \ell)$, suggested that $\mathrm{LuFe_2O_4}$ has a"$\sqrt{3} \times \sqrt{3}$" type superstructure [88]. The first hint of charge freezing

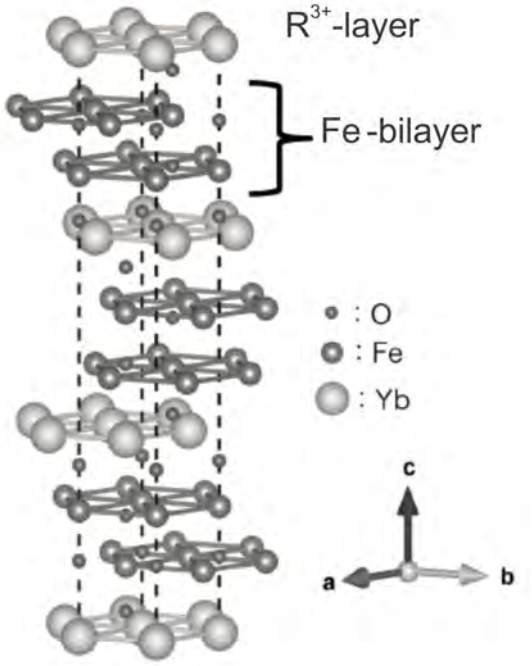

Figure 2.1: The high temperature $R\mathrm{Fe_2O_4}$ (R=rare earth) crystal structure in the $R\bar{3}m$ space group. Shown, is doubly stacked iron triangular layers (Fe-bilayer) separated by single rare-earth triangular layers (R^{3+}-layer).

in $LuFe_2O_4$ was obtained by early Mössbauer experiments [89], which are however not sensitive to the distinction between long-range ordering and disordered freezing. All of this aided the revelation of not only ferri and antiferromagnetism but also frustrated magnetism [36], where in the most stoichiometric samples a ferrimagnetic phase at T_N ~220 K was classified. In high magnetic field measurements at low temperatures, the observed saturation moment suggested a 2:1 ferrimagnetic spin structure with giant coercive fields of up to ~10 T [83, 84], in order to switch the magnetization direction. This expansion of knowledge was not limited to $LuFe_2O_4$ at this point, but studies into the magnetic phases present in YFe_2O_4 [80, 89–95] and $YbFe_2O_4$ [84, 87, 89, 96, 97] were prominent, some of which also described the occurrence of super-structure reflections. It was not until the late 90's, when the concept of incommensurate charge ordering in the mixed valence system $LuFe_2O_4$ was presented by Ikeda *et al.* [98], shortly after the term multiferroic was founded in 1994 by Schmid [99]. From this point the remaining rare earth candidates in this series were put to one side as many focused their efforts on the race to see if the charge order and magnetism of the system couple, which would lead to the first claim of ferroelectricity via charge ordering in $LuFe_2O_4$. The concept of ferroelectricity in this system was based on the structure which contains mono-layers of R-O separated by bilayers of Fe-O. Investigators then speculated that a charge distribution of the iron valency could occur in such a way, that one layer of each bilayer would contain a majority of Fe^{3+} ions and the other majority of Fe^{2+} ions, ultimately driving a net polarization across the sample (refer back to Sec. 1.7.1 and Fig. 1.7, left).

It was further experimentation with electron microscopy and x-ray/neutron scattering on $LuFe_2O_4$ [88, 98, 100–103] that provided solid evidence of charge order superstructure reflections in the $hh\ell$ plane when cooling through T_{CO}=320 K, and situated at positions $(\frac{N}{3}, \frac{N}{3}, \ell)$, where N=integer. In 2005, Ikeda *et al.* [63] published an influential Nature paper, declaring $LuFe_2O_4$ to be the first compound to exhibit ferroelectricity, arising from charge ordering. Ferroelectricity appeared to be confirmed in this paper by a pyro-electric current measurement indicating that a spontaneous polarization could be switched via the application of an electric field. However, speculation arose when no definitive proof of the actual charge configuration, and thus how the polarization in different Fe double layers is stacked was obtained. This paper and its implications led to a long line of detailed studies on $LuFe_2O_4$, conducted to not only investigate the charge configuration in the sample, but to find the correct one. As described above the tricky aspect, and one which has hidden the true intrinsic properties of $LuFe_2O_4$ and the remaining compounds in the series is the effect of oxygen off-stoichiometry. From the late 2000's and today emphasis was placed on creating the right conditions for the production of highly stoichiometric $LuFe_2O_4$, often characterized by simple magnetization curves, broad peak=bad, sharp peak=good at T_N. For example a lower temperature phase T_{LT} was only clearly identified in highly stoichiometric samples where the observed intensity on superstructure reflections is suppressed, and accompanied by strong diffuse magnetic scattering along the $(\frac{1}{3}, \frac{1}{3}, \ell)$ [104, 105]. Despite early classification of both charge and magnetic orders present in $LuFe_2O_4$ by [102], the proposed polar bilayers led to intense research of each already established phase transition, since it would be the first observation of ferroelectricity through electronic origin. The current status at this time on the magnetism was as perplexing as that of the charge

order, studies by Angst *et al.* [106] provided analysis of the 2D diffuse scattering above T_{CO} which uncovered broad and strongly overlapping peaks corresponding to a propagation vector ($\frac{1}{3}$, $\frac{1}{3}$, 0). However, upon actual ordering below T_{CO}, CO with the propagation vector ($\frac{1}{3}$, $\frac{1}{3}$, $\frac{3}{2}$) occurs. Interestingly, these strong but short range correlations under representation analysis resulted in ferroelectric correlations between the neighbouring bilayers consistent with this propagation vector. Symmetry analysis (assuming a single mode, see Sec. 6.6) led to two possible charge ordered states with polar bilayers: ferroelectric (FE) stacking corresponding to ($\frac{1}{3}$, $\frac{1}{3}$, 0) and antiferroelectric (AFE) stacking corresponding to the propagation vector ($\frac{1}{3}$, $\frac{1}{3}$, $\frac{3}{2}$). The latter of which according to DFT calculations are almost degenerate, and as a bi-product effects the stacking sequence of the charge distribution and thus the bilayers net polarization. It is therefore imaginable that, ferroelectric charge ordering could be established by cooling the sample in a high electric field, making the spontaneous ferroelectricity observed in the pyro-electric current measurement by [63] feasible. Further measurements, later conducted with the application of an E-field showed that it was not possible to induce a ferroelectric state [26, 107]. The tuning of synthesis led to the establishment of clear transitions temperatures in $LuFe_2O_4$, where the Néel temperature resides anywhere between 220 K and 240 K. The two magnetic ions Fe^{2+} and Fe^{3+} in $LuFe_2O_4$, with respective electronic configurations ${}^3d_6$ and ${}^3d_5$, contribute differently to the spin order in the system. The Fe^{3+} occupies all 5 orbitals singly meaning there is no orbital degree of freedom. However, due to the additional free electron of the Fe^{2+} ion, this extra spin can go to an orbital of the doubly-degenerate lowest level and as a result has an unquenched orbital momentum. From this there is a large magnetic anisotropy and the Fe spins in this system prefer to align $||c_{hex}$, which comes from the establishment of a orbital magnetic moment, making it a model Ising system [33]. The second magnetic transition in $LuFe_2O_4$ is T_{LT}, and has been described by several physical phenomena due to the lack of 3D ordering below this temperature, such as; a ferrimagnetic cluster state [87, 104, 108] and a spin glass state [109], the latter was obtained from the frequency dependence observed in AC susceptibility measurements. The most recent neutron experiments at this time also provided new insight into the 3D magnetic spin structure, which could be described with symmetry equivalent propagation vectors ($\frac{1}{3}$, $\frac{1}{3}$, 0), (-$\frac{2}{3}$, $\frac{1}{3}$, 0) and ($\frac{1}{3}$, -$\frac{2}{3}$, 0) in the temperature range $T_{LT} < T < T_N$. This then led to a refinement of the H=0 spin structure, which from representation analysis in the parent $R\bar{3}m$ space group, is built up of three magnetic domains with 120° rotational symmetry [104]. After this point, many researchers obtained a regained interest in the remaining rare earth compounds in this series, to see if the same applied for the isostructural neighbors of $LuFe_2O_4$. A prime example is that of YFe_2O_4, which due to the much larger Y^{3+} ion size [33] and on highly stoichiometric samples two different CO patterns were observed [110, 111]. A 4-fold propagation charge order at 160 K described by the vector ($\frac{1}{4}$, $\frac{1}{4}$, $\frac{3}{4}$) and a symmetry reduction from $R\bar{3}m$ to $P\bar{1}$. The second 7-fold propagation charge order described by the vector ($\frac{1}{7}$, $\frac{1}{7}$, $\frac{9}{7}$) and higher harmonics ($\frac{2}{7}$, $\frac{2}{7}$, $\frac{3}{7}$, also refined in the lower symmetry triclinic space group $P\bar{1}$ [110, 111]. One thing however, was missing which would bring all the information obtained over the many years together and this was the lack of structural refinement on charge ordered $LuFe_2O_4$, which incorporated all of the extra super-structure reflections observed. This changed in 2012 with the work completed by de Groot *et al.* [26, 32, 48] and discussed in the following section.

2.2 The current understanding of $LuFe_2O_4$

The current understanding of $LuFe_2O_4$, is rather different to the above conceptions. In 2012 research conducted by de Groot *et al.* [32,48] provided a new and refreshing take on both the magnetic and charge order super-structure observed, which are in general non-conformant with the literature previously published and discussed in the section above. Although published articles in 2008 by Christianson *et al.* [104] and Angst *et al.* [106] proposed 3D models of both charge and spin orders, full refinements were not given. In the case of the spin order a notable magnetic intensity at ($\frac{1}{3}$, $\frac{1}{3}$, $\frac{n}{2}$) (n=integer) reflections were omitted from modeling (assumed to be decoration by the CO). In the case of the CO no refinement was performed, but symmetry analysis provided suitable sub-group structures, which could potentially describe the reflections. At this point there were still pieces of the puzzle missing with regards to an exhaustive structural refinement and full comprehension of each phase transition. The following two subsections will detail both the magnetic and charge ordering which is currently understood in this system.

2.2.1 The magnetic structure

The ferrimagnetic spin structure proposed by Christianson *et al.* [104], for the time was the most comprehensive assessment of the spin ordering in $LuFe_2O_4$. However, there were a number of problems based on incorrect assumptions which ultimately lead to the wrong spin model, and described in following.

- The occurrence of a net magnetic moment in zero field; this alone contradicts the suggestion of an antiferromagnetic state observed in magnetization measurements in low fields. This at the time was assumed to be a consequence of domain formation.

- The presence of significant magnetic intensity on ($\frac{1}{3}$, $\frac{1}{3}$, half-integer) positions was not predicted by the model. At the time, it was assumed to be the result of a decoration by the not considered charge order.

- In later neutron diffraction and resonant x-ray diffraction experiments by de Groot *et al.* [32], on the same sample used by [104], found magnetic intensity on (0, 0, $\frac{3}{2}$)-type positions. These reflections were also not considered in the spin model and not explainable by the CO decoration.

The temperature dependent neutron diffraction experiments which were performed later by [32] in H=0 and applied fields saw a drastic effect of H on several reflections, which included a decrease of intensity on the ($\frac{1}{3}$, $\frac{1}{3}$, integer) and an increase of intensity of ($\frac{1}{3}$, $\frac{1}{3}$, half-integer) reflections. Not only this but further intensity was also observed on structural reflections (1 0 -5), (1 0 7) and (1 1 3). All of these factors plus a step feature seen in the Mvs$H$ at low fields around 240 K lead to the presence of a distinctive coherent effect, which was described in this case as a metamagnetic transition between two spin structures. In the refinement provided by [32], improvements were made from the spin model proposed by [104].

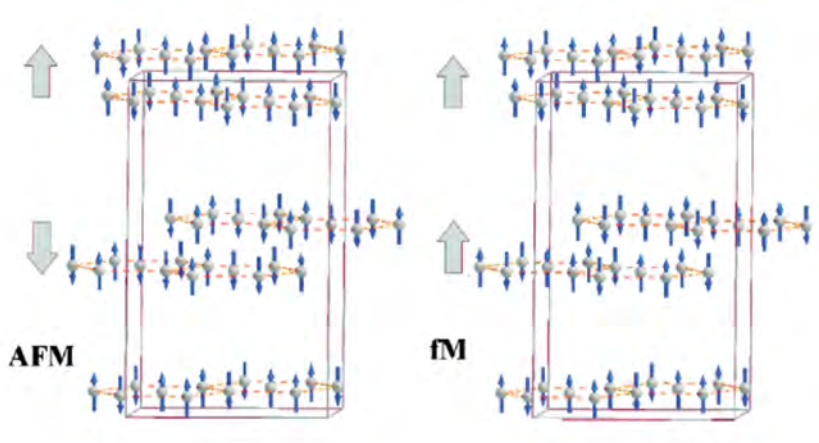

Figure 2.2: The final two refined spin structures in the $C2/m$ cell [48] which exist in $LuFe_2O_4$, left: the AFM phase, right: fM phase. Figure taken from [32].

Firstly, the CO was disregarded and the spin model assumed a single magnetic propagation vector per magnetic domain with no higher harmonics. An explanation of all the reflections observed in neutron diffraction, requires either the superposition of additional magnetic propagations $(\frac{1}{3}, \frac{1}{3}, \frac{3}{2})$, $(0, 0, \frac{3}{2})$ or the CO supercell rather than the high temperature $R\bar{3}m$ cell. The previous magnetic refinement by [104] used representation analysis based on the parent group $R\bar{3}m$, which was the only structure to that point considered for $LuFe_2O_4$. This high symmetry cell does not take into account the CO superstructure reflections and only considers a single Fe site, which would make the clearly defined metamagnetic transition proposed by [48] very doubtful. Therefore, in a paper published shortly before the new structural refinement of highly stoichiometric $LuFe_2O_4$ [48] (covered in the next section), a magnetic refinement was performed in a 6× larger monoclinic $C2/m$ CO cell that could potentially account for all the extra reflections observed. In the magnetic refinement with H=0 an initially very large approach was taken which ignored symmetry and as a result considered 3^{12} possible spin configurations of 12 Fe sing spins.

The next step was reducing these down to one. The first reduction was made by simply considering structures which yielded the same relative intensities at $(\frac{1}{3}, \frac{1}{3}, \text{integer})$ positions. From here further restrictions were put in place, for example the relative magnetic contribution from structural+$(0, 0, \frac{3}{2})$ reflections and an upper limit of the $(\frac{1}{3}, \frac{1}{3}, \text{integer})$ and structural+$(0, 0, 0)$ reflections [48]. From these restrictions a resultant 7 candidate spin configurations were consistent with the observed magnetic diffraction in zero field. A refinement of these 7 models, which included fitting domain populations and a Debye waller factor, 6 in this case were rejected due to a large χ^2 value. The re-

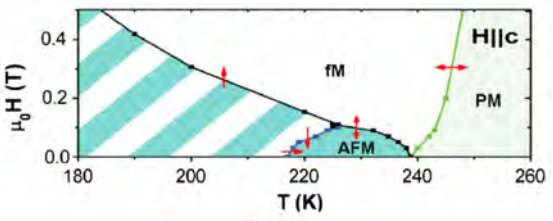

Figure 2.3: The magnetic phase diagram of $LuFe_2O_4$, which exhibits; paramagnetism (pm), antiferromagnetism AFM, ferrimagnetism fM and a hysteresis region where either fM or AFM states can be stabilized (hatched area). Arrows indicate what direction the measurement was performed (heating and cooling). Figure was taken from [32].

maining spin structure is a solution for the AFM phase in zero field and shown in Fig. 2.2 (left). The same approach was also taken for the ferrimagnetic H-field spin structure, but the contrast between the two spin structures lies in the Ising spins of one Fe-O bilayer, which flip sign giving a 2:1 configuration (see Fig. 2.2 (right)). The respective magnetic phase diagram including pM, fM and AFM transitions is provided in Fig. 2.3. The hatched area relates to the region where either fM or AFM states can be stabilized [32]. The mixed valency in the system and relative spin directions can not be resolved through neutron diffraction due to insufficient contrast between the two moments, the solution to this problem is discussed in the following section.

2.2.2 The new proposed structure and charge order

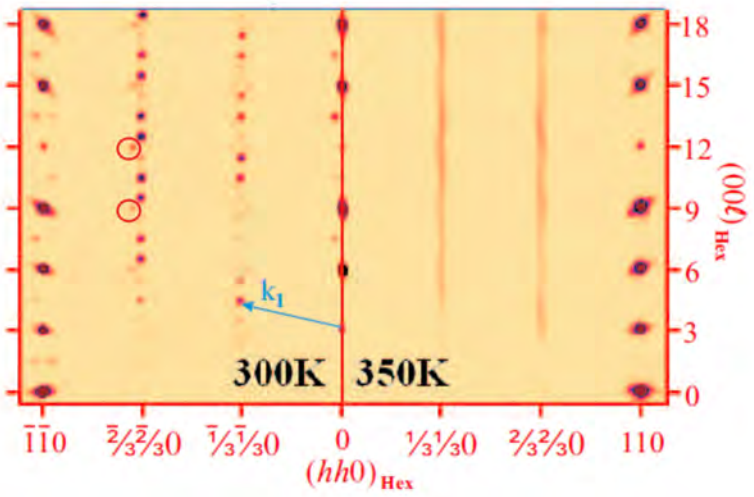

Figure 2.4: A composite precess-on image of a highly stoichiometric $LuFe_2O_4$ single crystal ($hh\ell$ plane). Left: 3D incommensurate CO superstructural pattern measured at 300 K, just below the main ordering temperature. Right: same crystal measured above T_{inCO} at 350 K. Only 2D CO correlations are observed. Image taken from [26].

The absence of a definitive structural refinement taking into account all the extra superstructure reflections observed in scattering experiments, limited the understanding of $LuFe_2O_4$. However, studies on a highly stoichiometric $LuFe_2O_4$ crystal by de Groot *et al.* [48], provided a revised view of the $LuFe_2O_4$ structure. Single crystal refinement was performed on data obtained, at various temperatures, from the Oxford diffraction in-house SuperNova diffractometer using Mo-K_α radiation. By measuring a large volume of reciprocal space, over 1000 unique reflections were obtained and allowed for detailed refinements. Below T_{CO} at ~320 K, the system goes from a 2D diffuse to 3D charge ordered state, and refinements in the already established $R\bar{3}m$ cell no longer provides a solution for these extra reflections.

The natural progression at this point is to go from the high symmetry $R\bar{3}m$ parent group to a symmetry subgroup. As mentioned in the previous section, the superstructure reflections originate from three individual CO domains corresponding to a 120° twinning with $(\frac{1}{3}, \frac{1}{3}, \frac{3}{2})$ and symmetry equivalent $(\frac{1}{3}, -\frac{2}{3}, \frac{3}{2})$ and $(-\frac{2}{3}, \frac{1}{3}, \frac{3}{2})$ propagation vectors. From representation analysis of the hexagonal cell with

propagation vector $(\frac{1}{3}, \frac{1}{3}, \frac{3}{2})$ two irreducible representations were obtained and both of which lowered the space group to $C2/m$, but each with a different origin (i.e. inversion centres).

One of the origins lies at (0, 0, 0), the position of Lu. This would result in a charge distribution with antiferroelectrically stacked polar bilayers, postulated previously [106]. The second case has the inversion centre at $(0, 0, \frac{1}{2})$ between the two Fe layers of a bilayer and corresponds to bilayers with a net charge (non-polar). Of the two refinements, the solution with the inversion at $(0, 0, \frac{1}{2})$ provided the best refinement statistics. The final structure obtained for $LuFe_2O_4$ in the monoclinic space group at 210 K is shown in Fig. 2.5. The incommensurate CO reflections at $(0, 0, \frac{3}{2})$ and $(\frac{1}{3}, \frac{1}{3}, 0)$ were considered as a discommensuration, and the structure solution and refinement was therefore based on an commensurate approximation. In this refinement it is highly possible that due to this incommensuration, some of the intensity may well have been lost in the peak integration, in particular, reflections of the type $(\frac{N}{3}\pm\tau, \frac{N}{3}\mp 2\tau, 0)$ (indicated by red circles in Fig. 2.5) and $(\pm\tau, \pm\tau, \frac{3}{2})$, leading to potential systematic errors. The commensurate approximation taken with this structural refinement will be addressed in Chapter. 6 when comparing the results obtained in this work.

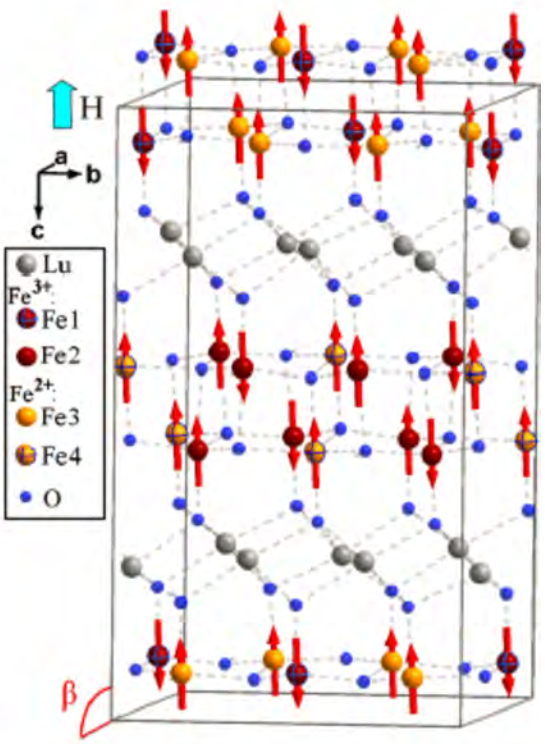

Figure 2.5: The refined monoclinic $C2/m$ structure of $LuFe_2O_4$ at 210 K with lattice parameters a=5.95 , b=10.30 , c=16.96, β=96.72°. The high-field ferrimagnetic spin order is given by arrows and the Fe^{2+} and Fe^{3+} charge order are represented by red and yellow atoms, respectively. Figure was taken from [48].

With the structure established, the Fe valences were determined by the bond valence sum method (BVS) (see Sec. 3.8.3), the result from BVS is shown in Fig. 2.5. The spin order observed in neutron diffraction and the CO seen in x-ray diffraction/BVS open a relation between the two orders, x-ray magnetic circular dichroism (XMCD) can therefore be used to address this. XMCD was performed on $LuFe_2O_4$, a measurement performed at 120 K in shown in Fig. 2.6 [48]. The XMCD signal (green curves in Fig. 2.6) were calculated from the difference between the x-ray absorption edge (XAS) for left and right circularly polarized light (μ_+ and μ_-) measured with total electron yield (for more detail on the experimental procedure see [112–114]). The prominent peaks seen in the L_3 region of the XAS spectra relates to the well identified chemically shifted Fe^{2+} and Fe^{3+} white lines [48, 115, 116]. The implications of this measurement suggest that with the large peak at the Fe^{2+} position and the smaller upward peak at the Fe^{3+} position, the net moment of the Fe^{2+} is in the field directions and a smaller net moment of the Fe^{3+} is in the opposite direction to

the field.

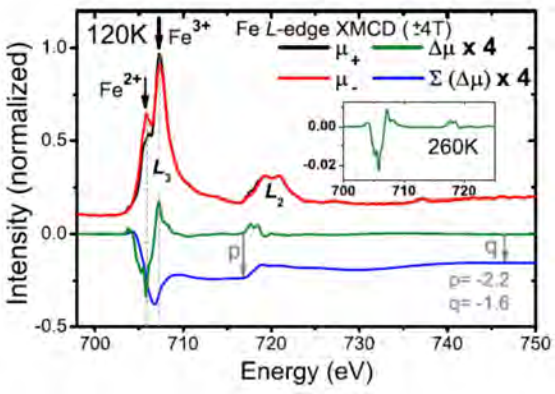

Figure 2.6: Highly stoichiometric $LuFe_2O_4$ XMCD spectra measured across the Fe $L_{2/3}$ edge at 120 K and 260 K (inset). For this measurement the XAS spectra with an applied field H parallel and antiparallel to the incoming beam by changed photon polarization, were averaged by subtraction from each other. Figure taken from [48].

Furthermore, when combining this data with the spin model obtained in [32] due to the difference in peak size for each iron valence it suggests that all of the Fe^{2+} moments and an additional $\frac{1}{3}$ of the Fe^{3+} moments all align in the H direction (up) and the remaining $\frac{2}{3}$ Fe^{3+} spins point in the opposite direction to H (spin down).

The same result was also determined from the two previously published XMCD studies on $LuFe_2O_4$ [115, 116], interestingly the samples used in these studies were off-stoichiometric, so the spin configuration, in terms of the high field ferrimagnetic phase is identical to that of highly stoichiometric samples. Combining the refined ferrimagnetic spin structure (Fig. 2.2, right) with the local spin-charge configuration from XMCD, it is inconsistent with any ferroelectric or antiferroelectric charge ordering that preserves mirror symmetry (such as the one proposed in [106]). The only CO preserving the mirror symmetry in this case and consistent with the combination of neutron diffraction and XMCD is the one with charged bilayers (Fig. 2.5), deduced from x-ray diffraction and thus provide independent verification. However, as mentioned in [48], there are a further 27 CO configurations that are consistent with both the spin order of Fig. 2.2 (right) and the XMCD results (Fig. 2.6), although they all break mirror symmetry. The therefore deduced coupled spin-charge order is shown in Fig. 2.5 and represents the current status quo for $LuFe_2O_4$. Several open questions, do however exist for this result. Firstly, as remarked in [32], the spin order cannot be described in terms of one of the appropri-

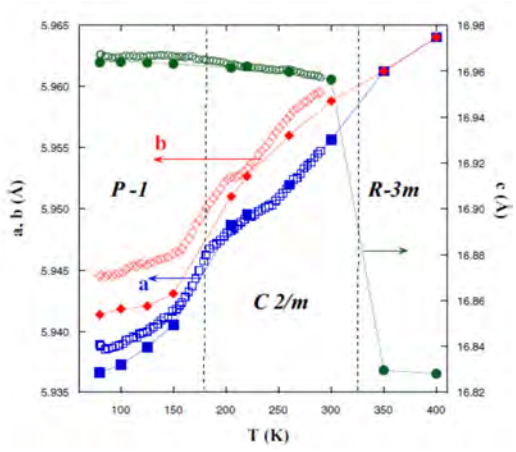

Figure 2.7: Temperature dependence of the lattice parameters obtained for $LuFe_2O_4$ in two monoclinic settings. The filled symbols and open symbols correspond to data gathered from high resolution measurements and data acquired every 5 min on cooling (0.5 K min^{-1} ramp), respectively. Figure taken from [117].

ate magnetic space groups ($C2/m$, $C2/m'$, $C2'/m$ or $C2'/m$). This situation alone is highly unusual and may be suggestive of a lower "real" symmetry, meaning reduction further to another subgroup symmetry. Secondly, as pointed out in [33] the CO with charged bilayers does not minimize electron-electron Coulomb repulsion and requires long distance electron transfer. Lastly, and perhaps more pressing are the lingering doubt with regards to the apparently incommensurate nature of the CO observed in $LuFe_2O_4$.

A more recent paper published in 2014 by Blasco *et al.* [117] covered temperature dependent powder diffraction studies on RFe_2O_4. It concluded the same $R\bar{3}m$ structure for $YbFe_2O_4$ at 400 300 and 80 K, however discovered a peak splitting of the $LuFe_2O_4$ data at lower temperatures, indicating that $LuFe_2O_4$ goes through three structural transitions as plotted in Fig. 2.7. The question now is, does the $C2/m$ structure provide the right solution for highly stoichiometric $YbFe_2O_4$ as it did for the current understanding of $LuFe_2O_4$, or is the data published by [117], which describes a lower symmetry structural solution closer to the truth? This question is answered over the following sections and chapters, at times being reaffirmed for clarity.

2.3 A brief history of $YbFe_2O_4$

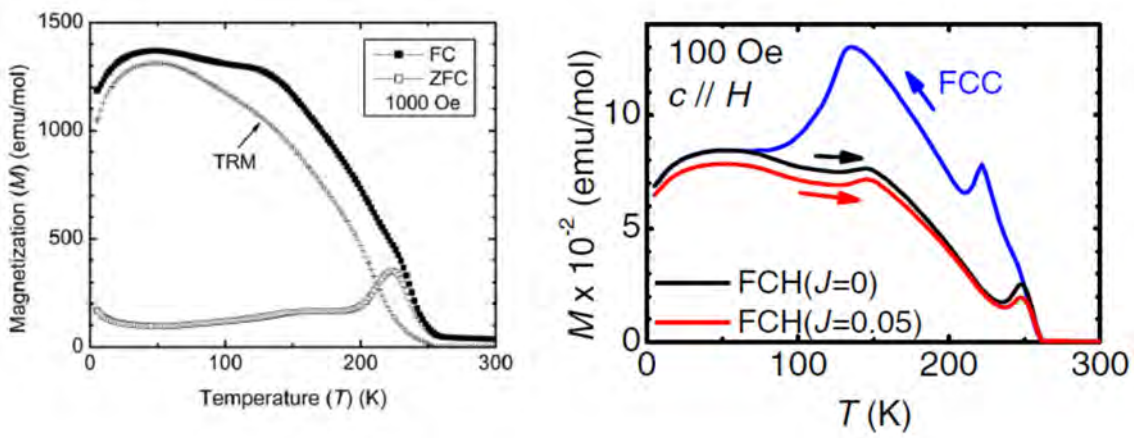

Figure 2.8: Magnetization as a function of temperature of various $YbFe_2O_4$ samples. Left: $M(T)$ measured on ZFC and FC in 1000 Oe and thermoremanent magnetization, figure taken from [118]. Right: $M(T)$ measured in 100 Oe showing field cooled cooling FCC (blue curve) and two field cooled heating curves which, were measured with an electric current of density J=0.05 (red curve) and J=0 (black curve). Figure taken from [119].

With $YbFe_2O_4$ being isostructural to $LuFe_2O_4$, it stands to good reason that the magnetic and charge order properties uncovered in highly stoichiometric $LuFe_2O_4$ should not be so different, given the similar ion size of Lu^{3+} and Yb^{3+} [33], but perhaps some differences in magnetic ordering temperatures etc can be expected. Unlike the extensively studied $LuFe_2O_4$, which has a multitude of publications exhibiting a wide range of varying magnetic characteristics, there are only a handful on $YbFe_2O_4$. This is attributed to the first claim of ferroelectricity via charge ordering in the well know nature publication by [63], and as a result effort was focused

almost solely on $LuFe_2O_4$, to see if this claim was reproducible as the technological implications would be great. A regained interest in the remaining rare earth ferrites originated from the revision of intrinsic properties of highly stoichiometric $LuFe_2O_4$ which led to charged bilayers [48], a continued search for ferroelectricity in the remaining compounds in this series is a primary focus.

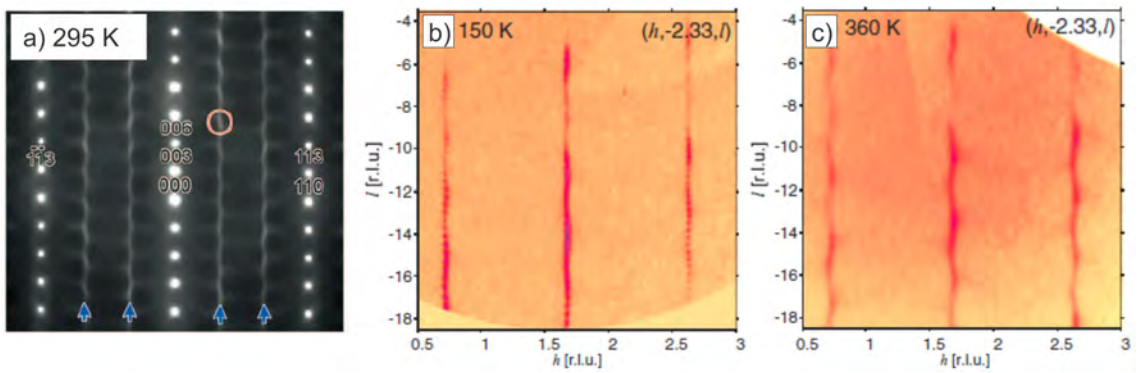

Figure 2.9: Charge ordering in $YbFe_2O_4$. (a) Electron diffraction from TEM of the $hh\ell$ plane at 295 K. Figure taken from [120]. (b) and (c) reciprocal space images from high resolution synchrotron data measured at 150 K and 360 K, respectively. Figures taken from [121].

It is well known that the topic of oxygen stoichiometry and its effects on these systems played a large part in understanding the true intrinsic charge and spin order, and when taken seriously, the conditions for growth by careful tuning of the atmosphere resulted in highly stoichiometric crystals exhibiting these sharp transitions in the magnetization $M(T)$ [32]. However, the few magnetization studies at present on $YbFe_2O_4$ [118, 122–124] provide curves with only smeared transitions, some examples are given in Fig. 2.8 (left, right). These curves are also similar to that shown in our off-stoichiometric data (see Chapter. 4 Fig. 4.5), and comparable to $LuFe_2O_4$ curves now classed as off-stoichiometric [87, 125–128].

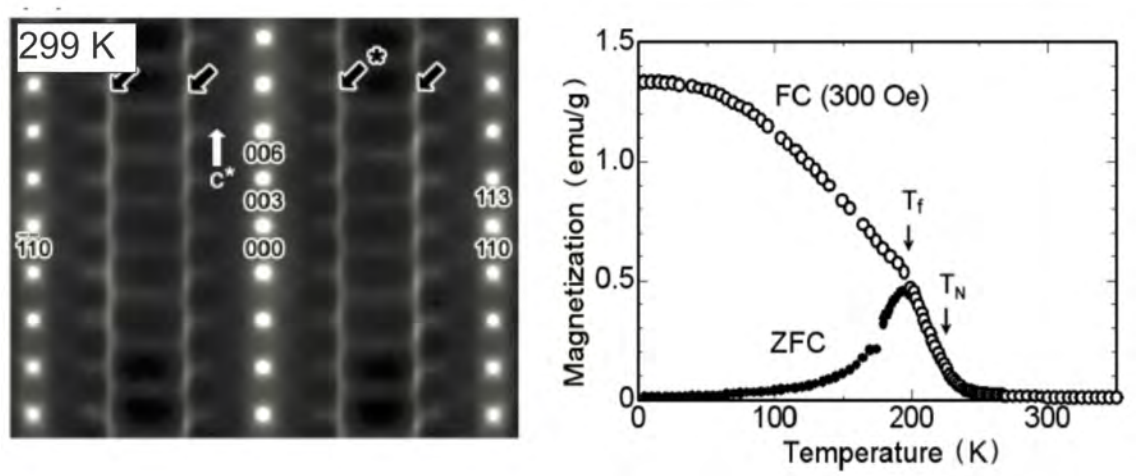

Figure 2.10: Top: $LuFe_2O_4$ TEM image of the $hh\ell$ plane measured at 299 K. Arrows show 2D CO along $(\frac{N}{3}, \frac{N}{3}, \ell)$. Bottom: relative $M(T)$ curve representative of sample quality, measured on ZFC and FC in 300 Oe. Figures taken from [129].

The charge order in $YbFe_2O_4$ has been investigated by energy-filtered Transmis-

sion Electron Microscopy (TEM) [120, 130] and high resolution x-ray diffraction at a synchrotron source [121]. The work done by both Murakami *et al.* [120] and Hearmon *et al.* [121] uncovered 2D-diffuse CO correlations which are typically defined as charge density waves. The data shown in Fig. 2.9 of the $hh\ell$ plane from a TEM measurement at 295 K (a) and two reciprocal space maps from x-ray diffraction (b) at 150 K and 360 K (c) each show low dimensional CO with no 3D peak intensity. A similar case also showing the $hh\ell$ plane in a TEM measurement on what is now classed as off-stoichiometric $LuFe_2O_4$ [129], is given in Fig. 2.10 (left). The right part of the panel in Fig. 2.10 shows the relative magnetization of the sample, showing only one very broad feature at T_N. The second TEM study published by Matsumoto *et al.* [130] provided the first glimpse of 3D peak intensity seen in an image of the $hh\ell$ plane, given in Fig. 2.11. Although there is a background of 2D diffuse CO, clear peak intensity at half-integer positions along ℓ are seen and described by the propagation vector $\mathbf{q}=(\frac{1}{3}, \frac{1}{3}, \frac{1}{2})$, consistent with the strongest super-structure reflections found in $LuFe_2O_4$ [48, 106]. A few studies on $YbFe_2O_4$ also address; the dielectric properties [131], electronic tunability [132] and AC susceptibility response for multiglass states [123].

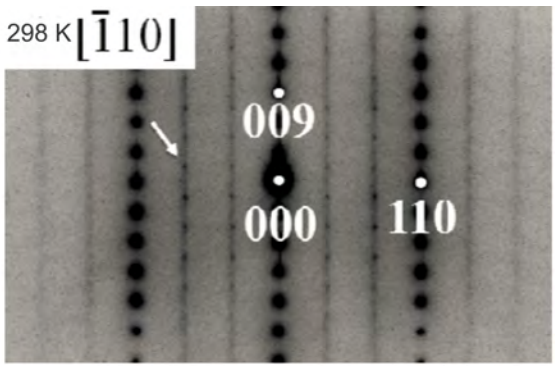

Figure 2.11: Electron diffraction study on $YbFe_2O_4$. TEM image of $hh\ell$ plane measured at 298 K, which exhibits 3D peak intensity described by propagation vector $\mathbf{q}=(\frac{1}{3}, \frac{1}{3}, \frac{1}{2})$. Figure taken from [130].

A comprehensive study, like that conducted on $LuFe_2O_4$ regarding both the structure and magnetism on a highly stoichiometric sample is lacking for $YbFe_2O_4$. Interestingly, on two separate occasions, $YbFe_2O_4$ has been distinctively classed as a system which exhibits only low dimensional order, once based on a very early Mössbauer and neutron study [97], claiming this system was a 2D antiferromagnetic on a triangular lattice. Neutron diffraction at low temperatures also presented in this paper exhibited magnetic Bragg lines rather than spots, which along with the Mössbauer spectra led to the assumption of a low dimensional model to describe this system. The second publication by Hearmon *et al.* [121], containing high resolution x-ray synchrotron data on $YbFe_2O_4$, again presents 2D diffuse CO rather than individual 3D peak intensity. It was concluded that the CO in this system is described by an incommensurate charge density wave. Furthermore, analysis shows that it cannot be ferroelectric, as the electrical dipole moments are also incommensurately modulated.

With a limited resources and dedication into this compound, a large majority of the publications describe samples which are all likely off-stoichiometric, and as a result the true intrinsic nature of $YbFe_2O_4$ remains hidden. With the regained interest in the rare earth series more studies on the effects of oxygen off-stoichiometry are being conducted, for example a recent publication in 2017 by Nicoud *et al* [133]. presented a comprehensive study of oxygen storage in $YbFe_2O_{4-x}$ ($x \leq 0.5$), performing powder refinement at RT on $YbFe_2O_4$ and $YbFe_2O_{4.5}$. Due to the two

different oxygen stoichiometries a refinement on each compound yielded an $R\bar{3}m$ and $\mathrm{P}\bar{3}$ space group, respectively. Moreover the recent work by us [43] highlighting for the first time sharp transitions at both the fM and AFM phase with the addition of a strongly defined low temperature transition, a long-overdue revision for the current understanding of $YbFe_2O_4$ is now in reach. The motivation of this thesis was to try and prove long-range order exists in $YbFe_2O_4$, and just like the case of $LuFe_2O_4$, control of the oxygen partial pressure used during single crystal growth is key, to obtain the right conditions for the production of highly stoichiometric $YbFe_2O_4$.

3 | Experimental methods and theory

3.1 Powder synthesis

Polycrystalline samples of $YbFe_2O_{4-\delta}$ were synthesized via soild state reaction [76] using high purity powders of Yb_2O_3 (Alfa Aeser 99.9%) and Fe_2O_3 (Alfa Aeser 99.99%). The individual quantities were ground together thoroughly using an agate mortar and heated in a single grade tube furnace (see Fig. 3.1, left). For all powder syntheses an oxygen partial pressure atmosphere of $CO:CO_2$ was used. The starting powders are heated in a $CO:CO_2$ gas flow at 1200° C for 48 hours, followed by an intermediate removal and regrinding of the powder to promote homogeneity and aid solid-state synthesis, after which a final heating was performed for 24 hours under the same conditions. The synthesized powder was then compressed into rods ranging from 6-8 cm in length and 6-8 mm in diameter via isostatic compression. In this method the polycrystalline powder is slowly and incrementally packed into a long shaped balloon using a flat ended plastic rod. On completion it is sealed tightly with two knots and placed into a press and isostatically compressed in water at high pressure $>150\,kg/cm^2$, to form rods for single crystal growth. Lastly the rods were sintered for 12-24 h in the same conditions used for initial synthesis.

3.2 Single crystal growth

All single crystals grown for both my master thesis [57] and during the course of this PhD thesis were done so using the traveling floating zone technique [134] on a Crystal Systems Inc. F-ZT-10000-H-IV-VPS four mirror furnace [135]. This particular method of crystal growth requires two sintered polycrystalline rods; a feed rod (typically 6-10 cm long) and a seed rod (around 1-2 cm long). The seed rod chosen for crystal growth can either be polycrystalline (quite typical for the crystal growth of new compounds) or single crystal boule saved from a previous growth. The latter is chosen for crystal growth improvements, whereby using a single crystal as a seed can promote crystallographic orientation and large grains during growth. Furthermore, the crystal seed does not need to be the same exact compound as that being grown, but an isostructural neighbour containing elements which melt congruently can also be used. This methodology was employed for some of the $YbFe_2O_4$ crystal growths using the isostructural $LuFe_2O_4$ as a single crystal seed. When mounting both rods, the seed is fixed at the bottom of the crystal growth shaft with nickel chrome wire and the feed rod is suspended above using platinum wire. The spe-

cific choice of platinum wire is based on two physical properties; the high melting point (∼1770°C) which prevents it weakening when the growth is coming to an end and the fact that it is inert which avoids contamination during growth. The wire suspension of the feed rod allows for accurate positioning above the seed rod, once complete a thick quartz tube is then inserted around the mounting area, which not only protects the mirrors and provides safety during growth but enables the use of specific gas environments and pressures required for the successful growth of many compounds. A molten zone is formed between the feed and seed rod by the halogen lights surrounding the quartz tube at right angles to each other and focused by four ellipsoidal mirrors (see Fig. 3.1, right). Temperature control of the directed heat is done so by input power of the lamps, where zone stability is primarily controlled with power input and zone length; the latter can be altered by moving the upper shaft up or down. To allow for a homogeneous distribution of heat during growth both the upper and lower shaft rotate in opposite directions (see [57, 134] for more information). To crystallize the whole feed rod, the mirrors move up relative to both feed and seed rods, and thus in the process moving the focus of the molten zone through the feed rod. The material left behind on the seed rod crystallizes on cooling, during which time the crystal growth can be monitored via a live video feed. Lastly, in order to obtain the best chances of achieving the right composition and high crystal quality a number of variables should be considered:

Feed/seed rod production: The formation of powder in to a cylindrical rod is a very delicate procedure, one which requires patience and time, however if done successfully, can ease the difficulties faced during crystal growth. In order to make the rod, small amounts (small spatula full) of powder must be placed into the balloon at any one time, and then gently press, not hammered, with a long blunt plastic rod. When done in such tiny increments, the powder is far more homogeneously distributed, which means, it will melt more congruently during crystal growth, resulting in a more stable molten zone.

The growth rate: This is the speed at which the mirrors move and thus the molten zone through the feed rod. Some crystal compounds require fast growth rates of 10 mm/h others, for example $YbFe_2O_4$ was grown at 1 mm/h. This particular variable can largely increase the chances of obtaining larger single crystals in the boule, but a slower growth rate doesn't always mean a better crystal as some compounds crystallize very quickly or decompose on cooling.

Gas flow: The atmosphere used during crystal growth is vital for instance in compounds which exhibit sensitivity to oxygen stoichiometry. In some cases the gas mixture is fixed and kept at a constant pressure in the quartz tube (often from premixed CO:CO_2 gas cylinders) others have a constant flow, where the individual flow rates of each gas component can be tuned carefully.

Gas pressure: Some crystal growths require ambient room pressure, however some more complicated compounds need high pressure to form single crystals. This can largely affect not only the stability of growth (when pressure is required) but also the intrinsic properties of the system can be explored with varying the pressure for each growth.

Power input: As the molten zone is produced from focused halogen lamps, the heat is stabilized in terms of power input to the lamps. This is one of the most sensitive and vital variables for growth, in principle once should always increase the power slowly, closely monitoring any changes in the feed rod (commonly the feed rod is positioned in the zone at the start of the experiment, then the seed is lifted into the zone when the feed tip is molten). The difference between a couple of percent in power input can vastly change the stability and size of the molten zone, these two factors of which, after joining both seed and feed rods, should be relatively stable for the entire growth. Constant changes will affect the size of the single crystals produced and the quality (e.g stoichiometry).

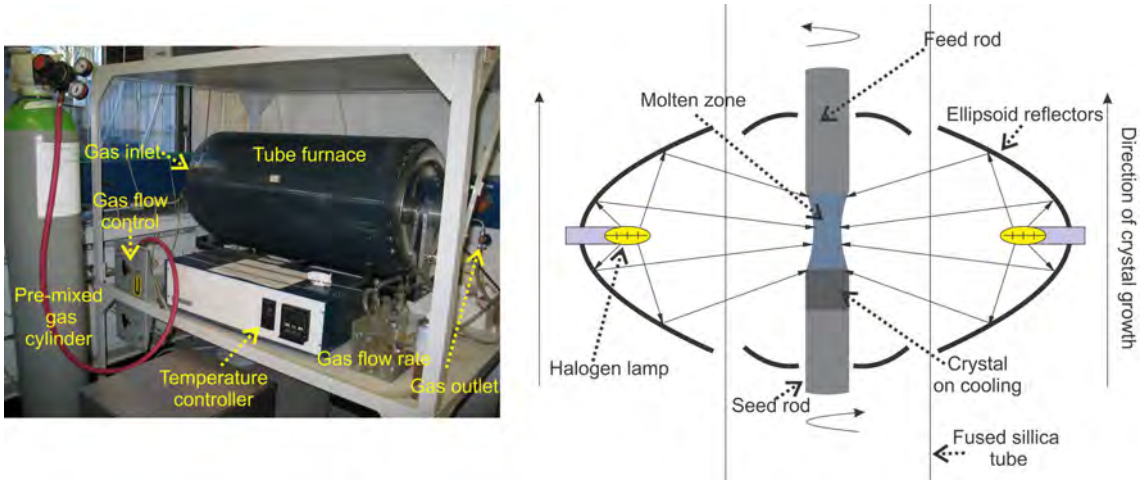

Figure 3.1: Experimental set-up for polycrystalline synthesis and single crystal growth. Left: single grade tube furnace with gas flow from pre-mixed gas cylinder. Right: schematic of crystal growth set-up.

3.3 Magnetometry

3.3.1 DC magnetization

To measure the magnetic response of samples as a function of temperature, the magnetization in a sample is extracted by Direct Current (DC) magnetic measurements. The sample is magnetized by a constant magnetic field (for example $M(T)$ measurement at 100 Oe between 10-300 K) and the magnetic moment of the sample is then measured as a function of temperature T or the applied magnetic field H. The magnetic hysteresis $M(H)$ of a sample can also be placed in the category of DC magnetization, as the changes in increasing or decreasing field are small enough to prevent large changes in the magnetization process.

3.3.2 SQUID option at the MPMS

The Magnetic Properties Measurement System (MPMS) uses a SQUID (Superconducting Quantum Interference Device) magnetometer to measure the magnetic response of the sample in a temperature range of 4 to 400 K and magnetic field range

0-7 T. The advantage of using a SQUID magnetometer for certain measurements is its great sensitivity to low magnetic fields. The SQUID superconducting chip consists of two superconductors separated by thin insulating layers which form two parallel Josephson junctions. These parallel Josephson junctions create an indefinite current flow without any applied voltage, known as the Josephson effect [136]. A current flowing through the two junctions results in a voltage, which also very sensitively depends on the magnetic flux encompassed by the junctions. The SQUID is attached to the pick-up coils, that are positioned inside the superconducting magnet. This forms a second order gradiometer, primarily sensitive to the flux difference between the inner and the outer coils (Fig. 3.2, left). The magnetic response of the sample is then determined by the SQUID magnetometer which measures the current generated in the pick-up coils by moving the sample in a series of 32 steps. The current is induced by the magnetic moment of the sample. In the process of moving the sample through the coils a characteristic response curve is produced and can be fitted for the sample magnetic moment. There are a multitude of ways in in which to mount a sample for measurement, most commonly the sample is glued with GE (General Electric) varnish to a non-magnetic Tufnol sample holder. The GE varnish can be easily removed with the use of acetone for reorientation of the sample for magnetic anisotropy measurements or complete removal from the holder.

There are two different ways of measuring the magnetization with the SQUID option, DC magnetization or Reciprocating Sample Option (RSO). The main difference between the two measurement techniques are time, the DC option has high sensitivity with regards to the magnetic moment as it moves the sample sequentially (as stated previously) in small steps upward through the superconducting coil. This process is much slower than the RSO measurement method, which moves with a typical amplitude of 5 mm through the pick-up coils. This particular method is used when fast M vs H measurements are required and the typical sensitivity is $\sim 5 \cdot 10^{-9}$ emu. To remove a remanent field from the superconducting magnet a degauss macro can be used. In this process a short macro which applies positive and negative fields ranging from the maximum field to the lowest field and then zero removes any remanent field from a previous measurement. This is specifically important for samples very sensitive to small applied fields, such as $YbFe_2O_4$.

3.3.3 PPMS/Dynacool VSM option

The Vibrating Sample Magnetometer (VSM) option was used on both a Physical Properties Measurement System (PPMS) and PPMS Dynacool. This basic magnetization measurement is achieved by oscillating the sample near a detection (pick-up) coil and synchronously detects the voltage induced (Faraday's law), see Fig. 3.2 (right) for VSM schematic. To obtain a sufficient resolution of the magnetization, a compact gradiometer [1] is used, which provides a relatively large oscillation amplitude (1-3 mm peak) and a frequency of 40 Hz, allowing the system to resolve magnetization changes in the order of 10^{-6} emu (two orders of magnitude worse than the SQUID). The main advantage of using the VSM option over MPMS magnetization is the speed. For general purpose $M(T)$ up to fields of 14 T, higher than those

[1] In essence, measures the direction and magnitude of magnetic fields, commonly composed of two magnetometers placed in series and the device records the difference in magnetic flux.

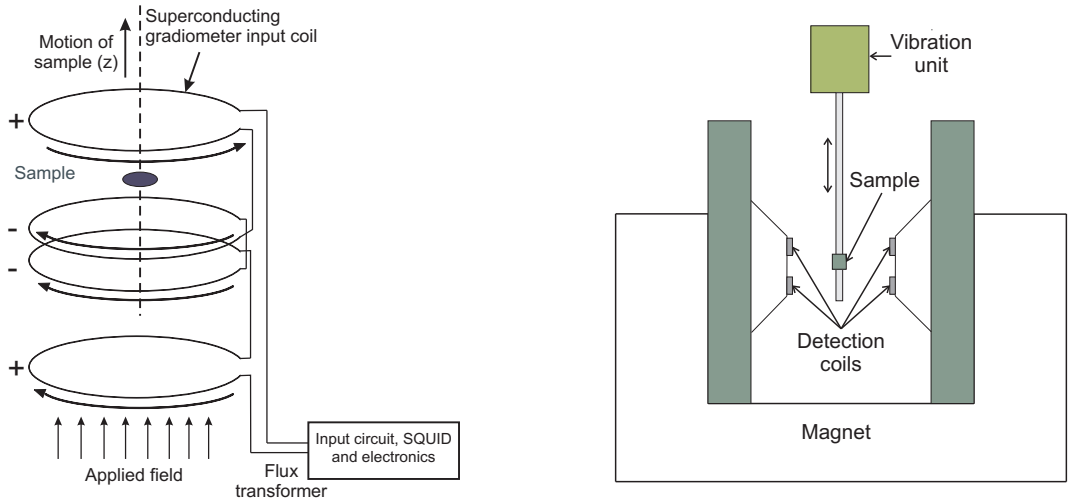

Figure 3.2: Left: schematic of SQUID magnetometer, image taken from [137] and adapted. Right: basic schematic of VSM set-up, image taken from [138] and adapted.

achievable with the MPMS, measurements can be performed quickly and efficiently. The PPMS Dynacool is practically the same as the PPMS, but uses a closed cycle cryostat instead of the constant need to refill helium and nitrogen, however it only has a maximum field of 9 T. The other major disadvantage with the PPMS and Dynacool is the absence of a low field option, this will affect the ability to start off in a demagnetized state (0 emu) for magnetic hysteresis, which is important for the careful mapping of magnetic phase diagrams.

3.4 AC susceptibility

Some systems exhibit time delayed behavior due to dynamical effects such as slow alignment of the magnetic moments or states where the spins are 'frozen' for example in spin glass systems, where the spins experience random interactions with one another [139]. Although time-delayed responses to the magnetic moment are not limited to this particular type of phenomena, it is not possible to probe it with DC magnetization (the applied moment is constant for the duration of the measurement). Instead an alternate measurement method called AC susceptibility is used. In AC measurements a small oscillating magnetic field typically around H_{AC}=10 Oe, (the AC drive field) is super imposed on the DC field causing a time dependent moment in the sample (generally a moment oscillating with the same frequency). The field of the time-dependent moment induces a current in the pick-up coils, allowing measurement of the sample without the need of sample movement. AC susceptibility measurements were performed using the Quantum Design PPMS ACMS option, and the operating frequencies available range between 1 and 10 kHz (taking it well out of the DC magnetism range which can be compared to 0 or very low frequencies applied [140]), with externally applied magnetic fields up to 7 T. Two important quantities are obtained from an AC measurement, the magnitude of the susceptibility, χ, and the phase shift, φ, due to dynamical effects in the sample. Alternatively, this can be written in terms of an in-phase component χ' (real part) and an out-of-phase component χ'' (imaginary part). The two representations are related by; $\chi'=\chi\cos\varphi$, $\chi''=\chi\sin\varphi$ and therefore $\chi^2=\chi'^2+\chi''^2$.

3.5 PPMS Heat Capacity

The Quantum Design PPMS heat capacity option measures the heat capacity at constant pressure, with a temperature range of 1.9-400 K for standard heat capacity and 0.4-400 K with ^{3}He dilution option. A schematic of the heat capacity set-up is shown in Fig. 3.3 (top). To set up the measurement, the calorimeter puck is inserted into the bottom of sample chamber followed by a contact baffle, this is to allow thermal contact with the isothermal region of the sample chamber (just above the puck), which helps to create a more uniform thermal environment for the puck. This feature is necessary when the hi-vac option is enabled, which reduces the amount of thermal exchange gas in the sample chamber. For the actual measurement heat is applied to the puck and the time dependent temperature rise is measured.

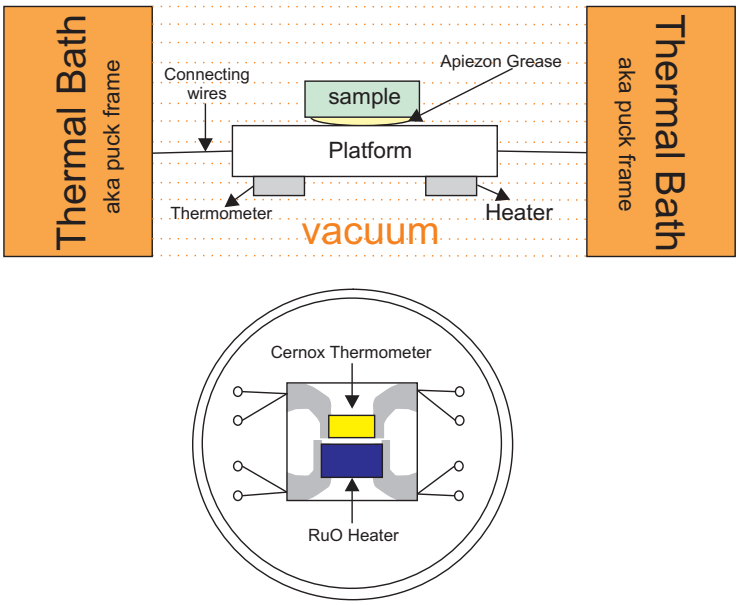

Figure 3.3: Top: vertical slice through PPMS puck and calorimeter platform. Bottom: birdseye view of puck, detailing calorimeter chip comprised of a Cernox thermometer and RuO heater.

3.5.1 The calorimeter puck

In essence the calorimeter puck contains a resistive platform heater, platform thermometer and puck thermometer. The platform heater (RuO Heater) and thermometer (Cernox Thermometer) are attached to the bottom of the calorimeter chip, which functions as the sample platform (see Fig. 3.3, bottom). The puck thermometer is buried within the puck itself. The platform thermometer measures the temperature of the puck, which serves as the calorimeters thermal bath. Eight wires (4 each side) of the calorimeter chip, which suspend it centrally above the puck, serve as both an electrical connection to the platform heater and thermometer as well as thermal connection between the platform and puck frame. When heat is applied to the puck, what is measured is the modification of the platforms thermal response due to the presence of the sample. In order to measure the sample heat capacity correctly a two step process is required. Firstly an addenda measurement (empty puck) is measured, with Apiezon grease, which allows thermal contact of the sample to the calorimeter chip. This is measured for the whole temperature range required

for the sample measurement, however not as many data points are required as the software used, interpolates between the points. It is essential to measure the grease alone as it contributes to the total heat capacity, and must be subtracted from the measured sample heat capacity. In the temperature range available for heat capacity measurements, two types of grease are required, a low temperature (N) grease used in the range of base temperature up to 300 K and above this a high temperature (H) grease is used. The H grease will begin to crystallize at low temperatures and will cause movement or decoupling of the sample, the N grease starts to melt at higher temperatures, it is for this reason that the two types of grease are used. Following the addenda measurement the sample is placed on the puck to measure the total heat capacity of the sample+addenda. The sample heat capacity is obtained by subtracting the addenda heat capacity.

3.6 The basics of scattering

The aim of this section is to provide the required information on each scattering technique used, where only a very brief overview of both powder and Laue x-ray diffraction will be discussed, based on their generic use in this line of work. Any further information required by the reader can be obtained from some recommended texts [141–145] or my masters thesis [57].

3.6.1 Scattering theory

Scattering of x-rays and neutrons have become one of the most valuable tools for probing matter and understanding the fundamental physics of a variety of complex systems [145]. To understand the experimental part of this work, scattering theory is briefly summarized. The account given is valid for neutron scattering, although the final result in Eqn. 3.9 holds for x-rays as well, for an appropriate potential, $V(\mathbf{r})$. In quantum mechanics, focus is placed on the state of a system at a given time (time dependent) described by a complex wave function. If we assume, firstly, that all the in-going particles are represented by wave-packets of the same shape and size, the time-dependent Schrödinger equation can be used. For such a wave packet the key is to find the probability amplitude ($\psi(\mathbf{r}, t)$) for the out-going waves in various directions, some time after the scattering process has taken place.

$$H\psi(\mathbf{r}, t) = \left[-\frac{\hbar^2}{2m}\Delta + V(\mathbf{r})\right]\psi(\mathbf{r}, t) \tag{3.1}$$

In Eqn. 3.1, H is the Hamiltonian operator, ψ the wave function, and $\hbar$, is Planck's constant. $\psi(\mathbf{r}, t)$ is the amplitude of probability that a particle will be present with respect to the position $\mathbf{r}$ in (x, y, z) and at time, t. m is the mass of the particle and $V(\mathbf{r})$ is the potential of the target during the scattering process [146]. This consideration is fine for a basic scenario with an incoming flux of particles with wave packets of the same energy, however in the case where the incident beam of particles is switched on for a time, longer than the time it would take a particle to cross the interaction region, *steady-state* conditions apply. Furthermore, if we assume that the incoming wave packet has a well-defined energy (and hence momentum) of many wavelengths long it can be considered a plane wave. In terms

of describing this with the Schrödinger equation, we set $\psi(\mathbf{r},t)$=$\psi(\mathbf{r})e^{-iEt/\hbar}$ and look for solutions of $\psi(\mathbf{r})$ using the time-independent Schrödinger equation:

$$E\psi(\mathbf{r}) = \left[-\frac{\hbar^2}{2m}\nabla^2 + V(\mathbf{r})\right]\psi(\mathbf{r}) \tag{3.2}$$

This is subject to the boundary condition that the incoming component of the wave function is a plane wave $e^{i\mathbf{k}\cdot\mathbf{r}}$. The energy of the incoming flux of particles E is given as $E = \mathbf{p}^2/2m = \hbar\mathbf{k}^2/2m$.

With this in mind, a model to describe such a scattering process can be done so by using Eqn. 3.1 in combination with Green's function to reach the so called Born approximation. We picture a beam of particles moving along the negative z axis towards the origin. When the particle is scattered by the potential $V(\mathbf{r})$ and goes off as an out-going spherical wave, the wave function must satisfy the time independent Schrödinger equation (Eqn. 3.2). Using the substitution $2mE/\hbar^2 = k^2$ we obtain the following:

$$\nabla^2\psi(\mathbf{r}) + k^2\psi(\mathbf{r}) = -\left[-\frac{2m}{\hbar^2}V(\mathbf{r})\psi(\mathbf{r})\right] \tag{3.3}$$

As the particle scatters from a potential, a solution with an asymptotic form is needed, the wave function is then given as

$$\psi(\mathbf{r}) \sim e^{i\mathbf{k}_0\cdot\mathbf{r}} + f_k(\theta,\varphi)\frac{e^{ikr}}{r} \tag{3.4}$$

Here $e^{i\mathbf{k}_0\cdot\mathbf{r}}$ is the incident plane wave with propagation vector $\mathbf{k}_0$, the subscript 0 is used to indicate that the direction of propagation is in the θ=0 (z-axis) direction. The magnitude of both k and k_0 are equal, e^{ikr}/r is the outgoing spherical wave with an angular dependent amplitude factor denoted as $f_k(\theta,\varphi)$. The differential probability $d\sigma/d\Omega$ is the scattering cross section per unit solid angle and can also be given by $|f_k(\theta,\varphi)|^2$. By using the time independent Schrödinger equation given in Eqn. 3.3 $[-(2m/\hbar^2)V(\mathbf{r})\psi(\mathbf{r})]$ and the standard Green's function $G(\mathbf{r}_1,\mathbf{r}_2)$ for a point source potential $-\delta(\mathbf{r}_1-\mathbf{r}_2)$ we obtain the following expression for the wave function:

$$\psi(\mathbf{r}_1) = e^{i\mathbf{k}_0\cdot\mathbf{r}_1} + \int \frac{2m}{\hbar^2}V(\mathbf{r}_2)\psi(\mathbf{r}_2)G(\mathbf{r}_1,\mathbf{r}_2)d^3r_2 \tag{3.5}$$

where $\mathbf{r}_1$ is the potential away from the origin and the charge at $\mathbf{r}_2$. When the term for the incident plane wave $e^{i\mathbf{k}_0\cdot\mathbf{r}_1}$ is left out of equation Eqn. 3.3 it no longer provides the required asymptotic form for the scattering process. Given that the Green's function we have used above is the function of $G = \nabla^2 + k^2$ (see Eqn. 3.1), the standard result for the calculated integral in 3-dimensions is as follows:

$$G(\mathbf{r}_1,\mathbf{r}_2) = \frac{e^{ik|\mathbf{r}_1-\mathbf{r}_2|}}{4\pi|\mathbf{r}_1-\mathbf{r}_2|} \tag{3.6}$$

By substituting in Eqn. 3.4 into the given expression for the wave function shown in Eqn. 3.3 and using $\psi_0(\mathbf{r}_1) = e^{i\mathbf{k}_0\cdot\mathbf{r}_1}$, gives the final derived form for the Born

approximation:

$$\psi(\mathbf{r}_1) = \psi_0(\mathbf{r}_1) + \frac{2m}{\hbar^2}\int G(\mathbf{r}_1, \mathbf{r}_2)V(\mathrm{r}_2)\psi(\mathbf{r}_2) \tag{3.7}$$

Eqn. 3.7 can be further formalized to $\psi^1(\mathbf{r})) = \psi_0 \int GV\psi^0$ and is known as the first Born approximation when solved for he incident wave ψ^0 as the first approximation. It works for the assumption that it takes the incident field rather than the total field as the driving force at each point scatterer. The approximation is more accurate when the scattered field is smaller than the incident field on the scatterer (weak scattering potential, V($\mathbf{r}$)) in a small scattering volume. These assumptions reduce the likelihood of multiple scattering. For example, in neutron diffraction the Born approximation often holds for not too large samples, except for neutron optical phenomena such as total internal reflection in a neutron guide, or Grazing Incidence Small Angle Scattering (GISAS) [147]. In a scattering experiment, when the size of the sample R is much smaller than the distance away from the detector for the scattered wave ($\mathbf{r}_2$) $R = |\mathbf{r}_1 - \mathbf{r}_2|$ (almost always fulfilled in a typical scattering experiment) the far field or Frauenhofer approximation can be included. Eqn. 3.7 can extended for incorporating the case that the distance between the sample and the scattered wave is much larger than the sample, by substituting for R we obtain the following for the far field approximation

$$\psi^1(\mathbf{R}) = e^{i\mathbf{k}\cdot\mathbf{R}} + \frac{e^{ik\cdot R}}{2\pi\hbar^2}\int V(\mathrm{r}_2)e^{i\mathbf{Q}\cdot\mathbf{r}_2}d^3r_2 \tag{3.8}$$

The first term on the right hand side represents the incoming plane wave, the second relates to the amplitude of the scattered wave. The second term is proportional to the Fourier transform of the scattering potential. The scattering vector $\mathbf{Q} = \mathbf{k}_f - \mathbf{k}_i$, discussed in more detail in the following section, depends on the incoming plane wave $\mathbf{k}_i$ and the scattered plane wave $\mathbf{k}_f$. Now that we have the amplitude of the scattered wave, the final point of call is to find the final form for the intensity. The intensity $I(\mathbf{Q})$ is calculated using the square of the absolute value for the scattering amplitude $F(\mathbf{Q})$; $I(\mathbf{Q}) \propto |F(\mathbf{Q})|^2$. Therefore, given that the square of the scattering amplitude is directly proportional to the observed intensity, it also follows that the observed intensity is proportional to the Fourier transformation of the scattering potential $|F[V(\mathbf{r}_1)]|^2$ and written as:

$$|F[V(\mathbf{r}_1)](\mathbf{Q})|^2 = \left|\frac{m}{2\pi\hbar^2}\int V(\mathrm{r}_2)e^{i\mathbf{Q}\cdot\mathbf{r}_2}d^3r_2\right|^2 \tag{3.9}$$

The following sections will include the different types of scattering used in this thesis, which are based on the result obtained in Eqn. 3.9.

3.6.2 Diffraction by crystalline materials

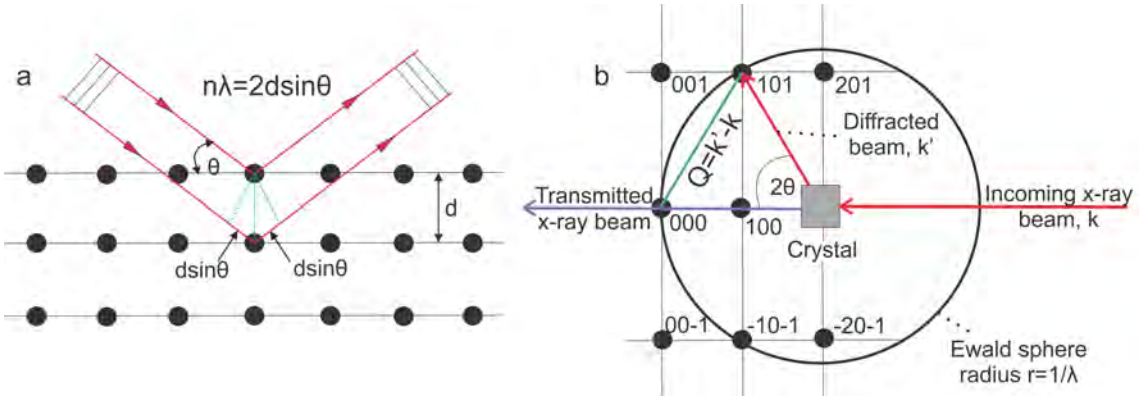

Figure 3.4: (a) Bragg's law of diffraction. Constructive interference occurs only when the path difference is equal to an integer number of wavelengths. (b) Ewald construction showing intersection of (101) reflection with Ewald sphere and thus meeting the Bragg condition. Q is the scattering vector, calculated from k and k', incident and diffracted wave vector, respectively.

In this section we will look at the scattering process from a periodic arrangement of atoms. In a crystal structure, the atoms are arranged in a specific pattern. This pattern is defined by various symmetry operations which, in crystallography terms is built up of 14 conventional Bravais lattices and of these 14 different structure types, can be further sub-categorized into 230 space groups [148] from low to high symmetry. High symmetry refers to atomic arrangements that can be identified with a multitude of symmetry operations for example N^o 166 is $R\bar{3}m$ the rhombohedral cell, and for this particular space group the given letters and symbols represent the symmetry of the structure. In this case there is 3-fold rotational symmetry and mirror symmetry. The lowest symmetry space group is that of $P1$, with no symmetry elements. When scattering from a periodic arrangement of atoms, constructive interference occurs when the path difference for elastically scattered waves is a multiple integer n of their own wavelength (illustrated in Fig. 3.4, left) and given in basic terms as

$$2\pi n = \mathbf{d} \cdot (\mathbf{k}_f - \mathbf{k}_i) \tag{3.10}$$

The scattering vector $\mathbf{Q} = \mathbf{k}_f - \mathbf{k}_i$ for a given crystal structure with constructive interference in 3D describes the relationship between the wave vector of the incident $\mathbf{k}_i$ and diffracted particle beam, $\mathbf{k}_f$. This construction is known as the Ewald sphere and shown in Fig. 3.4. For a periodic arrangement of atoms in a crystal, the positions of constructive interference are calculated via the Fourier transform of its lattice vectors $\mathbf{a}^*$, $\mathbf{b}^*$ and $\mathbf{c}^*$ with respective h, k, ℓ integers.

$$\mathbf{Q} = h\mathbf{a}^* + k\mathbf{b}^* + \ell\mathbf{c}^* \tag{3.11}$$

The h, k, ℓ integers, also known as Miller indices [148] denote the family of planes orthogonal to the basis of the reciprocal lattice vector. The individual reciprocal space lattice vectors can be calculated using the following relations:

$$\mathbf{a}^* = \frac{2\pi(\mathbf{b} \times \mathbf{c})}{\mathbf{a} \cdot (\mathbf{b} \times \mathbf{c})}, \qquad \mathbf{b}^* = \frac{2\pi(\mathbf{c} \times \mathbf{a})}{\mathbf{b} \cdot (\mathbf{c} \times \mathbf{a})}, \qquad \mathbf{c}^* = \frac{2\pi(\mathbf{a} \times \mathbf{b})}{\mathbf{c} \cdot (\mathbf{a} \times \mathbf{b})} \tag{3.12}$$

Continuing from the above notions, the angle of diffraction with respect to the scattering planes as depicted in Fig. 3.4 (left) is described by Bragg's law:

$$n\lambda = 2d_{(hkl)}sin\theta \qquad \text{with} \qquad d_{(hkl)} = \frac{2\pi}{|\mathbf{Q}(hkl)|} \tag{3.13}$$

In Eqn. 3.13, $d_{(hkl)}$ is the spacing between lattice planes. The Bragg equation allows one to ascertain information about the d-spacing, and with various substitutions, reciprocal lattice vectors. Based on the research conducted in this thesis regarding the single crystal refinements conducted on $YbFe_2O_4$, our interest is focused around the hexagonal and monoclinic lattice types described by the following relations:

Hexagonal relation:

$$\frac{1}{d_{hkl}^2} = \frac{4}{3}\left(\frac{h^2 + hk + k^2}{a^2}\right) + \frac{l^2}{c^2} \tag{3.14}$$

Monoclinic relation:

$$\frac{1}{d_{hkl}^2} = \frac{1}{sin^2\beta}\left(\frac{h^2}{a^2} + \frac{k^2 sin^2\beta}{b^2} + \frac{l^2}{c^2} - \frac{2hlcos\beta}{ac}\right) \tag{3.15}$$

The Bragg equation does not account for the atomic distribution inside a crystal therefore one must refer to the atomic form factor $f_j(\mathbf{Q})$, which depends on the scattering amplitude of the individual atoms, the Bragg angle and the type of radiation involved. If $\mathbf{R}_n = m\mathbf{a} + n\mathbf{b} + o\mathbf{c}$ are the lattice vectors that define the lattice and $\mathbf{r}_j$ the position of the atoms with respect to any one particular lattice site, then the position of any atom in the crystal is given by $\mathbf{R}_n + \mathbf{r}_j$. It therefore follows that for the scattering amplitude for the crystal factorizes into the product of two terms and written as:

$$F(\mathbf{Q}) = \sum_j f_j(\mathbf{Q}) e^{i\cdot\mathbf{Q}\cdot\mathbf{r}_j} \tag{3.16}$$

3.6.3 X-ray scattering

In an x-ray diffraction experiment, the incoming x-ray beam is directed from a source onto a given sample. The x-rays, unlike neutrons (see Sec. 3.6.4) only have the ability to interact with the electron cloud surrounding the nucleus of an atom. The scattered rays are collected on a detector, and intensities are read as a function of 2θ. The interaction of an x-ray incident on the electron cloud creates spherical waves, in most cases these waves interfere destructively. However, when they constructively add (difference between the paths is an integer number of wavelengths) in a few specific directions the process can be described by Braggs law (Eqn. 3.13) and illustrated in Fig. 3.4. The scattering process of a beam of photons is described classically by Thomson scattering: in essence the scattering of electromagnetic radiation by a free non-relativistic charged particle. It is also classed as the low-energy limit of Compton scattering: this describes the scattering of a photon by a charged particle (often an electron), in this case however it results in a decrease of energy (increase wavelength) of the photon called the Compton effect. Part of the photon energy is transferred to

the recoiling electron and thus known as an inelastic process, compared to Thomson scattering, which is elastic. In Thomson scattering it is the electric field of the incident wave which accelerates the charged particle, causing it to emit radiation at the same frequency as the incident wave, thus scattering the wave. For x-rays scattering off a densely populated electron cloud surrounding the nucleus, there is an increase of destructive interference, along with the constructive interference, the latter resulting in reflections. As a result this promotes a decay of the atomic form factor for increasing angle. Since the atomic form factor is element-specific, it relies on the Fourier transform of the spatial electron density distribution $\rho_j(\mathbf{r}_j)$ of the element in question.

$$f_j(\mathbf{Q}) = \int_{V_j} \rho_j(\mathbf{r}_j) e^{i \cdot \mathbf{Q} \cdot \mathbf{r'}_j} d^3 r' \tag{3.17}$$

The scattering vector $\mathbf{Q}$ can be recalled from Eqn. 3.13, and $\mathbf{r}'$ is the position vector of the scattered wave.

3.6.4 Neutron scattering

Neutron scattering is a very important tool when investigating both the atomic and magnetic structure of compounds. Although they are neutral in charge, the constituent quarks which make up a neutron, namely one up and two down quarks, give the neutron a magnetic moment, and thus allows them to interact with the magnetization in the system. The large magnetic moment of neutrons (-1.91μ_B) as a result make them an excellent and sensitive probe for the determination of magnetic structures. The scattering potential $V_n(\mathbf{r})$ of a neutron is made of two parts; the nuclear V_N and magnetic V_M scattering [143] which is described by the following equation:

$$V_n(\mathbf{r}) = V_N + V_M(\mathbf{r}) \tag{3.18}$$

The inter-atomic distances for crystals are in the range of Å. A neutron will need an energy of approximately 25 meV to achieve a wavelength of 1Å.

Nuclear scattering

With the already established energy requirements described above to probe an atomic structure with neutrons, the next step is to understand how the neutron interacts with a system. Unlike x-rays (see Sec. 3.6.3) which impinge off the electron cloud surrounding atoms, neutrons interact with the atoms nucleus via the strong force. As the neutrons force is short-range and the nuclei are very small compared to the wavelengths used, the interaction potential $V_N(\mathbf{r})$ is approximated by a delta function $\delta(r)$. This is formulated by using the Fermi pseudo potential which assumes a delta potential $\delta(r)$ and describes the scattering of free neutrons by a nucleus. The general form then given for the potential of a neutron scattering process is:

$$V_N(\mathbf{r}) = \frac{2\pi\hbar^2}{m_n} b_i \delta(\mathbf{r} - \mathbf{r}') \tag{3.19}$$

The new term b_i is the scattering length, and in terms of the structure factor, $N(\mathbf{Q})$, is very similar to that of the atomic form factor of x-ray scattering, but independent of the scattering vector $\mathbf{Q}$ and defined as:

$$N(\mathbf{Q}) = \sum_j b_j e^{i\mathbf{Q}\mathbf{r}_j} \tag{3.20}$$

Now, b_i varies greatly for different elements and respective isotopes, which are often not seen in normal x-ray diffraction since it depends strongly on the nuclei-neutron interaction. Therefore in order to ascertain the correct result of a nuclear scattering process, one must take into consideration the large variation of the scattering length. The variation in scattering lengths is due to the randomness of isotope distribution. This is resolved by averaging over the whole isotope distribution and shown in Eqn. 3.21.

$$\frac{d\sigma}{d\Omega} = \langle b^2 \rangle \sum_{i,j} e^{-\mathbf{Q}\cdot(\mathbf{R}_i - \mathbf{R}_j)} + \left(\langle b^2 \rangle - \langle b \rangle^2 \right) N \tag{3.21}$$

There are two contributing factors to the nuclear scattering, the left term on the right hand side of Eqn. 3.21 relates to the coherent scattering, dependent of the direction of the scattering vector $\mathbf{Q}$ (refer back to Sec. 3.6.1) and contains the phase information. The right term denotes the incoherent scattering which is uniform in all directions and gives rise to an isotropic background in experiments. N=the number of atoms in the scattering system.

Magnetic scattering

The neutron, based on its constituent building blocks has an intrinsic magnetic moment $\boldsymbol{\mu}_n$. The magnetic part of neutron scattering results from the interaction of the magnetic moments of the neutron, with the magnetic fields arising from the spin and orbital momentum of the unpaired electrons in the sample. The magnetic scattering potential of a neutron in simplistic terms is given as $V_n = -\boldsymbol{\mu}_n \cdot \mathbf{B}$ [150]. Since the neutrons scattered are dependent on both the spin $\mathbf{B}_S$ and unquenched orbital contributions $\mathbf{B}_L$, one can expand this potential into the following:

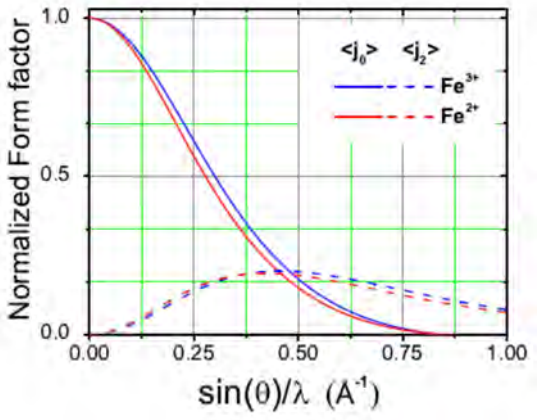

Figure 3.5: Neutron magnetic form factors of both spin and their orbital contributions, given for the different Fe^{2+} and Fe^{3+} valences. Figure taken from [26], original data from [149].

$$V_n = -\boldsymbol{\mu}_n \cdot (\mathbf{B}_S + \mathbf{B}_L) \tag{3.22}$$

Here $\mathbf{B}_S = \nabla \times \frac{\mu_e \times \mathbf{r}}{r^3}$ and $\mathbf{B}_L = -\frac{e.\mathbf{v}_e \times \mathbf{r}}{c \cdot r^3}$ [17]. The neutron interaction potential (Eqn. 3.22), for a scattering process in which a neutron changes its wave vector and the projection of the spin moment from the quantization axis z; from σ_z to σ'_z, can be expressed in the first Born approximation (see Sec. 3.6.1). The quantization axis in neutron scattering is often designated via a small guide field, which orientates the

neutron spins in a specific alignment incident on a sample. The magnetic scattering of neutrons can be used to elucidate the spin configuration in a magnetic material. The general form [151,152] given to describe the scattering cross section of a neutron is:

$$\frac{d\sigma}{d\Omega} = {\gamma_n}^2 {r_0}^2 \left| -\frac{1}{2\mu_B} \left\langle \sigma_z' \middle| \hat{\sigma} \cdot \mathbf{M}_\perp(\mathbf{Q}) \middle| \sigma_z \right\rangle \right|^2 \tag{3.23}$$

Here the terms γ_n=-1.913 and $r_0 = \frac{e^2}{m_e c^2}$ are the qyromagnetic ratio for the neutron and classical electron radius, respectively. The σ symbol is representative of the neutron spin operator [150]. Here $\mathbf{M}(\mathbf{Q})$ is defined as

$$\mathbf{M}(\mathbf{Q}) = \int_{-\infty}^{\infty} \mathbf{M}(\mathbf{r}) e^{(i\mathbf{Q}\cdot\mathbf{r})} d\mathbf{R} \tag{3.24}$$

$\mathbf{R}$, i.e the Fourier transform of the magnetization density. The $\mathbf{M}_\perp$ term in Eqn. 3.23 means that only magnetization components perpendicular to the scattering vector $\mathbf{Q}$ can be measured

$$\mathbf{M}_\perp(\mathbf{Q}) = \mathbf{Q} \times \mathbf{M}(\mathbf{Q}) \times \mathbf{Q} \tag{3.25}$$

When viewing equations Eqn. 3.24 and Eqn. 3.25 one can see that $\mathbf{M}_\perp$ is the perpendicular component to the scattering plane of the Fourier transformed magnetic moment $\mathbf{M}(\mathbf{Q})$ [150]. The last important aspect of the magnetic scattering which needs to be taken into consideration, which does not occur in the nuclear scattering, is the presence of the magnetic form factor. As described above there are two main aspects to the magnetic scattering, spin and orbital order. However, the form factor is best described when using solely the pure spin scattering. Referring back to Eqn. 3.24 the macroscopic magnetic moment $\mathbf{M}(\mathbf{Q})$ can be split into two separate components, each atom and the surrounding electrons with spin moments $\mathbf{s}_i$, this then gives a new form of Eqn. 3.24 in terms of each contribution.

$$\mathbf{M}(\mathbf{Q}) = -2\mu_B \cdot f_m(\mathbf{Q}) \cdot \sum_i e^{i\mathbf{Q}\cdot\mathbf{r}} \cdot \mathbf{S}_i \tag{3.26}$$

Here f_m is the magnetic form factor, and it is given in terms of the Fourier transform of the spin density distribution of a single atom:

$$f_m(\mathbf{Q}) = \int_{atom} \rho_s(\mathbf{r}) e^{i\mathbf{Q}\cdot\mathbf{r}} d^3r \tag{3.27}$$

As the magnetic scattering takes places in the electron cloud of the atom, interaction is only possible with electrons, and thus comparable to the atomic form factor for x-rays. But as it is only unpaired electrons in the outer shell which contribute to the magnetic moment, a resultant much stronger decrease in the scattering vector $\mathbf{Q}$ is observed compared to that seen in x-ray scattering [149]. The magnetic form factor describing the Q-dependence of the magnetic neutron cross section of a single magnetic ion can be determined using the following

$$F_{mag} = \langle j_0 \rangle(k) + \left(1 - \frac{2}{g}\right) \langle j_2 \rangle(k) \tag{3.28}$$

The different coefficients which approximate (k) of $\langle j_0 \rangle$ $\langle j_2 \rangle$ are determined experimentally [149] and the gyromagnetic ratio can given as $g = 2$, for the case of spin-only scattering. The next section will highlight the slightly more complex case of polarization analysis, which can be a very powerful tool for unveiling complex magnetic structures in a system.

Polarization analysis

The use of x, y, z polarized neutron scattering has been a key tool in determining complex magnetic structures. The technique allows for the simultaneous and unambiguous separation of the nuclear, magnetic, and nuclear spin-incoherent contributions to the scattering. The total scattering process which consists of several possible factors, simplistically nuclear and magnetic, more specifically can be broken down into coherent and incoherent scattering (see [153–155]). From the combined contributions of nuclear and magnetic scattering, when there is no polarization, $\mathbf{P} = 0$, the only terms remaining are each type of nuclear scattering and the magnetic component $|\mathbf{M}_{\mathbf{Q}}^{\perp}|^2$. When polarization analysis does take place and $\mathbf{P} \neq 0$ we can use a set of special rules in which: the neutron polarization $\mathbf{P}$ direction will be reversed (spin-flip) if the polarization is $\mathbf{P}||\mathbf{M}_{\perp}$, and not reversed (non-spin flip) if $\mathbf{P}\perp\mathbf{M}_{\perp}$. For the special case $\mathbf{P}||\mathbf{Q}$, all magnetic scattering is spin-flip (by definition of $\mathbf{M}_{\perp}$). For the polarized neutron measurements performed in this thesis, only the x and z polarization channels were measured, with both spin flip and non-spin flip scattering, to view the magnetic correlations in the $hh\ell$ plane.

3.7 Experimental scattering techniques and instruments used

3.7.1 Powder x-ray diffraction

Powder x-ray diffraction works on the principle of an x-ray source, powdered sample and detector. For a powder sample every possible crystalline orientation is represented equally, classed as isotropic texturing, compared to the case of a single crystal (see Sec. 3.7.3) which is classed as anisotropic (often with a specific orientation, unless twinned or multi-grain, and no longer a single crystal at that point). When the x-ray hits the random arrangement of the powder the sample itself in this case acts as a diffraction grating and will produce bright spots, reflections on the detector. The spacing of the spots can be determined using Bragg's law (See Eqn. 3.13). As powder represents a random orientation of the crystalline particle, a significant number of each plane of the crystal structure will be in the correct orientation to diffract the x-rays, however in some cases, it is necessary to rotate the sample to eliminate effects of texturing (preferential orientation of the crystallites).

The use of powder x-ray diffraction became a very standardized procedure for phase purity analysis of $YbFe_2O_4$ powder batches. A short powder diffraction measurement was also conducted on a section cut from the end of the crystal growth. This was to provide an initial indication of phase purity and whether it remained upon melting, due to the different gas atmospheres used for single crystal growth

compared to the same CO:CO_2=1:3 used for each powder synthesis. Powder diffraction was performed using a Huber Guinier D670, Philips PW1720 X-ray diffractometer and Bruker D5005.

3.7.2 Laue diffraction

Contrary to normal x-ray diffraction which uses a monochromatic beam, typically Cu-Kα or Mo-Kα, Laue diffraction uses a beam of white x-rays, otherwise known as Bremsstrahlung radiation, which is built up of many different wavelengths. When a thin, pencil-like beam of x-rays is allowed to impinge on a crystal, those of certain wavelengths will be oriented at just the correct angle to a group of atomic planes so that they will combine in phase to produce intense, regularly spaced spots on a film or detector plate. The use of Laue diffraction is fundamental, when primarily checking for crystal quality and later selecting parts of a boule which exhibit the same Laue pattern, often indicating a single crystal. In the set-up used for this work, back reflection Laue diffraction was used: in this method, the detector is placed between the x-ray source and the crystal, the beams which are diffracted in a backward direction are recorded. During the course of this PhD thesis all crystals were oriented using a MWL120 real time Laue system from Multiwire Laboratories Ltd., which has a 30x30 cm proportional wire chamber area detector. This particular set-up also includes a camera system in combination with a mirror that can be used to align the sample on the goniometer and to capture pictures of the crystal on a sample holder. The 3-axis goniometer allows the user to orient the sample during live feed back from the camera, as well as the continually updated Laue image. For more information on this technique, a more detailed overview is given in my masters thesis [57].

3.7.3 Single crystal x-ray diffractometer Supernova

Single crystal x-ray diffraction is an important and powerful experimental approach to uncover valuable structural information on a specific compound. It allows one the possibility to search for temperature dependent phase transitions with more sharp and clear reflections than those observed in powder diffraction (attributed to the texturing discussed in Sec.3.7.1). For the course of this thesis in-house single crystal x-ray diffraction, from sample allocation to the final data set for refinement were all conducted on a Rigaku Oxford diffraction SuperNova with both Cu-Kα and Mo-Kα radiation. For the vast majority of experiments the choice of MoKα radiation over the generic CuKα is of strategic use. The heavy rare earth elements in this series of compounds e.g Yb (Z=70) and Lu (Z=71), leads to a very large absorption. However by using $Mo_{k\alpha}$ radiation with a smaller wavelength of λ=0.709Å over the choice of $Cu_{k\alpha}$ with a wavelength λ=1.540Å, greatly reduces the absorption. Additionally the second disadvantage of using $Cu_{k\alpha}$ radiation is the close relation of the absorption edges, the Cu K-edge is 8.04 keV and in close range to the Fe-absorption edge (7.11 keV), and as a result would add a strong florescence background [156]. A schematic of the experimental set-up is shown in Fig. 3.6. The x-rays are generated by a micro-focus sealed tube Fig. 3.6(1), which is mounted on the goniometer and powered by a high voltage x-ray generator. To better focus the beam, focusing optics and a collimator are used. The sample holder and goniometer head, shown in

Fig. 3.6(7), can be viewed through the video microscope, Fig. 3.6(8). This is primarily used to provide visual aid whilst centering the sample, but also, importantly records a short video at the beginning of a full experiment for face indexing the crystal and absorption correction [157]. For temperature dependent measurements a Cryojet (Fig. 3.6(9)), which constantly blows cold N_2 gas on the sample is used, and controlled via a Lakeshore temperature controller. The CCD (Charge Coupled Device) area detector works on the principle that the incoming x-rays enter the detector through a Beryllium window, Fig. 3.6(6), to a vacuum sealed detector unit. A scintillation screen absorbs the incident x-ray photons and re-emits the energy in the form of light, which is then conducted via a fibre optic reduction taper [158] towards the scientific grade CCD chip. The CCD signal is then digitalized to an 18-bit resolution by a correlated double sampling circuit [159] with an analogue-to-digital converter located in the detector head. The final data transfer is done so via a gigabit Ethernet link to the PC, where the control program stores the data for further analysis to the hard disk [157].

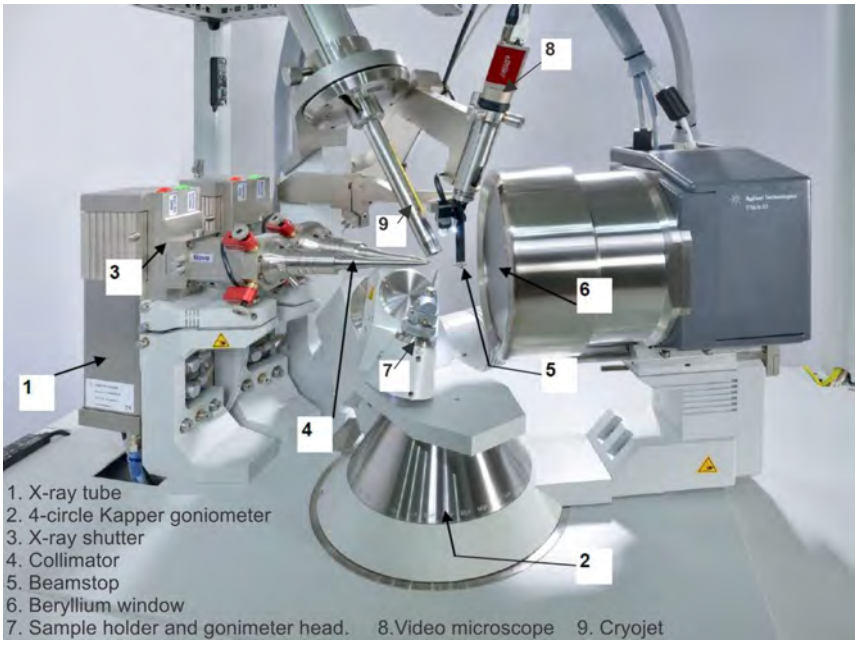

Figure 3.6: Image of general SuperNova experimental set-up taken from [157] and adapted.

Crystal selection and mounting

The selection of a suitable crystal for in-house single crystal diffraction, is perhaps one of the most important steps and also the most time consuming. In order to give an experiment the best chance of success, good crystal selection is a necessity. For in-house single crystal measurements small crystals in the range of 100 microns are commonly used [160](pp.35). Ideally, the best shape for a crystal with regards to better absorption correction (See Sec. 3.8.1) is that of a sphere, however, when working with such small crystals, this task becomes very difficult if not impossible to achieve. Fortunately, with the advanced standard of crystallography software, absorption correction of a variety of differently shaped crystals can be done successfully [144]. So, the question remains, what is a good crystal?

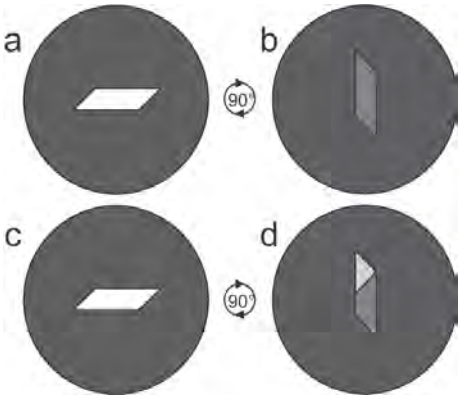

Figure 3.7: Optical extinction observed between crossed polars.

To obtain a selection of small crystals from a larger crystal sample, it is usual to smash the piece carefully, and to then place the small fragments into a plastic or thin glass petri dish. For analysis of the crystals a microscope with a polarizing attachment (which is actually a birefringent lens with light) and at least x40 magnification is required. The samples can then be placed on the microscope illuminating the crystals. The first step is to look for crystals that have a nice cubed or rectangular platelet-like shape. If the crystal selected transmits polarized light, on turning the sample through angles of 90 °, the light should be extinguished (the crystal turns dark), a clear example of this effect is shown in Fig. 3.7 (a,b). If on rotating the sample a section of the crystal remains illuminated, it is not a single crystal, and most likely contains a twin or an aggregate of smaller crystals [160](pp.35) [161] this crystal can then be removed as a possible candidate (see Fig. 3.7 (c,d)).

On the successful selection of a crystal following the previous criteria, it is mounted. There are a number of techniques which can be used depending on the size and shape of the selected crystal, some of these examples are shown in Fig. 3.8. The three methods used for the single crystal investigations in this research were techniques (a, b and e). I shall now explain briefly the pros and cons of each of these three sample mounting techniques.

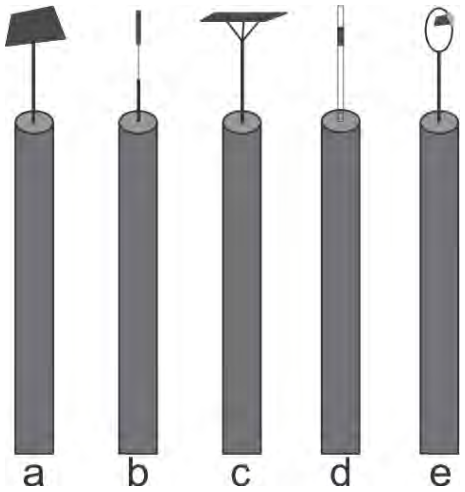

Figure 3.8: Various methods of mounting crystals: a) on a glass fibre; b) on a two-stage fibre; c) on a single fibre topped with several short pieces of glass wool; d) within a capillary tube and e) in a solvent loop.

Method (a): **Glass fibre and adhesive**:- this technique is by far one of the best methods of crystal mounting, once a good crystal has been acquired. For crystal scanning (which will be explained in the next section) type (e) sample mounting should be used initially. A glass fibre of ∼0.05 mm thickness and 5 mm length is attached to the pip with a two component glue. Once this has dried a second batch of this glue is made, to secure the sample on the end of the glass rod, ensuring that when dipping the other end of the glass fibre into the glue, removing any excess before contacting it with the crystal. It is necessary to hold it steady against the desired edge of the crystal, where the largest surface area should be exposed to the incoming x-ray beam, shown in Fig. 3.8a. After a few minutes it will be ready to mount on the goniometer for a measurement. The tricky aspect of this mounting is that it is incredibly easy,

especially if its a thin platelet, for the crystal to flip over on to the fibre, attaching itself in the completely wrong orientation. Sometimes the use of a special crystal handling tool (often a deer hair on the end of a metal handle, or a very thin metal probe) can be used to fix the crystal position. However if this is unsuccessful, both the pip and crystal mounting on the fibre glass will need to be submerged in ethanol or acetone to dissolve the glue and try again. With the mounting difficulty being the only main disadvantage, the advantages supersede, the absorption correction is much easier as a clearer profile of the crystal is obtained, often this can be hidden with the loop method (e), where the crystal can be obscured in the movie for face indexing absorption correction by the grease. Also, the sample will not move, or if so with only small wobbles due to the goniometer movement, which can be corrected for if needed by the CrysAlisPro software. This is a mounting method for an established good quality crystal, in which longer more detailed measurements are required.

Method (b): **Two staged glass fibre** :- this method, in principle is identical to (a), the only difference being that the glass fibre is necked. This can be achieved when making the thin glass fibres, and done by taking two larger glass rods, ∼3-4 mm in thickness and heating one side of each tip up, until melted and bringing them together. At which point turning them in the flame, then when homogeneously melted moving the combined rods out of the flame and pulling them apart, such that a thin string is produced. This is a type of glass fibre used for crystal mounting. With particularly small samples it may be necessary to heat a thick rod with a candle to thin the top part, so its affixed more easily (see Fig. 3.8b).

Method (e): **Grease and loop**:- this is one of the common sample mounting types, commercially available (costing about 5 Euros each) and attached magnetically to the goniometer head (see Fig. 3.8e). This is one of the easiest methods of crystal mounting, a small loop with a diameter of a few microns is dipped in a very small amount of vacuum grease, contact is then made by simply touching the loop on the selected crystal. The nice aspect with this method of sample mounting is the crystal can be moved more easily and freely around the loop to position it as desired. As shown in Fig. 3.8e, the crystal is fixed to the inside edge of the crystal, such that the largest area of the crystal will be hit by the incoming x-rays. It is also important to avoid using too much grease when it comes to absorption correction in the data analysis. The major disadvantage for this method, is that the sample can move in the grease after long measurement times (particularly at room temperature). The CrysAlisPro software for data handling can account for 'significant sample wobble' in the data reduction stage (see Sec. 3.8.1) but not for large movement. Therefore, this method is particularly useful for; crystal scanning, where several samples are checked for crystal quality, twins which have evaded you during the microscope process, which is highly possible if the twins are only a few degrees apart, or a large factor discussed in this thesis, the sample is off-stoichiometric and shows short range CO.

Crystal Screening and pre-experiments

The process of crystal screening and pre-experiments is perhaps one of the most important in determining the overall success of the experiment. A large majority

of the poor crystal candidates can be eradicated using the birefringent lens on the microscope, and intuition when looking at the shape and size. It is more beneficial to find 4-5 crystals (optimum size for SuperNova; crystal radius $\leq$0.3 mm [157]) and mount them on loop sample holders, Fig. 3.8e, performing back to back short pre-experiments to speed up the screening process. A pre-experiment allows one to cover a small section of reciprocal space in a short amount of time. Firstly, the crystal selected and mounted on the holder is placed on the 4-axis Kappa goniomter, shown in Fig. 3.6(2). The video camera shown in Fig. 3.6(8) is then used to bring the sample into the centre of rotation of the diffractometer. A small key allows one to move goniometers degrees of freedom. Once the sample is positioned such that the sample centre is always on the cross (indicated on the sample mounting option of the Crysalis software using the video feed), the experimental parameters for a short pre-experiment can be input and started. Screening measurements are performed at room temperature. In some cases a short pre-experiment of 5 minutes will not yield a sufficient number of reflections, giving little information to the quality of the crystal. However, sometimes with $YbFe_2O_4$ the observation of diffuse CO, even with the limited data collected was enough to deem the crystal of poor quality. In many pre-screening scenarios, an advised estimated measurement time of 30 minutes, should yield enough information to decide whether or not the sample is worth keeping for further measurements.

Long measurements and temperature dependence

For measuring particular phase transitions on warming and cooling the SuperNova is set-up with a Cryojet, which continuously blows hot or cold nitrogen directly on the sample during a measurement (see Fig. 3.6 (9)). The temperature range that the Cryojet uses is between $\sim$90-490 K [162]. Often, once a pre-experiment is completed, one can index the few reflections to the correct cell. These lattice parameters are then saved when using the CrysalisPro software [163] and can be used for the programming of longer experiment. A good data set is needed for refinement of all possible structural solutions obtained from symmetry analysis, which ultimately requires a long experiment. The inclusion of video capture, can be set before the main experiment starts or after, but it is essential for the face indexing necessary for a numerical absorption correction in the later stages of data analysis. The video camera will take anything from 60 frames of the oriented crystal which, is mounted on the goniometer head. Table 3.1 gives a brief overview of the experimental parameters used to maximize the coverage of reciprocal space and times allocated to specific theta positions, to pick up both the weaker reflections and ones that are in the outer most resolution shells. Typically the measurements conducted in this manner for final structural refinement run over 4 days, in this case 163 hrs. Of course, trial and error is a big part of performing such long measurements, and the ones stated in the table are those which provided optimal results. The detector distance is vital when considering both the reflection coverage and also the type of radiation used for the experiments. All final experiments used for the structure refinements reported in this thesis employed Mo-Kα (λ=0.709). This is due to its shorter wavelength compared to Cu-Kα, allowing more reflections to be collected.

Expo Param.	Given value
Resolution	0.355 Å^{-1}
Laue group	1
Detector distance	70 mm
Complete redu. data	Yes
Lattice type	P (primitive)
Scan width	1.0°
Θ (°):- 34.21 to 34.21	20 s
Θ (°):- 92 to 99.50	60 s
Redundancy	14
No runs	87
Total frames	10388

Table 3.1: Typical parameters used for long measurements on the SuperNova single crystal diffractometer, which provided the best reciprocal space coverage and data quality.

3.7.4 High energy x-ray diffraction at the APS 6ID-D beamline

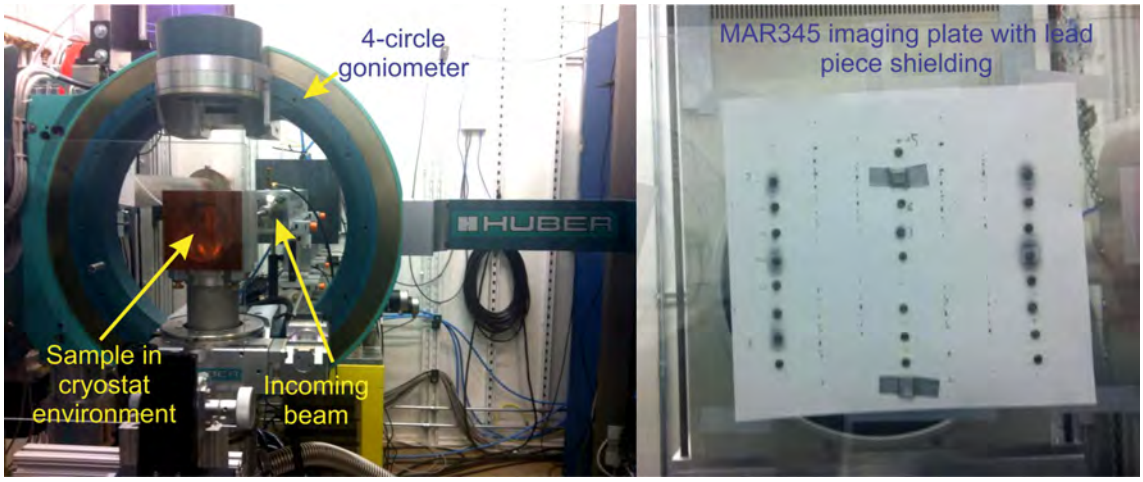

Figure 3.9: Experimental set-up at the beamline 6-ID-D. Left: image of goniometer and sample environment. Right: lead masking used for strong Bragg reflections, where over saturation on the MAR345 imaging plate will cause permanent damage.

High energy x-ray diffraction was performed at the Advanced Photon Source (APS) on the beamline 6-ID-D. The experimental set-up uses a 4 circle goniometor for single crystal diffraction with the added ability of low temperature measures with a Displex cryostat. The scattered x-rays are collected on a MAR345 imaging plate (diameter 345 mm) which has a sensitivity to a broad range of x-ray incident energies; 4 keV(3 Å) up to 100 keV(0.1236 Å) (the latter was used for all APS measurements provided in this thesis) and 10 μm^2 pixel size. Readout times range from 9 s for a 180 mm diameter, to 30 s for an area of 345 mm. For high energy x-rays, that have much smaller wavelengths ($\lambda = hc/E$, c=speed of light and h=Planck's constant), resulting in a larger radius of the Ewald sphere k_i and making detection of whole

reciprocal planes possible on the MAR detector, with just a small rocking of the crystal [26]. Measurements were performed by driving the vertical and horizontal tilting angles in a circular motion. The absence of rocking curves make the intensities obtained in this method unreliable. Typically, exposure times were usually in the order of some several seconds. However, longer scans can be performed to collect weaker reflection and/or weak diffuse scattering. To observe the weaker charge ordering peaks, the stronger more intense structural reflections were masked with 3 mm thick lead pieces, as shown in Fig 3.9 (left).

The lead masking also prevents over saturation and damage of the imaging plate [26]. An issue was encountered during measurements on cooling. The sample is mounted on a copper pin (∼3 mm diameter 20 mm in length), due to the expansion and contraction of copper when heated and cooled, the z vertical position of the sample changed, and thus no longer always in the direct beam. This was counteracted by performing scans at each desired temperature in 3 or 4 different z positions, to make sure that the crystal was measured when directly in the beam at temperatures down to 10 K.

3.7.5 Diffuse neutron scattering at MLZ, beamline DNS

The first neutron measurement was performed at the Heinz Maier-Leibnitz Zentrum (MLZ) in Garching, beamline DNS, which is a diffuse scattering cold neutron time-of-flight spectrometer with polarization analysis. This instrument is capable of successfully measuring smaller samples even of the order 3.5 mg, as shown by a $YbFe_2O_4$ sample discussed in Sec. 5.1 (S2-sample). This particular type of experiment, as discussed in the previous section, not only provides specific details about the various types of scattering and information obtained for both magnetic and nuclear contributions, it also allows one to map much broader region of reciprocal space compared to some of the other more standard neutron diffraction experiments. It is the use of a PG(002) double focusing monochromator which provides the large wavelength range of $2.4 < \lambda < 6.0$. An initial correction using a vanadium standard sample [1] was conducted before measuring the sample that was mounted on an aluminum holder.

DNS uses XYZ Helmholtz coils, which have the capability to generate a magnetic field pointing in any direction and thus change the incoming neutron polarization in the same direction. The instrument is equipped with 24 ^{3}He detector tubes, each filled with helium gas, and perhaps one of the most efficient ways of collecting neutrons with a polarization rate of 96% in such a set-up [164]. In order to perform the polarization analysis the detectors are equipped with m=3 Schärpf bender-type focusing supermirrors, where a polarized neutron flux as high as $5{\times}10^6$ n/(s·cm^2)

[1] Each detector sees a different amount of solid angle and each with varying efficiency, furthermore each analyzer has a different transmission. In order to make the appropriate correction, an initial run (experiment) is usually made with a standard vanadium sample. Vanadium is a purely incoherent scatterer and incoherent scattering is by definition isotropic. The scattering intensity seen in each detector is a measurement of detector efficiency, solid angle and analyzer transmission. If there are intensities picked up using the vanadium standard sample, then it typically means the instrument will need calibrating, and as the neutron cross section of vanadium is well known, it provides a systematic check of the experimental set-up.

is achievable at 4.74 Å. A neutron guide field preserves the neutron polarization between the polarizing supermirror benders and the sample. For time-of-flight spectroscopy the more recent installation of 128 position sensitive ^{3}He tubes each 1 m in height and 0.5 in diameter provide an increase of solid angle coverage [164]. Measurements conducted on the samples in this work were done so using the z and x ($x||\bar{\mathbf{Q}}$) polarization channel with a neutron wavelength (4.2 Å). For each experiment the cryostat was cooled to base temperature (∼3.5 K) and the specific temperatures of interest were measured on warming, typically 3.5, 100, 200 and 250 K. Information regarding both the magnetic spin-flip (SF) and nuclear non-spin-flip (NSF) contributions were obtained. Unfortunately, DNS provides only a vertical magnet for applied field experiments, as opposed to the horizontal magnet needed to probe the $hh\ell$ plane in $YbFe_2O_4$ and $LuFe_2O_4$ with a magnetic field applied in the c-direction, therefore the remaining neutron experiments covered in the following were conducted at neutron beamlines with an applicable horizontal magnet. In polarization measurements the most convenient and standard choice of an x, y, z-coordinate system for the setting of the polarization $\mathbf{P}$, is to have one axis, for instance x parallel to $\mathbf{Q}$, with the axes y and z perpendicular to $\mathbf{Q}$ pointing in- and out-of the scattering plane, respectively. However, with many polarized neutron experiments, most use a multi-detector system, in this case $\mathbf{P}$ can be set ideally parallel to $\mathbf{Q}$ only for a single detector.

3.7.6 Cold neutron diffraction at PSI, beamline DMC

Neutron diffraction in applied fields were performed at the Paul Scherrer Institut, Villigen on the beamline DMC. Although this beamline is primarily adept at performing powder neutron experiments, it is also possible to mount the crystal on an aluminum holder and perform rocking curves. This particular beamline is equipped with a linear position sensitive detector [165] and oscillating radial collimator system which suppresses peaks from the various sample environments. The optimized shielding reduces the effects from instrumental background. Since it is a cold neutron source the available wavelengths range between 2.3Å and 5Å. Measurements on ZFC and FC were performed in fields of 0 T and 1.8 T, the latter being the maximum field possible with the cryo-mag MA02 horizontal magnet, and operable in the temperature range 1.8-300 K. The temperatures of interest based on the initial magnetization measurements were focused at 200, 100 and 1.5 K. At a particular temperature and field, reciprocal space maps of the $hh\ell$ plane were measured, and 2D line integrals were taken of the magnetic peak intensity along ($\frac{1}{3}$, $\frac{1}{3}$, ℓ) and ($\frac{2}{3}$, $\frac{2}{3}$, ℓ).

3.7.7 Neutron diffraction at BER II, beamline E4

The E4 2-axis diffractometer is primarily used for magnetic structure determination. Like DNS, this beamline also uses a super mirror bender and a π-flipper, but rather than a multi-detector, the use of a 2D detector ($200\times200\,\mathrm{mm}^2$) with variable distance (640-900 mm) is used to detect the outgoing neutrons. The maximum magnetic field obtainable for the required horizontal magnet is <6 T, much higher than that obtainable at DMC, and thus provided a sound basis for further field and temperature dependent studies on $YbFe_2O_4$. There are two wavelengths accessible

depending on which monochromater is used, for a PG(002) (Pyrolytic Graphite) 2.44 Å or 1.2 Å with a Ge(113) (Gemanium) double focusing monochromator. As in all cases the sample was mounted using an aluminum holder, where several scans were done in the beginning to establish the dark angles of the horizontal magnet. Once achieved, the remaining theta positions can be used to reach specific reflections of interest; structural and magnetic. Both theta and omega rocking scans were performed about each selected reflection, during a field dependent measurement. Typical field increments of 0.02 T were used to carefully map the magnetic hysteresis at 200 K on both FC and ZFC. In principle, the experiment was very similar to those performed at DMC, the major differences being that this is more equipped for single crystals and the neutron flux is much lower than that provided at PSI. This means that the scanning times of each measurement take far longer, such that enough neutrons at each theta or omega angle are obtained.

3.8 Processing of diffraction data

3.8.1 Data reduction and absorption correction in CrysAlisPro

There are a few important steps required that fill the void between data acquisition and structure refinement. For long measurements, the data sets are large, the first point of call is to check the data using the peak finding option in the CrysalisPro software, there is also a smart peak hunting option, more sensitive to weaker reflections but as a result slightly slower. From the peaks found, a matching cell can be deduced in another module of the software. If the cell selected by the software is not fitting, perhaps a lower symmetry cell has to be tested, the possibility to search for a different cell manually is available. It is possible to also find twin components in the data using the "Ewald explorer" [163], such as actual twins due to lost symmetry elements going from a higher symmetry cell to a lower symmetry subgroup, or twins which occur from different grains of a mosaic crystal. The remaining steps after peak and cell finding confirmation are the peak integration and re-finalization of the data. but more importantly the choice to search for a different cell manually or automated via the software. The peak integration is performed at the reciprocal lattice position corresponding to the correctly found cell and processed in an output hkl file, the

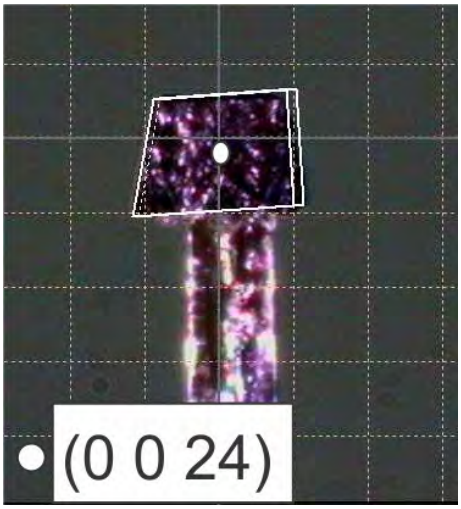

Figure 3.10: Face indexing image of $YbFe_2O_4$ single crystal. The faces can be manually added if one knows the orientation of the crystal. Alternatively there are two methods to highlight each face with either drag or point marking. If the sample holder is not straight, on rotation of the crystal during the experiment it will move about an axis, this can also be corrected for in the software.

completion time is dependent on the amount of runs/frames measured during the experiment but in most cases takes ∼30 minutes for a large data set. Before starting the peak integration, the software provides a number of options which allows one to improve the data set e.g, by correcting a potential sample wobble. After the peak integration is complete, the next step is re-finalization, and allows the user to incorporate appropriate absorption corrections and to determine a space group search (if desired) for the ideal space group for the final output file. The absorption correction option provided in the CrysalisPro software gives several analytical corrections for the data, a combination of empirical and numerical correction give the best outcome.

In absorption correction, two corrections are to be made, the absorption of the incoming beam and the diffracted beam. The amount of correction is dependent on: the shape, size of the crystal and its orientation. If a correction is not performed the intensity of reflections will not be accurate. Exact methods such as empirical corrections works on the principle analysis of spherical or cylindrical shaped crystals uses using a number of spherical harmonics in a least squares procedure. Where possible, for complete accuracy the sample can be shaped into a sphere or cylinder for an exact correction to be applied. Numerical correction on the other hand requires a description of the crystals in terms of its faces and their size, preferably well defined faces with clear outline of each will benefit the correction. The best result is obtained when a combination of both types of absorption correction are used. An image of the face indexing of $YbFe_2O_4$ is shown in Fig. 3.10, the face indexing can also be completed in Jana2006 if the user so chooses. Once the refinalization step is complete, a window with the final R_σ (signal to noise ratio) values for each resolution shell are given. The resolution shells are the reflections obtained from low to high angle in θ. The two important terms which one must consider before refining data is the R_σ and R_{int} values, which are obtained during the data reduction (peak integration, absorption correction) before a final output file is created. Software dependent, the user should have a clear idea as to the quality of the data before loading it into a refinement program, and is represented by these two experimental R-values. The R_σ value is the estimated standard deviation and R_{int}, the internal residual. Each are defined in the following;

$$R_\sigma = \frac{\sum_i \sigma(F_i)}{\sum F_i} \tag{3.29}$$

The standard deviation R_σ in Eqn. 3.29 uses the sum of all independent reflections i and in terms of internal R-factor, the additional term j us a sum of all equivalent reflections.

$$R_{int} = \sum_i \sum_j \frac{I_j - \langle I_i \rangle}{\langle I_i \rangle} \qquad \text{or} \qquad R_{int} = \sum_i \sum_j \frac{F_j^2 - \langle F_i^2 \rangle}{\langle F_i^2 \rangle} \tag{3.30}$$

If these values are reasonable after the refinalization step the data can be used directly in a refinement program, if not the refinalization step can be repeated, perhaps making changes to the space group or absorption correction.

3.8.2 Structure solution and refinement

For refinement of any single crystal data, the first step before structural solution is merging of the reflections, including space group determination and merging statistics. From here structure solution is implemented, via superflip [166] and the electron density map or with a direct method using SIR2014 [167]. The latter was used in each structural solution represented in this thesis. This is a complex program, using many algorithms to provide the best statistics for a structural solution, an example of one of the algorithms is the SPACE algorithm. This defines the Laue groups compatible with the space group symmetry and geometry of the unit cell and assigns a specific probability value to each of them, by analyzing the symmetry equivalent diffraction intensities. Following this and several more complicated algoritims a final structure solution is provided, giving a number of atoms which represent the unit cell of choice. There are some occasions, for complex structures, that the number of atoms given by SIR2014, are not correct, where the molecular density of the compound is short often by the lighter atoms in the compound. This can sometimes be remedied either by a recalculation of the structure solution via SIR2014 (running the program again) or by manually selecting the atoms that are obtained from the superflip program. This works on the basis that there can be nowhere a negative electron density, a reverse Fourier transform is used to calculate the random phases which obey Friedel's law. For each negative density, the charge is flipped [168] and the charge densities calculated this way relate to a specific atom. The larger electron densities will relate to the heavier atoms, and thus smaller values for lighter atoms. From here the structure solution can also be obtained, or aid that which has already been evaluated using SIR2014. The software JANA2006 was used for the final structural refinement. Refinement itself is improving the agreement between observed and calculated data, by the adjustment of parameters such as atomic positions, aiming for, in the process to minimize M given in Eqn. 3.31. In many refinement programs there is the option to refine in terms of either the structure factor, F or the structure factor squared F^2 [169]. Each one is equally applicable, however there are some small advantages to refining in terms of the F^2. The refinement based on F is given as;

$$M = \sum w\big(|F_o| - |F_c|\big)^2 \qquad \text{where} \qquad w = \frac{1}{\sigma^2\big(|F_o|\big) + \big(uF_0\big)^2} \tag{3.31}$$

Here F_o and F_c are the observed and calculated structure factors, respectively. The weighting factor denoted as w, is defined on the right of Eqn. 3.31, where σ is the estimated standard deviation. The instability factor u, is typically set to 0.01, as was the case with all the refinements presented in this thesis. The value set should remain for all data obtained under the same conditions. Similarly, the same variables apply for the structure factor in terms of F^2:

$$M = \sum w\big(F_o^2 - F_c^2\big)^2 \qquad \text{where} \qquad w' = \frac{w}{4F_o^2} = \frac{1}{4F_o^2 \cdot \sigma^2\big(\big(|F_o|\big) + \big(uF_o\big)^2\big)} \tag{3.32}$$

The only difference here is the weighting factor w' for the structure factor of F^2 is derived from the weighting factor w of the refinement based on F. The question

still remains, which one is better and why? In the past, crystallographers performed refinements against F, however in order to minimize this function (Eqn. 3.31). This involves the extraction of a root (one must recall that $I \approxeq |F|^2$,) which ultimately leads to mathematical problems with very weak reflections or reflections with negative intensities. To combat this issue with refinements against F, the negative measurements must be set to zero, or to an arbitrary small positive value. Such an approach already creates bias, as weak reflections, despite the lack of intensity do provide important information with regards to the final crystal structure determination. Another con of using a refinement against F stems in the difficulty of estimating $\sigma(F)$ values from $\sigma(F^2)$, the latter of which is determined during data reduction [169]. This follows through, since the least-squares method is sensitive to the weights applied to each reflection in the summation given above in Eqn. 3.31, problems will therein lie in the σ estimation leading to inaccuracies in the refinement. Refinements, however, against F^2 avoids all of these ambiguities, moreover aiding the overall refinement with advantages such as the refinement of twinned structures are mathematically simpler and refinement of these structure factors are less likely to settle in local minima [170, 171]. For this thesis all refinements were performed against F^2. The next point of call, after the establishment of the type of basis for the refinement, is to judge the quality of the structural refinement, this is done by the various types of R-values.

There are three final residual R-factors that are essential during structural refinement, each of these can be based against refinements of either F or F^2. The first two are termed $R1$ and $R2$, respectively, and each of which having a related weighted R factor wR and $wR2$. The $R1$ and wR factors are defined as

$$R1 = \frac{\sum_j ||F_o| - |F_c||}{\sum_j |F_o|} \qquad \text{and} \qquad wR = \sqrt{\frac{\sum_j w(|F_o| - |F_c|)^2}{\sum_j w(F_o)^2}} \tag{3.33}$$

The $R2$ and respective $wR2$ factor is given by

$$R2 = \frac{\sum_j F_o^2 - F_c^2}{\sum_j F_o^2} \qquad \text{and} \qquad wR2 = \sqrt{\frac{\sum_j w(F_o^2 - F_c^2)^2}{\sum_j w(F_o^2)^2}} \tag{3.34}$$

Unlike the refinement against F, the values obtained for $R2$ and $wR2$ are often 3 times larger, but based on the least squared method it gives a direct weighted and normed deviation as a result, which is far more accurate than that of $R1$. Lastly, the final quality indicator is the goodness of fit, written as $GooF$ or GoF and for refinements against both F and F^2 is written as

$$GoF = \sqrt{\frac{\sum_j w(|F_o| - |F_c|)^2}{N_R - N_P}} \qquad \text{and} \qquad GoF_2 = \sqrt{\frac{\sum_j w(F_o^2 - F_c^2)^2}{N_R - N_P}} \tag{3.35}$$

In these equations N_R is the number of unique (i.e merged) reflections and N_P the number of refined parameters. Theoretically, for an adjusted weighting scheme this value should be as close as possible to 1, however when manipulating or rescaling the weights, w, artificial improvement of this value may result. If the weights are altered early on in a refinement as the number of parameters influence strongly the

overall *Go*F. This should really be done if necessary near the end of the refinement. Values of $GoF < 1$ indicates over fitting; using too many fit parameters given the amount of reflections, or bad absorption correction. The latter is really one aspect of structure refinement, which can most largely effect the final result. The wrong choice of space group may also lead to an underestimated goodness of fit.

The end goal of the refinement is to minimize all of these values, where ideally the final R-value should be within the realms of 1 or 2 %. However, depending on the complexity of the structure and the number of parameters and variables which can effect data sets, values below R=5 % are often considered seriously when clear scientific argument is made. A final point of call is the Hamilton test [172] also known as the R-factor ratio test which checks whether or not the increase of parameters lead to a significant improvement of the model.

3.8.3 Bond Valence Sum (BVS) analysis

The different valences of atoms in chemical structures can usually not be determined directly by in-house x-ray diffraction. In the more complex cases like $YbFe_2O_4$, which has a mixed valence state of Fe^{2+} and Fe^{3+}, the atomic form factors are far too closely related to be easily distinguished. The Bond Valence Sum (BVS) is determined using a number of basic assumptions when calculating the bond length between neighboring atoms. There are two primary assumptions that are used to describe the BVS. Firstly, the bond between two atoms is formed by the pairing of electron density in the region where the valence shell of two or more atoms overlap, and secondly each atom contributes the same number of valence electrons to the bond [61]. In an ionic picture for example taking a transition metal ion, Fe, which is surrounded by O^{2-} ions with an equilibrium bond length. If an extra electron is added to the Fe ion (reducing the valency from Fe^{3+} to Fe^{2+}) the constant repulsion between this electron and the O^{2-} will push the O^{2-} away, resulting in a longer bond length; away from its equilibrium. The valence of an atom is described by the BVS in the following equation:

$$V_{ij} = \sum \exp \frac{R_0 - R_{ij}}{b} \tag{3.36}$$

Here V_{ij} is the bond valence of the neighbouring atoms i and j, and the bond length between the two atoms is given by R_{ij}. The final two parameters in the equation are b=0.37, the universal constant and R_0 the bond valence parameter, the latter of which only depends on the chemical identity of the atom and determined empirically [173, 174]. This tabulated bond length is determined from pre-existing experimental structures [61, 175] and since R_{ij} depends largely on the valence state of the particular ion and its environment, it is as a result not an exact parameter. BVS analysis can encounter a charge disproportionation issue, stemming from the inconsistencies in the BVS tabulated parameter. This requires further investigation to reduce ambiguity with, for example complex charge ordered structures [107, 176]. The experimental determinations of the characteristic bond lengths R_0 from literature are shown in Table. 3.2 for; Fe^{2+}, Fe^{3+} and Yb^{3+}, and all determined empirically.

Literature	R_0 (Fe^{2+})	R_0 (Fe^{3+})	Literature	R_0 (Yb^{3+})
[174]	1.734	1.759	[174]	1.985
[177]	1.7	1.765	[178]	1.969
[179]	1.713	1.751		
Mean	1.7156	1.7583	Mean	1.977

Table 3.2: The characteristic bond lengths R_0 from published literature of; Fe^{2+}, Fe^{3+} and Yb^{3+}.

4 | Oxygen stoichiometry and optimization in $YbFe_2O_4$

The first section will provide a brief overview of the steps taken to produce single crystals of $YbFe_2O_4$, from initial powder synthesis via solid state reaction to crystal growth via traveling floating zone method (for further detail on the specifics of this technique please refer to both Sec. 3.1 and 3.2 as well as [180] [181] (pp.244-246). The remaining parts of the chapter will be focused on comparisons between samples of different stoichiometry and their relative macroscopic characteristics. From the different mixed gas ratios used, synthesis was optimized using $CO:CO_2$=1:2.5. Many crystals from this batch exhibited sharp magnetic transitions in magnetization measurements; indicative of a more stoichiometric crystal.

4.1 Synthesis and crystal growth

For powder synthesis, commercial powders of Yb_2O_3 and Fe_2O_3 were used. All powder mixtures were heated in a $CO:CO_2$=1:3 gas flow, based on previous successful synthesis and single crystal growth of isostructural $LuFe_2O_4$, using gas ratios between $CO:CO_2$=1:5 and 1:2.5 [27, 74, 104]. For single crystal growth of $YbFe_2O_4$ four different gas ratios were used: $CO:CO_2$=1:5, 1:3.5, 1:3 and 1:2.5, where the typical pressure used during each crystal growth was set at a specific value in the range of 1.25-1.75 bar [43] (see Sec. 3.1 and Sec. 3.2 for experimental details). The $CO:CO_2$=1:5 atmosphere was first selected and used for crystal growth, based on a previous successful growth of a stoichiometric $LuFe_2O_4$ single crystal in this atmosphere [27]. The resultant crystal boule was about 5 cm in length and 5-6 mm in diameter, shown in Fig. 4.1 (top). The rod was a dull

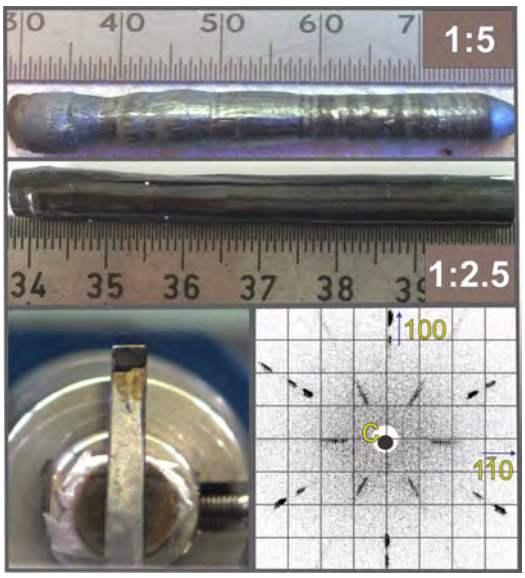

Figure 4.1: **Top**: crystals grown via optical floating zone in different oxygen partial pressures; $CO:CO_2$=1:5 and $CO:CO_2$=1:2.5. **Bottom**: image of $YbFe_2O_4$ single crystal mounted on real time Laue camera (left), Laue image along c-direction (right).

silver colour with multiple small lines running up its length. A small section of the rod was cut and the colour inside was light brown and powdery in texture. Powder x-ray diffraction (see Sec. 3.7.1) indicated multiple phases including; Yb_2O_3, Fe_2O_3, $YbFe_2O_4$, $Yb_2Fe_3O_7$ and $Yb_3Fe_5O_{12}$. These phases are seen clearly in the phase diagram of Fe-Fe_2O_3-Yb_2O_3 [78], indicating a too high oxygen partial pressure. Further growths in lower oxygen partial pressure atmospheres yielded single phase $YbFe_2O_4$, e.g. the crystal grown in CO:CO_2=1:2.5, given in Fig. 4.1 (top panel). The growths with lower oxygen partial pressure were much more stable than that of the CO:CO_2=1:5, requiring only minor adjustments in input power for stability. Single crystals of $YbFe_2O_4$ show a strong tendency to cleave along facets perpendicular to the **c** direction, which is similar to the behavior in $LuFe_2O_4$ [26,32]. Fig. 4.1 (bottom left) shows an image of the more stoichiometric GS sample (with magnetization comparable to the S1 sample, see in Fig. 4.3) mounted on a real time Laue set-up with dimensions 3x2x1 mm.

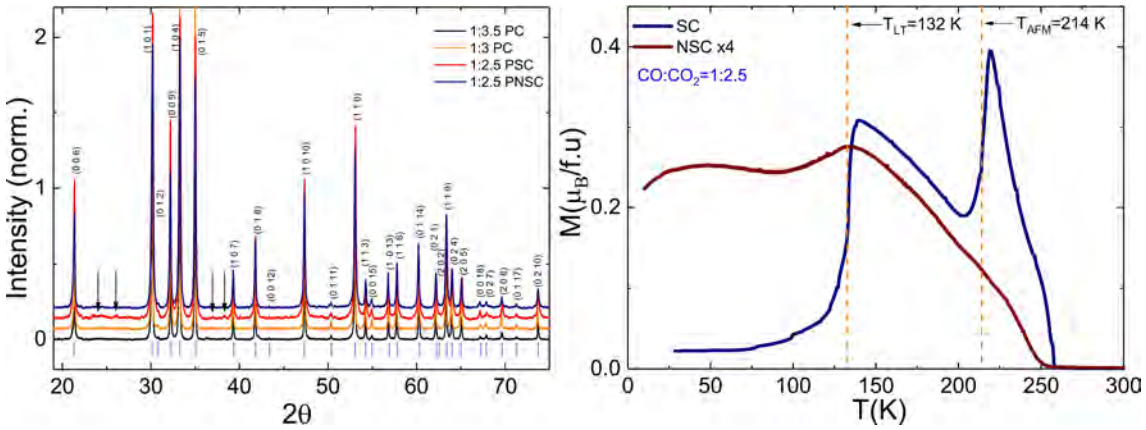

Figure 4.2: Left: powder diffraction of $YbFe_2O_4$ on: 1:3.5 Powdered Crystal (PC), 1:3 (PC), 1:2.5 Powdered Stoichiometric single Crystal (PSC) and 1:2.5 Powdered Non-Stoichiometric single Crystals (PNSC) with background subtracted. Arrows indicate peaks from mylar foil used for the powder diffraction measurement, which occurs strongly in the (PSC) due to the smaller mass of powder obtained from the 20.8 mg, more stoichiometric single crystal. The reflection positions of the $R\bar{3}m$ structure were taken from [75]. Right: FC magnetization measured on a Stoichiometric single Crystal (SC) (blue curve), and Non-Stoichiometric single Crystal (Brown curve) scaled by x4, both grown in CO:CO_2=1:2.5, and later ground for powder diffraction and named PSC and PNSC, respectively.

Here the flat shiny facet is perpendicular to the **c** direction where the respective Laue image is shown in Fig. 4.1 (bottom right). Powder diffraction was performed using a Huber Guinier D670 diffractometer on four different samples: powdered crystal (PC) from a 1:3.5 growth, PC from a 1:3 growth and lastly two powdered single crystals from the 1:2.5 growth a Powdered Stoichiometric single Crystal (PSC) and a Powdered Non-Stoichiometric single Crystal (PNSC) (see Fig. 4.2, left). The relative FC magnetization curves of the PSC and PNSC samples before being powdered are provided in Fig. 4.2 (right). All samples grown in oxygen partial pressures between CO:CO_2=1:3.5 and 1:2.5 yielded single phase $YbFe_2O_4$ [75], indicating that under these conditions $YbFe_2O_4$ is stable. A Le Bail fit of both the PSC and PNSC grown in CO:CO_2=1:2.5 gave lattice parameters; a=3.4578(3), c=25.1285(9) and a=3.4604(3), c=25.1320(5), with final refinement values of Rp=1.51% and 1.58%, respectively. There is only a small variation in lattice parameters between PSC and PNSC, which we can consider to not be statistically significant [43], despite of

the very different magnetization curves (Fig. 4.2, right), suggesting different oxygen stoichiometry.

4.2 Variations of intrinsic properties based on off-stoichiometry

This section will highlight the variations seen in both the magnetic and charge ordering properties in samples with off-stoichiometry, indicated by shifts or broadening of transitions and low dimensional ordering strongly related to the broadness of each respective transition. These effects are all accountable to either too much or too little oxygen during crystal growth, where as shown in Fig. 4.2 (right), sample to sample dependence can occur strongly even in one crystal growth. Such crystal to crystal variation within one batch were noted for $LuFe_2O_4$ [26,32]. The largest challenge in this work was to optimize the gas ratio used, as the intrinsic behavior can only be elucidated on highly stoichiometric samples with long-range spin and charge order, as clearly observed in $LuFe_2O_4$ [32,33,48]. This chapter covers the data and overall comparison of samples of different oxygen content, before heading into the final results obtained on the most stoichiometric crystals in the following chapters.

4.2.1 Off-stoichiometry and its effects on magnetic properties

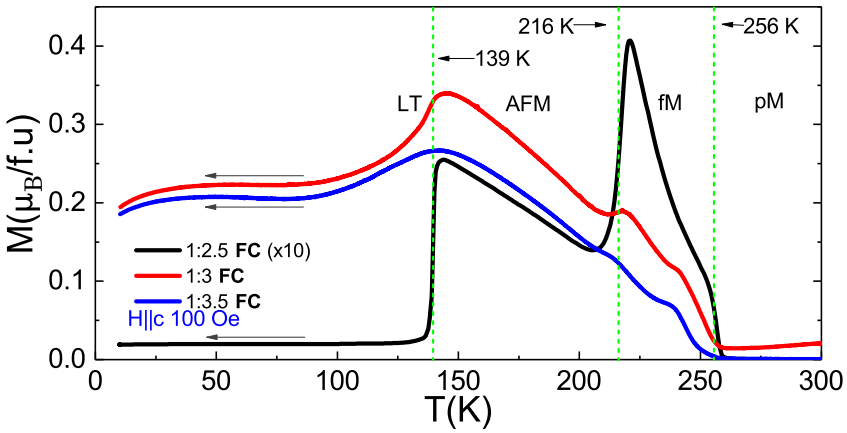

Figure 4.3: Field cooled magnetization measured on three different single crystals grown in three $CO:CO_2$ gas ratios: $CO:CO_2$=1:2.5 Sample 1 (S1) (black curve), $CO:CO_2$=1:3 (S2) (red curve) and $CO:CO_2$-1:3.5 (S3) (blue curve). Figure from own work [43].

The investigations on $YbFe_2O_4$ for the focus of this thesis have uncovered a wide range of magnetic and charge order transitions, largely similar to those observed in $LuFe_2O_4$ [26,27,32,33,82,87,182]. During the crystal growth of $YbFe_2O_4$, four different gas ratios were used: $CO:CO_2$=1:5, 1:3.5, 1:3 and 1:2.5 (see Sec. 4.1 for details). Due to the strong Ising nature of this system, the Fe spins prefer to align parallel to the **c** direction, therefore, in all DC and AC measurements, the fields were applied along this easy axis. Our magnetization studies on field cooling (FC) from 300-10 K on three $YbFe_2O_4$ single crystals grown in $CO:CO_2$=1:2.5 Sample 1 (S1) (black curve), 1:3 (S2) (red curve) and 1:3.5 (S3) (blue curve) are provided in Fig. 4.3, with masses m=32 mg, 4.5 mg and 3.5 mg, respectively. The crystals S2

and S3 grown in the more oxidizing conditions, the $CO:CO_2$= 1:3 and 1:3.5, only exhibit smeared features and shifts in transition temperatures. It is immediately clear that on reducing the oxygen content, going from $CO:CO_2$=1:3.5 to 1:3, the transitions become slightly sharper. These two $M(T)$ curves are almost identical to those published by Yoshii *et al.* [119] on single crystal $YbFe_2O_4$, which provided the most stoichiometric curves to date. Unfortunately, there was no mention of which gas ratio was used during the single crystal growth, and therefore no comparison can be made with our data, in terms of growth conditions. The vast majority of published magnetization data provide curves with broad transitions such as that shown in Fig. 4.5, and also grown in the $CO:CO_2$:=1:3.5 (a clear observation of sample to sample dependence) and very similar to previously published magnetization curves on both single crystal $YbFe_2O_4$ and $LuFe_2O_4$ [13,123,127,129,183] and polycrystalline samples [81, 84, 118, 124, 127]. The presence of these broad transitions in off-stoichiometric RFe_2O_4 (R=Yb, Y, Lu... etc) samples often indicate glassy features, inherent of low dimensional (i.e, limited to the a-b plane) magnetic ordering, [80,84,87,91]. A sweet point was reached in terms of the $CO:CO_2$=1:2.5 gas ratio used during growth, the S1 sample, as shown in Fig. 4.3 (black curve), exhibits sharp clearly defined transitions at T_c= 256 K, T_{AFM}=216 K and lastly T_{LT}=139 K [43]. These magnetic phase transitions are discussed in detail in Chapter. 5.

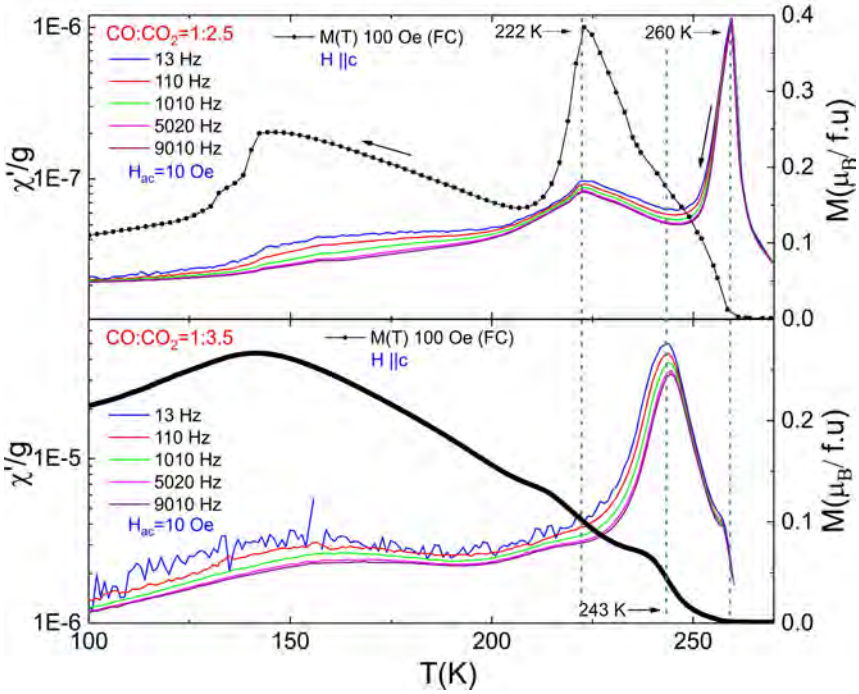

Figure 4.4: Real part of the AC susceptibility with 5 different driving frequencies ranging from 13-9010 Hz. Top: highly stoichiometric GS sample. Bottom: off-stoichiometric S3 sample. The black curve in each panel represents the relative FC magnetization for each sample measured in an applied field of 100 Oe.

Another way to simply probe the magnetic correlations macroscopically is with AC susceptibility (see Sec. 3.4 for experimental details), primarily used to identify spin glass transitions based upon frequency dependence, due to delayed magnetic response. The real part of the AC susceptibility measured at 5 different driving frequencies is given in Fig. 4.4, on the highly stoichiometric GS sample ($CO:CO_2$=1:2.5)

(top) and the off-stoichiometric S3 sample (bottom) ($CO:CO_2$=1:3.5). The fundamental difference between the two data sets is the clear frequency dependence seen in the off-stoichiometric S3 sample at 243 K, which on decreasing driving frequency results in a peak shift to lower temperatures, very similar to those published by Sun *et al.* [123] on a single crystal of similar quality. This is not seen in the GS sample at T_c= 260 K, the transition in AC susceptibility is taken at the top of the peak, contrary to the magnetization which is slightly lower at 256 K (also shown in Fig. 4.4, black curve (top)), as it is taken at the mid point of the slope. The T_c transition is pinpointed far more accurately in the AC susceptibility than in $M(T)$, where it is seen as a broad hump, making it far more difficult to isolate the exact transition temperature. The frequency dependence is a clear example of reduced magnetic order at T_c in the off-stoichiometric sample (See Fig. 4.4 black curve (bottom)), where not all magnetic moments are ordered, quite opposite to the GS sample, where the lack of frequency dependence at this temperature indicates a well ordered state. Interestingly, on further cooling to T_{AFM} (ferrimagnetic phase to the antiferromagnetic phase) [32, 43] (see Chapter. 5), the responses to different driving frequencies of the GS sample begin to split, suggesting that the latter magnetic phase is less well ordered with smaller domains. This frequency dependence continues beyond the lower temperature T_{LT}, but becomes uniform once again below ∼100 K. This frequency dependence is not surprising as it is going from one type of magnetically ordered to state to another, but the line spread of the different driving frequencies becomes more narrow when fully in the AFM phase at 222 K. The increase in frequency dependence beyond this point for both samples is attributed to the low temperature T_{LT} transition, also observed in $LuFe_2O_4$ and classed as a glassy re-entrant phase [33]. This low temperature transition can be stabilized in either an AFM or fM phase, depending on which starting conditions are used for the magnetization measurement. A comparison to the only published AC susceptibility data from Sun *et al* [123], shows large similarities with the 1:3.5 data, whereby taking the transition point to be the midpoint of the drop of the large peak, in our data the transition occurs around 237 K, analogous to that seen in [123]. Frequency dependence in the GS sample occurs only after the drop into T_{AFM}, in slight contrast to that observed in the 1:3.5 sample, where frequency dependence starts at around T=256 K. Although it is clear that the GS sample provides clearly sharper transitions, frequency dependence is still a large feature on cooling beyond the AFM transition, this was not the case in highly stoichiometric $LuFe_2O_4$ [26], which in there highest quality sample, saw no frequency dependence on cooling. A number of intrinsic physical properties can constitute such features in an AC susceptibility measurement. Off-stoichiometry of a sample, which typically exhibit only low dimensional magnetic ordering, will show a frequency dependence due to weakened magnetic correlations concomitant with glassiness or parasitic ferrimagnetism (PS) [26, 90, 184].

4.2.2 Neutron scattering in zero field

The first neutron scattering experiments used to exploit the magnetic ordering in $YbFe_2O_4$ was done so at the beamline DNS (Diffuse Neutron Scattering) (see Sec. 3.7.5) at the MLZ (Heinz Maier-Leibnitz Zentrum), Garching. Our first single crystal large enough for neutron measurements was a 60 mg sample obtained from the crystal growth in the $CO:CO_2$=1:3.5 atmosphere. Although the FC magneti-

zation shown in Fig. 4.5 (top left) exhibits only smeared transitions, with a poorly defined T_{AFM} and T_{LT} transition, no neutron investigations were published at all on $YbFe_2O_4$. Therefore an initial glimpse would provide invaluable information as to the type of magnetic ordering (long or short range correlations) on such a quality crystal and the onset of the main ordering temperature. The DNS instrument was operated in the neutron spin-flip configuration, where the neutron scattering process is sensitive to the pure magnetic scattering [150, 185]. The z-polarization spin-flip scattering was measured at 200 and 3.5 K and given in Fig. 4.5 (left). For all measurements performed at DNS the crystal was pre-mounted on an aluminum holder using Laue diffraction and oriented such that both $\overrightarrow{c}$ and 110 directions are in the horizontal scattering plane. All measurements were corrected by a vanadium standard measurement (see Chapter. 3, Sec. 3.7.5 for more details).

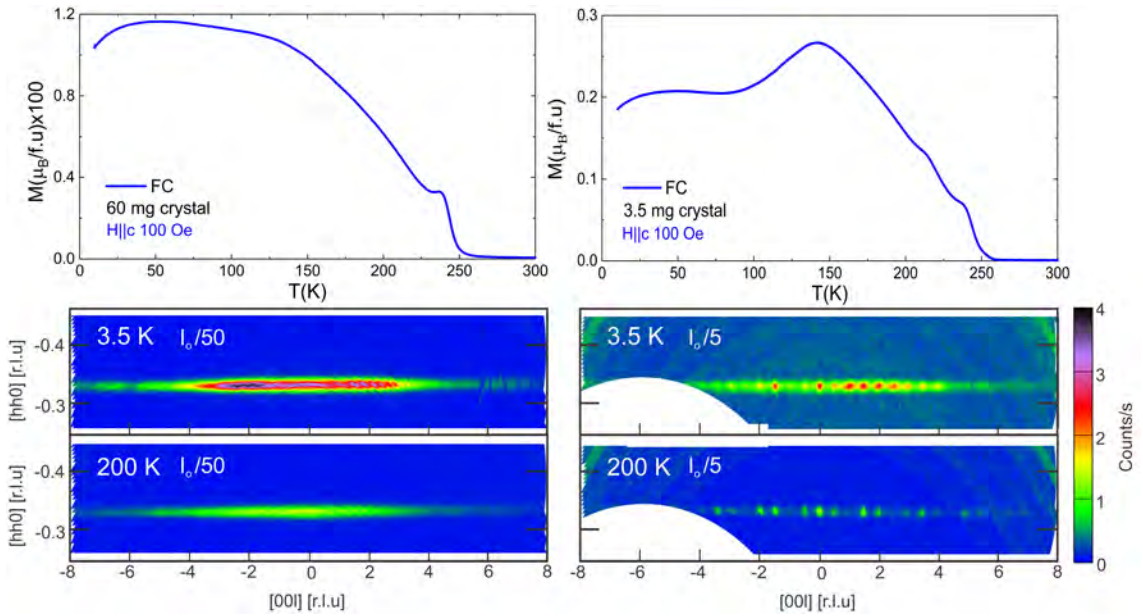

Figure 4.5: Field cooled magnetization and reciprocal space maps of the spin-flip (SF) scattering measured in the $hh\ell$ plane, at 3 different temperatures on two $YbFe_2O_4$ single crystals grown in the $CO{:}CO_2$=1:3.5 atmosphere. Left panel: 60 mg sample. Right panel: the S3 sample.

The two reciprocal space maps measured on the 60 mg sample, were done so on cooling to 200 K and 3.5 K, each exhibiting diffuse intensity along $(\frac{1}{3}, \frac{1}{3}, \ell)$, see Fig. 4.5 (left). On cooling to 200 K the intensity become much stronger at ~ 200 ct/s. The further increase in intensity of ~ 400 ct/s at 3.5 K, below T_{LT} is a direct effect of the competing AFM and fM orders. This particular diffuse magnetic behavior seen along $(\frac{1}{3}, \frac{1}{3}, \ell)$ strongly indicates an inability of the magnetic spins to align along the c axis, where magnetic correlations in this case are primarily limited to the a-b plane and stems from off-stoichiometry, i.e an excess or too little oxygen.

A later neutron experiment performed on the S3 sample (3.5 mg) is also shown in Fig. 4.5 (right panel), with corresponding FC magnetization. When first considering the FC $M(T)$ measured on each sample, one would ascertain that neither sample are of good stoichiometric quality, with the S3 sample exhibiting a few more smeared transitions than that of the 60 mg sample. However, despite of this, DNS measurements performed at the same temperatures as before but on warming from

3.5 K show the clear development of 3D magnetic peaks along $(\frac{1}{3}, \frac{1}{3}, \ell)$ at 200 K. There is a slight diffuse aspect seen at 200 K, in the neutron data, which increases on cooling down to 3.5 K along with the peak intensity. The 2D diffuse background comes from a combination of three factors; (1) 3.5 K is well below T_{LT}, which in $LuFe_2O_4$ is classed as a re-entrant glass phase. Strong diffuse scattering below this transition was also observed in $LuFe_2O_4$ [26]. Increased diffused scattering below T_{LT} stems from competing domains ordered both anti and ferrimagnetically. (2) the broadness of the transition seen in the magnetization data implies that not all spins are strongly correlated along the **c** direction. (3) As seen in neutron diffraction of $LuFe_2O_4$ [26, 32], 2D line scans along $(\frac{1}{3}, \frac{1}{3}, \ell)$ in both 0 T and 2.5 T show that there is a small diffuse component at 220 K even with an applied field. This effect is also clearly seen in the highly stoichiometric $YbFe_2O_4$ GS sample, where similar neutron diffraction measurements (see chapter 7 Sec. 7.2 for detailed analysis) show that even with the application of higher fields (>1.8 T), a diffuse background still remains, indicating that the system is not fully ordered in the AFM phase. This effect was also seen in $LuFe_2O_4$ [32]. The magnetization in 100 Oe of the 60 mg sample is a factor 100 less than that of the 3.5 mg sample, which is not only surprising based on the relative sizes of the crystals, but could be a primary reason as to why there is only 2D magnetic order present in the 60 mg sample, the overall lower magnetic moment is a result of very short range correlations in the sample.

4.2.3 Off-stoichiometry and its effects on charge order

The currently limited number of publications on $YbFe_2O_4$ (see Chapter. 2, Sec. 2.3), show mostly samples that exhibit off-stoichiometry when compared to the closely related $LuFe_2O_4$, in terms of the CO only 2D diffuse correlations have been observed [120, 121], except for two publications by Matsumoto *et al.* [130] and the other by Matsuo *et al.* [186], both using electron diffraction. They observe clear commensurate peak intensity in the $hh\ell$ plane, along $(\frac{n}{3}, \frac{n}{3}, \ell)$ at τ=$(\frac{1}{3}, \frac{1}{3}, \frac{3}{2})$ positions. The two TEM images (Tunneling Electron Microscope) from [130] and [186] are shown in Fig. 4.6, left and right, respectively. The image from [130] is coupled with diffuse scattering along ℓ, an indication of some short range ordering, which is not present in the imaged published by [186]. The clear intense CO spots indicate a highly stoichiometric crystal, however electron diffraction focuses on very small areas of a single crystal, and as a result long-range ordering may not have been present in the entire sample. Interestingly, there have been no observation of the 3D incommensurate CO in $YbFe_2O_4$, which occurs in highly stoichiometric $LuFe_2O_4$ below T_{CO}=320 K and remains down to low temperature [48]. This may be due to the lack of sufficiently stoichiometric crystals or due to commensurate CO existing in $YbFe_2O_4$. The investigation of the CO in $YbFe_2O_4$ for this work using different gas ratios for crystal growth, highlighted that the occurrence of 3D CO in samples produced in the more oxidizing gas ratios was limited, and provided in most cases 2D diffuse CO at all temperatures (see Chapter. 6).

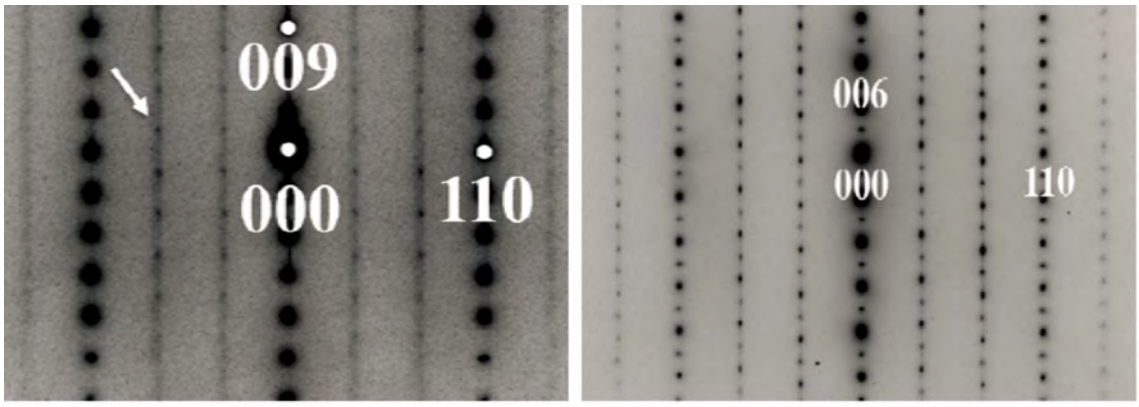

Figure 4.6: Tunneling Electron Microscopy (TEM) images of $YbFe_2O_4$ in the $hh\ell$ plane at room temperature. Left: image taken from [130] and adapted. Right: image taken from [186] and adapted.

This type of low dimensional CO is classed as Type 1 CO in this thesis as shown in Fig. 4.7. The remaining two types of CO also observed in this work are that of Type 2 (Fig. 4.7, middle panel) seen in the S1 sample using high energy x-ray diffraction, and exhibits for the first time identical 3D incommensurate CO at RT as in $LuFe_2O_4$ [48, 106]. Contrary to $LuFe_2O_4$, on cooling below 280 K (see Chapter. 6) the CO merges forming a commensurate phase, with an early onset at 287 K seen in the heat capacity (see Fig. 4.8 (red curve)).

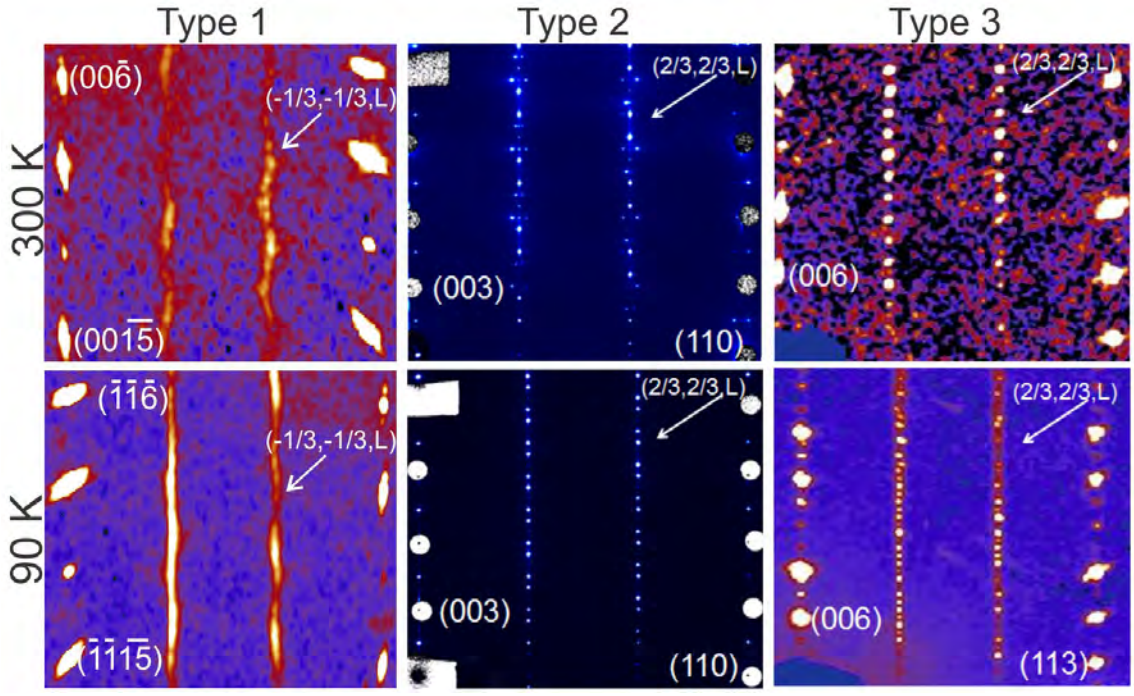

Figure 4.7: The three types of CO observed in $YbFe_2O_4$ at 300 and 90 K. Type 1: shows reciprocal space maps in the $(hh\ell)$ plane from a single crystal grown in the $CO:CO_2$=1:3.5 gas ratio, measured on the in-house SuperNova single crystal diffractometer. Type 2: was obtained from the highly stoichiometric S1 sample at the APS using high energy x-ray scattering and a MAR imaging plate. Lastly, Type 3: also observed on a single crystal from the $CO:CO_2$=1:2.5 growth, and measured using the same technique as Type 1.

In the final example of CO, Type 3, purely commensurate CO is seen at RT and

on cooling. This type of 3D commensurate CO has never been observed in $LuFe_2O_4$. Of these three types of CO observed in $YbFe_2O_4$, the type 3 is the most closely related to those previously published by [130, 186]. The analysis of the CO in this system, detailed in Chapter 6 uses a mono-domain-like sample (see Fig. 6.11) with commensurate CO peaks distributed almost identically to that published by [186].

The heat capacity data on the highly stoichiometric GS sample and the off-stoichiometric S3 sample (relative $M(T)$ shown in Fig. 4.4 and Fig. 4.3, respectively) is given in Fig. 4.8. The onset of T_{CO} ≈305 K in $YbFe_2O_4$ is lower than that of $LuFe_2O_4$ [48] (T_{CO} ≈320 K) and seen in crystals of varying quality. Of course, in the S3 sample, the peak is far less sharp than that of the GS sample, furthermore the GS sample exhibits a secondary peak in the heat capacity at ≈287 K, which stems from the system going from an incommensurate to commensurate CO phase (see Chapter. 6, Sec. 6.1.1) and not evident in the S3 sample. Based on previous investigations during my masters work [57], the S3 sample results in a Type 1 CO, and the GS sample as described previously relates to Type 2 CO. The question is where does the Type 3 CO lie in relation to the other two types? The Type 3 CO on cooling exhibits an increased number of CO domains, likely attributed to these peaks at room temperature being too weak, but on further cooling past the transition onset, increasing in intensity. When comparing these types of CO to the 3D charge order observed in highly stoichiometric $LuFe_2O_4$, type 2 seems to be the closest in comparison, besides the emergence of the commensurate phase. The Type 3 charge order has never been observed before, in any published data on $YbFe_2O_4$ or $LuFe_2O_4$.

Although emphasis in this thesis was placed on the type 2 CO, a further study, screening for crystals exhibiting this type of CO and performing an eventual refinement may be a next step in understanding how the stoichiometry affects the CO in these system. A recent paper [187] providing evidence of Fe vacancy in $YbFe_2O_4$, due to evaporation during crystal growth, may lead to an explanation. As there is sample to sample dependence from one crystal growth, which in $YbFe_2O_4$ is attributed to the atmosphere used during growth, like $LuFe_2O_4$, effects from the Fe evaporation during growth may count as an additional variable for the charge ordering. However, from the refinements discussed in Chapter. 6 there were no indications of less than fully occupied Fe sites, making it an unlikely variable affecting the CO. The CO in $LuFe_2O_4$ is similar to the one of $YbFe_2O_4$ as the R^{3+} radius is in close relation, but compared to the other rare earth elements such as Y^{3+}, much larger in comparison, and as a result provides a different CO pattern [110,111].

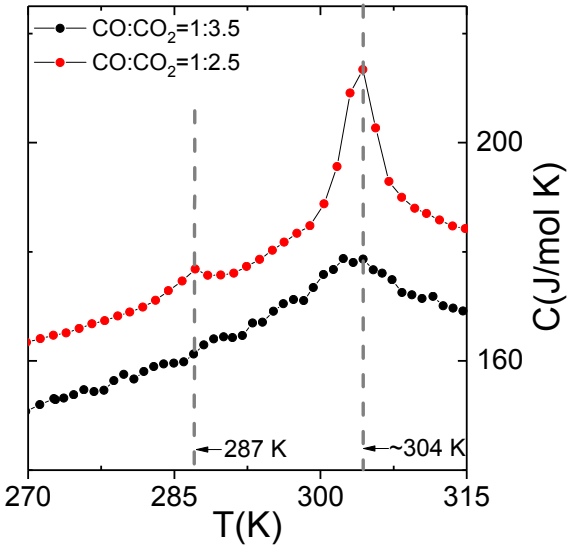

Figure 4.8: Specfic heat capacity measured on warming of; the GS sample grown in the $CO:CO_2$=1:2.5 gas ratio (red dotted curve) and the S3 sample grown in the $CO:CO_2$=1:3.5 gas ratio (black dotted curve).

The neutron experiment performed at DNS, given in Sec.4.2.2 also measured the non-spin-flip (nsf) channel of the two samples at 200 K and 3.5 K, given in Fig. 4.9. The smaller 3.5 mg sample does show peak intensity along $(\frac{1}{3}, \frac{1}{3}, \ell)$ at each temperature. However, when comparing the intensity distribution from the sf (Fig. 4.5) channel and nsf channel they are the same. Indicating that this is in fact bleed through from the sf channel and spin order rather than definitive observation of CO, due to sample size. There is important information to be taken from the nsf data shown in Fig. 4.9 (left) of the more off-stoichiometric 60 mg sample. The much lower intensity, $I_0/10$ from the nsf channel compared to $I_0/50$ for the sf, means that the diffuse scattering seen is due to CO correlations. At ℓ=5.5 there is distinct peak intensity, visible at both temperatures, but more clearly at 3.5 K. Previous neutron diffraction on $LuFe_2O_4$ [104]; measurements done using larger values of momentum transfer, **Q**, indicate that the peaks are not magnetic, and in accordance with [102] are attributed to the onset of 3D charge order. The line scan along ℓ (see Fig. 4.9, bottom) does show an intense peak at ℓ=5.5, the exact position of the peak observed in the nsf scattering in this work. This indicates that even in more off-stoichiometric samples there is still some long-range CO while having no long-range SO, meaning the SO is far more fragile than the CO in the system.

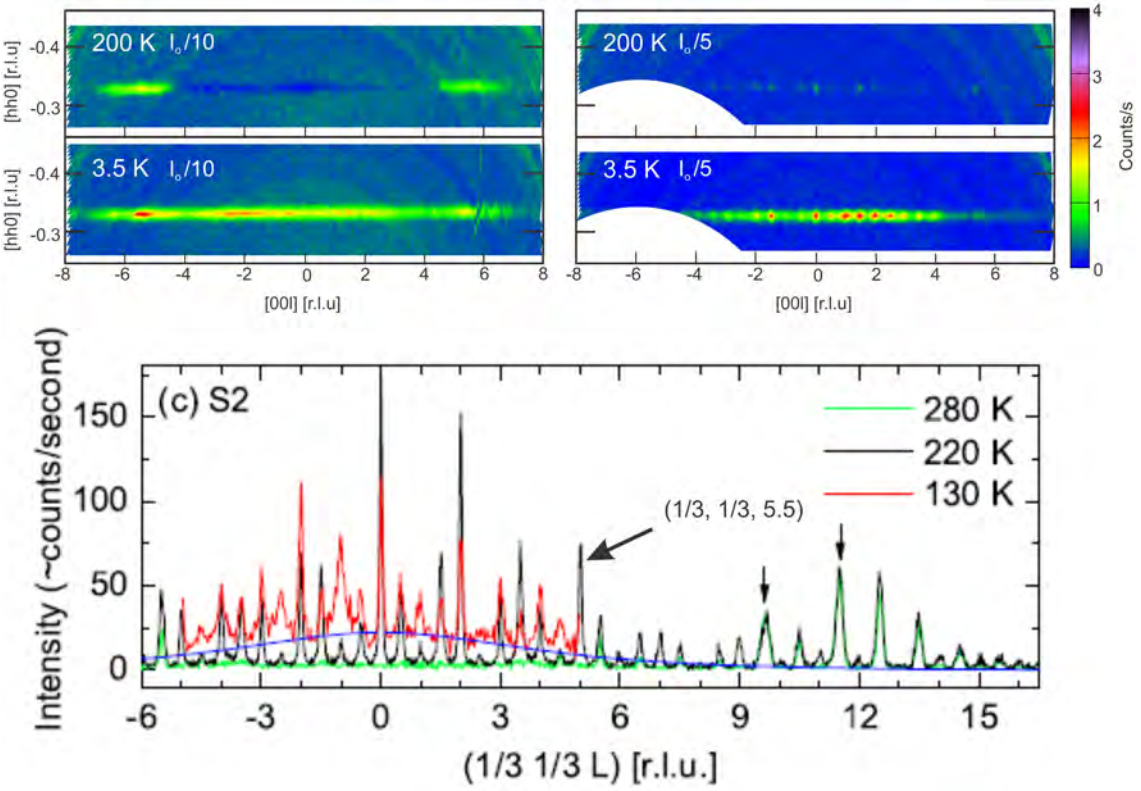

Figure 4.9: Reciprocal space maps of the non-spin flip (nsf) scattering in the $hh\ell$ plane, shown at 200 K and 3.5 K, cut specifically to show the $(\frac{1}{3}, \frac{1}{3}, \ell)$ line intensity. Left: the 60 mg sample. Right: the S3 3.5 mg sample. Bottom: 2D line scans along $(\frac{1}{3}, \frac{1}{3}, \ell)$ at different temperature. The large arrow indicates ℓ=5.5, the smaller black arrows indicate peaks contaminated by aluminum background scattering. The blue line, representing the magnetic diffuse scattering was fit using the scattering form factor, a Debye Waller factor and polarization factor. Taken from [104] and adapted.

The sensitivity of oxygen stoichiometry after heating the S1 sample

The S1 sample, being the highest quality sample we have isolated thus far, was used for a high energy x-ray diffraction measurement performed at the Advanced photon source (APS), to view the charge order in this system. Unlike the $LuFe_2O_4$, which in previous work [26] was heated to 360 K to look at the diffuse scattering above the main charge ordering transition, $YbFe_2O_4$ was far more sensitive to heat-induced changes. As a result of heating to 360 K in vacuum, the stoichiometry of the crystal changed and although 3D ordering was still strongly present, this was newly accompanied by a large diffuse aspect, indicating that (probably the outer most) parts of the crystal became oxygen deficient.

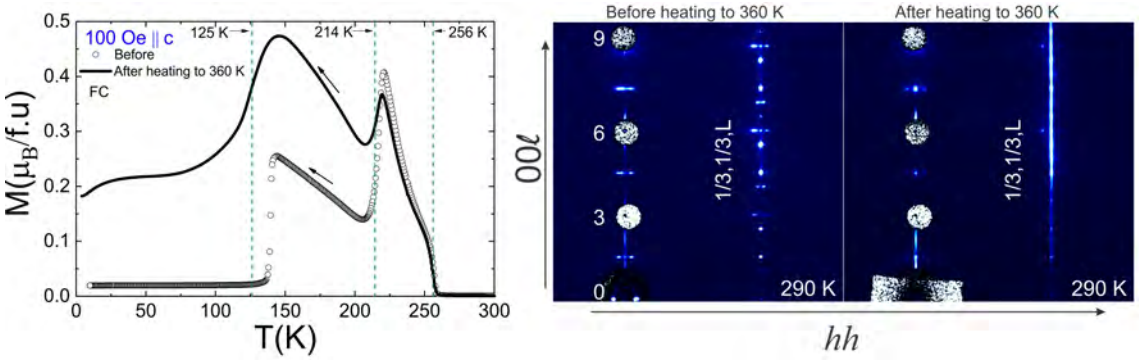

Figure 4.10: The S1 sample before and after heating to 360 K during the APS high energy x-ray experiment. Left: FC magnetization before heating (black circles and after (black line), measured in 100 Oe. Right: comparison of the CO observed at 300 K before and after heat to 360 K.

A remeasure of the ZFC, FC, FW magnetization conducted later after the experiment at the APS led to a clear insight of the changes which occurred in the sample after heating. Here, the main ferrimagnetic ordering temperature, at T_c is almost the same as that seen in the S1 sample before heating, also still appearing at 256 K. However the drop into the AFM phase no longer has the long straight drop before going into the low temperature phase, it is much shorter. The contrast continues, primarily with the difference in the T_{LT} transition which is very broad and similar to that observed in the S3 FC magnetization.

The vast majority of single crystals exhibiting long-range order observed in the form of Type 2 and Type 3 CO were obtained from the more reducing $CO:CO_2$=1:2.5 gas ratio. This atmosphere produced by far the largest content of crystals exhibiting long-range correlations in both the magnetism and CO, and is therefore considered close to optimal. The more oxidizing the oxygen partial pressure, for example the $CO:CO_2$=1:3 and 1:3.5 provided no single crystals with intrinsic properties comparable to that obtained from the $CO:CO_2$=1:2.5. On further increasing the gas ratio to 1:5, a complete phase break down occurs, where the single phase polycrystalline powder synthesized in in the 1:3 gas ratio, with the added oxygen of the 1:5 ratio during crystal growth results in several phases within one boule. Further investigation into lower oxygen partial pressures or further tuning growth using the $CO:CO_2$=1:2.5 may lead to larger single crystals of the same stoichiometry to that as the S1 and GS sample. This would be ideal for neutron inelastic measurements to probe the lattice dynamics of the system. It was interesting to see that the CO correlations in an off-stoichiometric sample (60 mg) were stronger than that of the spin order, where distinct peak intensity is seen in the nsf channel at ℓ=5.5 (Fig. 4.9,

left). Unfortunately due to the size of the 3.5 mg crystal no quantitative information of the CO could be ascertained from the DNS experiment. However, from the wide range of crystals studied using in-house x-ray diffraction, it was confirmed that the three types of CO which can occur due to stoichiometry were all reproducible. Furthermore, the evidence of a a new commensurate phase in $YbFe_2O_4$, has never been observed in any samples of $LuFe_2O_4$. The type 2 sample is the most similar to that observed in $LuFe_2O_4$, with an identical incommensurate CO at room temperature but on further cooling (beyond 287 K see Chapter. 6) a second commensurate CO phase emerges. The remaining chapters in this thesis will focus on the Type 2 charge order. Will this commensuration lead to the same structural solution obtained for $LuFe_2O_4$ [48] (see Chapter. 2)? Or will this new phase lead to an entirely new structural interpretation for $YbFe_2O_4$? (see Chapter. 6).

5 | Macroscopic properties of highly stoichiometric $YbFe_2O_4$

All experiments presented in this chapter were performed on the GS sample[1] obtained from the crystal growth using $CO:CO_2$=1:2.5 atmosphere. As reviewed in Chapter. 4 this gas ratio is the only one which, provided samples that exhibit long-range charge and magnetic order. The first half of this chapter focuses on measurements in either zero or low field, with a cross comparison of macroscopic measurements such as low field magnetization, heat capacity and AC susceptibility to better highlight the multiple transitions seen in $YbFe_2O_4$. In some cases, for example the heat capacity, a more thorough approach is taken with models being included, and directly compared to similar results obtained on a highly stoichiometric $LuFe_2O_4$ single crystals[2]. The second half of the chapter investigates the intrinsic effects of higher fields, using some of the macroscopic techniques used in the low field studies. Before leading to the final mapping of the magnetic phase diagram for $YbFe_2O_4$.

5.1 Low field studies

5.1.1 Magnetic and charge ordered phases

As discussed in Chapter. 2, stoichiometric $LuFe_2O_4$ exhibits four phases between room temperature (RT) and 10 K in low fields; paramagnetic (pM), ferrimagnetic (fM), antiferromagnetic (AFM) and a low temperature phase (LT). The question is do the magnetic phases in $YbFe_2O_4$ relate closely to those seen in $LuFe_2O_4$? Before assigning magnetic phases, a closer look at the transitions observed in various macroscopic measurements is required. A number of features are visible between RT and 10 K in $YbFe_2O_4$ as shown in Fig. 5.1. The top panel of Fig. 5.1 shows the $M(T)$ in 100 Oe (black circles) and heat capacity (open pink circles) of the GS sample. The lower two panels display the relative real and imaginary parts of the AC susceptibility measured with 5 different frequencies. The following bullet points discuss each transition point independently:

- **The 260 K transition**:- The sharpest peak at this temperature is seen in the AC susceptibility. There is no frequency dependence, which means the system

[1] As the intrinsic properties of the highest quality S1 sample were diminished on heating to 360 K (see Sec. 4.2.3), the following macroscopic studies and analysis are focused on the GS sample, the closest in comparison to the S1 sample with regards to stoichiometry.

[2] This crystal was grown at the University of Warwick, Physics department by Dr. R. Mckinnon, under the supervision of Dr G. Balakrishnan. This single crystal was used for several measurements during the course of this PhD thesis

is in a well ordered state. In the magnetization, initially the transition point was taken at the half way point of the broad bump seen at 256 K. However, based on the AC susceptibility, the transition point in the FC $M(T)$ is located at base (just before the up turn). Similarly, in accordance with the AC susceptibility, the onset of a small rise in the heat capacity is also present.

- **The 218 K transition**:- The second most predominant feature, is a fairly sharp drop in the magnetization at 218 K. This is complemented by a second small rise in the heat capacity and a peak in the AC susceptibility. The latter, does show at this temperature a distinct frequency dependence. Indicating that the system is not fully ordered.

- **The 138 K transition**:- This final transition point is seen as a further drop in magnetization. The two step feature is likely attributed to either a small secondary grain, which cleaved off during a later neutron experiment or a mix of differently ordered magnetic domains. At this temperature there is no feature in the heat capacity, most likely due magnetic phase competition (see Sec. 5.2.3). A small drop is visible at the low frequencies (13 and 110 Hz) in the AC susceptibility.

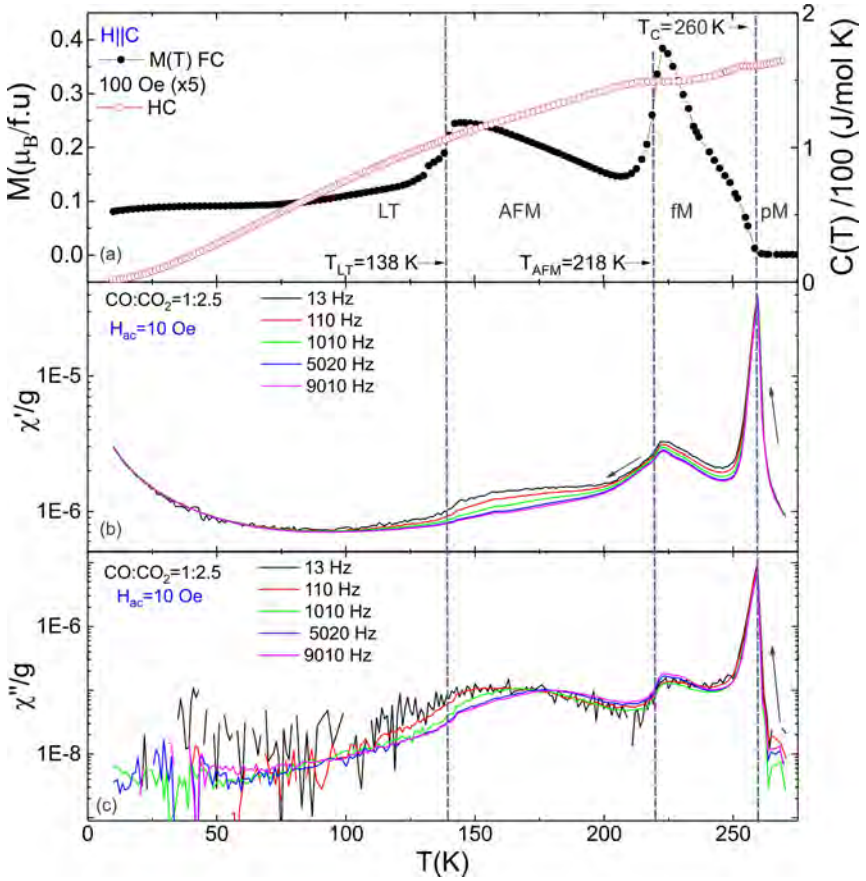

Figure 5.1: Macroscopic measurements on the highly stoichiometric $YbFe_2O_4$ GS sample. (a) Temperature dependent magnetization (black curve) measured on FC in 100 Oe and heat capacity measured on warming from 10 to 270 K (pink curve). (b) Real part of AC susceptibility; measured with five different driving frequencies (coloured lines) in the temperature range 260-10 K on cooling. (c) The imaginary part of the AC susceptibility measured on the GS sample shown in panel (b).

The next question is, what do these transitions mean in terms of magnetic phases; between 260 and 138 K in the system? Firstly, the sudden upturn in magnetization at 260 K with decreasing temperature, indicates the system is going from a paramagnetic (pM) phase to a ferro/ferrimagnetic phase (T_c). In this case the phase is described by ferrimagnetism, as the observed magnetization is much lower than $\sim$10 μ_B/f.u expected for a ferromagnet. Another prime indication of the fM nature of this transition, is a small dip below zero in the thermoremanent magnetization (refer to Sec. 5.2.4). The lack of frequency dependence at this temperature is a good indication of long-range spin ordering. On further cooling, the large drop seen in the magnetization at 218 K suggests an antiferromagnetic (AFM) phase, T_{AFM}, and the frequency dependence seen in χ' of the AC susceptibility, shows that the system is not fully ordered in this phase. Furthermore, the drop seen in the magnetization does not go to low values of μ_B/f.u., but just above 0.1 μ_B/f.u. This means that the system may have small regions still ordered in the fM phase, and the AFM ordering in this system is fragile. Below 138 K the system goes into the low temperature phase, T_{LT}, the very broad drop and two step feature seen in the magnetization is an indication of a glassy state. However, this transition in the S1 sample (see Fig. 4.3, black curve) has a much sharper drop in magnetization. This suggests that the sample is more ordered at this temperature in the S1 sample. Surprisingly there is little frequency dependence in χ', but distinct frequency splitting in χ''. A non-zero out-of-phase component in χ'' indicates the presence of an irreversibility in a spin-glass. The upturn in χ' below 50 K stems from the ordering of Yb^{3+} moments [188] (see Sec. 5.1.2). In relation to the magnetic phases present in $LuFe_2O_4$, the pM to fM in $LuFe_2O_4$ occurs only in applied field, and does not present this broad hump (s-shape feature) below 260 K.

There was no such peak in χ' at this temperature in $LuFe_2O_4$, but rather at T_N=240 K [26] (see Fig. 5.2). The AFM phase is very similar to that observed in $LuFe_2O_4$, where Fig. 5.4 shows both the magnetization and heat capacity on $YbFe_2O_4$ (top panel) and a $LuFe_2O_4$ single crystal (bottom panel). In this $LuFe_2O_4$ sample the drop in magnetization is even less than that observed in the GS sample magnetization, but this is an effect of stoichiometry, and in the highest quality samples, will see a drop to lower μ_B/f.u., indicating it is more ordered in the AFM phase [26]. The stoichiometry of the sample greatly effects the stability of the AFM phase, which is often suppressed by the fM phase when the sample is more off-stoichiometric (refer to Chapter. 4). The re-entrant spin glass state [33,104] observed in $LuFe_2O_4$, in the highest quality samples occurs at T_{LT}=$\sim$175 K, which is much lower in $YbFe_2O_4$ at 138 K. There is a large diffuse component in the neutron scattering (see Fig. 4.5, right) below this transition in $YbFe_2O_4$, that is also present below this temperature

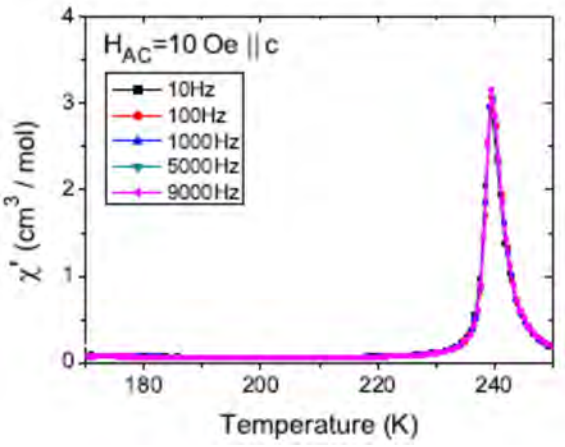

Figure 5.2: The AC susceptibility measured with 5 different driving frequencies, on a highly stoichiometic $LuFe_2O_4$ single crystal, figure taken from [26] and adapted.

in $LuFe_2O_4$ and tentatively identified with the LT phase. The following section will provide additional details obtained from a closer look at the heat capacity.

5.1.2 Heat capacity analysis

There are only four publications including heat capacity/ studies on $LuFe_2O_4$ [189–192] and currently none for $YbFe_2O_4$. The heat capacity curves seen in [189–191] exhibit only broad peaks at the main magnetic and charge ordering transitions and are analogous to that shown in my earlier masters work on $LuFe_2O_4$ [57]. In particular the absence of the charge ordering transition around 315 K, is an indication of large off-stoichiometry. However, their peaks at T_N are much sharper than that shown in our off-stoichiometric $LuFe_2O_4$ sample.

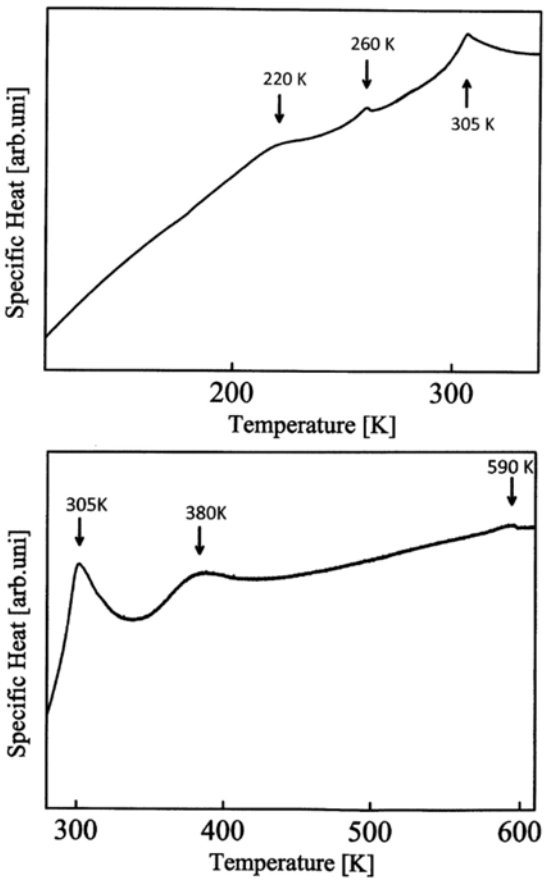

Figure 5.3: Temperature dependence of the specific heat of $LuFe_2O_4$; top: below room temperature and bottom: above 280 K. Figure taken from [192]

The more recent study published on $LuFe_2O_4$ by Hasegawa *et al.* [192] provides heat capacity data on what looks to be a highly stoichiometric sample, with regards to the sharpness of the transitions. However, there is a caveat. They report several transitions between the temperature range 100-650 K (see Fig. 5.3), yet the allocation of these transitions with respect to the intrinsic physical properties is questionable. This is based not only on our investigations (see Fig. 5.4), but those previously published [26, 32, 118]. There are five transitions seen in their data which they attribute to; a spin glass transition at 220 K (T_g), 260 K (T_N) the main ferrimagnetic ordering temperature, 305 K a new phase in $LuFe_2O_4$, 380 K (T_{3CO}) the onset of 3D charge ordering and lastly 590 K (T_{2CO}) 2D diffuse charge ordering. In the most highly stoichiometric samples of $LuFe_2O_4$ published by [32], an accurate placement of the transitions were made with both the Néel temperature T_N at 240 K, through magnetic structure refinement and magnetization, as well as the onset of 3D CO below T_{CO}=315 K. In accordance with much of the previously published data, their 220 K transition is most likely T_N, although lower than that seen in [32], variation in oxygen stoichiometry can suppress transition temperatures. The transition at 305 K, the lambda shaped peak is most likely attributed to the onset of 3D CO in the system, also observed in the $LuFe_2O_4$ and $YbFe_2O_4$ heat capacity data shown in Fig. 5.4, as well as single crystal x-ray diffraction [43,48] (refer to Sec.6.1). The 380 K transition, which they ascribe to 3D charge order is not present in our $LuFe_2O_4$ data, which

was measured up to 400 K [57]. This leaves the 260 and 590 K transition, the latter of which appears to be an experimental artifact. As there is no complementary magnetization data, a good precursor for crystal quality [32,33], it is hard to say if all of these features are intrinsic to the sample. Furthermore, the sample they used was a thin platelet crystal, measured on heating from 100-650 K, as mentioned in Sec. 4.2.3, heating $YbFe_2O_4$ beyond 360 K caused drastic effects in the stoichiometry. The same applies to $LuFe_2O_4$ beyond ~370 K the oxygen from the surface of the crystal will evaporate. For thicker crystals it will not be largely noticeable, as it is more a surface feature, however with a platelet crystal it will cause a complete change in stoichiometry when heated to 650 K. This reason, as well as synthesis and crystal growth conditions used to prepare the sample, including impurity phases, could begin to provide an explanation as to why the heat capacity of their crystal looks comparatively different to those published and to our own work.

The research conducted in this thesis shows for the first time, the specific heat capacity on highly stoichiometric $YbFe_2O_4$. The heat capacity as a function of temperature is plotted in Fig. 5.4 on $YbFe_2O_4$ (top panel, black open circles) and $LuFe_2O_4$ (bottom panel, black open circles) along with the relative $M(T)$ of each sample (black line). In correspondence to the $M(T)$ curve, the transition going from a pM to fM (T_c=260 K) phase and on further cooling a fM to AFM (T_{AFM}=218 K), are seen as two small discontinuous peaks in the heat capacity, indicative of first order phase transitions. A peak is seen in the $LuFe_2O_4$ data at T_N=233 K, corresponding to the fM to AFM phase, but no peak is seen at 260 K for the onset of the fM phase. This is the first distinctive difference between the two systems, regarding the magnetic transitions of more stoichiometric samples. Intrinsically, the fM ordering temperature is much higher than that observed in $LuFe_2O_4$, and based on the AC susceptibility (see Fig. 5.1) the system is well ordered in this phase. Both systems, however exhibit a very similar peak in the heat capacity at T_{AFM}/T_N. The T_{LT} transition is not featured in the heat capacity, which is not surprising based on the parasitic nature of the system below 140 K, similar to 175 K in $LuFe_2O_4$ [26,33]. At slightly higher temperatures, beyond the magnetic transitions, there are additional peaks that relate to the CO transitions. In $LuFe_2O_4$, there is one sharp lambda shaped peak at T_{inCO}=315 K, the onset of 3D long-range charge order. There is also a similar peak at T_{CO}=305 K in the $YbFe_2O_4$ data, also related to the same

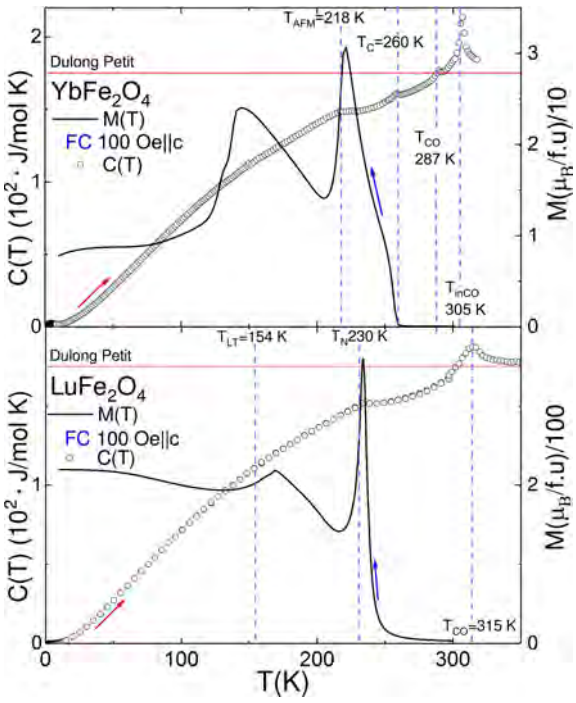

Figure 5.4: Top: $YbFe_2O_4$ (GS sample) heat capacity and $M(T)$ measured on FC in H=100 Oe. Bottom: the same measurements on highly stoichiometric $LuFe_2O_4$. Dotted lines represent transition points for each curve

.

CO transition, but at lower temperature. This peak is much sharper compared to that observed in the $LuFe_2O_4$ data, an indication of both better stoichiometry and long-range order of the $YbFe_2O_4$ sample. The fundamental difference between the two data sets, is the small peak at 287 K. This phase transition is not present in $LuFe_2O_4$, and only observable in the most stoichiometric samples of $YbFe_2O_4$. At this temperature the CO goes from an incommensurate phase to a commensurate phase T_{CO} and discussed in detail in Chapter. 6, Sec. 6.1.1.

Although no heat capacity analysis has been published on $YbFe_2O_4$, comparison can be made with a paper by Zhang *et al* [189] on polycrystalline $LuFe_2O_4$, which provides a low temperature fit of the Debye approximation up to 15 K, and a final Debye temperature of Θ_D=281 K. The Debye model estimates the phonon contribution to the specific heat in a solid. To see if the heat capacity curves given in Fig. 5.4 on $YbFe_2O_4$ and $LuFe_2O_4$ provide the same or similar value for Θ_D, a Debye fit was performed using the same temperature range. To establish a Debye temperature (Θ_D) from the heat capacity curves shown in Fig. 5.4 on $YbFe_2O_4$ and $LuFe_2O_4$, an integral form of the Debye equation, expressing the specific heat at all temperatures of a single empirical parameter Θ_D was used and given by [193]:

$$C_v = 9nk_B \left(\frac{T^3}{\Theta_D}\right) \int_0^{\Theta_D/T} \frac{x^4 e^x dx}{(e^x - 1)^2} \tag{5.1}$$

Where C_v is the specific heat capacity, n, the number of oscillators in the system, k_B is the Boltzmann constant (1.380×10^{-23} J/K), T, a given temperature range and $x = \hbar c/k_B T$. The $n \cdot k_B$ can be written in terms of $N \cdot R$, given that $R = N_A \cdot N$ and $n = N \cdot N_A$. Here R is the molar gas constant (8.31 J/mol K) and N_A is Avogadro's constant ($6.022 \times 1023\,\text{mol}^{-1}$). N, which has the unit of moles, is assumed as 1 mole= N_A atom and in the case for both systems there are N=7 atoms. The low temperature fits of the heat capacity are shown in Fig. 5.5, $YbFe_2O_4$ (left) and $LuFe_2O_4$ (right). $LuFe_2O_4$ is fit simply with the Debye integral as shown in Eqn. 5.1, however a broad peak is seen around 4.5 K in $YbFe_2O_4$, known as a Schottky anomaly [17, 194–196]. This feature further complements the broad up turn in χ' of the AC susceptibility (Fig. 5.1, middle panel) and a small hump in both the $M(T)$ (Fig. 5.1, top panel) and thermoremanent magnetization (Fig.5.12) data below 50 K. This feature is attributed to the parallel alignment of the Yb^{3+} $^4f_{13}$ electrons and the Fe^{2+}/Fe^{3+} $_3d^6/_3d^5$ electrons sub-lattices at low temperature [188]. The Schottky transition, in itself is highly unique and can only occur in systems with a limited number of energy levels and seen in the specific heat capacity $C = dU/dT$ (where U is the internal energy), as a broad maximum close to $k_B T$ [17]. In terms of the entropy, S, the heat capacity is then given as $C = TdS/dT$. For a two level system i.e the ground state to the 1st excited state, the specific heat coming from a Schottky anomaly has the form:

$$C_{Sch} = R\left(\frac{\Delta}{T}\right) \frac{e^{\frac{\Delta}{T}}}{\left[1 + e^{\frac{\Delta}{T}}\right]^2} \tag{5.2}$$

Here $\Delta = \left(\frac{\varepsilon 2 - \varepsilon 1}{k_B}\right)$ is the energy gap between two energy levels $\varepsilon 1$ and $\varepsilon 2$ and treated as the variable to be calculated from the fit. A scale factor (C) was also

used and calculated as a variable from the fit (further fits with and without the use of the scale factor are shown in Appendix. A.1). Of course with more discrete energy levels, the Schottky function can be expanded to include a more complex splitting of the energy levels beyond the $\varepsilon 1$ and $\varepsilon 2$ used here in this simple approximation. This can only be achieved when the specific energies of each state are known i.e via inelastic neutron scattering. Unfortunately, there have been no inelastic studies on $YbFe_2O_4$, and therefore to include a more complex model such as that shown in [196–198], for a Schottky anomaly with more discrete energy levels, further data is required.

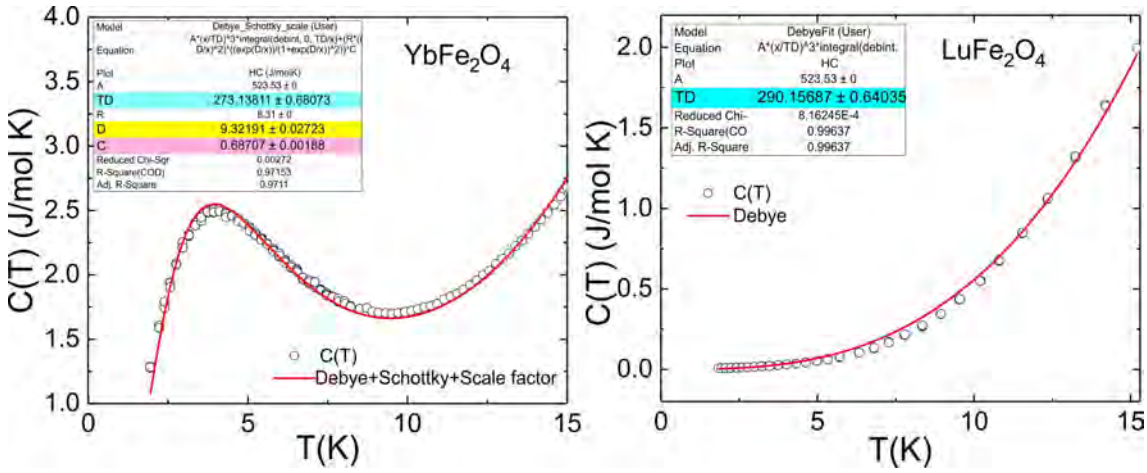

Figure 5.5: Low temperature heat capacity fits. Left: $YbFe_2O_4$ modeled with Debye+Schottky+scale factor. Right: $LuFe_2O_4$ with Debye model.

In our case the simple two energy level model used in Eqn. 5.2 for $YbFe_2O_4$, provides a reasonable fit to the broad maximum seen at ~4.5 K, although there is a slight deviation from the fit to the original data beyond 10 K. Likewise, in $LuFe_2O_4$, the Debye relation fits to a large majority of the data points measured in the 1.8-15 K range, except the region between ~6 and 10 K. The Debye temperatures obtained for each heat capacity are $\Theta_{D(Lu)}$= 290.1 K and $\Theta_{D(Yb)}$=273.1 K. If we then compare the Debye temperature obtained for the heat capacity on polycrystalline $LuFe_2O_4$ by [189] with the value Θ_D=281 K, there is a small discrepancy to our value of $\Theta_{D(Lu)}$= 290.1 K, but as this is an approximation, the two values are in good agreement. The slight difference in values could due to the poorer fit of the temperature region 6-10 K. As the temperature region for the fit is small, compared to the full temperature range initially measured, a lack of addenda points in this region could lead to a poor subtraction from the overall heat capacity, resulting in such a deviation. The calculated Debye temperature for $YbFe_2O_4$ ($\Theta_{D(Yb)}$=273.1 K), is lower than that calculated for $LuFe_2O_4$, having no other reference for this value, one can speculate that the lower value may stem from the Schottky anomaly. The energy difference Δ=9.88 meV calculated from the fit using Eqn. 5.2, is very close to the energy difference Δ=10 meV calculated for the Yb^{3+} D_2 crystal field splitting of ${}^2f_{7/2}$ and ${}^2f_{5/2}$ energy levels [199, 200]. This does indicate that the Schottky anomaly can be described by a 2-level model. However, further experimentation using resonant x-ray scattering would confirm this result. Regardless, this is the first heat capacity analysis on a highly stoichiometric single crystal of $YbFe_2O_4$ with complementary analysis on $LuFe_2O_4$ heat capacity data, providing reasonable

values for Θ_D, the latter in line with [189]. Lastly, the newly identified Schottky anomaly at ∼4.5 K in $YbFe_2O_4$, further supports the broad features observed below 50 K in a number of macroscopic measurements.

5.2 High field studies

5.2.1 Magnetization studies in higher fields

High field magnetization studies on $YbFe_2O_4$ have presented some further differences to that of its closely related neighbour, $LuFe_2O_4$, in addition to the already new ferrimagnetic phase, stabilized in a range of temperatures even in zero field (Sec. 5.1). There is also no presence of the well established 'anomalous field heating effect' in $YbFe_2O_4$ in low fields, which is intrinsically apparent in $LuFe_2O_4$ as shown in Fig. 5.6 (b) (for 0.03 and 0.05 T). This particular effect, first observed by Iida *et al.* [82] on polycrystalline $LuFe_2O_4$, occurs only when warming in a constant field through T_{LT}. Based on the $M(T)$ curves shown in Fig 5.6 on stoichiometric $YbFe_2O_4$ (a) and $LuFe_2O_4$ (b) [26], there is no distinctive plateau which is established on field warming through T_{LT} in $YbFe_2O_4$. On increasing to higher fields, the magnetization exhibits shifts of both the Tc and T_{AFM} transition to lower temperature.

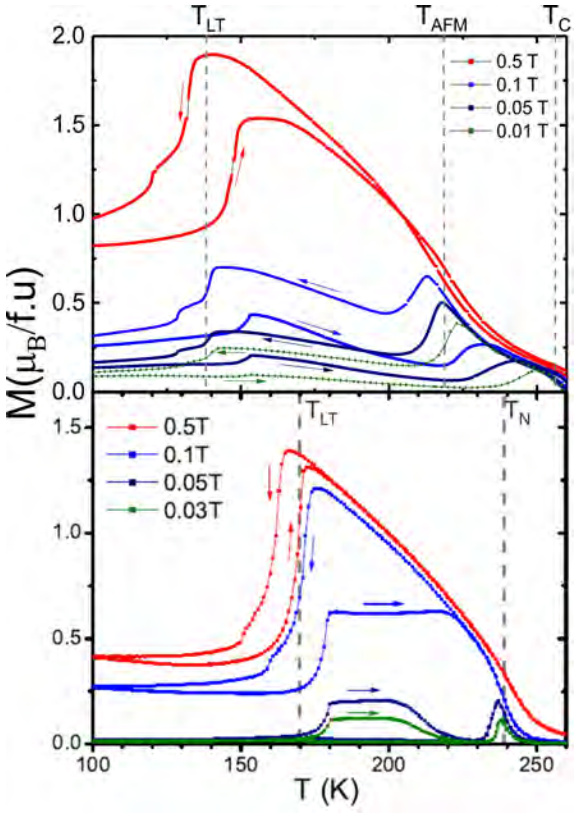

Figure 5.6: Temperature dependent magnetization for difference DC magnetic fields on (a) $YbFe_2O_4$ and (b) $LuFe_2O_4$. The latter was taken from [26] and adapted. The arrows indicate either field cooling (FC) or field warming (FW). Dotted grey lines denote main transition points.

The two sets of data shown in Fig. 5.7 provide both field cooled (FC) (a) and field warming (FW) (b) curves up to 4 T. The sharpness of both Tc and T_{AFM} begin to diminish above 0.1 T (1000 Oe) and they start to merge into the high field ferrimagnetic state from 0.5 T. The stabilization of the AFM phase is maintained only in low field, this is described in further detail in Sec. 5.2.5 for the magnetic phase diagram of $YbFe_2O_4$. The two step feature at T_{LT} is seen only in the FC magnetization. When coming from a low temperature state and measuring on warming this feature is no longer visible. This two step feature was initially thought to be due to a small secondary grain, which cleaved off during the latter stages of measuring this sample. However, its absence on FW shows that it is most likely due to inhomogeneity of the sample, and certainly not intrinsic to $YbFe_2O_4$, as there was no such feature in the S1 sample (see Chapter. 4, Fig. 4.3, black curve). Due to this inhomogeneity there are parts of the sample which order with a lower T_{LT} transition, and on FW there is a low temperature

suppression of some the magnetic domains, correspondent to the small part of the sample with a lower T_{LT} transition.

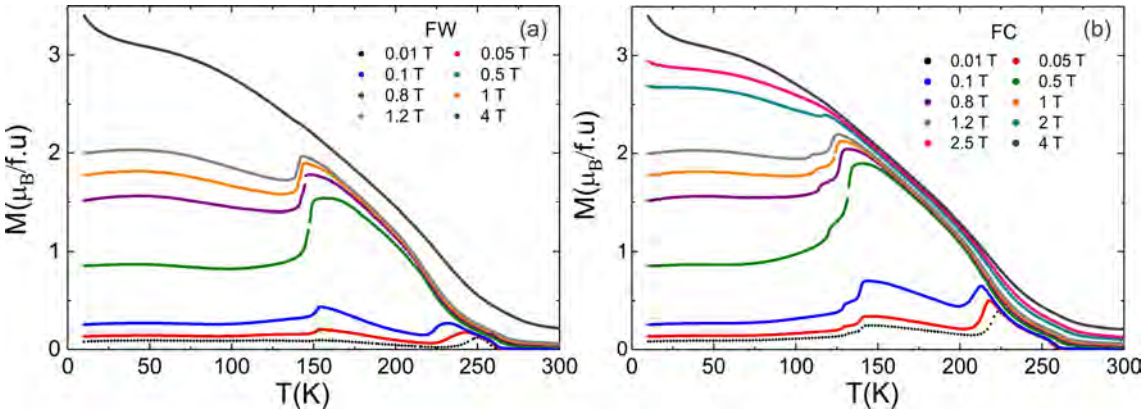

Figure 5.7: Temperature dependent magnetization on $YbFe_2O_4$ for different DC magnetic fields. (a): Field warming (FW). (b): Field cooling (FC).

This particular phase in $YbFe_2O_4$ also provides a further difference to the T_{LT} transition observed in $LuFe_2O_4$. Whereas in the case of $YbFe_2O_4$, the drop in magnetization at the T_{LT} transition gets smaller on increasing the applied field, observed in both FC (Fig. 5.7 (a)) and FW (Fig. 5.7 (b)) curves, this feature was not observed in $LuFe_2O_4$ [26]. A speculation as to why this difference occurs, is that it may be due to the varied metastable phase of each compound. The anomalous field heating effect in $LuFe_2O_4$, discussed above, is seen only in fields up to 0.1 T in $LuFe_2O_4$ (see Fig. 5.6), where some AFM order still remains. However, this effect does not occur on further increasing the field, when the system is in a majority fM phase, also deemed the high-field state. This is quite the contrast for $YbFe_2O_4$, where in fields up to 2 T in the FC magnetization, shows a small bump, indicating that there are still some regions of the sample with ordered AFM domains. The complete polarization of the sample into the fM phase is not achieved until 2.5 T.

5.2.2 Hysteretic response of T_{c} and T_{AFM}

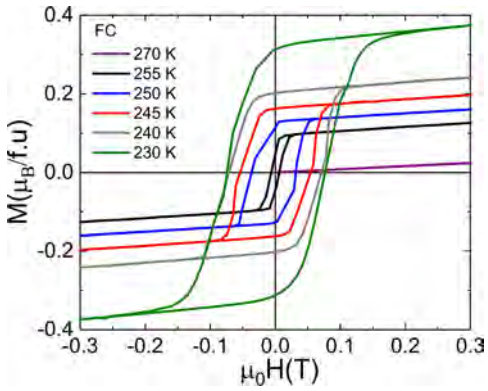

Figure 5.8: Magnetization M vs. field $||\mathbf{c}_{hex}$ of $YbFe_2O_4$ measured at temperatures though T_{c}, the purple line measured at 270 K is in the paramagnetic phase pM.

The behavior observed from the magnetic hysteresis, is complementary to that shown in $M(T)$. The onset of T_{c} below 255 K is shown in Fig. 5.8, the purple straight line measured at 270 K indicates the system is still in the paramagnetic phase (pM). On further cooling in increments of 5 or 10 K the fM order becomes stronger, indicated by the increasing size of the hysteresis loop. These ideal fM loops are maintained down to 225 K (see Fig. 5.9 ((inset) right panel). Below 225 K the system starts to move into the AFM phase. The plotted data set shown in Fig. 5.9 (left) was

measured such that the system for each scan would start in the AFM phase. To achieve this, the sample was first cooled down in zero field to 200 K, where a short wait time was added and then heated up to 255 K, the first temperature measured for the onset of T_c. After each scan was complete, the sample was heated to 300 K, cooled in zero field to 200 K and warmed under the same conditions to the next desired temperature. This process was maintained for the four temperatures measured (Fig. 5.9, left) to fully exploit the AFM phase and more accurately establish its true temperature onset. If this was not done, residual magnetic fields would push the system into the fM phase. The first indication of the AFM phase is seen at 210 K (slightly below T_{AFM}=218 K), where the measured virgin curve (green circles) deviates from the hysteresis loop at fields beyond 0.3 T. This deviation relates to an incomplete fM to AFM transition. In addition, the full hysteresis loops measured at 210 and 200 K are given in Fig. 5.9 (right).

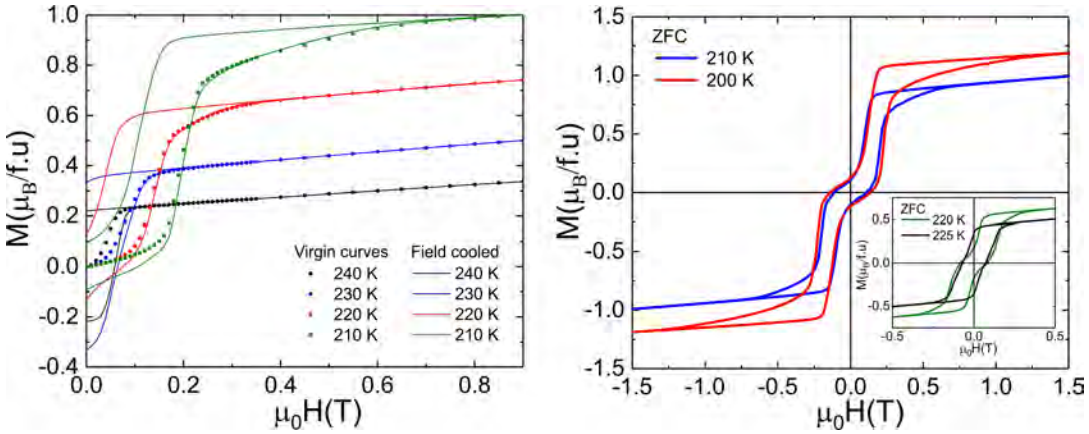

Figure 5.9: Magnetization M vs. field $||\mathbf{c}_{hex}$ of $YbFe_2O_4$ Left: hysteresis loops in the vicinity of T_c and T_{AFM}. Solid coloured lines were measured on FC. The virgin curves are indicated by coloured circles (see text for measurement description). Right: temperatures measured below T_{AFM}, inset shows M vs H curves just above the onset of the AFM phase.

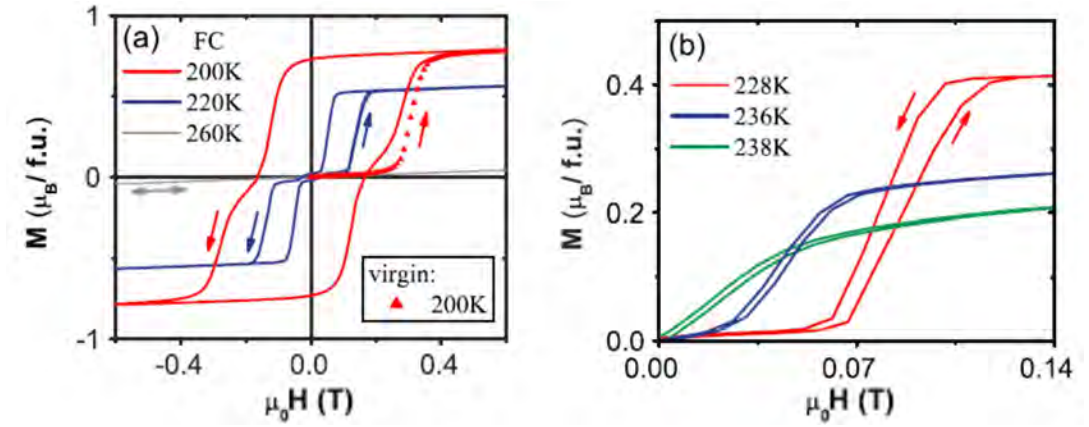

Figure 5.10: Magnetizations vs. field$||\mathbf{c}_{hex}$ of $LuFe_2O_4$. Left: FC M vs H with pM phase at 260 K (grey curve) and onset of the antiferromagnetic phase at 220 K. The data at 200 K is fully stabilized in AFM phase, the virgin curve at 200 K is represented by the red dotted line. Right: temperature region of T_N. Arrows indicate direction of measurement. Figures taken from [32].

The shape of the loops alter to a distinct AFM response with a 2 step feature,

whereby coming from high field the fM phase becomes unstable and (at least a large part of the sample) goes to the AFM phase upon decreasing field. The trends of these curves are similar to those seen in highly stoichiometric $LuFe_2O_4$ [26,32] when specifically looking at T_{AFM}, and considering the different temperature onsets of each transition. A primary difference, as seen in the $M(T)$ is the early onset of the fM phase at 255 K, when compared to the $LuFe_2O_4$ (see fig. 5.10). $LuFe_2O_4$ is still in the paramagnetic phase at 260 K, where the the fM order is seen as a narrow hysteresis loop at 238 K (green curve), just before the onset of the AFM phase, which begins around 236 K (blue curve). The large ferrimagnetic hysteresis loops seen in the temperature range 255 K-230 K is not apparent in the $LuFe_2O_4$. At 200 K, $YbFe_2O_4$ is stabilized in the AFM phase, however $LuFe_2O_4$ is only in the AFM state for the the virgin curve (up to 0.25 T), coming back from high fields the system does not recover the AFM and is majority in the fM phase. The AFM phase is stabilized at 220 K in $LuFe_2O_4$ as seen by the similar shape of the hysteresis loop to that seen at 200 K in $YbFe_2O_4$. The magnetic hysteresis, much like the $M(T)$ can change drastically based on the oxygen stoichiometry and quality of the sample measured. In terms of comparison to other magnetization studies conducted on $YbFe_2O_4$, the work published by [123], provide two $M(H)$ curves measured at 200 K and 45 K, respectively. For each of the two temperatures measured, only fM type loops are seen, which is quite in contrast to what is seen in this work. At 200 K on highly stoichiometric $YbFe_2O_4$ the AFM phase is almost fully established, however there is still a considerable remanent magnetization, which should not occur for a fully AFM state. The magnetic and AC susceptibility data also provided in [123] indicates the sample is similar to our more off-stoichiometric ones (described in Chapter. 4), in such samples the AFM phase is almost completely suppressed by the fM phase. This would explain why they see only fM type loops at 200 K and also at 45 K. The latter temperature is far below the LT transition discussed in the following section.

5.2.3 High field saturation of a metastable phase below T_{LT}

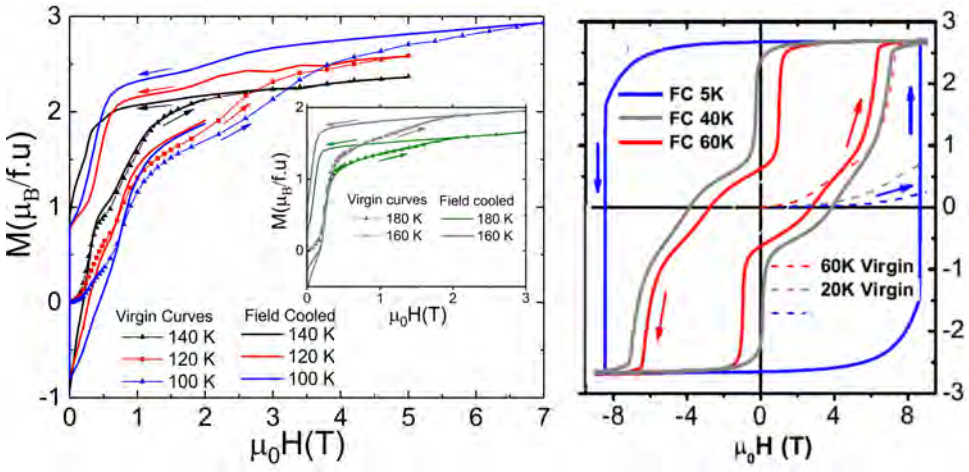

Figure 5.11: M vs H curves below the T_{LT} transition. Left: $YbFe_2O_4$ at three different temperatures on field cooling, the line and symbol plots represent the relative virgin curves at each temperature. Inset: shows M vs H just above the onset of the low temperature transition. Right: measurements below T_{LT} of $LuFe_2O_4$ under the same conditions, figure taken from [26]. Arrows indicate field directions.

The proposed magneto-structural transition [42] often denoted as T_{LT}, varies greatly from sample to sample. When considering the most stoichiometric samples available the state at temperatures below T_{LT} may be characterized as a metastable phase, where the sharpness of this phase observed in both neutron and magnetization data suggests that it is of 1st order, further confirmed by hysteresis in the magnetization [104]. Discussed previously in this chapter and based on the previous work by [33, 42, 104], this particular temperature region is rather difficult to fully comprehend. The onset of this transition in the FC $M(T)$ for $YbFe_2O_4$ is seen at 138 K, and 170 K in $LuFe_2O_4$, respectively. It is clear from the shape of the $M(H)$ curves measured above and below this transition, shown in Fig. 5.11, that this is a phase separated state, with instabilities in both fM and AFM orders. The inset figure, which displays the $M(H)$ curves measured at 180 and 160 K, still promotes the AFM phase, the degeneracy to the metastable state occurs below, near the onset at 140 K (Fig. 5.11, black curve). On further cooling below the transition, the hysteresis loop becomes much broader and a large difference is seen in the saturation of the moments at lower temperature, compared to that observed in $LuFe_2O_4$, where typically at low-T circa 60 K and below, the saturation moment of $LuFe_2O_4$ is 2.9 $\mu_B/f.u.$ [84, 87, 201]. However, at 100 K (Fig. 5.11, left (blue curve)) the lowest temperature measured for the magnetic hysteresis of $YbFe_2O_4$, the saturation moment is still not reached in an applied field of 7 T. There is still an incline of the magnetic hysteresis, and the saturation moment also tends towards $2.9\mu_B/f.u.$, but a larger field is still required to reach full saturation of the magnetic moment. The virgin curves of each measurement conducted at 100, 120 and 140 K on $YbFe_2O_4$, shown in Fig. 5.11 (triangle symbols) also extend outside the $M(H)$ hysteresis curves after field cooling, similar to $LuFe_2O_4$, and associated with the kinetic arrest of the first-order ferrimagnetic to antiferromagnetic transition [194]. This feature is also seen when reaching T_{AFM} (see Fig. 5.9) and describes an incomplete fM to AFM transition. Low temperature measurements of the magnetic hysteresis on $YbFe_2O_4$ published by [123] at 200 K and 45 K show distinctive and well formed ferro/ferrimagnetic type curves, which do not correlate with those shown in this work. This is likely attributed to the sample being off-stoichiometric with large suppression of the AFM phase. With a lack of complementary virgin curves in [123], which may have highlighted some AFM tendencies, there is only indication that the system at all transition temperatures is still in the fM phase. Hysteresis measurements at 150 K and 50 K published by Yoshii *et al.* [119], do indicate some small influence from the AFM phase, based purely on the shape of the curves, however the absence of virgin curves makes it difficult to pin point the stability of the phase at each temperature. From the $M(T)$ curves also shown in this paper, which are almost identical to the off-stoichiometric samples described in Chapter. 4 of this thesis (refer to Fig. 4.3, red curve), it is clear that the AFM phase is greatly suppressed, the more off-stoichiometric the sample is, and why in the few publications dedicated to $YbFe_2O_4$, exhibit only $M(H)$ curves with majority fM behavior. It is only by tuning of the initial crystal growth environment, obtaining a larger collection of stoichiometric crystals, as in the case of $LuFe_2O_4$ and this work, that will result in samples which promote a clear AFM phase (only stable in low fields). Detailed investigation of the LT phase, which for lower T would require higher fields, was not the main focus of this thesis. Therefore further measurements are required down to 5 K for detailed analysis of high field state in this temperature regime, and

comparison to that of $LuFe_2O_4$.

5.2.4 Thermo-remanent magnetization

To measure the thermoremanent magnetization (TRM) of the sample and its ability to remain in a magnetically polarized state once the magnetic field is removed, measurements were performed after cooling in two different fields. Firstly the sample was cooled in a field of 1.8 T (blue curve) shown in Fig. 5.12 (top panel) from 300 to 10 K, where the thermoremanent response was measured on ZFW to 300 K (blue dotted curve). The same procedure was applied for the 9 T measurement also displayed in Fig. 5.12 on FC (red curve) and ZFW (grey curve). The two fields investigated produce curves which are very similar, besides the higher peak intensity in the 9 T measurement around ∼28 K, due to the difference in field applied. An identical measurement was also performed on $LuFe_2O_4$ [26] and given in Fig. 5.12 (bottom panel). The response of $YbFe_2O_4$ is very similar to that observed in $LuFe_2O_4$, in each case there is a steep drop, below the LT transition (see grey curves). The drop in magnetization is much sharper in $LuFe_2O_4$ compared to $YbFe_2O_4$ and due to sample inhomogeneity. In $YbFe_2O_4$, the TRM disappears when the T_{LT} transition is complete, at which point it drops to zero. The $LuFe_2O_4$ differs slightly, as the TRM persists beyond LT on warming. It is likely, that measuring the TRM of the $YbFe_2O_4$ S1 sample would result in a very similar response to that observed in $LuFe_2O_4$, where the different shape of the warming curves stems from the sample dependent feature at LT in the GS sample. The large difference between the two thermoremanent responses is attributed to the magnetic ordering (at least short range) of the Yb^{3+} $4f$ electrons below 50 K. At this temperature there is a parallel alignment of the Yb^{3+} magnetic sub-lattices, which contributes to the total magnetic order [188]. The other contrasting feature between the thermoremanent response of each curve is the small dip in the magnetization below zero at 256 K in $YbFe_2O_4$. This is presented on the inset of Fig. 5.12 (top panel) at 9 T, and occurs at all fields. The horizontal green dotted line positioned at zero highlights the notable dip into negative magnetization, an effect which does not occur in $LuFe_2O_4$. Without the aid of temperature dependent neutron scattering around this transition, it is not possible to provide an accurate description as to the true nature of the magnetic ordering present here.

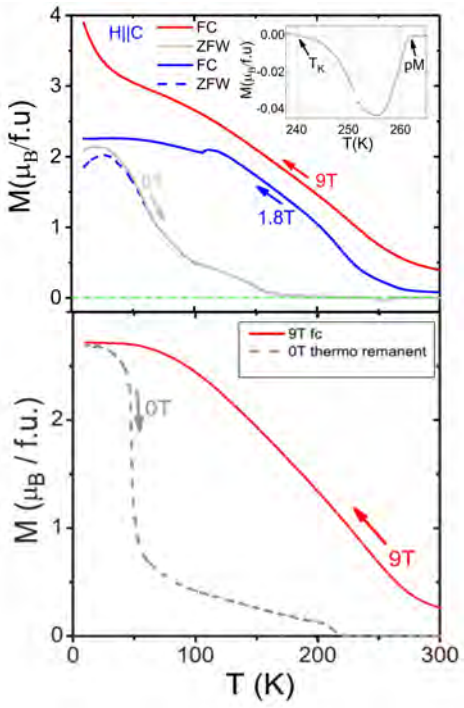

Figure 5.12: Top: TRM of $YbFe_2O_4$ on FC in 9 T (red curve) and 1.8 T (blue curve). ZFW after FC in 9 T (grey dashes) and 1.8 T (blue dashes). Inset: zoomed area around 256 K in 0 T. Bottom: $LuFe_2O_4$ measured on FC in 9 T (red curve) and TRM response on ZFW (grey dotted line). Arrows indicate measurement direction. Figure taken from [26] and adapted.

One should also note, that the pM phase starts at a higher temperature (∼262 K) in the TRM (see Fig. 5.12 top panel (inset)) in contrast to the AC susceptibility and $M(T)$ given in Fig. 5.1. When compounds have different sub-lattices (due to mixed valency), in our case two, with Fe^{2+} and Fe^{3+} a disproportionation of magnetic moments can occur, creating more complex magnetic behavior.

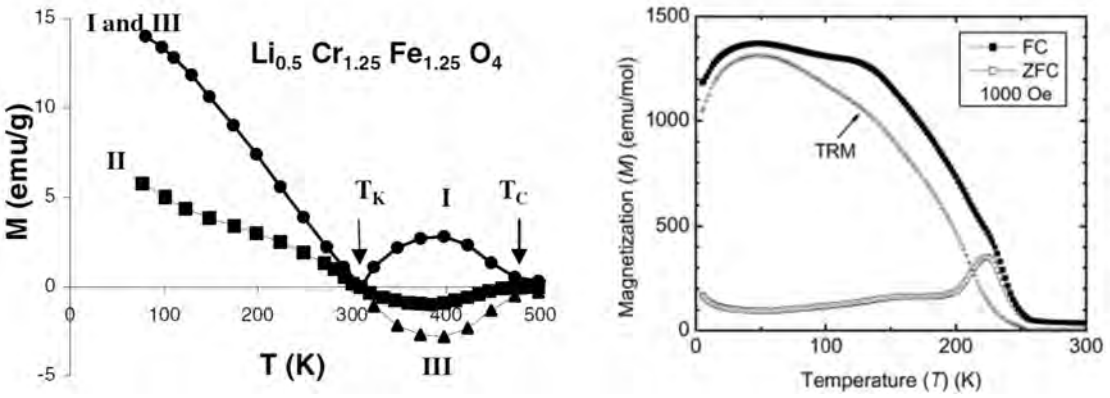

Figure 5.13: Left: magnetization vs temperature on heating of $Li_{0.5}Cr_{1.25}Fe_{1.25}O_4$. Curve I: the saturation magnetization at 13.5 kOe; curve II thermoremanent magnetization; curve III spontaneous magnetization. The annotation T_K refers to the temperature at which the compensation point is reached and T_c the Curie temperature. Graph taken from [202] Right: $M(T)$ plotted for $YbFe_2O_4$ on ZFC and FC measured with an applied magnetic field of 1000 Oe. The thermoremanent magnetization is labeled as TRM. Bottom figure taken from [118].

A similar example of the negative dip present in $YbFe_2O_4$ around 256 K is observed in the magnetization measured on heating of $Li_{0.5}Fe_{2.5-x}Cr_xO_4$ [202]. In this case the two sub-lattices A and B are Fe^{3+} and $Li_{0.5}Fe_{1.5}Cr_x$, respectively. The sublattice A contains only Fe, but B can contain either Cr or Li in the compound. The substitution of Cr^{3+} on site B magnetically weakens the effect of Fe^{3+} at x=1.05. At this value of x the spontaneous magnetization decreases to zero before the Curie temperature is reached. The material then develops a spontaneous magnetization in the opposite direction, in the process dropping below zero. At one temperature called the *compensation point*, the magnetization of the two sub-lattices are exactly balanced and the net magnetization is zero (refer to section Sec. 1.3 for more detail). The compensation point T_K, is more clearly identified in the thermoremanent magnetization, as shown in Fig. 5.13 (left) [202, 203], for the thermoremanent response of $Li_{0.5}Cr_{1.25}Fe_{1.25}O_4$ (x=1.25). The compensation point in $YbFe_2O_4$ using this criterion is around T_K=241 K (Fig. 5.12, inset). A previously published paper by [118] also shown in Fig. 5.13, presented magnetization studies on $YbFe_2O_4$ including both ZFC-FC magnetization and TRM measurements with an applied field of 1000 Oe. Their $M(T)$ curves exhibited very broad transitions, comparable to ours shown in Fig. 4.5. Similarly, both TRM curves exhibit a broad peak around 50 K, from the magnetic ordering of the Yb moments, however on further warming their TRM curve descends to zero at around 250 K, in contrast to ours reaching zero just after T_{LT}. Furthermore there is clear evidence of the negative dip in the magnetization in [118]. Based on the quality of the polycrystalline sample, many of the transitions were smeared out in the $M(T)$, and also therefore in the TRM, severely obscuring the intrinsic properties. Moreover, cooling in an applied field of 1000 Oe, may not have been high enough to stabilize the ferrimagnetic phase fully [26, 32], resulting in

the absence of the negative dip in the magnetization at 256 K seen in our data. In the case of our $YbFe_2O_4$, without further analysis, one could speculate that the negative dip is most likely attributable to the different temperature dependence of the Fe^{2+}/Fe^{3+} sub-lattice (like Fe and Cr in [202]) which, point in opposite directions (see Sec. 7.3.1).

5.2.5 Mapping the magnetic phase diagram

To map the magnetic phase diagram, a combination of different measurement types were required to obtain as much information as possible about each transition. Both $M(T)$ and $M(H)$ covered in the section above provide most of the transition points for T_{AFM} and T_{LT}. However, T_{c}, which is seen as a broad hump in the $M(T)$ data, was acquired more accurately via the AC susceptibility, seen as a sharp peak in zero field which broadens on increasing H, as shown in Fig. 5.14. Two sets of measurements were done, the first on field cooling and the second on field warming using a single frequency of 9010 Hz. The FC curves plotted in Fig. 5.14 range between 100 Oe (0.01 T) to 40000 Oe (4 T), where the inset shows no hysteresis between heating and cooling. The variation of the background for each peak increasing field, made a group fit of all the curves together more challenging. Therefore to accurately pin point the peak maximum, individual fits at each field were performed using a standard Lorentzian, the background was subtracted using a linear baseline.

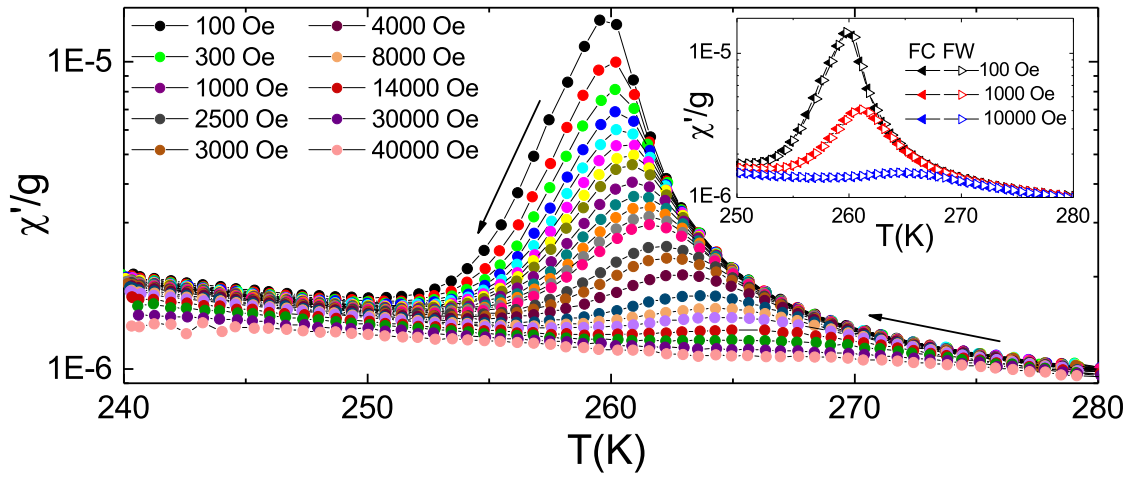

Figure 5.14: Field dependent AC susceptibility measured on FC between 240-280 K using a single frequency of 9010 Hz. Inset: AC susceptibility on FC and FW, at three selected fields and exhibits no temperature hysteresis.

The AC susceptibility data given in Fig. 5.14 was used to determine the phase boundary between the paramagnetic and ferrimagnetic transition. A collection of $M(T)$ on FC and FW, as well as the up and down transitions obtained from the magnetic hysteresis were used to establish the boundaries between the other phases, some of which are presented in Fig. 5.10 and Fig. 5.6.

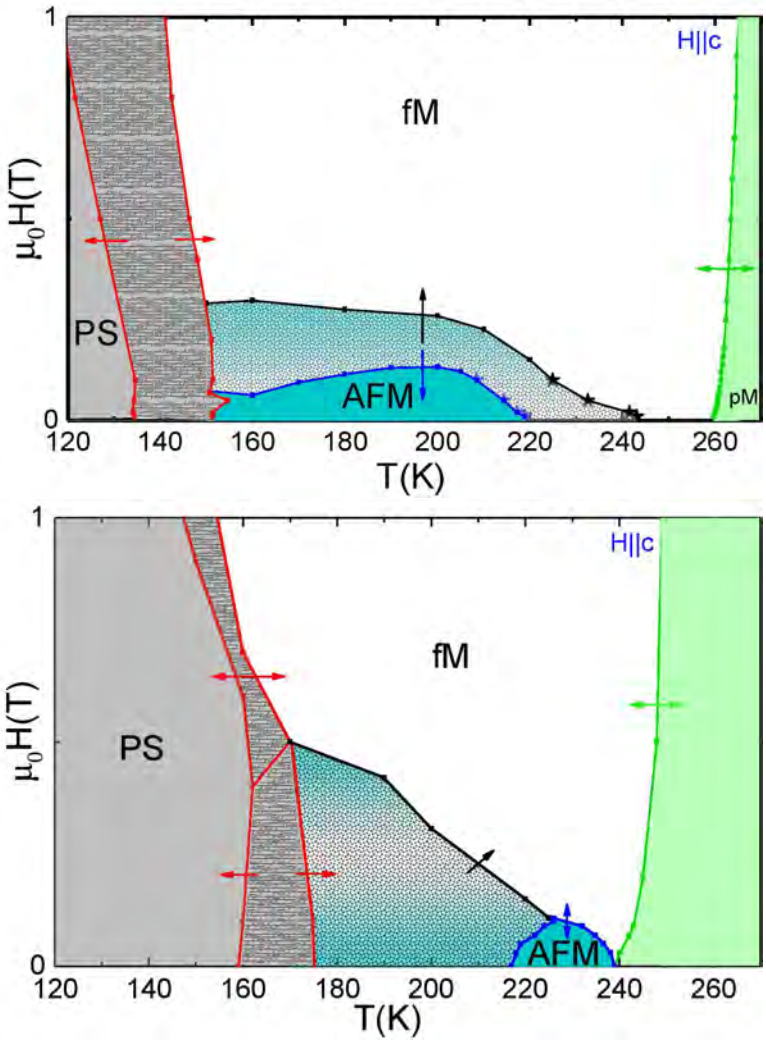

Figure 5.15: Phase diagrams of magnetic field H and temperature T for different starting conditions for $YbFe_2O_4$ (top) and $LuFe_2O_4$ (bottom). For $YbFe_2O_4$ (star symbols) represent $M(T)$ for the AFM phase, the transition to the pM phase was obtained from AC susceptibility measurements. The remaining points were obtained by Mvs$H$ on FC and ZFC for both AFM and fM phases (blue and black square symbols) and hysterestic hatched region (red squares). The latter region is shaded blue and white to indicate either AFM or fM phase stabilization is possible. The grey textured area indicates where either fM, AFM or PS (phase separated) phase can be stabilized. The solid grey area is the low-T range not yet investigated. $LuFe_2O_4$ is plotted using the same colour scheme and data taken from [26].

As a result a comprehensive magnetic phase diagram was thus established for $YbFe_2O_4$ and displayed in Fig.5.15 (top). This phase diagram also combines hysteresis effects seen in the magnetization measurements, rather than separating them into two phase diagrams (denoted by arrows). A direct comparison can be made with the already established phase diagram of $LuFe_2O_4$ [26], also shown in Fig.5.15 (bottom), each are plotted using the same colour, field and temperature scale. On direct observation, there is a large difference between the paramagnetic (pM) phase to AFM phase in $YbFe_2O_4$ compared to that of $LuFe_2O_4$. The phase boundary between these two states is connected at the onset of AFM in $LuFe_2O_4$, there is a temperature gap in $YbFe_2O_4$ from T_c to the AFM phase, where only ferrimagnetic order is seen in any field. Furthermore, the AFM phase extends for a longer temperature range and is stabilized in slightly higher fields up to $\sim$0.3 T. The black

and blue lines plotted for T_{AFM}, which contain two symbol types; square symbols indicating points taken from $M(H)$ curves and star symbols for transition points taken from $M(T)$, exhibit a rather large hysteresis. On the FC magnetization for example, the onset of T_{AFM} is 218 K, however on field warming the AFM phase is elongated up to 240 K. From both phase diagrams an extension of the AFM phase observed in $YbFe_2O_4$ is in large contrast to that seen in $LuFe_2O_4$. The purely AFM phase in $LuFe_2O_4$ is visible for a temperature span of ∼20 K on both heating and cooling. In $YbFe_2O_4$, this phase stems over a much larger temperature range, approximately 65 K on FC and down hysteresis measurements, and 85 K on FW. The low temperature transition T_{LT} is also phase separated (PS) in $YbFe_2O_4$ with glassy dynamics, similar to $LuFe_2O_4$ in which it is also associated with as a structural distortion. The red lines here indicate the FC and FW $M(T)$ data, which is also divided by a substantial temperature hysteresis. A temperature difference of approximately 7 K occurs between FC and FW magnetization data at T_{LT}, which is also distinctly different to that seen in the phase diagram of $LuFe_2O_4$. The grey shaded area below the red line describing the field cooling of T_{LT} has yet to be fully investigated. As mentioned previously in Sec. 5.2, the magnetization change at the T_{LT} transition observed in $M(T)$ measurements, on application of larger magnetic fields the transition becomes smaller, finally vanishing at 2.5 T see Fig. 5.7 (left panel, pink curve). This effect is not apparent in $LuFe_2O_4$ [26, 32, 182].

5.3 Discussion

The data presented in this chapter provides a detailed look at the magnetic properties of a highly stoichiometric single crystal of $YbFe_2O_4$. Although, these transitions may not be resolvable in the majority of $YbFe_2O_4$ samples, due to oxygen off-stoichiometry, the results given here provide a similar story to those published on highly stoichiometric $LuFe_2O_4$ [26, 32, 182]. Therefore, one can say that $YbFe_2O_4$ exhibiting magnetization curves similar to those observed in both the S1 and GS single crystals are the closest to the intrinsic behavior of ideal $YbFe_2O_4$. In samples which exhibit only a single broad transition at T_{N}, due to off-stoichiometry it is natural to expect that the 3D long-range order in the system would be replaced by 2D (spin glass) ferrimagnetic order. It is the glassy freezing and 2D order that will largely affect the weak interlayer correlations in the system. The large fM component and low dimensional ordering, now known to be related to off-stoichiometry, has been reported in early neutron studies on $LuFe_2O_4$ [87] and YFe_2O_4 [204].

The new understanding of the magnetic phases present in $YbFe_2O_4$ through the establishment of a magnetic phase diagram, allows for the first time to see both clearly; similarities and differences to its closely related isostructural neighbour $LuFe_2O_4$, not accessible before. The main phases in $YbFe_2O_4$ are similar to that of $LuFe_2O_4$, each going from pM to fM, then on further cooling (depending on field) the fM to AFM can be stabilized. Cooling further below T_{LT} each system reaches what is known as the phase separated state (PS) [26], where either AFM or fM orders can be stabilized strongly depending on whether the system was cooled or heated to this phase and what field was applied. Despite exhibiting the same phases, there are large contrasts at the phase boundaries at each transition point.

The magnetic phase diagram for $YbFe_2O_4$ does show that the fM phase is stabilized in H=0, this does not occur in $LuFe_2O_4$. This feature can only be addressed with the intrinsic spin structure of the fM and AFM phases and is discussed in Chapter. 7, Sec. 7.2. Furthermore, this fM stabilization in zero field is accompanied by a compensation point [202,203], that is seen as a small dip into negative magnetization when measuring the thermoremanent response. As this feature most likely stems from delayed ordering of the Fe^{2+} and Fe^{3+} spins after cooling in a field, it may also go to explain why the fM phase is stable in H=0. When the Curie temperature is reached in such a system, the magnetic moment should be at zero, however in complex ferrimagnetic systems, a sudden spontaneous magnetization can flip the spins in the opposite direction, thus creating a negative moment, leading to a compensation point. This phenomenon does not occur in $LuFe_2O_4$, as the system is not fM in zero field, displayed clearly in the magnetic phase diagram (see Fig. 5.15, bottom panel). The low field AFM phase is clearly defined in both compounds, but based on the he magnetic phase diagram of $YbFe_2O_4$, this phase is stable in a larger temperature range on cooling (220- ∼150 K), contrary to $LuFe_2O_4$ with an AFM range of 240- ∼218 K. Interestingly, the hysterestic region in $LuFe_2O_4$ where either AFM or fM phases can be stabilized covers a higher field range than $YbFe_2O_4$ (see Fig. 5.15, top panel). It seems, at least for $YbFe_2O_4$, that there is less ambiguity in the hysterestic region, where only a small field range exists before going into the full fM phase. The phase boundary for the low temperature transition in $YbFe_2O_4$ has been achieved via $M(T)$ and Mvs$H$ measurements. Below T_{LT} a tendency of competition exists between micro domains ordering both ferri and antiferromagnetically. Stabilization of the fM phase is only reached beyond fields of 2.5 T, and seen as a field dependent peak decrease at the transition point.

Having discussed the phases apparent in each system, it is now important to address (where possible at this stage) why the differences in phase boundaries occur. Starting with the most complex phase T_{LT}, this phase has not been thoroughly investigated, besides defining the phase boundary, as it was not the main focus of the thesis. However, this phase is often identified with a possible magneto-structural transition or re-entrant spin glass, one could speculate that the commensurate CO (discussed previously in Chapter. 4 4 and analyzed in Chapter. 6, Fig. 6.7) may hold the key to understanding this phase more. In terms of the higher T phases, these are better understood based on the microscopic studies, allowing one to ascertain the correct spin structure related to the transitions observed in macroscopic experiments, and as such will be discussed in more detail in Chapter. 7. Regardless, some initial pointers will be addressed. The diffuse magnetic scattering, observed in $LuFe_2O_4$ up to RT, and the measured XMCD signal at 260 K [32] indicate that the individual bilayers are already ordered in the pM phase, each with a net moment, leaving the open question of; how do the net magnetization of the bilayers stack? There could be better ordering of the bilayers in the pM phase of $YbFe_2O_4$, due to the onset commensurate CO below 287 K, yet this is still only speculation. As each system in high field will ultimately go into the fM phase the Zeeman energy should be equal for $YbFe_2O_4$ and $LuFe_2O_4$ under these conditions. Furthermore, the minimization of stray fields should favor the AFM phase, given that no externally applied field is present. This should again be equal for both compounds. In a highly stoichiometric system, there are very weak but long distance superexchange interactions connecting the neighbouring bilayers [33]. These are extremely long

and complex exchange paths and of course as the Fe bilayers are separated by R-O (R=rare earth) mono-layers, the superexchange paths run through these layers to, thus involving the rare earths themselves as there are no O-O bonds. This means that changing the rare earth element will alter the exchange coupling between neighbouring bilayers. All of these factors; the Zeeman energy, ordering of the bilayers in the pM phase and the complex exchange interactions, should be T-independent. This however, does not help us understand how you can get both AFM and fM phases stabilized in H=0 at different temperatures in $YbFe_2O_4$, further analysis is required here.

Despite these differences, many of the phases present relate strongly to that seen in $LuFe_2O_4$, and the clarity of what appears to be the truly intrinsic properties of highly stoichiometric $YbFe_2O_4$ is now uncovered. The next focus points of the remaining chapters, is that of the charge ordering, and later the coupling between the spin and charge order in the system. At this point it is still necessary to see if the spin structure of the AFM and fM phases for $YbFe_2O_4$ is the same as that previously reported on $LuFe_2O_4$ [26, 32, 104], or if the slight differences seen in the phase diagram provide an alternative solution. Chapter. 6 and 7 will hopefully answer all of these questions and more.

6 | Charge order studies and crystallographic refinement of $YbFe_2O_4$

Highly stoichiometric samples of $YbFe_2O_4$ have been successfully produced, via careful tuning of the oxygen partial pressure atmosphere used during powder synthesis and crystal growth. They exhibit magnetic transitions of unprecedented sharpness seen in magnetization (discussed in the previous chapters), a common precursor used for checking crystal quality [32]. As already briefly mentioned in section Sec. 4.2.3, a striking novelty with regards to $LuFe_2O_4$ is the observation of commensurate CO in $YbFe_2O_4$. In the first section of this chapter the incommensurate-commensurate CO transition is examined in detail. The following sections, after briefly discussing the room temperature crystal structure are devoted to the establishment of the charge configuration in the commensurate CO phase, followed by an analysis; in terms of symmetry and modes. The chapter closes with a discussion of the CO in light of the final solved structure, its implications and what comes next for $YbFe_2O_4$.

6.1 Charge ordering in $YbFe_2O_4$

The recent CO investigations on these high quality samples have uncovered for the first time an identical 2D diffuse (T_{2DCO}) to 3D incommensurate (T_{inCO}) CO phase transition, as previously reported in highly stoichiometric $LuFe_2O_4$ [33,48,106]. This type of CO transition observed in $YbFe_2O_4$ is classed as Type 2, defined previously in Chapter. 4, Sec.4.2.3. High energy x-ray diffraction (see Sec. 3.7.4) was used to map the $hh\ell$ plane at different temperatures, employing the S1 sample (see Fig. 4.3 black curve, for characterization of low-field magnetization). Two combined sets of diffraction images obtained from a MAR345 imaging plate are shown in Fig. 6.1, on previously published $LuFe_2O_4$ data [48] and that recently published by us on $YbFe_2O_4$ [43] (left panel). The two temperatures shown at 350 K (top) and 300 K (bottom) represent the approximate temperature at which each CO phase is strongly stabilized.

The short range CO correlations observed at 350 K for each compound show a very similar 2D diffuse nature in Fig. 6.1 (left panel). A 2D box integration along $(\frac{2}{3}, \frac{2}{3}, \ell)$ taken from the image measured at 350 K (Fig. 6.1 right panel (a)) does indicate sharper peak intensity than that observed in $LuFe_2O_4$ at 360 K [106]. This means that $YbFe_2O_4$ has better correlations along **c**, even above the 3D CO ordering temperature. Fig. 6.2 shows a set of progression images in the temperature

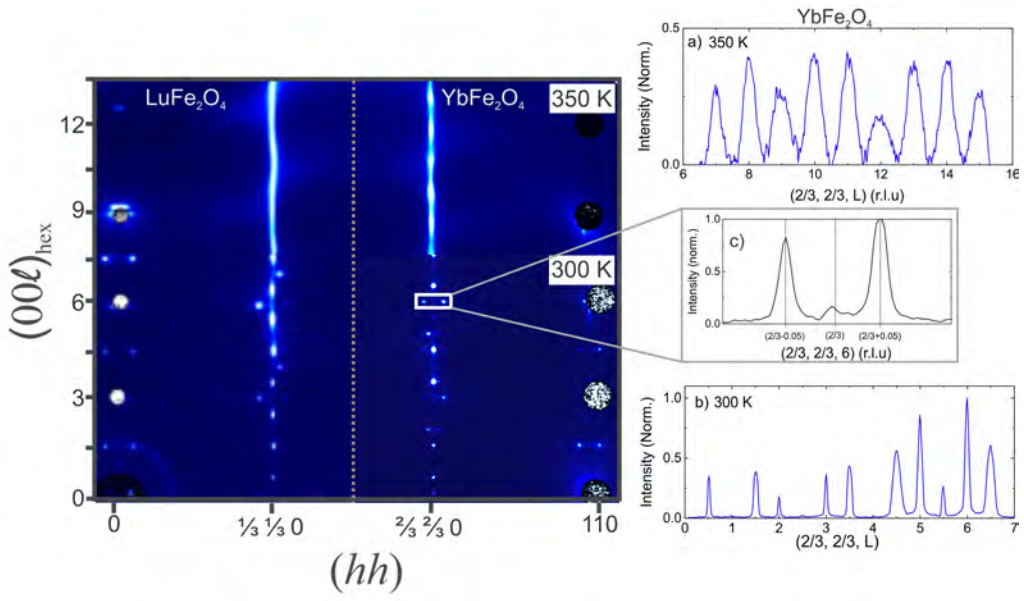

Figure 6.1: Left: images of the $hh\ell$ plane at 350 and 300 K on $LuFe_2O_4$ [26] and $YbFe_2O_4$ [43], the grey dotted line is used to distinguish between the two data sets. Right: $YbFe_2O_4$ vertical box integration along ℓ taken from images at 350 K (a) and 300 K (b). A linear and spline background subtraction was used for the data set in (a) and (b), respectively. (c) 2D line integration in hh of incommensurate CO region, highlighted by white box. Data was treated with linear background subtraction.

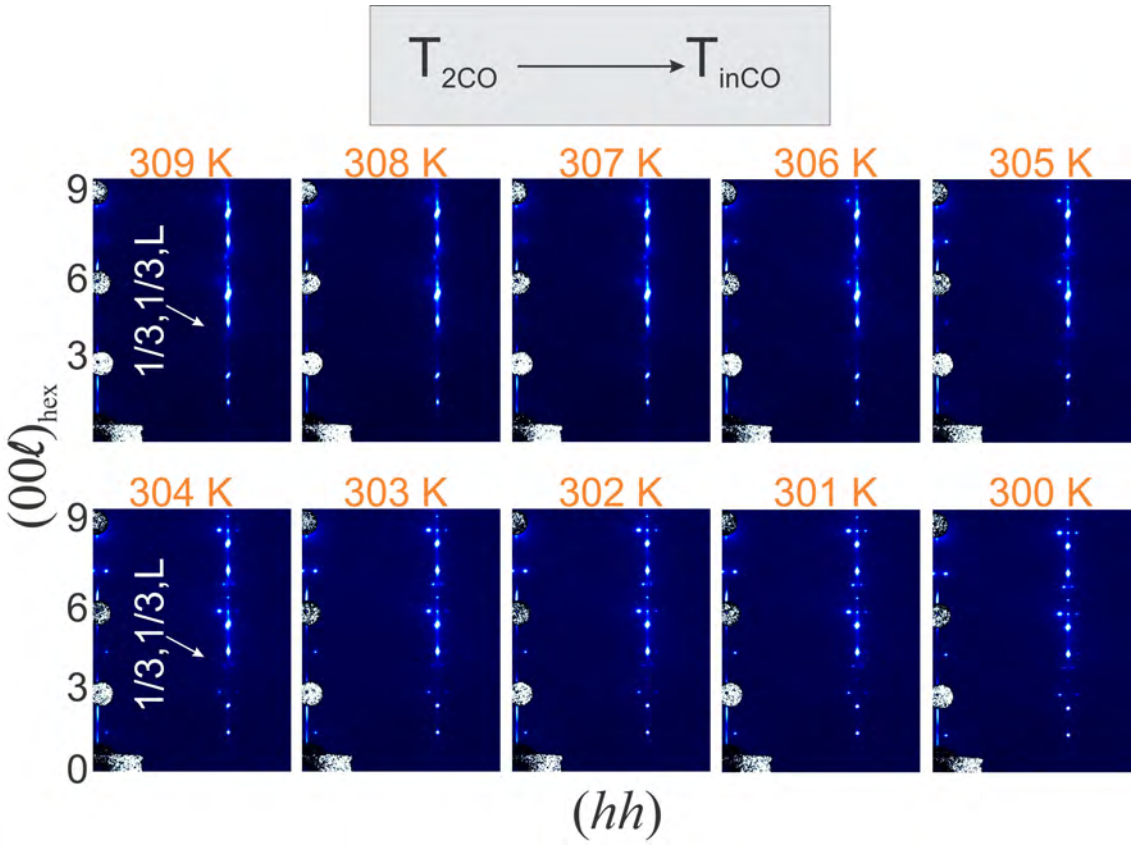

Figure 6.2: A set of progression images cut to show the $(\frac{1}{3}, \frac{1}{3}, \ell)$ line ($hh\ell$ plane) at decreasing temperature from 309 K to 300 K in 1 K steps.

range 309-300 K (1 K steps). A clear development of τ incommensurate satellites appear at $(\frac{1}{3}\pm\tau,\ \frac{1}{3}\mp 2\tau,\ 15)$ and $(\pm\tau,\ \pm\tau,\ \frac{3}{2})$ like positions, going from a 2D to 3D CO phase below 306 K. In the publication by Hearmon *et al.* [121], using high resolution synchrotron diffraction on $YbFe_2O_4$ single crystals, show this type of low dimensional ordering at 360 K and on further cooling to 150 K. Reviewing the gas ratio they used during crystal growth, a mix of $CO:CO_2$=4:5 ($CO:CO_2$=1:1.2) and indicate a too reducing oxidizing atmosphere and therefore an effect purely of stoichiometry. At 300 K Fig. 6.1 (left panel, bottom) shows that the CO in both $LuFe_2O_4$ and $YbFe_2O_4$ is very similar if not identical, with both systems exhibiting the incommensurate CO phase (T_{inCO}). The nature of this CO in $LuFe_2O_4$ was attributed to discommensurations in τ [33] (see Appendix. A.2), as mentioned above. There is a small difference seen between these two images, and that is the observation of sharper peaks in $YbFe_2O_4$ along $\mathbf{P}$=$(\frac{2}{3},\ \frac{2}{3},\ \ell)$, compared to the more elongated peaks in $LuFe_2O_4$, an indication of improved correlations between the bilayers. For a clearer idea of how sharp the peaks are at this temperature along ℓ, a 2D box integration along hh, including τ satellites is also plotted in Fig. 6.1 (right panel, (b)). This may not be based on stoichiometry as the $LuFe_2O_4$ crystal used for this study was of the highest quality, meaning that this is more likely an intrinsic effect.

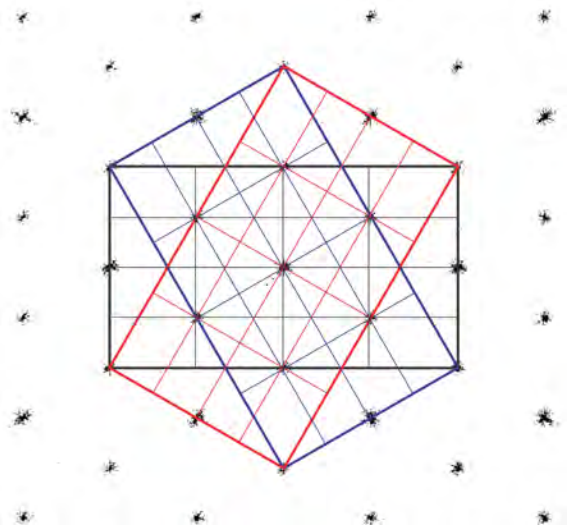

Figure 6.3: Reflections observed at 200 K along $\mathbf{c}_{hex}$. Each 120° domain is represented by a different coloured cell.

The incommensurate CO superstructure reflections, observed in $YbFe_2O_4$ at RT, can be described by the same three propagation vectors as used in $LuFe_2O_4$ [106]: $\mathbf{P}_A$=$(\frac{1}{3}$+$\delta,\ \frac{1}{3}$+$\delta,\ \frac{3}{2})$, $\mathbf{P}_B$=$(\bar{\frac{2}{3}}$-$2\delta,\ \frac{1}{3}$+$\delta,\ \frac{3}{2})$ and $\mathbf{P}_C$=$(\frac{1}{3}$+$2\delta,\ \bar{\frac{2}{3}}$-$2\delta,\ \frac{3}{2})$. These vectors originate from a 120° twining around $\mathbf{c}_{hex}$ with $(\frac{1}{3},\ \frac{1}{3},\ \frac{3}{2})$ and symmetry equivalent directions $(\frac{1}{3},\ \bar{\frac{2}{3}},\ \frac{3}{2})$ and $(\bar{\frac{2}{3}},\ \frac{1}{3},\ \frac{3}{2})$, as shown in Fig. 6.3. These vectors however do not include higher harmonics such as $(\pm\tau,\ \pm\tau,\ \frac{3}{2})$ and $(\frac{1}{3}\pm\tau,\ \frac{3}{2}\pm\tau,\ \frac{3}{2})$, which based on the analysis shown in Fig. 6.4 (middle panel) deviation of δ from the commensurate peak is quite large (τ»δ) in $LuFe_2O_4$ compared to $YbFe_2O_4$. In this plot, horizontal 2D box integrations enclosing around reflections at $(\pm\tau,\ \pm\tau,\ 13.5)$ (blue circles) and $(\frac{1}{3}\pm\tau,\ \frac{1}{3}\mp 2\tau,\ 14)$ (black squares) for $LuFe_2O_4$ and $(\frac{1}{3}\pm\tau,\ \frac{1}{3}\mp 2\tau,\ 15)$ (red circles) and $(\pm\tau,\ \pm\tau,\ \frac{3}{2})$ (grey squares) for $YbFe_2O_4$, are shown respectively. All the peaks were fitted with a standard Gaussian and linear background subtraction. In the case of $LuFe_2O_4$, in which the incommensurate phase remains down to low temperature, there is a notable decrease of τ, when the system reaches T_{N}, τ ~0.025 has a minimum (blue circles and black squares), and on further cooling τ starts to increase until entering the LT phase. This feature stems from the commensurate nature of the magnetic order [104] observed along $(\frac{1}{3},\ \frac{1}{3},\ \ell)$, which forces the CO to become more commensurate. The story for $YbFe_2O_4$ is quite different. Mapping the τ change as a function of temperature shows that, not only is the incommensuration of τ much smaller in general to that observed in $LuFe_2O_4$,

but on cooling, the τ positions shift more and more to the central commensurate peak at $(\frac{1}{3}, \frac{1}{3}, \ell)$, until reaching zero below 280 K, at which point the system enters the commensurate CO phase and remains down to low temperature, as shown in an image of the $hh\ell$ plane at 10 K in Fig. 6.4 (left panel). This is clear evidence that the phase transition going from incommensurate to commensurate is of first order (see also Fig. 6.5), seen first in the specific heat capacity, discussed in Chapter 5 Sec. 5.1.2. A plot of the heat capacity in the temperature range 320-260 K is also provided in Fig. 6.4 (right panel).

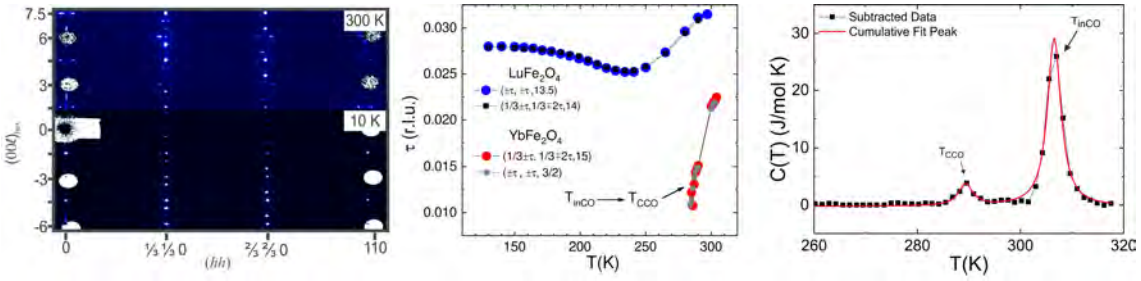

Figure 6.4: Left: MAR345 images of the $hh\ell$ plane, measured on $YbFe_2O_4$ at 300 K (top) and 10 K (bottom). Middle: incommensuration τ, plotted as a function of temperature at 2 positions for $LuFe_2O_4$ (blue circle and black square) and $YbFe_2O_4$ (red circle and grey squares). Arrows indicate CO phase transition from T_{inCO} to T_{CCO}. The data was taken from the MAR345 images measured at different temperatures. Box integrations were taken of the selected positions and each were fit with a standard Gaussian and linear background subtraction. Right: heat capacity of the GS sample between 260-320 K. Red line represents cumulative peak fit using a Lorentzian function and background was subtracted using a spline.

The data shows two clear features; the first; a sharp peak at 305 K which relates to the onset of T_{inCO}, on further cooling a second smaller peak around 287 K emerges, and represents the onset of T_{CCO}. If in the case of $LuFe_2O_4$, the long-range commensurate magnetic order forces the CO to go more commensurate (a reduction in τ), this could provide an answer as to why a full commensurate phase occurs in $YbFe_2O_4$. To better elucidate, one must firstly refer back to Chapter. 4, which discussed the effects of stoichiometry on both the charge and magnetic order. The S3 sample, which provides $M(T)$ similar to that published by [119], showed that 3D magnetic peak intensity occurs even in some off-stoichiometric samples (see Fig. 4.5, right panel for neutron spin-flip scattering). The magnetic phase diagram given in Chapter. 5, Fig. 5.15 shows that fM ordering in $YbFe_2O_4$ is stabilized even in H=0, a clear spontaneous magnetization, not present in $LuFe_2O_4$. These two facts indicate that $YbFe_2O_4$ has much stronger magnetic correlations, particularity in the fM phase. If a more commensurate CO is driven by the magnetic order in $LuFe_2O_4$ at T_{N}, it stands to good reason the improved magnetic correlations in $YbFe_2O_4$ may be strong enough to drive the CO to this newly observed commensurate phase (the implications of this are discussed more in Chapter 7). The following subsection will include more detailed analysis of this commensurate CO phase.

6.1.1 Incommensurate to commensurate charge order phase transition

The new incommensurate to commensurate CO phase transition has only been observed in highly stoichiometric single crystals of $YbFe_2O_4$ around 280 K and comes

under the category Type 2, as detailed in Sec. 4.2.3.

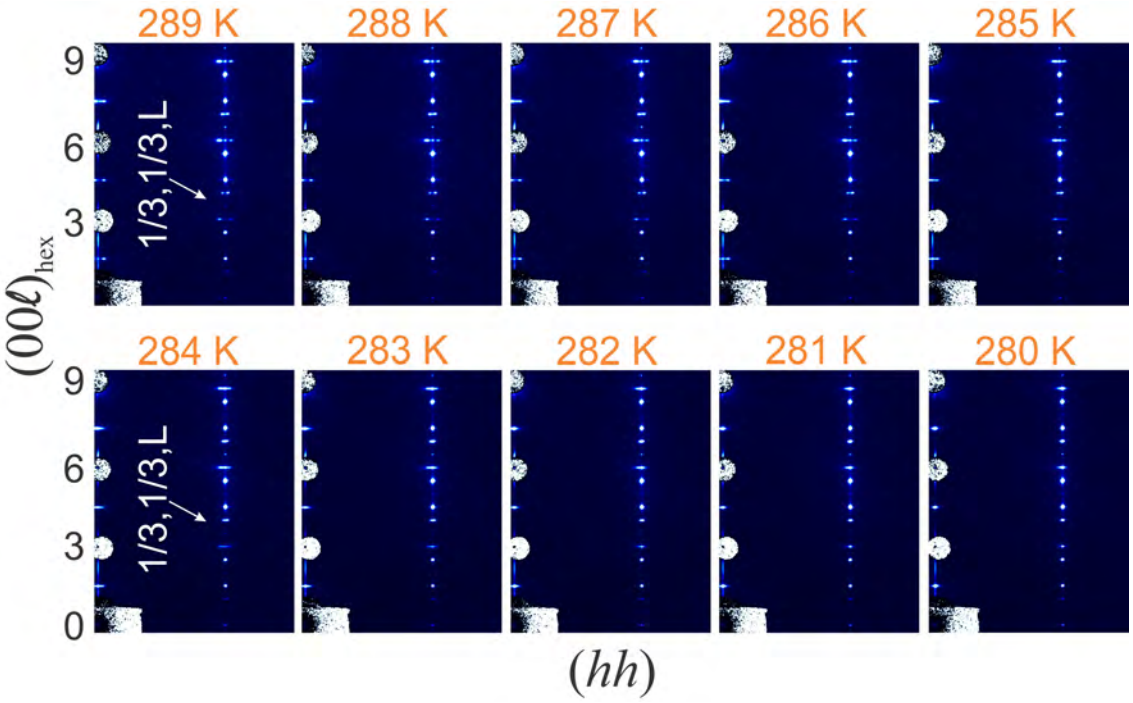

Figure 6.5: A set of progression images cut to show the $(\frac{1}{3}, \frac{1}{3}, \ell)$ line ($hh\ell$ plane) at decreasing temperature from 289 K to 280 K in 1 K steps.

Unlike $LuFe_2O_4$ which maintains the 3D incommensurate CO phase from its onset T_{inCO}=∼315 K down to low temperature, Type 2 $YbFe_2O_4$ samples exhibit a merging of the incommensurate peaks forming reflections at $\tau(\frac{n}{3}, \frac{n}{3}, \ell)$ and $\tau(0, 0, 3n + \frac{3}{2})$ in the hexagonal notation. This is shown clearly in Fig. 6.5 with a set of progression images of 1 K steps between 289-280 K. At 289 K the incommensurate τ positions are still well defined, but on cooling through to 285 K the peaks start to shift to the central peaks along $(\frac{1}{3}, \frac{1}{3}, \ell)$, before becoming completely commensurate below 280 K. Further analysis of this transition was performed using the same data used to plot the τ positions as a function of temperature in Fig. 6.4 (middle panel). The plots shown in Fig. 6.6 look at the integrated area as a function of temperature for two positions $(\pm\tau, \pm\tau, \frac{3}{2})$ (top panel) and $(\frac{1}{3}\pm\tau, \frac{1}{3}\mp 2\tau, 15)$ (bottom panel). In each case there are three plotted curves, the temperature dependence

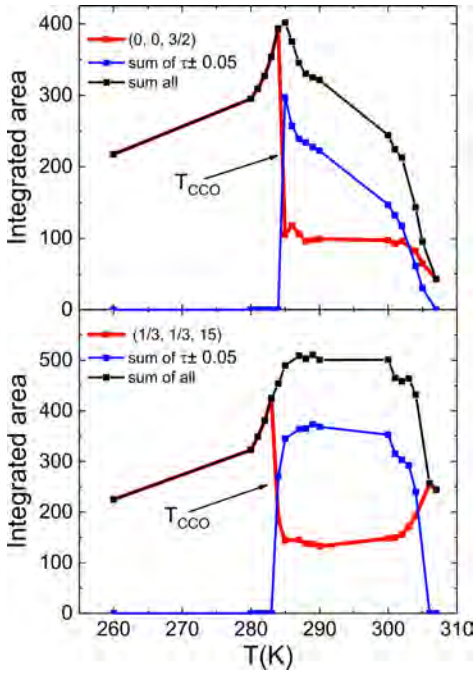

Figure 6.6: Integrated intensity as a function of temperature of the central peak intensity (red curve), the sum of $\tau \pm 0.05$ intensity (blue curve) and the sum of all intensities (black curve). Top: the $(0, 0, \frac{3}{2})$ reflection. Bottom: the $(\frac{1}{3}, \frac{1}{3}, 15)$ reflection.

tracking the central peak (red curve), the sum of τ (black curve) and the sum of both the central peak and τ positions. The intensity at the τ satellites above T_{CCO} are much higher than the central peak intensity above T_{CCO}, until the system reaches the commensurate phase transition, at which point the intensity of the incommensurate peaks shift to the central peak position. This is indicated in Fig. 6.6 (bottom), for the $(\frac{1}{3}\pm\tau, \frac{1}{3}\mp 2\tau, 15)$ position, where for the sum of intensity for the τ satellites (blue curve), drops to zero at T_{CCO}, but the intensity of the central peak $(\frac{1}{3}, \frac{1}{3}, 15)$ increases at the commensurate phase transition. For both selected positions, the sum of τ (blue curves) shows a clear first order phase transition with an extremely sharp increase in intensity that occurs at 284 K for $(\pm\tau, \pm\tau, \frac{3}{2})$ and 283 K for $(\frac{1}{3}\pm\tau, \frac{1}{3}\mp 2\tau, 15)$. These temperatures relate to the heat capacity shown in Fig. 6.4 (right panel), but not at the peak maximum, that is rather the onset, but more so coming down from the peak to lower temperatures. For the $(\frac{1}{3}\pm\tau, \frac{1}{3}\mp 2\tau, 15)$ position the sum of all peaks (black curve) fits almost perfectly with the central peak (red curve), and indicates that the intensity of the sum of τ positions merges to the central peak. This happens to some extent with the $(\pm\tau, \pm\tau, \frac{3}{2})$ position but the sum of all peaks is higher before the onset of T_{CCO}, as shown in Fig. 6.6 (bottom panel). One must note however, that there were some problems with peak saturation from the images obtained from the MAR imaging plate, therefore the extracted intensities are somewhat tentative. The question remains, do the lower temperature magnetic transitions, more specifically T_{LT}, affect for example the $(\frac{1}{3}\pm\tau, \frac{1}{3}\mp 2\tau, 15)$ position, as was the case for $LuFe_2O_4$?

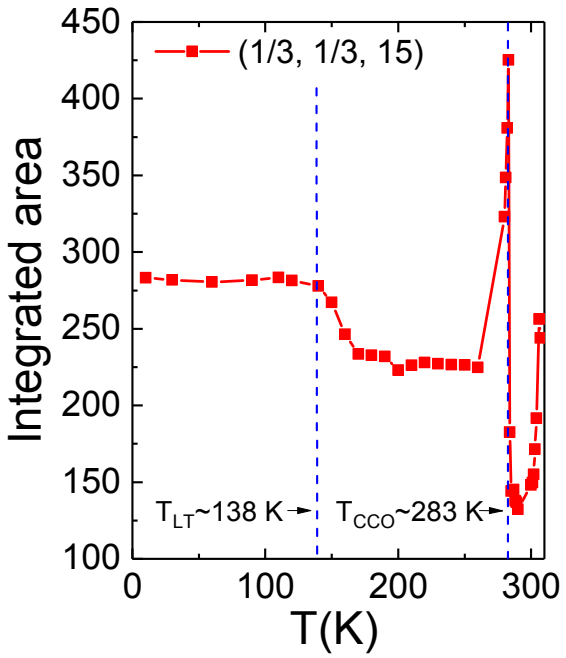

Figure 6.7: The integrated intensity as a function of temperature for the $(\frac{1}{3}, \frac{1}{3}, 15)$ reflection.

This would imply that it may be related to a magneto-structural transition [104]. Without refinement at this stage, one can look initially at the T-dependence of the central peak down to low temperature. A plot of the integrated area as a function of temperature in the range 310-10 K is shown in Fig. 6.7. There is no evidence of a feature related to the T_{c} transition at 260 K (see Sec. 5.1, Fig. 5.1, middle panel for AC susceptibility), the commensurate CO remains on a plateau in and around this temperature. This is quite different to $LuFe_2O_4$, which exhibits a broad dip around T_{N}, at this point the difference in τ becomes smaller. This feature in $LuFe_2O_4$, as mentioned in the previous section, is the spin order (SO), which is commensurate along ℓ, trying to drive the CO in the system from incommensurate to commensurate, an indication that the magnetic order maybe part of the driving mechanism for the CO in these two systems. The absence of this feature in $YbFe_2O_4$ is therefore no surprise as the system is already in a commensurate phase. There is, however, a distinct rise of intensity below 170 K seen in Fig. 6.7, for the onset of T_{LT} at 138 K, as was also

observed in $LuFe_2O_4$ (Fig. 6.4, middle panel). Below 138 K the intensity remains constant to 10 K. The metastable phase associated with low temperature transition, in which there are competing AFM and fM domains, could explain the intensity increase, due to the lack of stabilization of one phase. However, there are also other contributions that may play a role; for example, those indicated by the images provided in Fig. 6.8 (a) show the commensurate peaks at 210 K and 90 K, above and below T_{LT}. There is some notable deviation for example of the ($\frac{2}{3}$, $\frac{2}{3}$, -6) reflection at 90 K which is not present at 210 K (highlighted with white box) and is seen at half-integer positions along ℓ, relating to the same CO domain. This is likely attributed to slight structural distortions, where each reflection corresponds to a CO domain with different cell orientations. A plot of integrated intensity along ($\frac{1}{3}$, $\frac{1}{3}$, ℓ) at 300 (red curve), 210 (blue curve) and 90 K (black curve) is also shown in Fig. 6.8 (b).

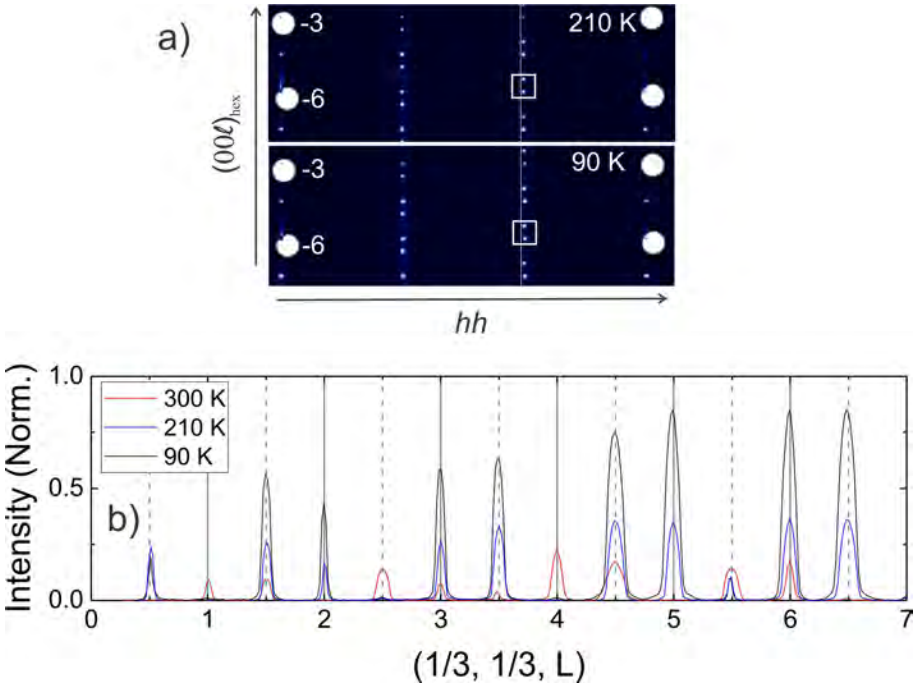

Figure 6.8: (a) Images of the $hh\ell$ plane at 210 and 90 K. White boxes and line show deviation of half-integer reflections at 90 K. (b) Vertical box integrations along ($\frac{1}{3}$, $\frac{1}{3}$, ℓ) of three temperatures 300 K (T_{inCO}), 210 K (in the T_{CCO} phase) and 90 K below T_{LT}. Spline background subtractions were performed for each dataset. Grey lines/dotted mark integer and half-integer positions, respectively.

Although there is no notable feature relating to the shift of the half-integer positions, it does show the peak intensity increasing on cooling to 90 K. This results from the combined intensity of the central peak seen in the incommensurate CO phase with the added intensity from the merging of the τ satellites below T_{CCO}. From this analysis, one can say that both the spin and charge ordering in $YbFe_2O_4$ is far more correlated than that in $LuFe_2O_4$, although they are closely related in terms of the ionic radius [33]. The slight difference in bilayer separation may explain why $LuFe_2O_4$ has slightly weaker correlations in both the CO and SO along **c**. Furthermore, had the magnetic correlations been stronger in $LuFe_2O_4$ perhaps even the observation of a spontaneous fM as seen in the magnetic phase diagram of $YbFe_2O_4$ (see Fig. 5.15, top panel), the incommensurate CO in this system could

well have been forced into a commensurate phase, as indicated by the drop in τ at T_N. Although both systems show an upturn and increased intensity at T_{LT}, only structural refinement of the CO phase at 200 K above and below T_{LT} at 90 K will elucidate whether this is a magneto-structural transition. This will test whether the system goes from a $C2/m$ to $P\bar{1}$ space group, as more recently proposed by [117] or the sudden increase in intensity stems from either competition between the magnetic domains or small structural distortions (lattice effects). It is also possible that it is really a combination of both. The following section covers briefly a refinement in the $R\bar{3}m$ space group at 300 K, before leading on to the sections for the CO refinements at 200 K and 90 K, respectively.

6.1.2 Crystal selection and measurement strategies

Expo Param.	Given value	Given value
T(K)	90 K	200 K
Resolution $Å^{-1}$	0.355	0.355
Laue group	1	1
Detector distance (mm)	70	70
complete redu. data	Yes	Yes
Lattice type	C lattice	P (primitive)
Scan width (°)	1	1
θ:-34 to 34	5s	20s
θ:-92 to 92	10s	60s
Redundancy	8	14
No runs	84	87
Total frames	5867	10388

Table 6.1: Experimental parameters used for the refinements at 200 and 90 K.

Single crystal x-ray diffraction measurements were performed for refinements at 300, 200 and 90 K on the same microgram size crystal as shown in Fig. 6.9. The selection of 200 K and 90 K for final refinement, is to elucidate if there is an intrinsic magneto-structural transition apparent below 138 K (see Fig. 5.1 (a)) in $YbFe_2O_4$, as was proposed in $LuFe_2O_4$ [104]. The crystal was selected from the boule grown in the $CO:CO_2$=1:2.5 atmosphere, where a part of it was smashed to look for small single crystals. As in the case for $LuFe_2O_4$, the search for a mono-domain sample (see Fig. 6.11, left panel) for final refinement, limits the search of structures to a k=($\frac{1}{3}$, $\frac{1}{3}$, $\frac{3}{2}$) propagation vector and in the process eliminates multi-k structures. An example of a crystal with multiple domains can be seen in the Type 3 class CO shown in Chapter. 4 Fig. 4.7. By conducting a number of short experiments (∼30 mins) on each candidate crystal, it was possible to determine if the crystal selected exhibited long-range CO. Long measurements spanning 3-4 days (see Sec. 3.7.3) were only performed at 90 K and 200 K, whereas the 300 K measurement was much shorter (see Sec. 6.2). The 90 K measurement was done first, as a reduced Debye waller factor

(largely apparent at 300 K) would aid refinements. The experimental strategies employed at 90 K and 200 K are shown in the table of Fig. 6.1.

As the first long measurement was performed at 90 K, some variables were altered for the later measurement at 200 K, for example the counting times in different theta ranges (for weaker reflections), the lattice type was changed to primitive P and the redundancy was almost doubled to 14. The latter helps for several reasons, it corrects for measurement outliers [205], improves confirmation of symmetry and data precision. All of these factors allow for an increased number of reflections (double the number of total frames). These changes were implemented to allow for a better refinement of the twin components due to lost symmetry and for a larger reciprocal space coverage. Although, as shown in the later sections detailing the refinement results at each temperature, it was only the twin components at 90 K which were effected due to a slight lack of data. For the integration at each temperature, certain prerequisite information was selected: for example, the Friedel mates were considered as equal for the purpose of outlier-rejection and no lattice extinctions were selected. The sample wobble and possible discontinuous movement of the sample during the experiment was also accounted for. The data set was integrated without incorporating the twin components and set so that a manual selection of the space group after the peak integration was possible. Once the peak integration was complete data reduction was performed as described in more detail in Sec. 3.8.1.

6.2 Single crystal x-ray diffraction at 300 K and the average $R\bar{3}m$ structure

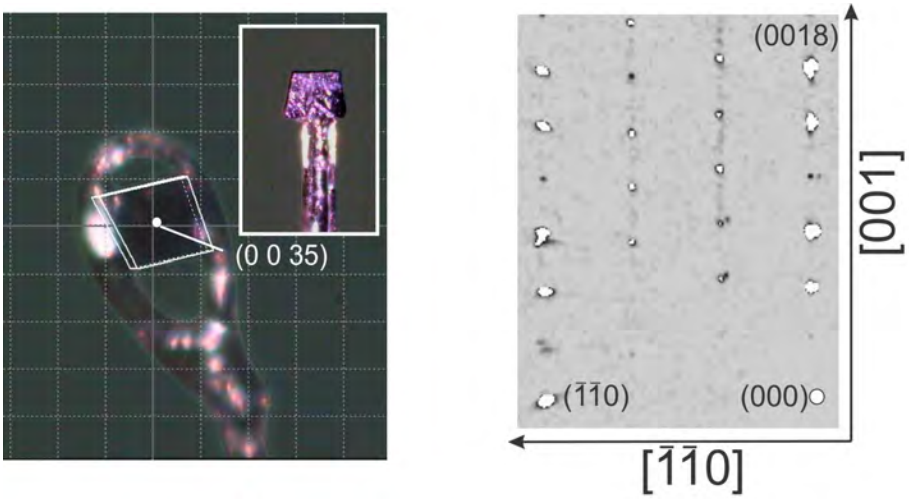

Figure 6.9: Left: $YbFe_2O_4$ single crystal mounted on a small loop holder fixed with vacuum grease with c_{hex} perpendicular to large shiny facet. Inset: same crystal remounted on thin glass rod again with $\mathbf{c}_{hex}$ perpendicular. Right: respective reciprocal space map obtained using the CrysalisPro software, of the $hh\ell$ plane ($R\bar{3}m$ space group) at 300 K.

Single crystal x-ray diffraction was performed at room temperature using the SuperNova diffractometer on a mono-domain-like sample (see Sec. 6.1.2), with MoK_α radiation (refer to Sec. 3.7.3). An image of the microgram-sized crystal is shown

in Fig. 6.9 (left) (see Sec. 3.7.3 for all experimental details). All acquired data was processed using CrysAlisPro and later refined using JANA2006. The crystal image shown in Fig. 6.9 (inset) depicts an alternative mounting method of the same crystal used for a measurement at 200 K, where instead of the loop and grease method the crystal was glued to the end of a very thin glass rod (see section 3.7.3). A reciprocal space precession image of the $hh\ell$ plane is shown in Fig. 6.9 (right), showing that it is already charge ordered, as expected. The final structure for $YbFe_2O_4$ at 300 K is shown in Fig. 6.10 (left). The anisotropic displacement parameters (ADP's) of the atoms are depicted as ellipsoids and the relative values obtained from the refinement are given in Table. 6.3. After distinct changes in stoichiometry at 360 K (described in Sec. 4.2.3), heating to 350 K for a refinement with only diffuse CO (which is omitted from the refinement) was too risky, as the sample was of high quality. Moreover, higher temperatures often provide increased risk of effects such as the Debye-waller factor, hampering the outcome of clean definitive structural solution. Therefore, a refinement was done at 300 K, but ignoring the CO reflections, in this case an average structure based on $R\bar{3}m$ symmetry was determined. The refinement at 300 K was achieved in the $R\bar{3}m$ space group, with 688 reflections (of which 110 were unique, redundancy ~6). Although, this was a short measurement, it provided a reasonable refinement factor of R=2.79 %, lower than those previously published [75, 117].

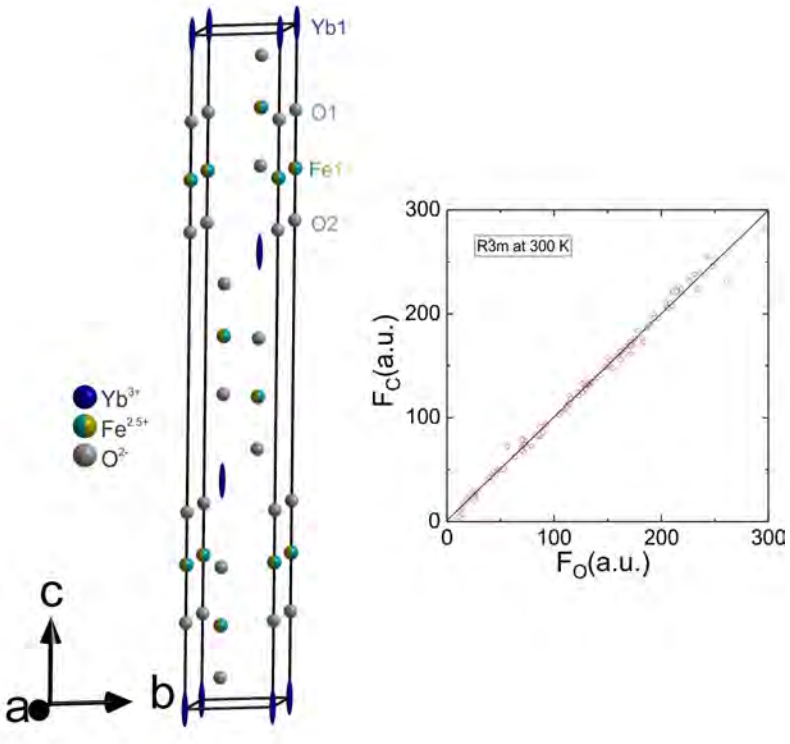

Figure 6.10: Left: $YbFe_2O_4$ structure refined at 300 K in the $R\bar{3}m$ space group. Bi-colouration of Fe site represents Fe^{2+} or Fe^{3+} mixed site valency. Right: plot of the calculated vs observed reflections used for this refinement.

Parameter	This work	Blasco *et al.*	Kato *et al.* [75]
Space group	$R\bar{3}m$	$R\bar{3}m$	$R\bar{3}m$
a (Å)	3.4635(8)	3.4575(1)	3.455(1)
c (Å)	25.216(4)	25.1098(1)	25.054(10)
V (Å^3)	261.96(10)	259.961(1)	259.00
R_{int}/R_σ (%)	9.82/1.62	R_p 8.8	
$R_{obs}/\mathrm{w}R_{obs}$ (%)	2.79/3.44	R_{Bragg} 4.7	
R_{all}/wR_{all} (%)	2.94/3.49	R_F 4.4	wR 5.6
GoF_{obs}/GOF_{all}	2.09/2.07		
N^o of reflections	688	Powder	2435
Calc. Density $\rho(g.cm^{-3})$	6.63	6.68	6.71

Table 6.2: Refinement parameters at 300 K. The definitions for powder R-values were obtained from [206] for comparison with the single crystal values.

This is further complemented by the good match between the observed vs calculated structure factors (Fo vs Fc) shown in Fig. 6.10 (right). The goodness of fit (see Sec. 3.8.2) GoF_{obs}=2.09 on the other hand, was slightly higher than the ideal value of 1. There is common twining possibility in the rhombohedral compounds, corresponding to 180° rotation around the **c**-axis: this implies different centerings called "obverse and reverse", leading to different reflection conditions. Switching between each setting can be described by a matrix transformation corresponding to a two-fold rotation around the threefold axis [207]. Obverse/reverse twinning was not found in the refinements. A list of the obtained parameters from this refinement are shown in Table. 6.2. Comparison with published room temperature refinement results (within $R\bar{3}m$) by [117] using powder and [75] on a single crystal are also included in the table. Both **a** and **c** lattice parameters from this work are slightly larger than those previously published. The small difference seen in the lattice parameters from this work and those by [75, 117] are most likely attributed off-stoichiometry, with excess or deficient oxygen. A strong indication of off-stoichiometry in $YbFe_2O_4$ is seen in [117] on ZFC-FC magnetization curves, both of which exhibit a broad transition at T_N=252 K. Although this temperature is close to that observed in highly stoichiometric $YbFe_2O_4$ from this work (see Sec. 4.2.1, Fig. 4.3), the characteristics of the curves are similar to that shown in Fig. 4.5 (Sec. 4.2.1) on a 60 mg crystal used for diffuse neutron scattering at DNS, and presented only 2D CO correlations. Due to the symmetry restrictions of the $R\bar{3}m$ space group only two of the anisotropic displacement parameters (ADP) are independent, namely U11 and U33 (shown in Table. 6.3) the remaining 4 parameters are given in the following relations: U13=U23=0, U11=U22 and 2*U12=U11 [208]. Some of the ADP values published by [75] are unrealistically small, and do not always correlate with those obtained in this work. Regardless, the refinement statistics obtained in this work, in particular R_{obs}=2.79 %, and GoF_{obs}=2.09 % are reasonable. The comparison of lattice parameters to [117] and [75] show that in each case our refined **a** and **c** have larger values as shown in Table. 6.2. The slight difference in values are likely attributed to the effects of oxygen stoichiometry, where the values published by [117] were refined on

more off-stoichiometric $YbFe_2O_4$, based on their $M(T)$ measurement.

Atom (Wyck.)	Param.	this work	[75]	Atom	Param.	this work	[75]
Yb (3a)	Z	0	0	Fe (6c)	Z	0.21477(99)	0.2150(1)
	U11	0.0013(6)	0.0096(2)		U11	0.0094(9)	0.0035(7)
	U33	0.0392(9)	0.00148(5)		U33	0.0091(12)	0.00029(19)
O1 (6c)	Z	0.12810(69)	0.2925(3)	O2 (6c)	Z	0.29212(43)	0.1292(5)
	U11	0.022(5)	0.0054(2)		U11	0.0051(35)	0.0108(5)
	U33	0.028(7)	0.000241(1)		U33	0.0083(49)	0.00114(2)

Table 6.3: Anisotropic displacement parameters at 300 K. The conversion from β to U ADP parameters from [75] is shown in Appendix. A.3.

The elongation of Yb ellipsoids, pictured in Fig. 6.10 (left), stems from the CO crystal structure, which involves particularly large vertical displacements of Yb (see Sec. 6.6). As a refinement was performed in the averaged ($R\bar{3}m$) structure, the corresponding splitting of Yb positions is not included. When left un-split, the refined ADP ellipsoid elongates as a best approximation of the splitting. This feature also occurs in samples with no long-range CO (off-stoichiometric) as shown in the refinement at 350 K in [26], the elongated ellipsoids are still present indicating the same CO-distortions, but in this case only short-range, as seen also by the diffuse lines. This is not limited to Lu and Yb, but also observed in YFe_2O_4 refinements, and therefore intrinsic to the charge ordered structure [111].

6.3 What is the correct structure at 200 K?

The new discovery of the commensurate CO phase observed in Type 2 samples below 280 K, has brought to light overlooked aspects of the original $LuFe_2O_4$ structural refinement by [48], which now needs to be reassessed based on this new knowledge. As described in the sections above, the presence of this new CO phase indicated that there was in fact strong intensity at integer positions along **c** in both the hexagonal and monoclinic notation. Two reciprocal space maps obtained from single crystal diffraction using the SuperNova are shown in Fig. 6.11 on $LuFe_2O_4$ (left) (210 K) taken from [48] and $YbFe_2O_4$ (right) (200 K), the same crystal used for all the refinements performed beyond this point. As one can see, only weak intensity is observed at the incommensurately modulated CO peaks in $LuFe_2O_4$ along $(\frac{n}{3}, \frac{n}{3}, \ell)$ ($\mathbf{c}_{hex}$), for example at $(\frac{1}{3}, \frac{1}{3}, 9)$. The most intense peaks as previously reported are seen at half-integer positions along ℓ. This is quite contrary to $YbFe_2O_4$, which exhibits stronger peak intensity at both integer and half-integer positions (see previous sections). In the following, the $C2/m$ charged bilayer structure suggested for $LuFe_2O_4$ at 210 K, will first be tested against the data collected on the $YbFe_2O_4$ crystal at 200 K.

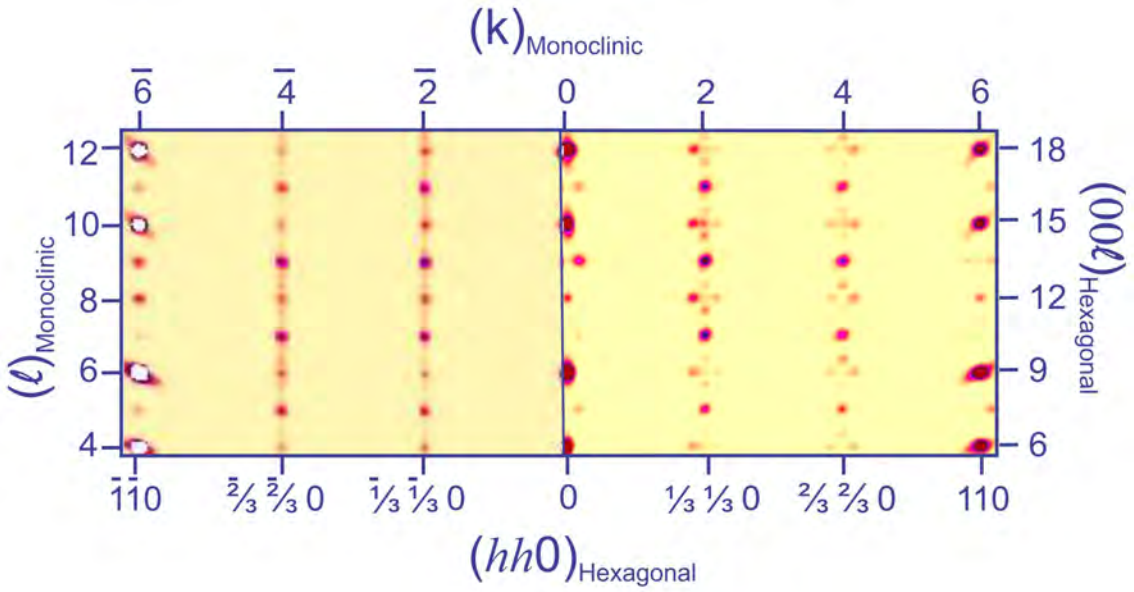

Figure 6.11: Composite reciprocal space maps with scales of both monoclinic and hexagonal axes. Left: $YbFe_2O_4$ at 200 K and right: $LuFe_2O_4$ at 210 K. Image for $LuFe_2O_4$ was taken from [48] and adapted. Blue line down the middle of the image indicates separation of the two different images.

6.3.1 Tested $C2/m$ structures solutions at 200 K

To ascertain the possible structure solutions in a subgroup of $R\bar{3}m$, it is essential to view the likely irreducible representations (IR's) (see Sec. 6.6) based on specifically selected k-points. In terms of the studies conducted previously on $LuFe_2O_4$ by [48] and [117], also our current work on $YbFe_2O_4$, the number of k-points used to describe the structural possibilities in all cases was limited to the use of a Y1 or Y2-mode, thus a $(\frac{1}{3}, \frac{1}{3}, \frac{3}{2})$ propagation. As mentioned in Sec. 6.1.2 the use of a mono-domain sample eliminates multi-k structures, which involve more than one propagation vector related by symmetry. In the majority of cases, the CO reflections could be described by solutions obtained from either a Y1 or Y2 mode; for instance, the final $C2/m$ structural solution published by [48] corresponds to a Y2(0,a;0,0;0,0) mode, and established that when the centre of inversion lies between the Fe bilayers, a better final R-value was obtained. Not only this, but the BVS and XMCD results further supported the final CO superstructure of charged bilayers. Despite of this and during the evaluation process, structural solutions from both Y1 and Y2-modes were tested during investigations by [48] and [117]. Earlier work by [106], which presented an antiferroelectric configuration in the ground state using a combination of synchrotron x-ray scattering

Order param.	SG	Origin
Y1(a,0;0,0;0,0)	$C2/m$	(0, 0, 0)
Y1(0,a;0,0;0,0)	$C2/c$	$(-\frac{2}{3}, -\frac{5}{6}, \frac{1}{6})$
Y1(a,b;0,0;0,0)	$C2$	(0, 0, 0)
Y2(a,0;0,0;0,0)	$C2/c$	$(-\frac{5}{6}, -\frac{2}{3}, \frac{1}{3})$
Y2(0,a;0,0;0,0)	$C2/m$	$(-\frac{4}{3}, -\frac{5}{3}, -\frac{1}{6})$
Y2(a,b;0,0;0,0)	$C2$	$(-\frac{3}{4}, -\frac{3}{4}, \frac{1}{2})$

Table 6.4: Structure solutions based on symmetry analysis of Y1 and Y2-modes with propagation vector $(\frac{1}{3}, \frac{1}{3}, \frac{2}{3})$ obtained from the ISOTROPY software suite [209]. The basis for each solution is identical and given by (-1, 1, 0), (-3, -3, 0), $(\frac{1}{3}, -\frac{1}{3}, \frac{2}{3})$. Space group is shortened to (SG).

(without structural refinement) and DFT calculations, even at this early stage, determined that a lowering of space group symmetry at least to $C2/m$ would result, due to the CO superstructure reflections [62]. The key now is to ascertain if one of these structural possibilities holds true for $YbFe_2O_4$ with the additional observation of intense reflections at integer positions in $\mathbf{c}_{hex}$.

Representation analysis using ISODISTORT [210] from the ISOTROPY software suite [209] allows one to upload a structure CIF file and simulate possible structure solutions given the k-point and propagation vector. A single propagation vector at point Y1(a, a, $\frac{1}{3}$) $a = \frac{1}{3}$, provides 3 possible IR's as shown in Table. 6.4. The first two IR's Y1(a,0;0,0;0,0) and Y1(0,a;0,0;0,0) are the lowest order parameters and provide space group possibilities of $C2/m$ and $C2/c$, respectively. A third structural solution can be achieved when combining these two, and results in a more complex order parameter, Y1(a,b;0,0;0,0) and space group $C2$. These IR's in terms of the specific Y2-mode are also displayed in Table. 6.4, the main difference besides the $C2/m$ and $C2/c$ being in reverse in terms of order parameter to Y1, the origins of each structure solution are also vastly different. Although refinements of all possible IR's have been tested, focus is placed on the $C2/m$ structural refinements in relation to $LuFe_2O_4$, for the additional refinements of the lower symmetry monoclinic space groups, please refer to Appendix. A.4.

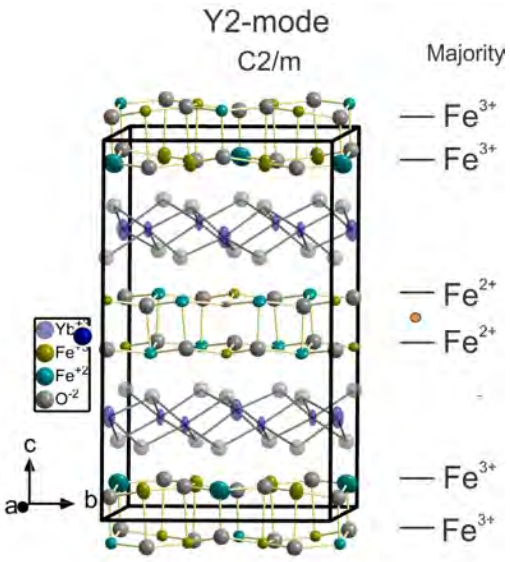

Figure 6.12: Structural representation of $C2/m$. The overall charge of each iron layer is depicted by a line and respective Fe valence, presenting charged bilayers. The orange dot next to the centre represents the point of inversion.

For comparison to the structures investigated previously on $LuFe_2O_4$ [48], two symmetries of the $C2/m$ space group were primarily investigated, the first with the inversion centre between the Fe bilayers (Y2-mode), shown in Fig. 6.12, this was the natural structural solution produced by the refinement program and also corresponds to the model proposed by [48]. Later a forced refinement was attempted with the inversion centre at the Yb layer (Y1-mode), the CIF was obtained from the Y1-mode decomposition from the uploaded parent CIF file to the isodistort website [1]. The refinement of the $C2/m$ (Y1) with the inversion centre at the Yb layer which corresponds to the antiferroelectric CO proposed in [106] was not possible. The best refinement values achievable for R_{obs} and GoF_{obs} in this symmetry was R_{obs}= 71.85 % and GoF_{obs}=22.30 %, respectively, and therefore not included in the detailed discussion. The best refinement values of

[1]The specific CIF file selected for symmetry analysis was the refinement conducted at 300 K shown in Sec. 6.2. At this temperature the diffraction data was refined in the $R\bar{3}m$ space group. It can then be uploaded to the ISODISTORT website and based on the symmetry restrictions, a list of possible subgroups are produced. From here it is easy to look over all k-points for the most reasonable lower symmetry structural solutions.

all the space groups tested (see Appendix. A.4 for lower symmetry monoclinic structures) was that with the inversion centre between the Fe bilayers, with a final R_{obs}=9.63 %, closely followed by the refinement in $C2$ R_{obs}=9.45 %. The C2 (Y2-mode) was excluded as a possible candidate as the oxygen atoms could only be refined isotropically, an indication that the space group symmetry is wrong, based on the observed reflections and the GoF_{obs}=4.14 is also quite above the ideal value of 1 (see Table. 6.13 in Appendix. A.4.1). The remaining structures tested from single Y1 and Y2 modes provided in Appendix. A.4, show much poorer refinement statistics and were therefore omitted as potential structures. The $C2/m$ symmetry with the inversion centre at Fe-bilayer also yielded the same CO arrangement as that previously published on $LuFe_2O_4$ [48], when using the bond valence sum (BVS) calculated in the refinement program. The BVS for each iron atom from this refinement is shown in Fig. 6.13 (right table). Although this particular $C2/m$ symmetry was refined, providing the same CO pattern as that obtained previously on $LuFe_2O_4$, the final R-factor was much higher for $YbFe_2O_4$ with R_{obs}=9.63 %, compared to R_{obs}=5.96 % from [48]. Furthermore, the goodness of fit obtained for this $C2/m$ symmetry was very high (GoF_{obs}=6.25), much larger than that obtained for the refinement of the $LuFe_2O_4$ with GoF_{obs}=1.11 [26].

Parameter	Y1-$C2/m$	Y2-$C2/m$
R_{int}/R_{σ} (%)	49.26/1.98	9.94/1.62
R_{obs}/wR_{obs} (%)	71.85/91.62	9.63/25.66
R_{all}/wR2$_{all}$ (%)	72.13/97.91	9.81/25.82
GoF_{obs}/GOF_{all}	22.30/21.97	6.25/6.19
Uniq. ref (obs/all)	6855/7211	11766/12344
Neg. ADPs	Fe1,3,O2,4,5,7	No
Neg. Twins	No	No
Giso	25.97	0.11

Site	$C2/m$ (Y2)
Fe1	2.99(3) (3+)
Fe2	2.241(15) (2+)
Fe3	2.52(3) (3+)
Fe4	2.16(2) (2+)

Figure 6.13: Left: refinement parameters obtained for individual Y1 and Y2 mode structure solutions at 200 K. Right: the calculated BVS of all each Fe-sites from the $C2/m$.

These two factors alone indicate that this particular symmetry is not correct to explain the overall structure of $YbFe_2O_4$. The question is, why? One can find an explanation when comparing the observed (red line and symbols) and calculated (blue line and symbols) intensities given in Fig. 6.14 of reflections along ($\frac{1}{3}$, $\frac{1}{3}$, ℓ), from the refinement of $YbFe_2O_4$ in the $C2/m$ space group. The two plots show that the $C2/m$ model greatly underestimates the intensities of many of the CO superstructure reflections.

The relative intensities of the integer ℓ reflections at room temperature on both $YbFe_2O_4$ and $LuFe_2O_4$ in the incommensurate phase are similar, $LuFe_2O_4$ does not go to a commensurate phase. It is the addition of the intensity from the merging of $\pm\tau$ peaks in $YbFe_2O_4$ which gives a higher intensity of integer reflections, picked up in the integration and included in the refinement. That being said, even with the increased intensity of integer reflections from the commensurate CO in $YbFe_2O_4$, the underestimated intensity for the calculated reflections shows that this structure

is incorrect. In terms of $LuFe_2O_4$, as the majority of the intensity lies at the incommensurate τ positions, and the refinement was performed in a commensurate approximation [48] it is likely that during the integration process of the data, the intensity of these types of reflections was systematically underestimated, implying the $C2/m$ structure does not hold for this system either. When the initial refinement of $LuFe_2O_4$ was published, only space groups resulting from single Y1 and Y2 modes were considered.

And as a result a final structural solution of a $C2/m$ space group with inversion symmetry at the Fe bilayer was presented [48]. This refinement for the time provided the best R-values of all the possible IR's of that subgroup and additionally an alternative view on the CO configuration of charged bilayers, compared to the previous thoughts and opinions that $LuFe_2O_4$ was the first ferroelectric compound though CO [63]. As none of these higher symmetry Y1 and Y2 IR's provide clear and definitive structural solutions for $YbFe_2O_4$ and $LuFe_2O_4$, it is now time to address the possibilities of further symmetry reduction, by using a combination of Y1 and Y2 modes.

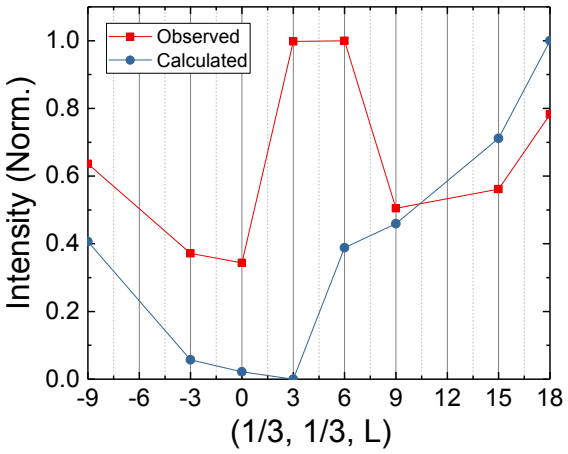

Figure 6.14: Observed (red squares) and calculated (blue circles) intensities along $(\frac{1}{3}, \frac{1}{3}, \ell)$ in the $C2/m$ space group.

6.3.2 Is lower symmetry is the answer?

Order param. Y1+Y2	SG	Origin	Basis
(a,0;0,0;0,0|b,0;0,0;0,0)	$P\bar{1}$	(0,0,0)	(1,-1,0),(2,1,0),($\frac{1}{3}$,-$\frac{1}{3}$,$\frac{2}{3}$)
(0,a;0,0;0,0|b,0;0,0;0,0)	Cc	(-$\frac{5}{6}$,-$\frac{2}{3}$,$\frac{1}{3}$)	(-1,1,0),(-3,-3,0),($\frac{1}{3}$,-$\frac{1}{3}$,$\frac{2}{3}$)
(a,0;0,0;0,0|0,b;0,0;0,0)	Cm	(0,0,0)	(-1,1,0),(-3,-3,0),($\frac{1}{3}$,-$\frac{1}{3}$,$\frac{2}{3}$)
(0,a;0,0;0,0|0,b;0,0;0,0)	$P\bar{1}$	(0,0,$\frac{1}{2}$)	(1,-1,0),(2,1,0),($\frac{1}{3}$,-$\frac{1}{3}$,$\frac{2}{3}$)
(a,b;0,0;0,0|c,d;0,0;0,0)	$P1$	(0,0,0)	(1,-1,0),(2,1,0),($\frac{1}{3}$,-$\frac{1}{3}$,$\frac{2}{3}$)

Table 6.5: Structure solutions based on symmetry analysis from the ISOTROPY software suite [209] for a combined Y1 and Y2 mode. SG=spacegroup.

For the current understanding of both $YbFe_2O_4$ and $LuFe_2O_4$, the need to look at lower symmetry structure solutions is key. The paper published by Blasco *et al.* [117], a short time after the proposed charged bilayers in $LuFe_2O_4$ by [48], conducted a temperature dependent study on $YbFe_2O_4$ and $LuFe_2O_4$ powder using high resolution x-ray diffraction. They reported that in the case of the $LuFe_2O_4$ there are two structural transitions, the first of which goes from $R\bar{3}m$ to $C2/m$ in the temperature range 325 K$\sim$175 K. They described this type of transition as a result

of condensing modes which belong to the Y2 mode IR. Below the typically stated magneto-structural transition at 175 K [104] they reported a second transition from $C2/m$ to the triclinic $P\bar{1}$. This lower symmetry space group can only be deduced using a combination of 2 IR's namely a Y1 and a Y2 mode. While the reports from this paper highlight an alternative structure at low temperatures for $LuFe_2O_4$, compared to previous reports, there are a number of structures which have been omitted from symmetry analysis, based on this combination.

Symmetry analysis using a combination of Y1 and Y2 modes have been included in Table. 6.5. Similarly, as for the individual Y1 and Y2 IR's and resultant monoclinic structures, the lower symmetry Cc and Cm structures did not provided viable structural solutions (discussed in more detail in Appendix. A.4.2). Although the latter Cm structure has a lower R_{obs}=7.57 %, compared to the refinement of the $C2/m$ with inversion centre at the Fe bilayer (R_{obs}=9.63 %), three of the twin components due to lost symmetry were not possible to refine and the GoF_{obs}=3.44 % is still high to consider this a reasonable structural model (see Table. A.3). The remaining structures left to investigate are the two in the lowest symmetry triclinic space groups, namely the $P\bar{1}$ and $P1$ structures. From the symmetry analysis obtained from the ISOTROPY software suite [209], three structures are provided (see Table. 6.5). In the case of the $P\bar{1}$, two settings are possible, one with the origin (0, 0, 0) with the Yb-O layer at the inversion centre and the second with the origin at (0, 0, $\frac{1}{2}$) with the Fe bilayer at the inversion centre, and lastly the $P1$. As previously described, three twin components are obtained by going from the rhombohedral $R\bar{3}m$ to monoclinic $C2/m$ and $C2/c$ (see Appendix. A.4.1 for refinement) due to lost symmetry elements. These account for the loss of the 3-fold roto-inversion (120° twinning) symmetry. On further reduction of the symmetry to $C2$, Cm, Cc (see Appendix. A.4.2 refinements) and $P\bar{1}$, six twin components are required to refine the structure. These particular lost symmetry elements stem again from the 3-fold rotation, but now also the loss of the 2-fold (180° twinning) rotational symmetry.

6.3.3 Representation analysis and basis transformations for the triclinic space group

The matrix transformations required to go from a higher symmetry space group to a lower symmetry space group, can for example be done using the basis' shown in Table. 6.5. The transformation from the $R\bar{3}m$ to the $P\bar{1}$ space group can be described by the following basis transformation matrix **M** and origin shift **O**:

$$P\bar{1}: \qquad \mathbf{M} = \begin{pmatrix} 1 & -1 & 0 \\ 2 & 1 & 0 \\ \frac{1}{3} & -\frac{1}{3} & \frac{2}{3} \end{pmatrix} \quad \text{and} \quad \mathbf{O} = \begin{pmatrix} 0 \\ 0 \\ 0 \end{pmatrix} \text{ or } \begin{pmatrix} 0 \\ 0 \\ \frac{1}{2} \end{pmatrix} \tag{6.1}$$

The two different origins obtained from the symmetry analysis of the combined Y1 and Y2 modes are stated in Table. 6.5. The basis used for the $P1$ structure is identical to the $P\bar{1}$, however as this space group lacks the inversion symmetry, the origin in this case is arbitrary. The basis vectors **a**, **b**, **c** of the original lattice can be transformed into the new basis **a**′, **b**′, **c**′ vectors of the new cell via a linear

transformation:

$$\begin{pmatrix} a' \\ b' \\ c' \end{pmatrix} = \mathbf{M} \cdot \begin{pmatrix} a \\ b \\ c \end{pmatrix} \tag{6.2}$$

This expression in terms of the Miller indices is identical as they are covariant. When considering the reciprocal lattice vectors, they are transformed by the inverse of the original matrix:

$$\begin{pmatrix} \mathbf{a}^* \\ \mathbf{b}^* \\ \mathbf{c}^* \end{pmatrix} = \mathbf{P} \cdot \begin{pmatrix} \mathbf{a}^{*'} \\ \mathbf{b}^{*'} \\ \mathbf{c}^{*'} \end{pmatrix} \qquad \mathbf{M}^{-1} = \begin{pmatrix} \frac{1}{3} & \frac{1}{3} & 0 \\ -\frac{2}{3} & \frac{1}{3} & 0 \\ -\frac{1}{2} & 0 & \frac{3}{2} \end{pmatrix} \tag{6.3}$$

The term $\mathbf{P}$ is derived from the reciprocal lattice vectors which are transformed by the inverse of the matrix, $\mathbf{P} = \mathbf{M}^{-1}$. One should be aware that these transformation rules also apply to the quantities covariant with respect to the reciprocal basis vectors $(\mathbf{a}^*, \mathbf{b}^*, \mathbf{c}^*)$ and contravariant with respect to the direct lattice vectors $(\mathbf{a}, \mathbf{b}, \mathbf{c})$ which, are written as column matrices in Eqn. 6.2. This transformation rule is also valid for the directions in direct space, namely (u, v, w). However, unlike the reciprocal space transformation, the affine transformation of coordinates (x, y, z) is affected by an origin shift $(\mathbf{O})$ in direct space [211]:

$$\begin{pmatrix} x' \\ y' \\ c' \end{pmatrix} = \mathbf{P} \cdot \begin{pmatrix} x \\ y \\ z \end{pmatrix} - \mathbf{O} \tag{6.4}$$

For a matrix using the basis vectors $(\mathbf{a}^*, \mathbf{b}^*, \mathbf{c}^*)$ written in Eqn. 6.3, a transformation is performed by the inverse of $\mathbf{M}^{-1}$ given as $\mathbf{M}^{-1} \cdot \mathbf{M} = 1$ (see Eqn. 6.3) and its transpose $[\mathbf{M}^{-1}]^t$:

$$\begin{pmatrix} \mathbf{a}^{*'} \\ \mathbf{y}^{*'} \\ \mathbf{c}^{*'} \end{pmatrix} = [\mathbf{M}^{-1}]^t \cdot \begin{pmatrix} \mathbf{a}^* \\ \mathbf{b}^* \\ \mathbf{c}^* \end{pmatrix} \tag{6.5}$$

This transformation rule is also valid for co-ordinates in real space. Going from $R\bar{3}m$ to $P\bar{1}$, 3-fold rotation symmetry, which is a 120° twining around $\mathbf{c}_{hex}$ and $||\mathbf{c}^*$ is the first lost symmetry element (twin, **Tw**). The transformation to the Miller indices that describe the triclinic cell (see Eqn. 6.4) for a respective twin components can be written as:

$$\begin{pmatrix} h_t \\ k_t \\ l_t \end{pmatrix} = \mathbf{Tw}_i \cdot \begin{pmatrix} h \\ k \\ l \end{pmatrix} \tag{6.6}$$

Here i is a an element of real numbers $i \in 1, 2, 3, 4...$ and this transformation can be completed for calculating any twin component which would arise through lost symmetry. Using the above relation and the required rotational matrix that

describes the 120° twinning around $\mathbf{c}_{hex}$ Eqn. 6.6 can be written as;

$$R_{120^\circ} = \begin{pmatrix} \frac{1}{3} & \frac{1}{3} & 0 \\ -\frac{2}{3} & \frac{1}{3} & 0 \\ -\frac{1}{2} & 0 & \frac{3}{2} \end{pmatrix}, \quad \text{and thus} \quad \begin{pmatrix} h_t \\ k_t \\ l_t \end{pmatrix}_{tric} = \mathbf{R}_{120^\circ} \cdot \begin{pmatrix} h \\ k \\ l \end{pmatrix} \tag{6.7}$$

When viewing the **c**-axis of each structure both in the $R\bar{3}m$ and $P\bar{1}$, they all align parallel to $\mathbf{c}_{hex}$ such that $\mathbf{c}_{hex}$=$||\mathbf{c}^*_{hex}||\mathbf{c}^*_{tric}$ [111]. In this case it a direct relation of the ℓ co-ordinates given in the triclinic basis matrix shown in Eqn. 6.8:

$$\begin{pmatrix} 0 \\ 0 \\ 1 \end{pmatrix}_{hex} = \begin{pmatrix} \frac{1}{3} \\ -\frac{1}{3} \\ \frac{2}{3} \end{pmatrix}_{tric} \tag{6.8}$$

The second lost symmetry element to consider is the 2-fold rotation (mirror plane) that incorporates additional 180° rotations around $[100]_{hex}$,$[110]_{hex}$, $[010]_{hex}$. The direct translation to the triclinic setting for each of the three rotations is thus:

$$\begin{pmatrix} 1 \\ 0 \\ 0 \end{pmatrix}_{hex} = \begin{pmatrix} \frac{1}{3} \\ -\frac{1}{3} \\ 0 \end{pmatrix}_{tric}, \quad \begin{pmatrix} 0 \\ 1 \\ 0 \end{pmatrix}_{hex} = \begin{pmatrix} -\frac{2}{3} \\ \frac{1}{3} \\ 0 \end{pmatrix}_{tric}, \quad \begin{pmatrix} 1 \\ 1 \\ 0 \end{pmatrix}_{hex} = \begin{pmatrix} -\frac{1}{3} \\ \frac{2}{3} \\ 0 \end{pmatrix}_{tric} \tag{6.9}$$

When combining all these lost symmetry elements, a resultant 6 twin domains need to be incorporated into the final refinement. The order in which the 180° twin is input into Jana2006, will change the resultant twin configuration in terms of which one represents which lost symmetry element. In the case of all the refinements in this thesis, order and twin components are given by:

$$\mathbf{Tw1} = \begin{pmatrix} 1 & 0 & 0 \\ 0 & 1 & 0 \\ 0 & 0 & 1 \end{pmatrix}_{tric} \quad \mathbf{Tw2}^{180^\circ} = \begin{pmatrix} 0 & 1 & 0 \\ 1 & 0 & 0 \\ \frac{1}{3} & \frac{1}{3} & -1 \end{pmatrix}_{tric}$$

$$\mathbf{Tw3}^{120^\circ} = \begin{pmatrix} 0 & -1 & 0 \\ 1 & -1 & 0 \\ -\frac{1}{3} & -\frac{1}{3} & 1 \end{pmatrix}_{tric} \quad \mathbf{Tw4}^{240^\circ} = \begin{pmatrix} 0 & -1 & 0 \\ 1 & -1 & 0 \\ -\frac{1}{3} & -\frac{1}{3} & 1 \end{pmatrix}_{tric}$$

$$\mathbf{Tw5}^{180^\circ} = \begin{pmatrix} 1 & -1 & 0 \\ 0 & -1 & 0 \\ \frac{2}{3} & -\frac{1}{3} & -1 \end{pmatrix}_{tric} \quad \mathbf{Tw6}^{180^\circ} = \begin{pmatrix} -1 & 0 & 0 \\ -1 & 1 & 0 \\ 0 & 0 & -1 \end{pmatrix}_{tric}$$

Twin 1 is the first twin at 0° (identity matrix) of the 3-fold rotation, twin 2 and twin 3 are the 120°, and 240° rotation around $\mathbf{c}_{hex}$, respectively. The remaining

twins form the second lost symmetry element of the 180° 2-fold axis. In this case twin 2 ($[1\ 1\ 0]_{hex}$) is the first 180° rotation about twin 1, and the remaining twins 5 and 6, were obtained by multiplying twin 3 and 4 with twin 2 to form the final lost symmetry 2-fold rotations.

6.3.4 Structural refinement of $P\bar{1}$ at 200 K

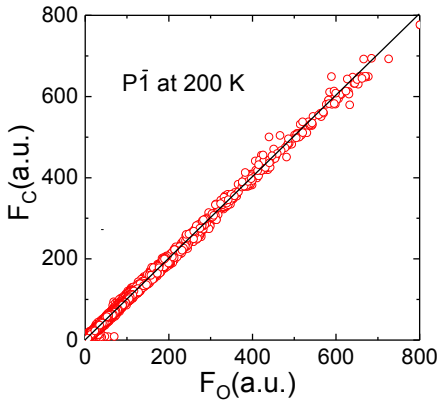

Parameter	This work	
Space group	$P\bar{1}$	$P\bar{1}$
Origin	(0, 0, 0)	(0, 0, $\frac{1}{2}$)
R_{int}/R_{σ} (%)	8.01/2.03	8.01/2.03
$R_{obs}/wR2_{obs}$ (%)	4.71/11.72	8.91/23.37
R_{all}/wR_{all} (%)	4.95/11.90	9.20/23.58
GoF_{obs}/GOF_{all}	2.38/2.34	4.73/4.62
Uniq. ref. obs/all	17363/18467	17363/18467
Parameters	199	191

SG	a (Å)	b (Å)	c (Å)	α(°)	β(°)	γ(°)
$P\bar{1}$ (0,0,0)	5.982(2)	5.986(1)	16.877(4)	86.556(9)	83.1680(1)	59.962(5)
$P\bar{1}$ (0,0,$\frac{1}{2}$)	5.982(1)	5.986(1)	16.877(4)	86.556(9)	83.1680(1)	59.962(5)

Figure 6.15: Tables of refinement for both $P\bar{1}$ structures. Left: a plot of the observed vs calculated intensities for $P\bar{1}$ (0,0,0). Right: obtained refinement parameters and below the lattice parameters.

The mono-domain crystal (see Sec. 6.1.2) used for all refinements made it possible to integrate the peaks solely within Twin 1. A structural solution was in each case performed using SIR2014 [167] (refer back to Sec. 3.8.2 for more details), which is integrated into the Jana2006 software and used instead of the internal super-flip. As with all the refinements conducted in this thesis, the large set of reflections were processed into a *hkl* file using the CrysalisPro software [163], a readable format for Jana2006. In order to obtain the most reflections for refinement, either the $P1$ or $P\bar{1}$ space-group was selected in CrysalisPro and later merged depending on the symmetry of the structure being refined.

The final refinement parameters obtained for each of the $P\bar{1}$ refinements (each with a different origin) are shown in Fig. 6.15, with an additional plot of the calculated vs observed (F_c vs F_o) reflections (left) for the $P\bar{1}$ (0,0,0) refinement, which exhibits no major outliers. Initial focus shall be placed on the $P\bar{1}$ refinement with the shifted origin (0, 0, $\frac{1}{2}$) as this is not a candidate structure due to a number of factors which will now be addressed. In terms of acceptable refinement parameters, all atoms except the O7 atom were refined anisotropically, the O7 atom gave a non-positive definite ADP tensor and was therefore refined isotropically (highlighted by a blue circle in Fig. 6.16 (right)). This is already a strong indication that this particular symmetry is not correct. More pressing are the unusual ellipsoid shapes obtained for the Fe and more specifically the O atoms. In a well-behaved structure the occurrence of slightly elongated ellipsoids, for example the Yb and Fe atoms

shown in the structural representation of the $P\bar{1}$ with origin (0, 0, 0) (see Fig. 6.16, left), are the standard expected result, where the specific inclination of the ellipsoid is based on the symmetry of the unit cell [212, 213]. However, the implications of the flat, typically deemed pancake-like ADPs of the oxygen atoms seen in the $P\bar{1}$ with origin (0, 0, $\frac{1}{2}$) imply that one of a number of issues with this SG exist.

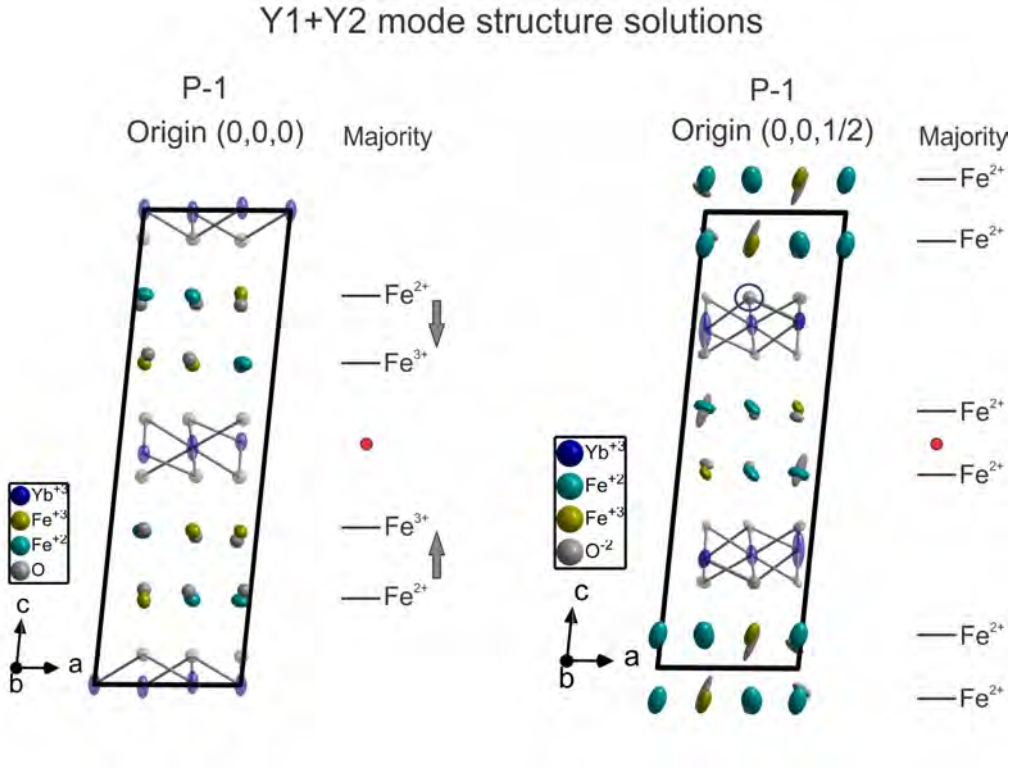

Figure 6.16: Structural representations using symmetry analysis of the combined Y1 and Y2 IR's at 200 K. Left: $P\bar{1}$ with origin at (0, 0, 0) and right: $P\bar{1}$ with origin at (0,0,$\frac{1}{2}$). The overall charge of each iron layer is depicted by a grey line and relative iron valence. The red dot represents the point of inversion. Grey arrows highlight polarization of the layer, which in the case of $P\bar{1}$ (0, 0, 0), is polar bilayers antiferroelectrically stacked. The alternate $P\bar{1}$ structure presents charged layers of majority Fe^{2+}. The O7 atom (marked with blue ring) for the (0, 0, $\frac{1}{2}$) structure was maintained as isotropic, anisotropically it was refined as a non-positive definite ADP tensor.

The primary cause that can be ruled out first is temperature, although it is at 200 K, classed still as a higher temperature in x-ray diffraction, when compared to the other $P\bar{1}$ structure with origin (0, 0, $\frac{1}{2}$), there is no observation of a oddly shaped ADPs, apart from natural distortion. The most probable factors therefore are either conformational transitions[2] or in the majority of cases, atoms which form a long chain to a heavy atom from the outer most atoms can cause more thermal vibration and as a result larger ellipsoids. Disorder and poor atom assignation from the electron density map can also contribute to poor ADPs. However, in this particular case it is attributed to wrong structure selection, where the specific orientation of the ellipsoids do not follow the correct symmetry operations of the selected space group. This factor along with the non-positive definite ADP tensor of the O7 atom, clearly indicate this is not the correct structure solution for this compound. The high refinement values complement this assertion, where R_{obs}=8.91 % and the goodness

[2]Any spatial arrangements of a molecule that can be obtained by rotation of the atoms about a single bond.

of fit is very high at GoF_{obs}=4.73 % (see Fig. 6.15). Furthermore, the calculated BVS for the oxygen atoms of this structure do not correlate with the natural O^{2-} oxidation state of this system, where the atoms ranging from O7-O12, shown as highlighted cells in the table of Fig. 6.17 (right), give values of circa 0.5; far too low to be considered realistic, mostly likely attributed to badly estimated bond lengths due to the model being incorrect. Still, based on the Fe valences calculated using the BVS method, the final CO state for this structure with the inversion centre at the Fe bilayer gives charged layers of majority Fe^{2+} over the whole unit cell. Since this particular symmetry cannot be a candidate for the final structure solution of $YbFe_2O_4$, it is now necessary to look at the $P\bar{1}$ structure with origin (0, 0, 0).

Site	$P\bar{1}$ (0, 0, 0)	$P\bar{1}$ (0, 0, $\frac{1}{2}$)
Fe1	2.851(14) (3+)	1.981(19) (2+)
Fe2	2.842(15) (3+)	2.02(3) (2+)
Fe3	2.103(9) (2+)	2.31(3) (2+)
Fe4	2.864(15) (3+)	2.59(4) (3+)
Fe5	2.119(10) (2+)	2.61(3) (3+)
Fe6	2.050(9) (2+)	2.32(3) (2+)

Site	$P\bar{1}$ (0, 0, 0)	$P\bar{1}$ (0, 0, $\frac{1}{2}$)
O1	2.003(9)	1.86(2)
O2	2.031(10)	1.81(3)
O3	2.015(9)	1.76(2)
O4	1.981(11)	1.52(3)
O5	1.954(12)	1.63(2)
O6	1.962(11)	1.93(3)
O7	1.968(10)	0.627(11)
O8	1.922(10)	0.531(9)
O9	1.850(12)	0.537(9)
O10	1.789(12)	0.558(10)
O11	2.027(12)	0.505(8)
O12	1.877(13)	0.573(10)

Figure 6.17: The calculated BVS of each Fe site (left table) and oxygen site (right table) for both $P\bar{1}$ structures. The highlighted oxygen sites (yellow) show unrealistically low BVS calculated for the $P\bar{1}$ with shifted origin (0, 0, $\frac{1}{2}$).

The refinement of the alternative $P\bar{1}$ structure which has the inversion centre at the Yb layer, as with all the lower symmetry refinements including $P1$ described in the next section, a number of restrictions were needed before running an initial refinement cycle [3]. The final refinement parameters are also shown in Fig. 6.15 and provide the lowest final R-value of R_{obs}=4.71 %, from all the tested structures. The goodness of fit (GoF_{obs}=2.38) is still above the ideal value of 1, however the

[3]Lowering space group symmetry incurs more parameters and atoms, leading to more ADP parameters as well as the already established 6 twins components, making stabilization of the refinement in the beginning difficult. Remedied by the following restrictions; setting identical coordinates for each atom, using a random seed and a lower damping factor in the refinement settings. A convergence during the first 10 cycles of the refinement can thus be achieved. From there inclusion of the correct twin components and an isotropic extinction factor will better the refinement parameters. Lastly, slow removal of the restrictions on heavier atoms to light atoms and the eventual move from isotropically defined atoms to anisotropic, should yield a successful refinement. All restrictions were removed for the $P\bar{1}$ structure with origin zero.

remaining positive factors such as the extremely reasonable ADP ellipsoids obtained for each atom, shown in Fig. 6.16 (left), none of which yielded a non-positive definite ADP tensor, still inspire confidence that this is correct. The $wR2_{obs}$=11.72 % is also in good relation to the observed R-value, where in poorer refinements it is typically much higher. The corresponding BVS values calculated and shown for both Fe and O sites in the unit cell (Fig. 6.15) for this structure are also in good agreement with the oxygen valence O^{2-}, where the lowest value obtained for the O10 atom was 1.789. The BVS calculated for the Fe sites provided a clear distinction between the Fe^{2+} and Fe^{3+} valences in contrast to the previously tested higher symmetry structures, the values in some cases were either higher or lower than the ideal value (see Appendix. A.4). The refined coordinates and respective ADPs of each atomic site at 200 K are displayed in Table. 6.6. The final CO structure for this refinement is polar bilayers stacked antiferroelectrically. The results of the refinements so far clearly indicate $P\bar{1}$ with a Yb at the origin to be the most likely structure, and the corresponding antipolar CO to be the correct charge configuration. This is validated by a refinement in the $P1$, with no symmetry restrictions, to which we turn to now.

Site	x	y	z	U11	U22	U33	U12	U13	U23
Yb1	0	0.5	1	.00413(6)	.00486(7)	.01371(6)	-.00223(6)	-.00107(7)	.00030(7)
Yb2	.33317(3)	.82922(4)	.99587(14)	.00407(4)	.00394(4)	.014907(4)	-.00194(5)	-.00152(5)	.00041(4)
Yb3	.17037(3)	.16645(3)	.48594(12)	.00429(4)	.00376(3)	.010004(3)	-.00230(3)	-.00086(3)	.00019(3)
Yb4	0.5	0.5	0.5	.00388(5)	.00359(6)	.01964(10)	-.00216(4)	-.00195(8)	.00035(6)
Fe1	.43980(16)	.83445(18)	.67556(2)	.00658(15)	.0066(14)	.00647(9)	-.00390(16)	-.00098(13)	.00078(12)
Fe2	.88912(16)	.50416(16)	.32379(2)	.00565(13)	.00614(15)	.00585(8)	-.00313(13)	-.00114(12)	.00097(11)
Fe3	.21602(2)	.82591(2)	.32410(3)	.01031(2)	.01662(2)	.00626(11)	-.00748(2)	-.00135(15)	.00103(16)
Fe4	.72377(16)	.83944(16)	.82290(2)	.00535(13)	.00587(15)	.00795(10)	-.00306(14)	-.00119(13)	.00083(12)
Fe5	.39379(19)	.49769(17)	.81869(3)	.00807(16)	.00822(18)	.00709(9)	-.00406(17)	-.00181(14)	.00136(14)
Fe6	.93887(2)	.83021(2)	.17927(3)	.00991(18)	.01061(2)	.00564(9)	-.00515(2)	-.00102(15)	.00124(14)
O1	.84009(7)	.52380(6)	.43920(15)	.00716(8)	.00447(7)	.00784(5)	-.00263(6)	-.00131(5)	-.00018(4)
O2	.17672(7)	.82093(8)	.43987(14)	.00742(8)	.00831(8)	.00639(5)	-.00567(7)	.00010(5)	.00037(5)
O3	.45802(6)	.84408(7)	.56052(14)	.00586(8)	.00747(7)	.00615(4)	-.00325(7)	-.00088(5)	.00114(5)
O4	.98572(8)	.83044(9)	.06104(14)	.00535(7)	.00723(7)	.00748(5)	-.00242(7)	-.00187(6)	.00123(6)
O5	.72725(8)	.15100(7)	.79872(17)	.00924(8)	.00551(8)	.00977(6)	-.00395(7)	-.00119(7)	.00104(6)
O6	.35331(9)	.49270(8)	.93923(13)	.00831(9)	.00699(4)	.00593(4)	-.00190(8)	-.00111(7)	.00145(6)
O7	.68732(8)	.84125(8)	.93697(14)	.00629(7)	.00583(7)	.00710(5)	-.00171(7)	-.00204(6)	.00160(6)
O8	.04218(8)	.53142(7)	.80046(17)	.00912(3)	.00821(9)	.00906(6)	-.00378(8)	.00003(6)	.00036(6)
O9	.42380(7)	.82590(8)	.80366(18)	.00686(9)	.00786(8)	.01240(7)	-.00263(8)	-.00264(6)	.00051(7)
O10	.7743(8)	.81238(8)	.67259(2)	.00766(8)	.01085(12)	0.01834	-.00483(9)	-.00323(8)	.00098(9)
O11	.87162(7)	.83392(8)	.30536(15)	.00973(9)	.00753(7)	.00808(5)	-.00393(8)	-.00187(5)	.00046(6)
O12	.41585(8)	.52416(7)	.68633(19)	.01163(2)	.00759(9)	.01135(7)	-.00626(9)	.00090(7)	-.00043(6)

Table 6.6: Atomic positions and anisotropic displacement parameters of the $P\bar{1}$ structure refined at 200 K. All of the coordinates were changed to values between 0 and 1, by adding or subtracting 1 to standardize the positions in the unit cell.

6.4 $P\bar{1}$ or $P1$.. that's the question?

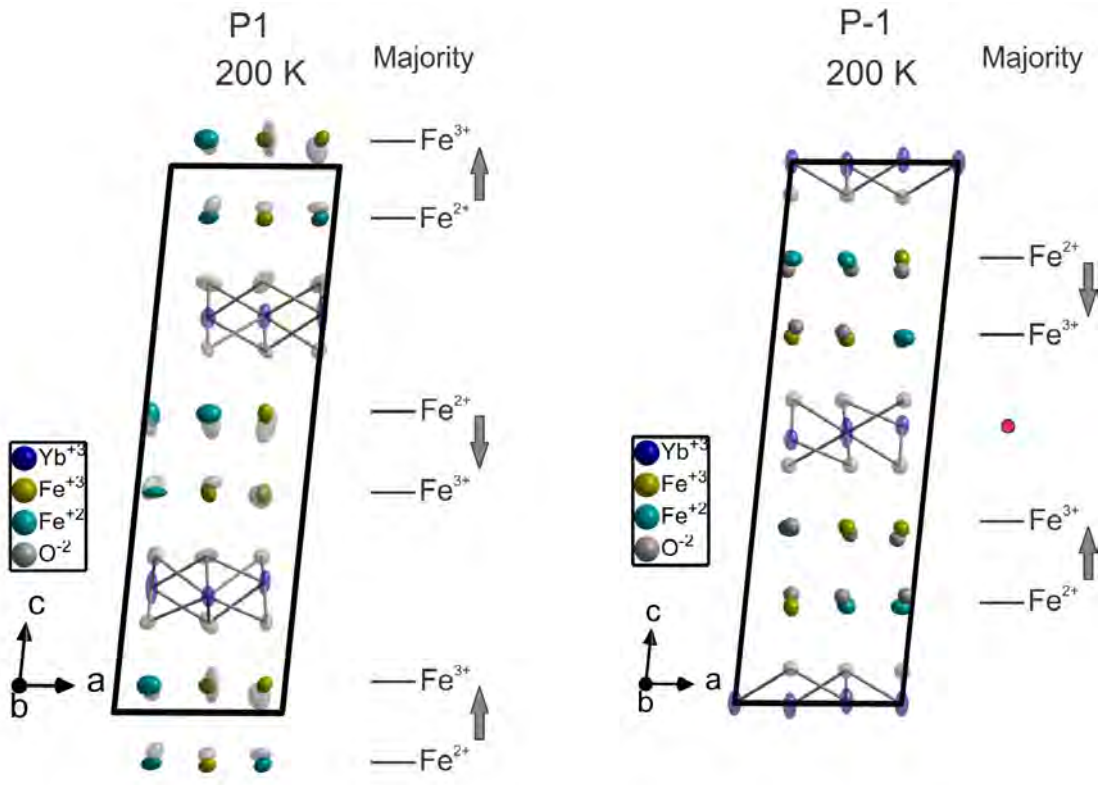

Figure 6.18: Structural representation of left: $P1$ and right: $P\bar{1}$. The arrows indicate direction of polarization for each Fe bilayer. The red dot marks the inversion centre of the $P\bar{1}$ structure.

The question still remains, does $P\bar{1}$ symmetry still hold when we refine the structure in the lowest space group symmetry $P1$. As $P1$ imposes no symmetry constraints, a successful refinement can unambiguously determine which, symmetry elements can possibly be present and thus which space groups can be appropriate. A refinement of the $P1$ structure was successfully achieved again with the same restrictions mentioned in the previous section. The $P1$ reflection list was recreated from the available list of unmerged reflections. In order, to account for the loss of inversion symmetry, extra atoms at general Wyckoff positions (2i) in $P\bar{1}$ were incorporated (the only two special atomic positions in the $P\bar{1}$ unit cell belong to the Yb1 (Wyck=1c) and Yb4 (Wyck=1h)). This can be done either manually or by adding an extra atom for each general position. Due to the loss of an inversion centre the coordinate will take the opposite value (positive becomes minus etc), and from here you obtain all the atoms for the $P1$ unit cell. In the case of the refined structure shown in Fig. 6.18, the $P1$ structure was obtained using the structure solution from SIR2014 [167]. The final refined atomic coordinates and lattice parameters of the $P1$ structure at 200 K are shown in Appendix. A.5. When comparing, the two structures correctly, the refinement of the $P\bar{1}$ space group needs to be completed with the same reflection file used for the $P1$ [4].

[4]This was done simply by taking the original refinement in Jana2006 and modifying the space group in the M50 files (basic structural parameter file) to space group symmetry $P1$. It then

Parameter	P1	$P\bar{1}$
R_{int}/R_{σ} (%)	6.99/2.91	6.99/2.91
$R_{obs}/wR2_{obs}$ (%)	5.56/13.07	5.90/13.75
R_{all}/wR2$_{all}$ (%)	6.05/13.47	6.41/14.17
GoF_{obs}/GOF_{all}	2.21/2.15	2.32/2.26
Uniq. ref. obs/all	30497/34123	
Parameters	386	199
Twins restricted	7,8,9,10,11	None

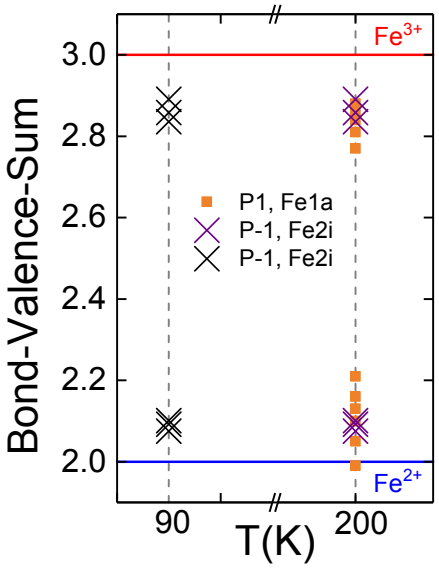

Figure 6.19: Left: table of refinement statistics for both $P1$ and $P\bar{1}$, the latter with merged reflections from the $P1$ structure at 200 K. Right: a plot of the calculated BVS at 200 K for $P\bar{1}$ (purple crosses) and $P1$ (orange squares) and at 90 K the same $P\bar{1}$ (black crosses). The red and blue lines represent the Fe^{3+} and Fe^{2+} valence, respectively.

The refinement statistics obtained for each structure at 200 K are given in Fig. 6.19 (left table). The higher overall refined parameters given here for the $P\bar{1}$ structure (compared to those in Sec. 6.3.4), are natural given the extra reflections, but it is important to now see which structure is correct. When considering first the structural outcome, both $P1$ and $P\bar{1}$ provide a reasonable R_{obs}=5.56 and 5.90 % and GoF_{obs}=2.21 and 2.32, respectively. The BVS analysis from each refinement is plotted as a function of temperature in Fig. 6.19. At 200 K the BVS from the 6 Fe (Wyckoff 2i) atoms from the $P\bar{1}$ (purple crosses) refinement and 12 Fe (Wyckoff 1a) atoms from the $P1$ refinement (orange squares) show the same valence distribution. As discussed in Sec. 6.4.1, this implies from unrestricted ($P1$) refinement that the CO really has $P\bar{1}$ symmetry. On further cooling to 90 K, the BVS of the $P\bar{1}$ (black crosses) is also provided. At each temperature both structures present the same CO pattern, with half of the Fe atoms taking Fe^{3+} and the remaining half taking Fe^{2+}. The $P1$ refinement gave extremely reasonable values, allowing easy distinguishability of each Fe valence. The ADP ellipsoids of some of the oxygen atoms are not agreeable compared with the $P\bar{1}$ as shown in Fig. 6.18, where some are more elongated and flatter in shape but not beyond the realm of acceptable, and attributed to the lowering of symmetry, increased parameters and in particular the presence of strong correlations due to inversion symmetry or at least pseudo inversion symmetry. The five negative twin components seen in the refinement of the $P1$ structure, are also problematic, but stem from a lack of reflections in the area of each of these lost symmetry elements; in this case the inversion centre. From this point it is difficult to see which structure is representative of the CO pattern observed. Therefore, in order to find the correct structure, one must examine the symmetry elements, and which, if any, are preserved.

gives you the option of creating a new reflection file. Once complete, the current space group $P1$ and respective reflections are obtained. Then by changing the space group back to $P\bar{1}$, and not selecting the option of create a new reflection file. You obtain an identical set of reflections for both structures without symmetry restrictions.

6.4.1 Which structure represents the correct CO? based on symmetry

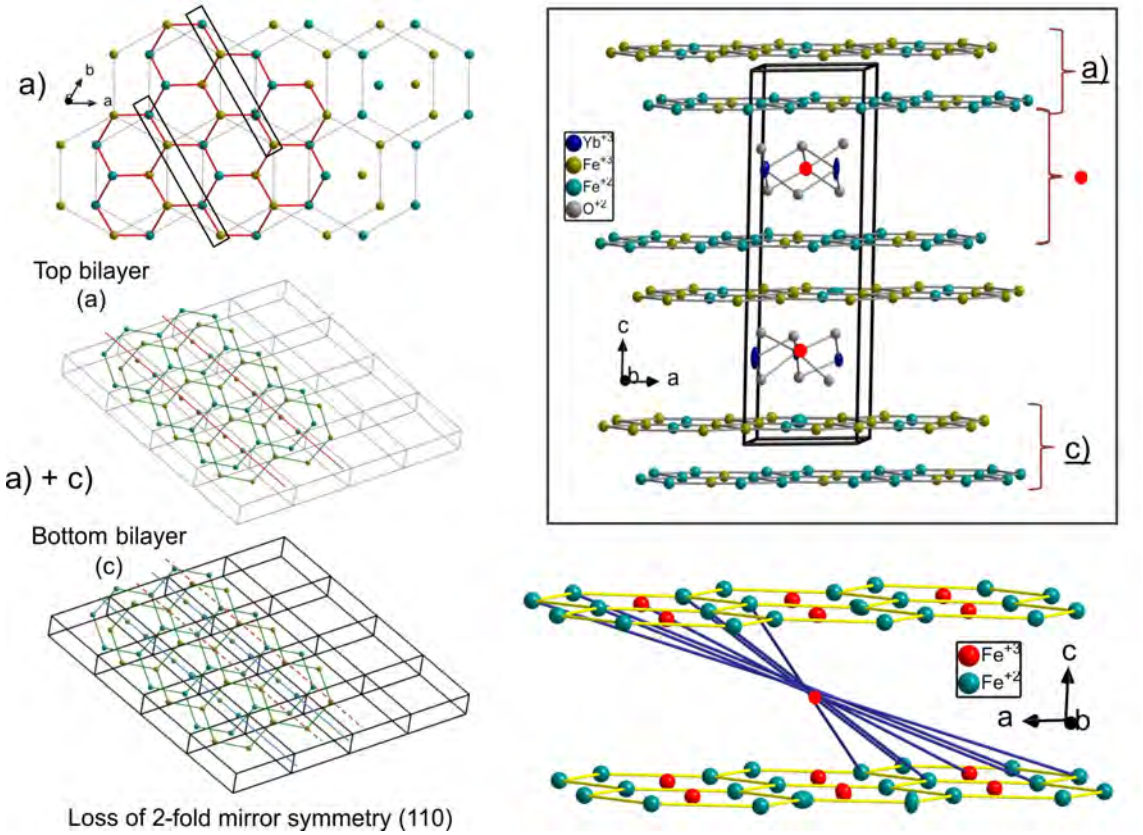

Figure 6.20: The charge order deduced in $P1$. The $P\bar{1}$ unit cell boxed in black (top right) is broken into 3 sections; a)-c) representative of each bilayer in the unit cell. (a) the top bilayer of the unit cell in a view direction along ℓ, where a central red dot describes a point of inversion. Due to the mapping of Fe^{3+} to Fe^{2+} of each layer; 3 2-fold and mirror (rectangle boxes) symmetries are broken. The loss of 2-fold mirror symmetry $(110)||\mathbf{c}_{hex}$ is described in the (a) + (c) diagram, showing the top and bottom bilayers of the unit cell. The two layers are projected in the same orientation, where red and blue lines represent the 2-fold mirror symmetry of each layer, respectively. The additional red dotted line on the bottom layer (c) shows that the symmetries do not map over bilayers, since the **c** axis in this structure is not perpendicular to the a-b plane. A red dot shows the Fe layers affected by Yb inversion in the unit cell, and in this case the Fe^{3+} ions are coloured in red for better distinction to the Fe^{2+}. The blue lines present the clear mapping of like atoms to like atoms through inversion symmetry of each layer, which for this CO arrangement is preserved.

To ascertain which structure fits the CO configuration presented by BVS analysis, one needs to see which lost symmetry elements going from the higher symmetry $R\bar{3}m$ to the much lower symmetry $P1$ subgroup are still needed and, which ones are broken by the charge order. The only one which needs to be clarified is the inversion symmetry at the Yb position, which is lost when entering the $P1$ space group. A brief explanation of proof for the loss of the higher symmetry elements: the 3 and 2-fold symmetry plus mirror operations are however, required first. Some of the diagrams shown in Fig. 6.20, highlight the lost symmetry elements with the final exception of inversion (discussed later). Initially, the refined $P1$ structure (boxed) shown in Fig. 6.20 (top right) is broken up into sections and categorized using a)-c), each representing a bilayer in the unit cell. The red dots indicate the valid inversion

centers of the $P\bar{1}$ structure. The separated bilayer shown in a) prevents both 3-fold and 2-fold symmetry due to mapping of Fe^{3+} rich to Fe^{2+} rich positions from one layer to the other, thus breaking the higher symmetry operations. The loss of mirror symmetry is highlighted with black rectangles. The second fundamental symmetry element is the 2-fold mirror, which is seen as lines passing through $(110)||\mathbf{c}_{hex}$. This particular symmetry element is more difficult to see, and requires both the top (a) and bottom (c) bilayer for clarity. The 2-fold mirror symmetry in the top layer is represented by red lines, and in the bottom, blue lines, respectively. When one positions the red lines as they stood on the top layer (see Fig. 6.20 (dotted red line)) to the bottom layer's blue lines, one can see they do no map from one bilayer to the next, since the **c** axis is not perpendicular to the *a*-*b* plane, and as a result also breaks the mirror symmetry.

With all those symmetry elements gone, the CO necessarily has to be described with a triclinic space group. The final point of call, is to check the inversion symmetry to see if the correct structure is $P\bar{1}$ or $P1$. The inversion centers at the Yb layer are marked by a red dot in the main unit cell, shown in Fig. 6.20 (boxed panel). The panel below the box shows the two Fe layers affected by inversion, the blue lines between the two layers of the bilayer indicate that from the BVS calculated from the refinement, the inversion symmetry is preserved based on the CO arrangement. From this it is clear that the CO pattern can be described by the $P\bar{1}$ space group with inversion centre at the Yb position, and although the same CO pattern results in the $P1$ refinement, all Fe atoms are connected by inversion symmetry. In this case, for describing the CO, the best structure is $P\bar{1}$. Furthermore, the BVS values given in Fig. 6.19 (right) at 90 K of the $P\bar{1}$ refinement (discussed in detail in Sec. 6.5), indicates no change of CO pattern going below the LT phase. This does not account for the peak intensity observed below T_{LT}, given in Sec. 6.1.1 Fig. 6.6, which is attributed to small distortions, whether this results in a reduction to $P1$ symmetry still needs to be addressed by refinement. However, the fact that the $P\bar{1}$ refinement has no negative twins, less parameters and has very comparable refinement statistics to $P1$, although slightly higher, it still comes to the right choice of space group for the crystal structure. In this case, it comes down to the decision between centro and non-centrosymmetric, and the higher symmetry system should always selected [214]. This final result elucidates the $P\bar{1}$ structure as the final solution for $YbFe_2O_4$ at 200 K, and describes with this cell; polar Fe^{2+}/Fe^{3+} majority bilayers stacked antiferroelectrically, ruling out ferroelectricity in this system. Although there are antipolar bilayers, it still remains to be seen if this system can be deemed a proper antiferroelectric material, which would imply that application of a sufficiently large electric field can provide a potential drop large enough across the bilayers to flip the polarization of one bilayer, inducing a ferroelectric state. Furthermore this result provides a new revised model and insight into $LuFe_2O_4$. The next point of call is to establish whether or not the T_{LT}=138 K transition affects the structure at 90 K. An increase of peak intensity was observed below this temperature as shown in Fig. 6.4, which looks at the temperature dependence of the $(\frac{1}{3}\pm\tau, \frac{1}{3}\mp 2\tau, 15)$ and $(\pm\tau, \pm\tau, \frac{3}{2})$ reflections. It remains to be determined whether there is a structural change below this transition as proposed by [117]. The following section details a refinement at 90 K.

6.5 $P\bar{1}$ refinement at 90 K

Parameter	This work	
T(K)	200 K	90 K
Space group	$P\bar{1}$	$P\bar{1}$
R_{int}/R_{σ}	8.01/2.91	11.59/3.11
$R_{obs}/wR2_{obs}$ (%)	4.71/11.72	4.17/9.38
R_{all}/wR2$_{all}$ (%)	4.95/11.90	4.92/9.80
GoF_{obs}/GOF_{all} (%)	2.38/2.34	1.39/1.35
Uniq. ref. obs/all	17363/18467	15854/18257
Redundancy	10	8
Parameters	199	198
Neg. twins	No	Twin 5

Site	$P\bar{1}$ 200 K	$P\bar{1}$ 90 K	BVS
Fe1	2.851(14)	2.836(12)	(3+)
Fe2	2.842(15)	2.858(14)	(3+)
Fe3	2.103(9)	2.092(9)	(2+)
Fe4	2.864(15)	2.891(13)	(3+)
Fe5	2.119(10)	2.101(8)	(2+)
Fe6	2.050(9)	2.075(8)	(2+)

Figure 6.21: $P\bar{1}$ refinements at 200 K and 90 K. Left: tables of refinement parameters. Right: the calculated BVS of each Fe ion, the BVS column stands for the oxidation state taken for each obtained value for the final CO arrangement.

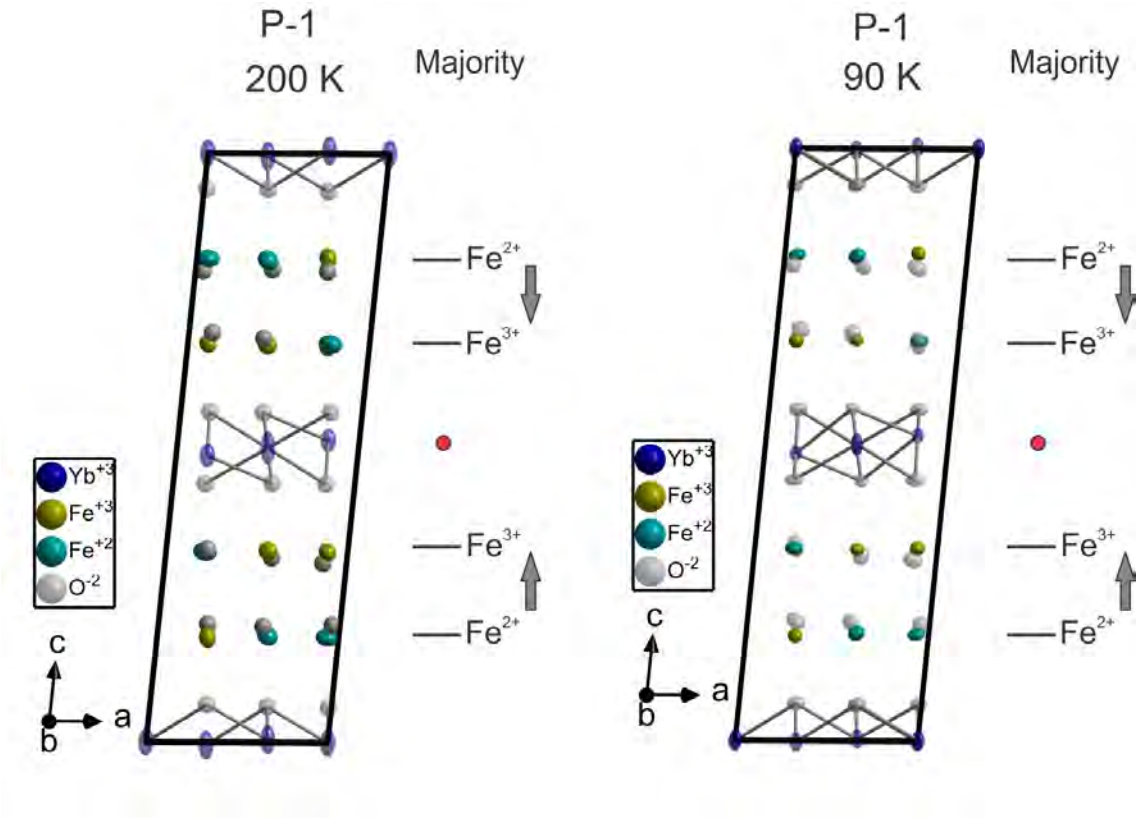

Figure 6.22: Structural representations using symmetry analysis of the combined Y1 and Y2 IR's at 200 K of the $P\bar{1}$ structure. Left: 200 K. Right: 90 K. The overall charge of each iron layer is depicted by a grey line and relative iron valence. The red dot represents the point of inversion. Grey arrows highlight polarization of the layer, which is described at each temperature by the same $P\bar{1}$ space group (origin:(0, 0, 0)). The final CO structure presents polar bilayers which are antiferroelectrically stacked.

As the refinement in $P\bar{1}$ (origin (0,0,0)) provided correct final structural solution explaining the CO in this system, a long experiment was also performed at 90 K. This was in fact done before the 200 K experiment, as based on thermal effects, refinement at a lower temperature is far more stable and was therefore conducted first. A comparison of refinement parameters for the $P\bar{1}$ at 200 K and 90 K respectively, is provided in Fig. 6.1 (left). The only unfortunate aspect in regards to the refinement at 90 K is that Twin 5 was negative, and thus in the final refinement had to be restricted to 0. Besides this all ADP's shown in Fig. 6.22 gave reasonable values, and conform to more isotropically shaped ellipsoids due to the lower temperature. The overall R-values are slightly lower than that obtained at 200 K in particular the goodness of fit is more reasonable and close to the ideal value of 1 (GoF_{obs}=1.39 %). The single lost parameter in the 90 K data is accredited to the negative twin component, which was set to zero before the final refinement cycle. The occurrence of this negative twin contrary to the 200 K data can be reasoned by the experimental procedure and crystal mounting (see Table 6.1). The refinement parameters for $P\bar{1}$ at 200 and90 K are given in Table fig:Twins-p-1-expo-para.

The specific θ intervals used for the 200 K measurement were maximized by measuring for a longer time. The main contributing factors that affected twin component 5, are highlighted green in the experimental parameter table of Fig. 6.1. To refine this twin, based on its orientation in the unit cell would require a number of more reflections and coverage in order to be refined. 1509 more reflections were recorded during the 200 K measurement based on the experimental setting at 200 K, compared to that initially measured at 90 K, consequently provided enough for a successful refinement of all twin components. Another variable which must be considered; during the time between each measurement, the crystal was removed from the loop and grease holder, used previously for the 90 K measurement and glued on a much more stable thin glass rod. This alone will improve the refinement outcome, as the crystal is not obscured by grease, improving the resolution for the video camera (used for absorption correction). All of these aspects resulted in non-comparable twin components for each refinement, where the statistically better twin populations are obtained at 200 K. In order to understand the twin population based on each lost symmetry element, a brief revision and break down of their specific orientation in reciprocal space is required. Twin 1 relates to the identity matrix (0°) around $\mathbf{c}_{hex}$, twin 2 is the 2-fold rotation around $(110)_{hex}$ (direct lattice). From this point, twin 3 and twin 4 are representative of the 120°, and 240° rotation around $\mathbf{c}_{hex}$, respectively. The 2-fold rotations occur at $(100)_{hex}$, $(110)_{hex}$ and $(010)_{hex}$. Which means that when calculating the final two twin components 5 and 6, they relate to the 180° twinning around $(100)_{hex}$ and $(010)_{hex}$. The highest populated twin around $(001)_{hex}$ is twin 4, followed closely by twin 1. The lowest populated twin for the 3-fold rotations around **c** is twin 3, while the highest populated twin component comes from twin

Twin	Population (%)	
T(K)	200 K	90 K
1	0.1587(6)	0.2194(4)
2	0.1098(4)	0.5677(7)
3	0.0728(4)	0.0060(3)
4	0.1918(2)	0.1231(6)
5	0.0572(8)	0
6	0.4094(7)	0.0835(8)

Table 6.7: The 6 refined twin components at 200 and 90 K and relative domain populations.

6=0.409 %, 2-fold rotation.

Site	x	y	z	U11	U22	U33	U12	U13	U23
Yb1	0	0	1	.00296(5)	.00306(6)	.00733(4)	-.00197(5)	-.00050(5)	.00032(5)
Yb2	.33314(3)	.32926(4)	.99669(11)	.00281(4)	.00290(4)	.00674(3)	-.00179(4)	-.00075(3)	.00011(3)
Yb3	.17136(3)	.66574(3)	.48497(10)	.00263(3)	.00238(3)	.00435(2)	-.00150(3)	-.00042(2)	.00012(2)
Yb4	0.5	0	0.5	.00250(5)	.00224(6)	.00886(5)	-.00147(4)	-.00117(5)	.00028(5)
Fe1	.56080(11)	.66471(14)	.32368(2)	.00377(13)	.00395(12)	.00266(9)	-.00185(13)	-.00026(9)	.00020(10)
Fe2	.73052(12)	.33842(15)	.82284(2)	.00382(13)	.00393(13)	.00386(10)	-.00242(13)	-.000517(9)	.00030(10)
Fe3	.39619(14)	.99843(15)	.81835(2)	.00471(14)	.00512(15)	.00360(8)	-.00293(13)	-.00001(10)	.00029(12)
Fe4	.88951(12)	.00176(13)	.324925(2)	.00383(13)	.00382(14)	.00306(8)	-.00180(12)	-.00039(9)	.00026(10)
Fe5	.78508(13)	.67645(15)	.67572(2)	.00609(15)	.00706(17)	.00301(10)	-.00324(15)	-.00036(10)	.00016(11)
Fe6	.93178(13)	.33483(16)	.17953(2)	.00530(15)	.00559(14)	.00292(10)	-.00313(15)	.000228(10)	-.00006(11)
O1	.98339(6)	.33367(8)	.06142(14)	.00497(7)	.00668(7)	.00359(5)	-.00301(7)	-.00029(5)	-.00030(5)
O2	.35508(7)	-.00863(7)	.93925(13)	.00556(7)	.00508(7)	.00327(4)	-.00266(7)	.00049(5)	.00022(5)
O3	.68769(6)	.33910(8)	.93689(14)	.00575(7)	.005531(7)	.00387(5)	-.00355(7)	-.00017(5)	-.00028(5)
O4	.54509(5)	.65261(6)	.43947(13)	.00332(6)	.00476(7)	.00323(4)	-.00147(6)	-.00041(4)	.00082(4)
O5	.82345(6)	.68154(6)	.56010(13)	.00635(7)	.00601(8)	.00281(4)	-.00389(7)	.00008(4)	-.00014(4)
O6	.73480(6)	.65153(7)	.79862(15)	.00734(8)	.00617(9)	.00537(5)	-.00367(7)	-.00214(6)	.00160(5)
O7	.83942(6)	.02433(6)	.43982(14)	.00664(7)	.00457(8)	.00363(4)	-.00352(7)	-.00031(4)	-.00039(4)
O8	.04890(6)	.02911(6)	.80252(15)	.00501(7)	.00502(8)	.00553(5)	-.00201(6)	-.00048(5)	-.00009(4)
O9	.87175(5)	.33080(6)	.30544(14)	.006766(8)	.00429(6)	.00489(5)	-.00278(7)	-.00098(4)	-.00014(5)
O10	.43327(5)	.32778(7)	.79999(14)	.00529(7)	.00726(8)	.00501(5)	-.00373(7)	-.00127(4)	.00007(5)
O11	.58655(5)	.97728(6)	.31398(16)	.00496(7)	.00590(8)	.00716(5)	-.00326(7)	-.00052(5)	.00033(5)
O12	.22172(6)	.68906(6)	.32858(17)	.00493(7)	.00718(11)	.00925(6)	-.00287(7)	-.00158(6)	.00067(6)

Table 6.8: Atomic positions and anisotropic displacement parameters of the $P\bar{1}$ structure refined at 90 K. All of the coordinates were changed to values between 0 and 1, by adding or subtracting 1 to standardize the positions in the unit cell.

From the commensurate CO observed in this crystal at 300 K (see Sec. 6.2 Fig. 6.9), it was only apparent that one CO domain was present. However, on cooling to 200 K (see Sec. 6.3 Fig. 6.11) a clear second domain emerged. This explains the relatively close values of twin 1 and 4, much smaller than twin 3=0.07 %, as it is primarily populated by the other two domains. All other vital parameters from the 90 K refinement are exceptionally good, in particular when one views the comparison of the BVS of each Fe site calculated for each temperature, (see table in Fig. 6.1 (right)), all of which are in good agreement; with very similar values for each atom. The final atomic positions and thermal displacement parameters refined at 90 K are shown in Table. A.6. As the refinement at 90 K was successfully achieved in the $P\bar{1}$ space, it is clear that there is no (symmetry-changing) structural change related to the T_{LT} transition. Further investigation into the low temperature phase is required to elucidate the observed changes. Now it is important to address what modes contribute to the antiferroelectrically stacked polar bilayers in this system by mode decomposition.

6.6 Mode decomposition

The principle of mode decomposition allows one to look at the structural distortions that occur from an undistorted higher symmetry parent cell to a lower symmetry distorted structure. These distortions can be attributed to a number of phenomena

for example structural phase transitions and charge ordering to name a few. In this case the cell, which originally corresponded to the reflections observed through, for instance x-ray diffraction at one temperature, no longer fits with the reflections observed beyond one of the types transitions mentioned above. One can even revert back to first principles in terms of dynamic distortions (thermal vibrations), which since the development of Landau theory [21], systems that exhibit static frozen distortions (often present in ferroic structures) and distorted structures, in general can be explained by *modes*.

Mode	Γ1+	Γ3+	Σ1	Σ2	T1+	T3+	Y1	Y2
A_s	0.04159	0.05071	0.09252	0.31002	0.43534	0.07167	0.19437	0.69740
A_p	0.01698	0.02070	0.03777	0.12656	0.17773	0.02926	0.07935	0.28471

Table 6.9: The sum of each mode amplitude for both the superstructure A_s and parent structure A_p. The two mode amplitudes are related by the volume $Ap = As \cdot \sqrt{V_p/V_s}$, with V_p the volume of the primitive parent structure and, V_s the volume of the primitive CO supercell. Each value was obtained using ISODISTORT [209].

The modes that describe these distortions are a collection of correlated atomic displacements fulfilling certain symmetry properties. Furthermore, the structural distortions can be decomposed into contributions from different modes with symmetries given by the irreducible representations (IR's) (used exhaustively in previous sections for symmetry analysis). The table shown in Tab. 6.9 provides all the modes which correspond to the distorted superstructure $P\bar{1}$ (A_s) and the initial parent structure $R\bar{3}m$ (A_p). From the A_s superstructure modes displayed in this table, the four main contributing to the distortion are: Σ2= 0.34, T1+=0.43, Y1=0.19 and the largest mode value Y2=0.69. To determine which modes are responsible for the charge ordering at 200 K and 90 K one must first relate the Fe atoms in the original parent cell to those now present in the lower symmetry $P\bar{1}$. This can be achieved using WYCKSPLIT from the Bilbao crystallographic server [215]. This program is used for the determination of the relations of Wyckoff positions for a group-subgroup pair, and as the CO in this system is formed from the Fe valence disproportionation, this is the only atom which needs to be considered. At room temperature the $R\bar{3}m$ structure has only one Fe atom at the Wyckoff 6c position, when incorporating both the parent group and the subgroup into this program, the 6c position is split into 6 Fe Wyckoff 2i positions, each comprising of two positions related by inversion. When importing the $P\bar{1}$ distorted structure (see Sec. 6.4), the resultant structure gave a none zero origin. This of course does not fit with the refined structures presented in the previous sections. The solution to the discrepancy was the lack of standardized units in the original refinement file. These were changed to ensure that the Yb1 atom was sitting at the usual (0, 0, 0) position, and additionally translating the remaining atoms in the cell. This yielded the correct structural outcome in ISODISTORT, with the same lattice parameters and origin (0, 0, 0). The 12 positions obtained from WYCKSPLIT will in some order relate to the 6 Fe atoms obtained from the mode decomposition of the distorted superstructure cell. Since the propagation vector describing the CO in this system is given in the hexagonal notation ($\frac{1}{3}$, $\frac{1}{3}$, $\frac{2}{3}$), the correct hexagonal coordinates for each of the 6 Fe atoms needs to be established. Using the initial value obtained for the Fe1 atom

in the parent cell $R\bar{3}m$ (z=0.2147) the Fe atoms can be identified as:

$$\begin{aligned} \mathrm{Fe1}^{2+}_{tric} = (0,0,z), \quad \mathrm{Fe2}^{3+}_{tric} = (\frac{5}{3},\frac{1}{3},\frac{1}{3}+z), \quad \mathrm{Fe3}^{3+}_{tric} = (1,0,z) \\ \mathrm{Fe4}^{3+}_{tric} = (\frac{2}{3},-\frac{2}{3},\frac{1}{3}+z), \mathrm{Fe5}^{2+}_{tric} = (2,0,z) \quad \mathrm{Fe6}^{2+}_{tric} = (\frac{5}{3},-\frac{2}{3},\frac{1}{3}+z) \end{aligned} \tag{6.10}$$

As the input into ISODISTORT was done with the newly standardized coordinates of the $P\bar{1}$ refinement, to obtain the correct values for each Fe site (hexagonal setting) when calculating the matrix expansion of Eqn. 6.12, the coordinates displayed in Eqn. 6.10 and obtained from WYCKSPLIT were also standardized by subtracting the $\mathrm{Fe1}^{2+}_{\mathrm{tric}} = (0,0,z)$ from each Fe position. For each Fe position the relative valence can be decomposed into a Fourier expansion:

$$Val_k = \sum_{j=-m\ldots m} A_j \cdot exp(2\pi i \cdot j\mathbf{p}\cdot\mathbf{r}_k) \quad \text{for} \quad Val = \begin{cases} 1 \text{ for } \mathrm{Fe}^{3+} \\ 0 \text{ for } \mathrm{Fe}^{2.5+} \\ \text{-1 for } \mathrm{Fe}^{2+} \end{cases} \tag{6.11}$$

The possible modes from this equation can also be expressed in terms of the sine and cosine, with shifting the phase ϕ_i into different amplitudes for each respective sine and cosine, and given as:

$$\begin{aligned} Val = A\cdot sin(2\pi\cdot\mathbf{p}\cdot\mathbf{r}) + B\cdot cos(2\pi\cdot\mathbf{p}\cdot\mathbf{r}) + C\cdot sin(2\pi\cdot 2\mathbf{p}\cdot\mathbf{r}) \\ +D\cdot cos(2\pi\cdot 2\mathbf{p}\cdot\mathbf{r}) + E\cdot sin(2\pi\cdot 3\mathbf{p}\cdot\mathbf{r}) + F\cdot cos(2\pi\cdot 3\mathbf{p}\cdot\mathbf{r}) + G \end{aligned} \tag{6.12}$$

The Fourier expansion given in Eqn. 6.12 describes the valence of each Fe atom, in terms of the propagation vector P for the j^{th} harmonic and r_k the relative position of the k^{th} Fe ion. The variables A-G describe the respective modes associated with each Fe ion, G, is a constant corresponding to the identity operator j=0. The aim now is to establish which of the modes and respective amplitudes (see Table. 6.9) obtained from mode analysis in ISODISTORT, relate to the charge ordering refined in this system. Using the correctly identified Fe coordinates and CO propagation vector $(\frac{1}{3},\frac{1}{3},\frac{3}{2})$, the mode parameters A-G can be calculated in terms of the inverse matrix multiplied by the calculated BVS from the structural refinement. When computing the independent values in the Fourier expansion for matrix entries, each element with parameter E, gave 0. Which means that E can be eliminated from the matrix calculation (see Table. 6.11), leaving a 6x6 matrix with 6 mode parameters A, B, C, D, F, G to be calculated (G=identity matrix) and shown in Eqn. 6.13.

$$\begin{pmatrix} -1 \\ 1 \\ 1 \\ 1 \\ -1 \\ -1 \end{pmatrix} = \begin{pmatrix} 0 & 1 & 0 & 1 & 1 & 1 \\ 1 & \frac{1}{2} & -1 & -\frac{1}{2} & -1 & 1 \\ 1 & -\frac{1}{2} & -1 & -\frac{1}{2} & 1 & 1 \\ 0 & -1 & 0 & 1 & -1 & 1 \\ -1 & -\frac{1}{2} & 1 & -\frac{1}{2} & 1 & 1 \\ -1 & \frac{1}{2} & -1 & -\frac{1}{2} & -1 & 1 \end{pmatrix} \cdot \begin{pmatrix} A \\ B \\ C \\ D \\ F \\ G \end{pmatrix} \tag{6.13}$$

The values given in the matrix above were normalized to ±1 or ±0.5 to avoid rounding errors in the calculation, furthermore this approach is also taken with the mode details listed on the ISODISTORT mode decomposition. In the process of rearranging in terms of the required mode parameters, the resulting 6x6 matrix is inverted, the final form of the matrix equation after calculation of the inverse is given as:

$$\begin{pmatrix} A \\ B \\ C \\ D \\ F \\ G \end{pmatrix} = \begin{pmatrix} 0 & \frac{1}{4} & \frac{1}{4} & 0 & -\frac{1}{4} & -\frac{1}{4} \\ \frac{1}{3} & \frac{1}{6} & -\frac{1}{6} & -\frac{1}{3} & -\frac{1}{6} & \frac{1}{6} \\ 0 & \frac{1}{4} & -\frac{1}{4} & 0 & \frac{1}{4} & -\frac{1}{4} \\ \frac{1}{3} & -\frac{1}{6} & -\frac{1}{6} & \frac{1}{3} & -\frac{1}{6} & -\frac{1}{6} \\ \frac{1}{6} & -\frac{1}{6} & \frac{1}{6} & -\frac{1}{6} & \frac{1}{6} & -\frac{1}{6} \\ \frac{1}{6} & \frac{1}{6} & \frac{1}{6} & \frac{1}{6} & \frac{1}{6} & \frac{1}{6} \end{pmatrix} \cdot \begin{pmatrix} -1 \\ 1 \\ 1 \\ 1 \\ -1 \\ -1 \end{pmatrix} \tag{6.14}$$

The calculated modes obtained by solving Eqn. 6.14 are shown in Table. 6.10 can be directly compared to the Fe occupancy mode definitions calculated when following the mode decomposition in ISODISTORT, of the refined superstructure. Table 6.11 gives the calculated occupancy of each Fe site along with the mode that relates to it. As one can see when normalizing the calculated values of each Fe site, the values correspond directly to that output by ISODISTORT, furthermore these rounded values were used in the matrix calculation given in Eqn. 6.13 producing the resultant modes shown in Table. 6.10.

Atom	A	B	C	D	E	F	G
	sin(..p..)	cos(..p..)	sin(..2p..)	cos(..2p..)	sin(..3p..)	cos(..3p..)	1
Fe1	0	1	0	1	0	1	1
Fe2	0.866	0.500	0.866	-0.500	0.000	-1.000	1
Fe3	0.866	-0.500	-0.866	-0.500	0.000	1.000	1
Fe4	0.000	-1.000	0.000	1.000	0.000	-1.000	1
Fe5	-0.866	-0.500	0.866	-0.500	0.000	1.000	1
Fe6	-0.866	0.500	-0.866	-0.500	0.000	-1.000	1
	Y2	Y1	Σ2	Σ1	T3+	T1+	Γ1+
Fe1	0	1	0	1	0	1	1
Fe2	1	0.5	-1	-0.5	0	-1	1
Fe3	1	-0.5	1	-0.5	0	1	1
Fe4	0	-1	0	1	0	-1	1
Fe5	-1	-0.5	-1	-0.5	0	1	1
Fe6	-1	0.5	1	-0.5	0	-1	1

Table 6.11: Parameters and modes for the $P\bar{1}$ structure at 200 K. Top: values obtained for the valence of each Fe atom, using the Fourier expansion in Eqn. 6.12. Bottom: modes and respective valences from ISODISTORT.

Mode	A	B	C	D	F	G	E
Value	1	$-\frac{2}{3}$	0	0	$-\frac{1}{3}$	0	0

Table 6.10: The final calculated modes. The position of E at the bottom of the table is to indicate it was not included in the final matrix calculation.

From these final values it is clear that 3 modes contribute to the CO in this system. A=1, relates as shown in Table. 6.11 to the Y2 mode, B=-2/3 relates to the Y1 mode and lastly F=-1/3 corresponds to the T1+ mode. Now one must look back to the original modes which were obtained using the mode decomposition in ISODISTORT from the refined superstructure under investigation. Table. 6.9, includes 8 possible modes compatible with the space group and the $P\bar{1}$ symmetry. With the position of superstructure reflections measured, the Y1, Y2 and T1+ with respective propagation vectors ($\frac{1}{3}$, $\frac{1}{3}$, $\frac{3}{2}$), ($\frac{1}{3}$, $\frac{1}{3}$, $\frac{3}{2}$) and (0, 0, $\frac{3}{2}$) fit to the CO pattern. The combination of Y1 and Y2 modes, which was not considered before for the structural refinements of $LuFe_2O_4$, does provide the lower symmetry structures discussed in Sec. 6.3.2, with the $P\bar{1}$ giving the final crystal and CO structure. The question is: why was this combination of modes not examined before? The main reasoning for this stems from Landau's theory of phase transitions.

Atom	Fe1	Fe2	Fe3	Fe4	Fe5	Fe6
BVS	2.449	2.448	2.452	2.449	2.448	2.452

Table 6.12: The bond valence sum of the Σ2 mode. For each Fe atom the BVS calculated is close to $Fe^{2.5+}$.

The Y1 and Y2 modes correspond to two irreducible representations, the Y1-mode relates to the $C2/m$ antiferroelectric CO model proposed by [106], the Y2-mode on the other hand relates to the $C2/m$ charged bilayer model [48]- two very different structures for $LuFe_2O_4$, both of which are discussed in Sec. 6.3.1. The combination of Y1 and Y2 modes means that there is a mixture of different irreducible representations, and according to Landau's theory this is not possible for a continuous phase transition (2nd order) and very rare for 1st order phase transitions. However, based on; i) the final structural refinement in $P\bar{1}$, ii) the clear contribution of Y1 and Y2-modes to the final CO pattern, and iii) the fact that the incommensurate to commensurate phase transition seen in the heat capacity (Fig. 6.4, right panel), and that observed in the temperature dependent studies on two higher harmonics ($\frac{1}{3}\pm\tau$, $\frac{1}{3}\mp 2\tau$, 15) and ($\pm\tau$, $\pm\tau$, $\frac{3}{2}$) (Fig. 6.7), is clearly first order. This means that $YbFe_2O_4$ and $LuFe_2O_4$ require the rare case of two combined IR's to describe the system. Although rare, it is most likely attributed to the complex spin-charge coupling in these system. The Σ2 mode with propagation vector ($\frac{1}{3}$, $\frac{1}{3}$, 0) gives a large contribution of 0.31. To better understand why this mode does not aid the CO observed in $YbFe_2O_4$, one can look at the mode and strain amplitudes of the Σ2 and simulated BVS. The resultant BVS obtained with this mode are displayed in Tab. 6.12. The calculated BVS of each Fe atom is $Fe^{2.5+}$. This mode does contribute to atomic displacements for example of the Yb atoms. However based the BVS calculated for the final $P\bar{1}$ refinement, it does not relate to the BVS of the Fe atoms. It is likely, that this additional mode leads to the elongation of the Yb^{3+} atomic displacement parameters seen in the refinement at room temperature (see Sec. 6.2, Fig. 6.10). The modes relate to vectors in and out of plane, the Σ2 represents the general ADP displacement seen only in the **c**-direction

of all Yb atoms. Therefore, we can conclude that the CO superstructure intrinsic to highly stoichiometric $YbFe_2O_4$, is a direct result of three specific modes; Y1, Y2 and T1+.

6.7 Discussion

The final CO configuration for the $P\bar{1}$ structure (origin: (0, 0, 0)) at 200 K, (Fig. 6.16, left), gives a very different picture to that previously published on $LuFe_2O_4$ [48], which presented charged bilayers in the monoclinic $C2/m$ cell with the inversion centre at the Fe bilayer. The CO of this $P\bar{1}$ structure obtained via BVS gives definitive anti-polar bilayers. This result, was introduced in 2008 by Angst *et al.* [106], the only difference being that they proposed the antiferroelectric stacking to occur in a higher symmetry space group, namely the $C2/m$. This work was later continued by de Groot *et al.* [48] in 2012 with the exhaustive refinements within this symmetry, providing the alternative concept of charged bilayers in this space group. Unfortunately, due to what is most likely poor integration of the incommensuration ($\frac{1}{3}\pm\tau$, $\frac{1}{3}\pm\tau$, 3n) type reflections, systematic bias may have been introduced, rendering the results unreliable. As the refinement was performed in a commensurate approximation reflections such as ($\frac{1}{3}$, $\frac{1}{3}$, 15) (0, 0, $\frac{3}{2}$) have much weaker intensity, as much of the intensity resides at the incommensurate τ positions. In this case the $C2/m$ model fit. With the observation of the commensurate phase in $YbFe_2O_4$, the stronger intensity of these reflections at integer position in ℓ were incorporated and as a result elucidated the final lower symmetry structure. This lowering of the space group symmetry to $P\bar{1}$ has been proposed only once before by Blasco *et al.* [117] in 2014 using temperature dependent powder diffraction. Comparison to their study on $YbFe_2O_4$ is not possible, as they determined that in all temperatures measured; the system remains in the $R\bar{3}m$ space group. This result also implies that the quality of the powder they measured is one that exhibits only low dimensional CO (2D). This is complemented by both the $M(T)$ and heat capacity, which show curves with broad peaks at the main transitions. Therefore, a comparison is made with their more extensive results on $LuFe_2O_4$. The heat capacity data they provide on $LuFe_2O_4$ powder, show sharp transitions implying better stoichiometry, since they observe both a sharp lambda shaped peak at the main 3D CO temperature, followed by a peak at T_N. The other two heat capacity curves in this paper, on $YbFe_2O_4$ and $TmFe_2O_4$, exhibit much broader transitions, indicating more off-stoichiometric powders with only 2D CO. This could provide a strong reasoning as to why refinement of their $YbFe_2O_4$ powder was only possible in the high symmetry $R\bar{3}m$ cell.

Their study on $LuFe_2O_4$ determined that the CO present in $LuFe_2O_4$ does lower the symmetry further to $P\bar{1}$, but only below circa 175 K above which they refine in the $C2/m$ space group. This is seen in their powder diffraction as a combination of peak splitting and broadening of (0, 0, ℓ) reflections at high diffraction angles, indicating that the cell is no longer monoclinic but triclinic. With the large number of tested refinements presented in this chapter, it is clear that the $P\bar{1}$ with origin (0, 0, 0) model provides the best structural solution for highly stoichiometric $YbFe_2O_4$. Furthermore, this was shown at 200 K, higher than that previously shown by [117] on $LuFe_2O_4$. It therefore stands to good reason that the CO in this system is not

affected by the magnetic transitions above 200 K, since their temperature range for the $C2/m$ structure includes the paramagnetic phase at room temperature and the well documented intrinsic fM (ferrimagnetic) and AFM (antiferromagnetic) phases [32] at ∼230 K in their $M(T)$ data, the latter two of which do not cause structural distortions as the $C2/m$ symmetry is maintained. It is surprising that, with the sharp features seen in their heat capacity data (similar to that shown in this thesis on highly stoichiometric $LuFe_2O_4$ see Fig. 5.4 (bottom panel)), no observation of the peak splitting is seen at room temperature. Especially since the onset of the 3D order in their data starts at 322 K, a little bit higher than that observed in this work. An explanation for the lack of peak splitting at the higher temperatures measured could simply be due to lower intensity of the superstructure reflections at room temperature, which on further cooling sees an increase in intensity. In addition, thermal effects such as the Debye waller factor, will hamper the refinement of any superstructure reflections at higher temperatures.

In addition to the refinement at 200 K provided in this work, a refinement at 90 K was employed to see if the low temperature phase, as seen in [117], causes a structural phase transition below T_{LT}=138 K in this work. From the refinements, it is clear that the $P\bar{1}$ structure is maintained, with the same resultant BVS and CO pattern as that established at 200 K. This indicates that the increased intensity of superstructure reflections observed below T_{LT} in $YbFe_2O_4$ (see Fig. 6.7) is not caused by a (symmetry-altering) magneto-structural transition [104]. The main magnetic transitions in both their $LuFe_2O_4$ and $YbFe_2O_4$ powder samples do not present the sharpest peaks, which would indicate long-range order and good stoichiometry. Furthermore, when comparing this data to those provided by us in Chapter 4 on more off-stoichiometric samples, the CO distortions in these weakly correlated samples will only show stronger peak intensity of the CO reflections at lower temperature, much below the transition onset. Interestingly, to be able to ascertain whether the peak splitting observed by [117] is due to the low temperature transition, one should look at the relative $M(T)$. However, there is no clear indication of a transition at 175 K in any of the three samples measured. This fact alone makes it more difficult to attribute the peak splitting they observed below this temperature to a magneto-structural distortion [104]. In summary, the crystal structure and CO pattern can be described by the $P\bar{1}$ space group. Moreover, it is unlikely that any of the magnetic transitions cause a structural symmetry change in $YbFe_2O_4$, as this was tested by refinements at 200 and 90 K. However, a change was seen in the integrated intensity (see Fig. 6.6) below T_{LT}, indicating small distortions, though distortions that do not change the space group symmetry. To elucidate this a refinement in the $P1$ space group is still required. It is, however, more clear that there is a strong possibility that the magnetism in this system may drive the CO. This concept was highlighted earlier in the chapter. The CO studies on $LuFe_2O_4$ by [106] (see Fig. 6.4, middle panel), observe a definitive drop in the τ incommensuration around T_{N}. This means that at the main magnetic ordering temperature the incommensurate satellites shift closer to the central peak, and attributed to the commensurate nature of the magnetic order. This of course is not seen in $YbFe_2O_4$ as it is already in the commensurate phase below 280 K, however it does provide complementary information to this concept. It is clear that the magnetic ordering in the system is far more strongly correlated, even in samples considered off-stoichiometric based on M(T) data, 3D peak intensity was sometimes observed (see Sec. 4.2.2,

Fig. 4.5, right). Therefore, it is likely that large parts of the sample, even in the pM phase have 2D magnetic ordering, even more so than $LuFe_2O_4$. As a result, it is intuitive to assume that in this case the CO, if it is driven by the magnetism, would go to explain why we see a commensurate CO in $YbFe_2O_4$, and also why the τ satellites in $LuFe_2O_4$ at T_N try to shift to a more commensurate CO. One could argue that maybe this is a case of stoichiometry in $LuFe_2O_4$. However, the samples measured were of comparable quality to those provided in this work, and therefore the observed differences have to be considered as being purely intrinsic in nature. Explanation of this can be appertained to the bilayer separation, even in two neighbouring rare earths, the subtle differences play a large role in producing the more ordered nature in $YbFe_2O_4$. However, it is unlikely that spin-exchange is the only driving force for the CO. Other aspects that should also be considered are e-e Coulomb interaction and lattice effects (the former works far better in terms of polar bilayers than the previously determined charged layers [48]), all of which still need to be investigated for $YbFe_2O_4$.

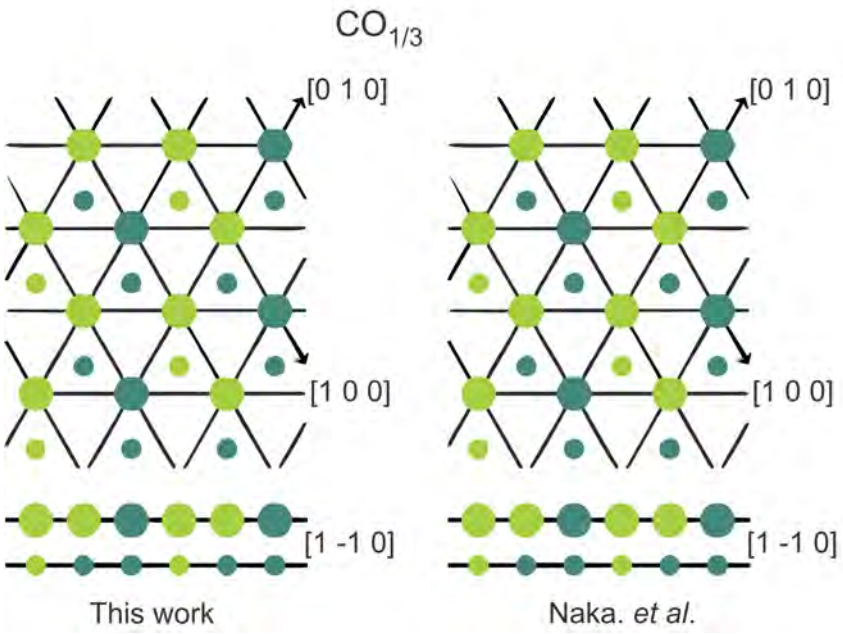

Figure 6.23: The 3-fold CO superstructure observed in RFe_2O_4 proposed by Naga *et al.* [216]. Left: the CO structure refined in this work. Right: the CO structure proposed from theory in [216]. The bottom part of each diagram is a different view along [1, -1, 0].

A theoretical study on the types of CO within a single bilayer, based on the Fe valence of this series by Naka *et al.* [216], describes several types of CO with various propagations. In terms of $LuFe_2O_4$ and $YbFe_2O_4$, one of the vectors of interest is that of q=($\frac{1}{3}$, $\frac{1}{3}$, 0). The CO diagrams from the superstructure refined in this work, Fig. 6.23 (left) and that originally proposed by Naka *et al.* given in Fig. 6.23 (right), provide the same CO structure. One must note however, that the pattern by [216] is limited to one bilayer, which means that the CO pattern they provide also fits for both the proposed $C2/m$ AFE stacking by [106] and the CO pattern revealed in this work. This model, is however inconsistent with the charged bilayers proposed by [48], as the general consensus is that CO is usually assumed to be driven by the repulsion of electrons between different sites [33], and as a result reduces the

chances of neighbouring charges of the same valence. Therefore, the new refinement in the $P\bar{1}$ structure and relative BVS associated with this structure now conforms to this expectation. In addition, an alternative model published by [217] on a 3D level (more than one bilayer) did not support the AFE CO proposed by [106] meaning there are still large ambiguities with the theoretical interpretation of the CO in these systems. With the newly refined $P\bar{1}$ symmetry and BVS analysis, the Fe^{2+} is majority on the top bilayer in the unit cell, leaving a 2:1 pattern of Fe^{2+} to Fe^{3+} respectively, and better shown in Fig. 6.23 (bottom).

The CO distribution theorized by Naka *et al.* [216] as they describe, shows a finite electric polarization, due the $Fe^{2/3+}$ disproportionation. This fits with our analysis, as each bilayer in the unit cell has a polarization direction due to each layer having either Fe^{2+} or Fe^{3+} majority. The bilayers are anti-polar, which means that there can be no net polarization across the unit cell and as a result classed as antiferroelectrically stacked. The theoretical predictions for $LuFe_2O_4$, described by the propagation vector $\mathbf{q}=(\frac{1}{3}, \frac{1}{3}, 0)$ is in good agreement with our refined structure. Recent structural refinements on YFe_2O_4 by Mueller *et al.* [111] in contrast to the theoretical predictions published by [216], did not match.

With the establishment of a new lower symmetry cell, which accounts for all superstructure reflections, the initial assumption of antiferroelectricity by [106] is now realized, although not with a monoclinic space group but rather by a triclinic one. A review paper by [33], addresses in much more detail the possible four CO corresponding to $(\frac{1}{3}, \frac{1}{3}, \frac{3}{2})$ and special point $(\frac{1}{3}, \frac{1}{3}, 0)$. The general assumption, throughout most of the research into these compounds is that a single mode can be used to describe the CO. This was reported previously from Mössbauer studies [42], which from analysis deduced a bimodal valence distribution. The four resulting CO patterns, are split up into two Γ1 and two Γ2 valence states, shown in Fig. 6.24. Of the four CO patterns described here, (a) Γ1 and (c) Γ with combined $(\frac{1}{3}, \frac{1}{3}, 0)$ and (0, 0, 0) propagation vectors relate to: ferroelectric CO with polar bilayers as proposed by [63] or bilayer with net charge [48], respectively. However, two more considerations can also be included due to the clear observation of superstructure reflections at $(\frac{1}{3}, \frac{1}{3}, \frac{3}{2})$. These are shown in (b) and (c) of Fig. 6.24. The CO pattern in (d) can be understood as stacking of oppositely charged bilayers, but the formation of this CO

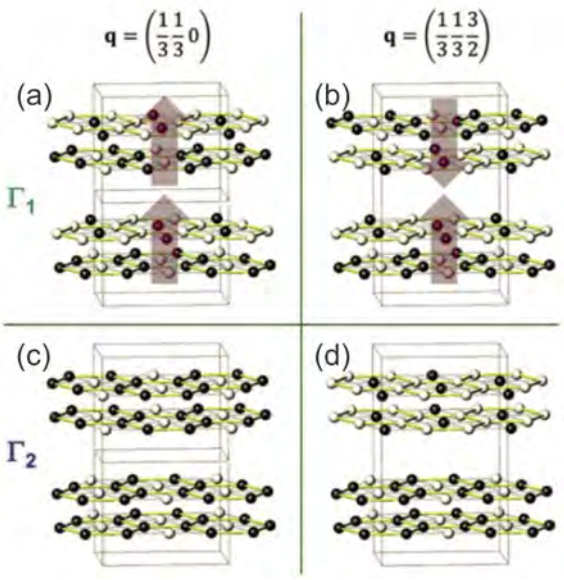

Figure 6.24: A diagram of 4 possible symmetry allowed CO configurations, based on the propagation vectors describing reflections observed in $LuFe_2O_4$. The Fe^{2+} (black) and Fe^{3+} (white) of each bilayer are split up into 4 possible Γ points. (a) and (c) charge configurations following $\mathbf{q}=(\frac{1}{3}, \frac{1}{3}, 0)$ and combined contribution from (0, 0, 0). (b) and (d) alternative charge arrangements with $\mathbf{q}=(\frac{1}{3}, \frac{1}{3}, \frac{3}{2})$ and additional point $(0, 0, \frac{3}{2})$. The arrows indicate bilayer polarization direction. Image taken from [33] and adapted.

would require a charge transfer between neighboring bilayers which are separated by ∼6 Å [33]. The pattern in (c) relates to antiferroelectric CO with polar bilayers, but consequently zero net polarization. This latter option was first examined by [106], and as described earlier assumes still a monoclinic $C2/m$ cell. From the refinement done in this work, in order to refine all the reflections observed in $YbFe_2O_4$, not one but two Y modes were required to obtain all possible structural representations from symmetry analysis. With a single Y mode, only structures of the monoclinic subgroup are possible. Using Y1($\frac{1}{3}$, $\frac{1}{3}$, $\frac{3}{2}$) and Y2($\frac{1}{3}$, $\frac{1}{3}$, $\frac{3}{2}$), a number of possible structures were obtained. Of those, three triclinic structures were also listed; $P\bar{1}$ with two different origins and from 2 combined order parameters the lowest symmetry structure $P1$. In our research the $P\bar{1}$ with a non-zero origin was, from refinement, not applicable. However, the $P\bar{1}$ with zero origin provided the best refinement statistics of all previously tested. Furthermore, the calculated BVS and charge arrangement gives rise to an antiferroelectric stacking of polar bilayers, complementing the initial assumptions and thoughts by [33, 106]. Using two IR's to describe a second order continuous transition is not possible and extremely rare in terms of a first order transition. However, based on the heat capacity data (see Chapter. 5, Fig. 5.4), and tracking the intensity of super-structure reflections as a function of temperature (see Fig. 6.6) the CO transitions are seen as sharp lambda shaped peaks and a sharp increase in intensity, respectively, indicative of 1st order phase transitions. This means that the complexity of both the CO and SO in this system is still yet to be fully understood. When looking at the final modes calculated in the previous section, the ones which relate to the CO pattern are; Y1, Y2 and T1+ with respective propagation vectors ($\frac{1}{3}$, $\frac{1}{3}$, $\frac{3}{2}$), ($\frac{1}{3}$, $\frac{1}{3}$, $\frac{3}{2}$) and (0, 0, $\frac{3}{2}$). However, there is also a strong contribution from the $\Sigma 2$ mode with propagation vector ($\frac{1}{3}$, $\frac{1}{3}$, 0) which, with BVS analysis gives a 2.5+ valence for each Fe ion. This is not described by the refined CO structure, but the atomic displacement of the Yb^{3+} ions. There are also other driving mechanisms such as magnetic exchange which may play an effect here but the implications of this will be discussed further in Chapter. 7. That being said it still leaves one large question still unresolved, is the magnetism driven by the CO, or vice versa? Moreover, are these the only mechanisms which drive each other? Or is the large $\Sigma 2$ contribution and need for 2 IR's, indicative of more subtle interactions in the system. Given all of this new information, one can re-open the question of whether the CO in $YbFe_2O_4$ can be nudged from a AFE to FE state. Given the spontaneous fM phase between 240 and 260 K, the latter not too far away from room temperature, and the clear commensurate CO resulting in anti-polar bilayers, if it is possible to apply a stable E-field (and not incur too much joule heating due to the conductivity of the sample) all pre-requisites for a fully functional multiferroic material are there. A full investigation into this prospect given the new status quo for $YbFe_2O_4$, is required to validate if this system is classed as an AFE material or a proper AFE material, the latter being of great potential use. Some of these questions will not be possible to answer at the current stage of research, primarily, the more subtle complexities that have now come to light from the mode decomposition. The next chapter focuses on the spin order in $YbFe_2O_4$, leading to the combined spin and charge order model for both fM and AFM phases.

7 | The spin and charge structure of $YbFe_2O_4$

As we have seen in Chapter 5, from macroscopic magnetization measurements, three main magnetic transitions in highly stoichiometric $YbFe_2O_4$ have been uncovered: T_c, to a ferrimagnetic (fM) phase, T_{AFM}, a drop in magnetization to an antiferromagnetic spin state and T_{LT} to a low temperature phase below which resides a AFM/fM cluster state [26, 32, 42, 104]. The establishment of first magnetic phase diagram for highly stoichiometic $YbFe_2O_4$ uncovered a spontaneous fM state (stable in H=0) in the temperature range 260-240 K, not present in $LuFe_2O_4$. Previously described (Fig. **??**) neutron diffraction with polarization analysis on a sample considered more off-stoichiometric, provided strong peak intensity at integer and half integer positions along $(\frac{1}{3}, \frac{1}{3}, \ell)$ (refer back to Sec. 4.2.2 Fig. 4.5, right panel), indicating that even in such samples 3D long-range magnetic order occurs. Although there is a strong diffuse aspect also present in the spin-flip data, it does suggest that the magnetic correlations in $YbFe_2O_4$ are in general stronger. Chapter 6, focused on the structural refinement of $YbFe_2O_4$, leading to a final solution of $P\bar{1}$ and an anti-polar CO pattern. The final point of call is to investigate the magnetic low and high field spin structure from neutron diffraction to see if it is the same or different to that proposed by [32] for $LuFe_2O_4$. The chapter is then finalized by looking at the spin-charge coupling using x-ray magnetic circular dichroism (XMCD).

7.1 Temperature and field dependent studies of structural and magnetic reflections

Temperature dependent neutron diffraction was performed on the DMC diffractometer located at the Paul Scherrer Institut (PSI) (see Chapter. 3 Sec. 3.7.6 for experimental details). The main focus of this particular measurement was to do detailed scans along $(\frac{1}{3}, \frac{1}{3}, \ell)$ at 200 K in zero field and 1.8 T, to investigate the low and high field spin structure (see Sec. 7.2, Fig. 7.4 for related data), but some short measurements were also performed at specific temperatures on cooling to gain an initial insight into the temperature-evolution of the spin structure. A scan along $(\frac{1}{3}, \frac{1}{3}, \ell)$ in H=0 field is displayed in Fig. 7.1 (top panel). In zero field from 260-240 K the system is in the fM phase, as seen also in the magnetic phase diagram (see Fig. 5.15, top panel). However, on cooling further to 100 K (Fig. 7.1 top panel, black curve) broader peaks and an increased diffuse component is seen below the T_{LT} transition, and stems from a phase competition between the fM and AFM order, also reported in $LuFe_2O_4$ [32]. There is also a distinct increase of intensity at

integer positions $\ell \pm 1$ at 100 K indicating better order from these reflections in the respective magnetic domains.

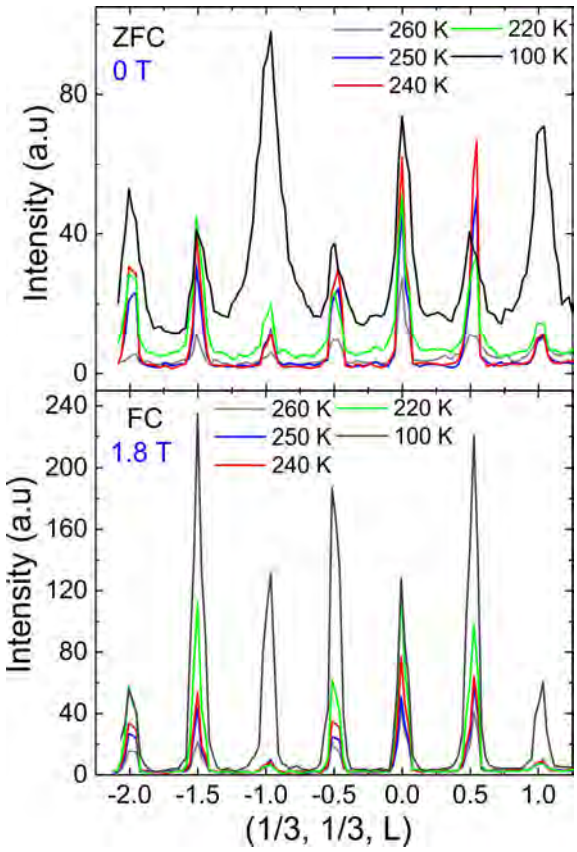

Figure 7.1: Scans along ($\frac{1}{3}$, $\frac{1}{3}$, ℓ) in different temperatures measured on ZFC in H=0 top, the latter focuses on the ($\frac{1}{3}$, $\frac{1}{3}$, 0) reflection. Identical scans performed on H=1.8 T (b) and (d).

On application of an applied field, H=1.8 T, the peaks are much sharper and a notable higher intensity of the half-integer positions is observed (see Fig. 7.1 , bottom panel), analogous to that reported in $LuFe_2O_4$ when in the fM phase [26,32]. On further cooling below T_{LT}, there is no presence of the diffuse background as seen in the 0 T data. This is in contrast to data published on $LuFe_2O_4$, which shows a diffuse component in 0 and 2.5 T (see Fig. 7.4, bottom panel), and indicates that stabilization of the fM phase occurs in a lower field than in $LuFe_2O_4$. This continues down to 100 K, showing the system is at least majority in the fM phase in 1.8 T. A detailed analysis viewing the integrated intensity as a function of temperature is shown in Fig. 7.2, with $YbFe_2O_4$ (a) and $LuFe_2O_4$ (b) [26]. Fig. 7.1 (a) shows three curves: a magnetic reflection ($\frac{1}{3}$, $\frac{1}{3}$, 0) measured in 0 T (blue squares) a magnetic reflection (-$\frac{1}{3}$, -$\frac{1}{3}$, -1.5) (black squares) and the almost relative $M(T)$ (red curve) in H=2 T, each measurement was performed on cooling. The corresponding data on $LuFe_2O_4$ is given in Fig. 7.1 (b) [26], showing the integrated intensity as a function of temperature on FC (blue squares) for the ($\frac{1}{3}$, $\frac{1}{3}$, 0) reflection. The zero field T-dependence (blue squared) shows the onset of the ferrimagnetic T_c transition around 260 K (see Fig. 5.1 middle panel, for AC susceptibility) and the drop into the AFM phase at ∼218 K. There is a contrast between the zero field cooling of $YbFe_2O_4$ and $LuFe_2O_4$, where the same reflection on cooling in $LuFe_2O_4$ has a much higher integrated peak intensity, and takes place until T_{LT} is reached. On further cooling to 100 K, the zero field data for the $YbFe_2O_4$ ($\frac{1}{3}$, $\frac{1}{3}$, 0) reflection sees a slight increase in intensity below T_{LT}, similar to the data provided on $LuFe_2O_4$ for the same reflection. The warming curve (red) for $LuFe_2O_4$ has much lower intensity until it re-enters the stable AFM phase around ∼220 K. The high field T-dependence for YbF_2O_4 tracking the (-$\frac{1}{3}$, -$\frac{1}{3}$, -1.5) reflection, shows the same tendency at T_c to the 0 T data, but the intensity continues to increase as it remains in the high field ferrimagnetic phase. This is in general agreement with the $M(T)$ data shown in Fig. 7.2 (top panel, red curve) and the magnetic phase diagram with stabilization of the AFM phase occurring only in fields up to ∼ 0.3 T (see Fig. 5.15, top panel). There is a slight misalignment of the $M(T)$ curve in relation to the T-dependence of the magnetic (-$\frac{1}{3}$, -$\frac{1}{3}$, -1.5) reflection at 250 and 240 K, but this may be attributed to the shorter counting times for the

T-dependence on cooling, indicated by the error bars. On further cooling to 220 and 100 K the intensity continues to increase, showing that the sample is strongly in the fM phase, as shown in the magnetic phase diagram (Fig. 5.15). Here again, there is some discrepancy between the scaling of integrated intensity of the (-$\frac{1}{3}$, -$\frac{1}{3}$, -1.5) reflection and the $M(T)$ in H=2 T at 100 K, below the LT transition. This is also likely attributed to the shorter counting times and statistics of the neutron measurement at this temperature, along with the slightly higher field used with the relative $M(T)$. However, for a more accurate comparison between the two data sets, a more detailed temperature dependence study would need to be performed on $YbFe_2O_4$.

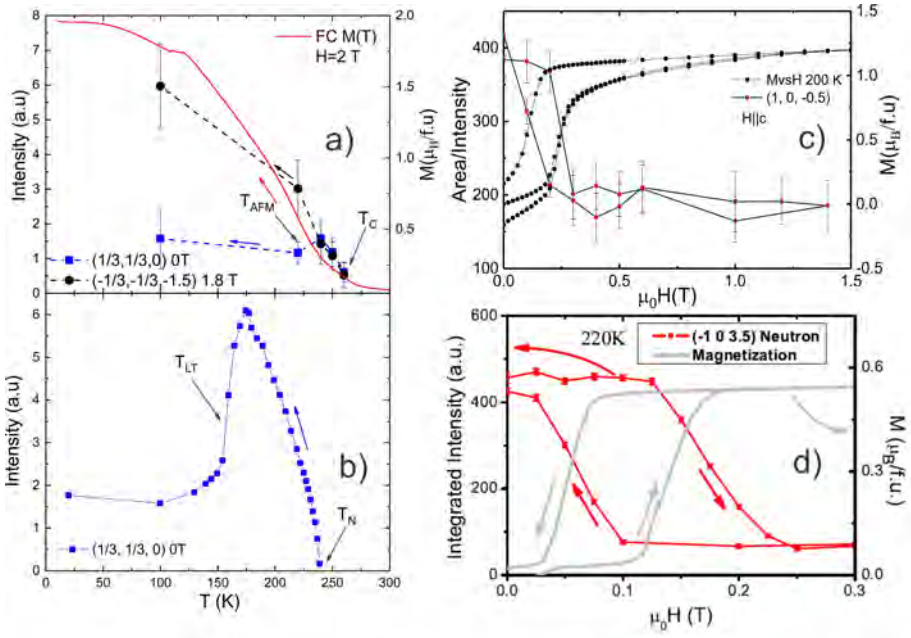

Figure 7.2: (a): $YbFe_2O_4$ Temperature dependence on cooling of the integrated intensity in zero field of the ($\frac{1}{3}$, $\frac{1}{3}$, 0) structural reflection (blue squares) and in H=1.8 T for the magnetic (-$\frac{1}{3}$, -$\frac{1}{3}$, -1.5) reflection (black squares). The red curve represents relative magnetization on field cooling in 2 T. (b) $LuFe_2O_4$ T-dependence of the integrated intensity in H=0 of the structural ($\frac{1}{3}$, $\frac{1}{3}$, 0) reflection on both cooling (blue squares), figure taken from [26]. (c) Integrated intensity of the (1, 0, -0.5) reflection (red circles) at 200 K with relative Mvs$H$ (black circles). (d) A similar plot for $LuFe_2O_4$, for the integrated intensity of the (-1, 0, 3.5) (red squares) reflection at 220 K, with relative magnetization (grey curve), figure taken from [32]

A field dependent neutron diffraction study was performed at the reactor BER II, on the beamline E4, where the integrated intensity of the (1, 0, -0.5) reflection (not along ($\frac{1}{3}$, $\frac{1}{3}$, ℓ)) was measured at fields between 0 and 1.5 T at 200 K (see Fig. 7.2 (c)). The sample was cooled to 200 K from RT in zero field, to focus on the low field AFM phase. A measurement was also performed on a structural reflection (1 0 -1) to observe how the magnetic contribution evolves in applied fields, and shown in Appendix. A.5(a). Unfortunately the statistics of this measurement (indicated by the extremely large error bars) were very poor and no credible data for the (1, 0, -1) structural reflection was obtained for comparison to that of $LuFe_2O_4$ [26, 32], given in Appendix. A.5 (b). Despite the slightly poorer statistics from the measurement of the purely magnetic reflection (1, 0, -0.5), compared to those obtained on the (-1, 0, -3.5) reflection for $LuFe_2O_4$, they are directly comparable. The magnetic

hysteresis (see Fig. 7.2 (a), black circles) is also plotted with the integrated intensity of the reflection at specific fields (red circles). For the $YbFe_2O_4$ M vs H curve, the distribution of the plotted neutron data is in good agreement in terms of the width and the shape, as is the case for the $LuFe_2O_4$ [32], shown in Fig. 7.2 (d) with both $M(T)$ (grey curve) and the integrated intensity of the (-1, 0, -3.5) reflection (red squares). This indicates that they both originate from the same low-H AFM phase. The basis for comparison was to see if $YbFe_2O_4$ also exhibited a hysterestic trend of the integrated intensity of the (1 0 -2)+(0 0 $\frac{3}{2}$) reflections (obverse setting), which strongly relate to the low-H spin structure seen in the magnetic hysteresis. As the data for the neutron experiment was conducted at 200 K, in correspondence to the AFM phase in $YbFe_2O_4$, it is of course 20 K lower than that reported on $LuFe_2O_4$. Therefore, for better comparison, Fig. 7.3 (top panel) shows the M vs H curves at 200 (black curve) and 220 K (grey curve) measured after ZFC from RT, an inset shows $M(T)$ of S1 and GS sample in H=100 Oe.

When comparing the two sets of data at 220 K, both $LuFe_2O_4$ (Fig. 7.2 (d) grey curve) and $YbFe_2O_4$ exhibit fundamental differences, due to the different temperature onsets of T_{AFM} from the ferrimagnetic state. This is expected, however, because the saturation tendency of each compound at this temperature, measured under the same conditions, is very different. The 220 K data on $LuFe_2O_4$ begins to saturate just below 0.2 T, which is in good agreement with the data points from the integrated intensity of the (-1, 0, -3.5) magnetic reflection. However, the M vs H at 220 K shown in Fig. 7.3 (grey curve) is strongly in the AFM phase, but does not tend towards saturation until ∼1.25 T. This can be explained, by viewing the two $M(T)$ curves of $YbFe_2O_4$, both measured on FC and shown in Fig. 7.3 (top panel, inset). Each $M(T)$ curve is representative of the GS sample (red curve), detailed in Chapter. 5 and the highly stoichiometric S1 sample used solely for the measurement at the APS (blue curve). The reason for including both curves in this explanation, stems from the slight difference in stoichiometry between the two. Clearly the APS sample is of better quality, especially when one looks at the T_{LT} transition, which has no two step feature as observed in the $M(T)$ of the GS sample. However, more critical is the magnetization drop going from T_{c} to T_{AFM}, for both curves, despite the slight difference in stoichiometry, the plateau after the AFM drop in the better quality APS sample is

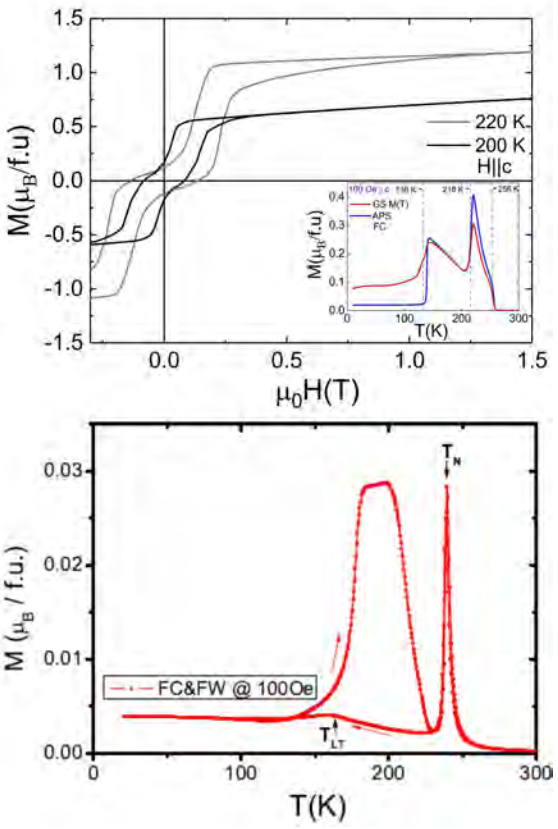

Figure 7.3: Top panel: Mvs$H$ measured at 200 K (black curve) and 220 K (grey curve). Inset: $M(T)$ on FC in H=100 Oe of the S1 sample (blue curve) and GS sample (red curve). Bottom panel: $M(T)$ on both FC and FW (red curves) measured in H=100 Oe, figure taken from [26] and adapted.

identical to that of the GS sample. This indicates that during this transition, it is most likely the magnetic domains in each single crystal, regardless of the stoichiometric differences, that retain some ferrimagnetic micro domains. This is in large contrast to the $LuFe_2O_4$ $M(T)$ data, shown in Fig. 7.3 (bottom panel, red curve), which exhibits a drop to much lower magnetization indicating a better ordering of the AFM phase. This alone promotes the lower field trend to saturation in $LuFe_2O_4$ compared to $YbFe_2O_4$. The overall magnetization at ∼200 K is, in low fields up to a maximum of 0.3 T, for stabilization of a majority AFM phase in $YbFe_2O_4$ and extracted from the magnetic phase diagram (Fig. 5.15). Unlike $LuFe_2O_4$, the lack of saturation present in lower fields is probably due to the competing fM and AFM domains at this temperature. Regardless of these subtle differences, the neutron intensities plotted with the Mvs$H$ at 200 K for $YbFe_2O_4$ are in good agreement for the AFM phase, and similar in this respect to that observed in $LuFe_2O_4$. Having looked at both the temperature and field dependence of specific reflections observed in $YbFe_2O_4$, it is now time to address the detailed nature of the low field (AFM) and high field (fM) spin structure at 200 K.

7.2 Low and high field spin structure

Detailed scans along $(\frac{1}{3}, \frac{1}{3}, \ell)$ were performed also at DMC to primarily investigate the magnetic domain population in both 0 (red curve) and 1.8 T (blue curve) at 200 K, as shown in Fig. 7.4.

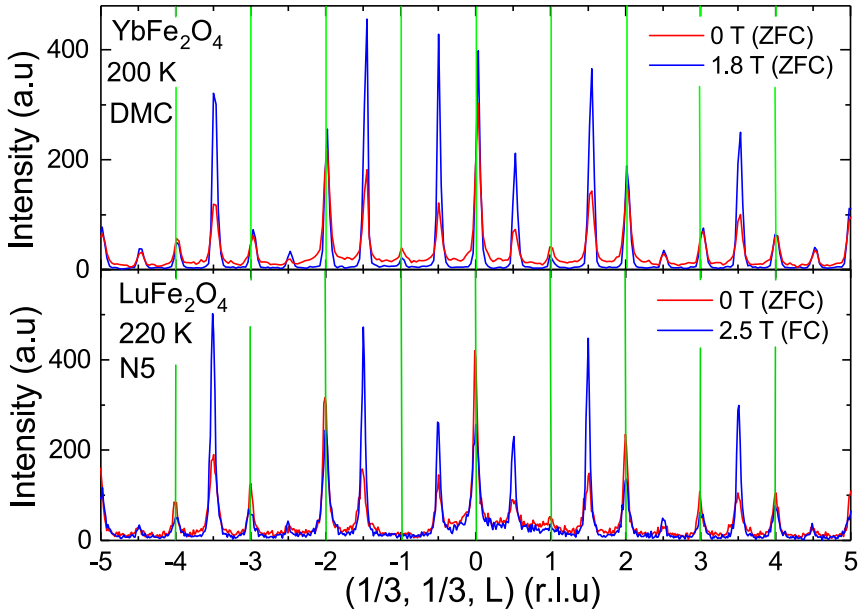

Figure 7.4: Neutron diffraction patterns along $(\frac{1}{3}, \frac{1}{3}, \ell)$. Top: $YbFe_2O_4$ (DMC) at 200 K in H=0 and H=1.8 T. Bottom: $LuFe_2O_4$ (N5) at 220 K in H=0 and H=2.5 T, figure taken from [32]. Green lines indicate integer and reflections along ℓ.

A similar experiment was first published on $LuFe_2O_4$ [26,32]. Here the magnetic domain population was investigated in both 0 (red curve) and 2.5 T (blue curve) at 220 K displayed in Fig. 7.4 (bottom), relevant to the onset of the T_N transition. The red diffraction pattern relates to the AFM phase, but based on the magnetic phase diagram of $LuFe_2O_4$ (see Fig. 5.15, bottom panel) this phase is only stabilized

up to ∼0.1 T, therefore, with the application of higher fields (2.5 T) the system will enter the high field ferrimagnetic phase. The AFM phase, which only in more recent years has been successfully established, was once deemed ferrimagnetic, the AFM phase was ruled out due to a lack of intensity at the $(\frac{1}{3}, \frac{1}{3}, 0)$ and other symmetry equivalent positions [104]. However, the dedicated study by [32] on the magnetic structure refinement of $LuFe_2O_4$ found that at 220 K in zero field an AFM phase was strongly apparent, where the absences of significant remanent magnetization (see Fig. 5.12, bottom) at this temperature is due most likely to compensating fM domains [104] (see Sections. 2.1 and 2.2). Furthermore, the magnetic peak intensities observed at both integer and half-integer positions followed by the emergence of increased intensity on structural reflections, led to the conclusion of a metamagnetic transition between two spin structures. The magnetic peak intensity at integer and half-integer positions are described by three propagation vectors analogous to those representing the CO superstructure reflections and related to a 120° twinning around c_{hex}: P_A=(hkl)+$(\frac{1}{3}, \frac{1}{3}, \frac{3}{2})$, P_B= (hkl)+ $(\frac{\bar{2}}{3}, \frac{1}{3}, \frac{3}{2})$ and P_C= (hkl)+ $(\frac{1}{3}, \frac{\bar{2}}{3}, \frac{3}{2})$ (see Sec. 7.2.2, Fig. 7.6). The following two subsections will compare the data obtained on highly stoichiometric $YbFe_2O_4$ neutron diffraction along $(\frac{1}{3}, \frac{1}{3}, \ell)$ in both zero and 1.8 T, to that previously obtained on $LuFe_2O_4$ in order to see if the relative spin structures and domain populations are the same.

7.2.1 Low field spin structure

The intensity at $(\frac{1}{3}, \frac{1}{3}, \ell)$ measured in the AFM phase of $YbFe_2O_4$ (at 200 K in zero field) shown in Fig. 7.4 (red plot). Compared to the in field data (1.8 T, blue curve), there is a diffuse background, similar to that observed in $LuFe_2O_4$ Fig. 7.4 (red plot). The diffuse nature of the AFM phase seen in both compounds in zero field is attributed to the microscopic competing fM domains, which would affect a completely long-range ordered state of the AFM phase. $YbFe_2O_4$ exhibits strong intensity of the $(\frac{1}{3}, \frac{1}{3}, 0)$ reflection in zero field, which eliminates this also being a ferrimagnetic phase [104], this is further exploited with a plot of the integrated intensity as a function of temperature in Fig. 7.2 (a), which for this reflection in zero field, shows a distinct drop in intensity at the T_{AFM} transition. This result is in good agreement with that published on $LuFe_2O_4$ [32], where strong intensity of this reflection was also observed. With additional intensity observed at structural reflections and a clear step feature seen in the M vs H curve of $LuFe_2O_4$ [32] and $YbFe_2O_4$ (see Fig. 7.3 top panel, black curve), indicates that there is a clear metamagnetic transition at 200 K in $YbFe_2O_4$ and 220 K in $LuFe_2O_4$ (see Fig. 7.2 (d)).

7.2.2 High field spin structure

The high field fM phase observed at 1.8 T is provided in Fig. 7.4 (top, blue plot). Interestingly the diffuse background seen for the zero field scan is almost negligible in applied field, contrary to that observed in $LuFe_2O_4$ which, seems to exhibit the same diffuse background to that of the zero field scan for the AFM phase. Although the fM phase seems to stabilize well in an applied field of 1.8 T, the relative FC $M(T)$ given in Sec. 5.2, Fig. 5.7, measured in fields up to 4 T show a feature related to the AFM transition up to 2.5 T. The M vs H given in Fig. 7.5, shows an upward

slope of the hysteresis, indicating that full saturation is not reached even in 9 T and an incomplete alignment of all ferrimagnetic domains remains.

For a more detailed analysis of the relative domain populations and intensity distribution, a second plot of the high field integrated intensities for $YbFe_2O_4$ (black curve) and $LuFe_2O_4$ is given in Fig. 7.6. To illustrate the three different domains the data for $LuFe_2O_4$ was colour coded for each domain: Domain 1 (blue), Domain 2 (green) and Domain 3 (orange), each containing both integer (solid line) and half-integer (dashed line) reflections. Again the relative intensities of both integer and half-integer reflections for each domain are in good agreement with those seen in $LuFe_2O_4$. There is some discrepancy with the relative intensities of the ($\frac{1}{3}$, $\frac{1}{3}$, -0.5) reflection; here the intensity for $LuFe_2O_4$ is half of that for $YbFe_2O_4$ along with a flattening of the ($\frac{1}{3}$, $\frac{1}{3}$, -1) reflection due to the dark angle of the magnet, where the beam at these positions partially and completely hit the magnet, respectively.

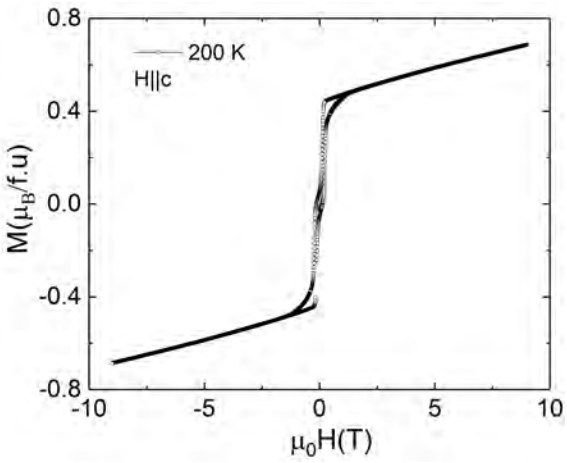

Figure 7.5: Magnetization as a function of Field for $YbFe_2O_4$ at 200 K.

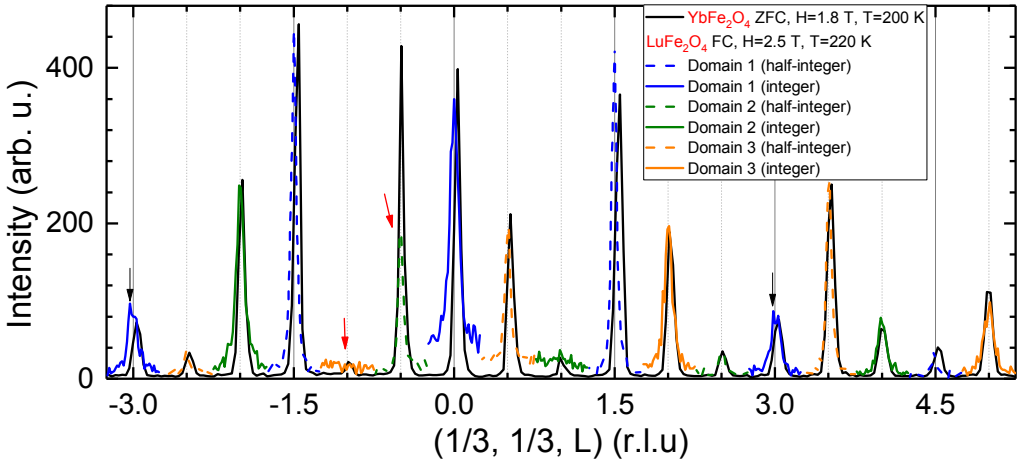

Figure 7.6: Integrated intensity of $YbFe_2O_4$ (black line) along ($\frac{1}{3}$, $\frac{1}{3}$, ℓ) at 200 K in H=1.8 T. A similar plot is also given for $LuFe_2O_4$ at 220 K in 2.5 T. The different colours used for various reflections represent the three magnetic domains: Domain 1 (blue), Domain 2 (green) and Domain 3 (orange), each consisting of integer (solid lines) and half-integer (dashed lines) reflections. The black arrows mark a secondary grain in $LuFe_2O_4$, red arrow show region of magnet dark angle for measurement on $LuFe_2O_4$. The data for $LuFe_2O_4$ was taken from [32] and adapted.

When comparing, also the intensities of half-integer and integer reflections in H=0 (AFM) and 1.8 T (fM), both systems exhibit greater intensity of half-integer reflection in applied field going from the AFM-fM phase. The intensity of integer reflections remains fairly consistent in both magnetic phases. Of course going from the fM phase to the AFM phase the intensity of half-integer reflection decreases, the difference is due to the AFM phase being less well established, as indicated by

the diffuse background in H=0 in both systems, and slightly broader peaks. Given that the relative intensity distribution for both systems is directly comparable for each domain and magnetic phase, including the complementary field dependence of the (1, 0, -0.5) reflection, not along ($\frac{1}{3}$, $\frac{1}{3}$, ℓ), which shows a similar trend to the magnetic hysteresis at 200 K, both the fM and AFM phases correspond to the same spin structure in both compounds. This spin structure, in $LuFe_2O_4$ was described with a $C2/m$ cell, though not consistent with a proper magnetic space group, (see Sec. 2.2) with a 2:1 spin arrangement in each Fe layer and each Fe bilayer, the same for all bilayers in the fM phase. In the AFM phase, all spins are reversed in every second bilayer [32]. The final non-valence resolved spin structure, which is analogous to that observed in $LuFe_2O_4$ is given Fig. 7.7, with the AFM (low field) spin structure at the top and fM (high field) spin structure at the bottom.

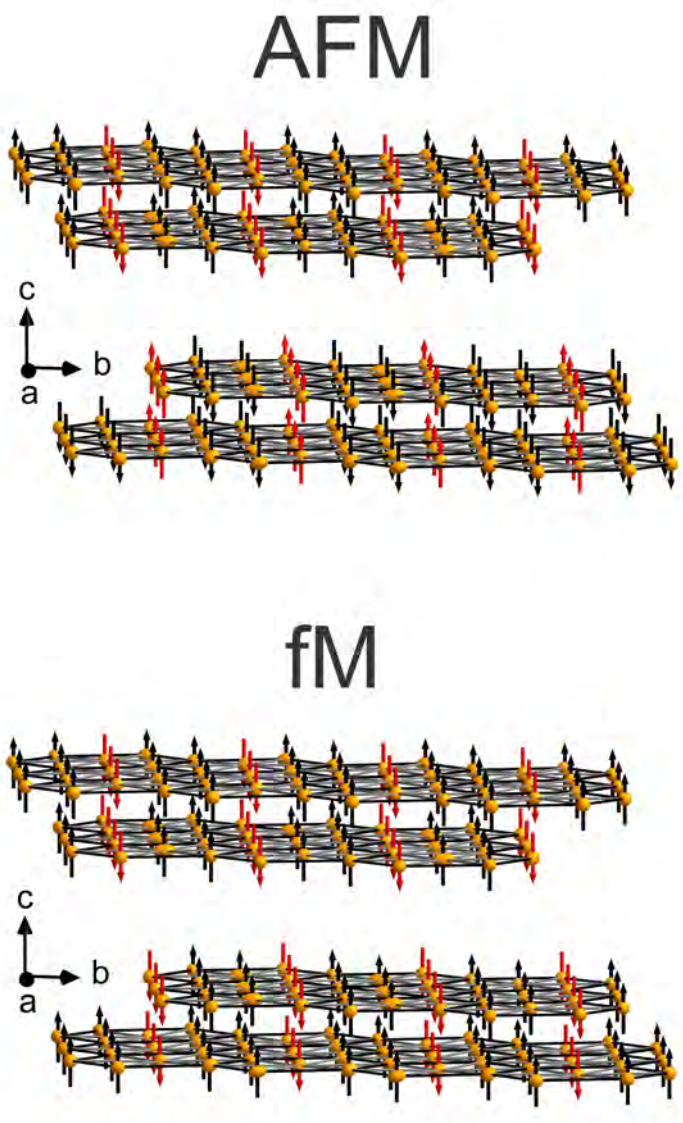

Figure 7.7: Not valence resolved 2:1 spin up (black arrows) spin down (red arrows) low and high field spin structures, respectively, for $LuFe_2O_4$ and $YbFe_2O_4$. Top: AFM low field spin structure. Bottom: fM high field spin structure. Orange atoms represent Fe atoms in each bilayer.

Since the new refinement of $YbFe_2O_4$ in the $P\bar{1}$ space group, detailed in the

previous Chapter, it is likely that the magnetic space group describing the spin structure is also of lower symmetry. This will be discussed, along with combined spin and charge order, the latter solved using x-ray magnetic circular dichroism (XMCD) data, in the following section.

7.3 Combined spin and charge order

7.3.1 X-ray magnetic circular dichroism

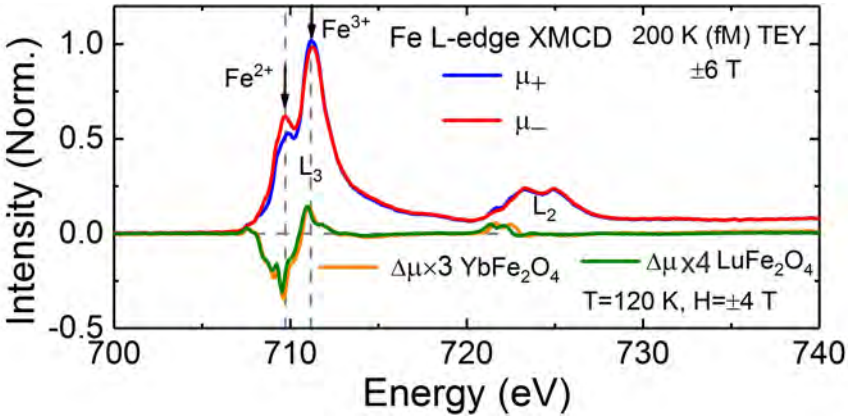

Figure 7.8: XMCD spectra across the Fe $L_{2/3}$ measured with total electron yield (TEY). The blue and red curves are the measured circular dichroism for $YbFe_2O_4$, μ_+ and μ_-, respectively. Each dichroism was treated with a linear background subtraction. The XMCD data $\Delta\mu \times 3$ (orange curve) was calculated by subtracting μ_- from μ_+. Complementary XMCD data $\Delta\mu \times 4$ (green curve) on $LuFe_2O_4$ is also plotted and measured in applied fields of $\pm$ 4 T at 120 K.

The X-ray magnetic circular dichroism (XMCD) presented in this section was measured at the beamline 4-I-DC of the advanced photon source (APS) [1]. The data obtained from $YbFe_2O_4$ was measured at the Fe $L_{2/3}$ edges at 200 K in applied fields of $\pm 6\,\mathrm{T}||c_{hex}$ and is displayed in Fig. 7.8 (orange curve). The XMCD signal of $LuFe_2O_4$ is also included in Fig. 7.8 (green curve), taken from [26, 48]. The two polarizations, or x-ray absorption spectra (XAS) μ_- and μ_+ were each treated with a linear background subtraction and normalized. The XMCD signal for $YbFe_2O_4$ (orange curve) $LuFe_2O_4$ (green curve) was then calculated from the difference between μ_+ and μ_-, measured with total electron yield. The two sets of XMCD data provided in Fig. 7.8 show a very similar curve, indicating the same Fe^{2+} and Fe^{3+} spin arrangement. No previously published XMCD studies exist for $YbFe_2O_4$, however three studies currently reside on the $LuFe_2O_4$ ([115, 116]). The first two of those were performed on samples which exhibit no long-range charge or magnetic order, the last of three, published by de Groot *et al.* [48], was measured on a highly stoichiometric $LuFe_2O_4$ single crystal. From all three studies, regardless of stoichiometry, the same high field fM spin structure results: all Fe^{2+} and $\frac{1}{3}$ of Fe^{3+} spins point in the field direction direction, the remaining $\frac{2}{3}$ of Fe^{3+} spins point opposite to H.

[1] The sample was measured as a backup sample by two colleagues Dr Waschk and Dr Mueller, and hence, only the final result is presented in this thesis for further information on XMCD, please refer to the following text [114, 141].

The large downward peak (see Fig. 7.8 (orange curve)) is larger due to the Fe^{2+} net moment, which is 3 ↑ per 3 spins, whereas the Fe^{3+} net moment is per three spins.

7.3.2 High and low field combined spin and charge structures

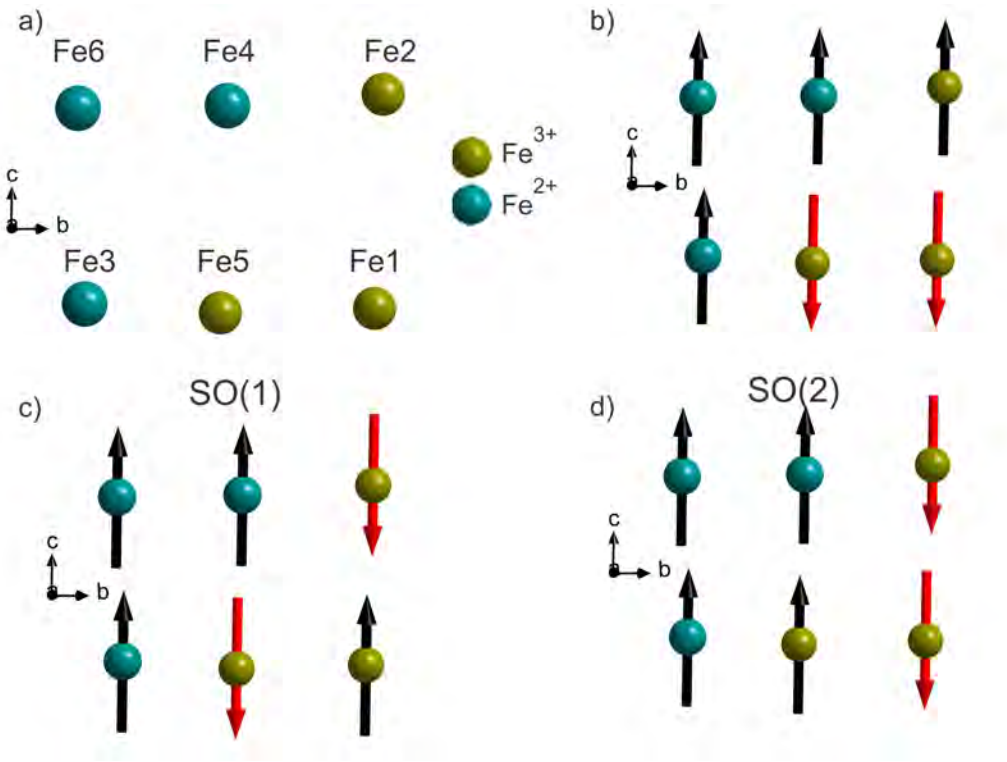

Figure 7.9: a) the 6 Fe sites and valences of the top bilayer of the unit cell. b) spin arrangement taking Fe2 as ↑. c) spin arrangement taking Fe1 as ↑ and d) the final spin configuration taking the Fe5 ion ↑. The altered Fe^{3+} ion is differentiated by a black arrow, in accordance with the Fe^{3+} sites.

Since both systems exhibit the same XMCD result in the high field fM phase, it is now essential to establish the correct combined spin and charge order arrangement in the new $P\bar{1}$ cell. From XMCD we see that all Fe^{2+} ions are spin up, and 2/3s of Fe^{3+} ions have spin down, leaving 1/3 of the remaining Fe^{3+} sites with spin up. In order assign the correct spins, we can use the already established BVS, calculated in Sec. 6.4 and given in Fig. 6.19 (right) for the $P\bar{1}$ cell at 200 K. The valence distribution in a single bilayer is illustrated in Fig. 7.9, with each atom labeled by site. In this case the sites Fe2, Fe5 and Fe1 are the sites that can take either spin up or down. Now, as it was stated in the previous sections and in Chapter. 2, the magnetic refinement of $LuFe_2O_4$ by [32] did not yield a proper magnetic space group. In particular, for the spin structure with H=0 (AFM phase), on a crystal refined in $C2/m$, conform to 4 possible magnetic spaced groups corresponding to one of four irreducible representations. However, for both high and low field spin configurations this was not the case. Trials were performed with symmetry equivalent structures (shifted cell) and testing structures with each of the two inversion centers in the monoclinic cell, because the spins on different sites order according to different representation, but of the 40 possible structures, all were inconsistent with the measured neutron diffraction data [32]. However since, it is now clear that the correct crystallographic

structure is in fact $P\bar{1}$, where it was shown in Fig. 6.14 that the simulated intensities along $(\frac{1}{3}, \frac{1}{3}, \ell)$ in the $C2/m$ space group grossly underestimates the intensities at integer positions that are present in $LuFe_2O_4$ (see Sec. 6.1.1), it therefore stands to good reason the magnetic space group also is a triclinic one, and for the high field fM phase the spins also order in the $P\bar{1}$ magnetic space group. To test this, a set of 3 bilayers, is also shown in Fig. 7.9. Assuming the proper magnetic space group $P\bar{1}$, there are only 3 possible spin configurations which can result, by taking either Fe1, Fe2 or Fe5 as spin up. The use of only one bilayer stems from the fact that in the $P\bar{1}$ space group, inversion symmetry is preserved, but when in the fM phase the inversion does not in effect invert the spin direction as it is being described by the $P\bar{1}$ magnetic space group. The only other option from symmetry analysis is the $P\bar{1}'$ magnetic space group, but this would not provide a net magnetic moment and therefore not relatable to the fM phase (which has a net moment). In Fig. 7.9 b), taking the Fe2 as spin up gives the top layer of the bilayer with all spins pointing up. This possibility violates the 2:1 ratio of spin up to spin down on the triangular lattice, and is therefore not a possible candidate for the final spin arrangement [116].

Site	Val.	SO(1)	SO(2)
Fe1	3+	↑	↓
Fe2	2+	↑	↑
Fe3	2+	↑	↑
Fe4	2+	↑	↑
Fe5	3+	↓	↑
Fe6	3+	↓	↓

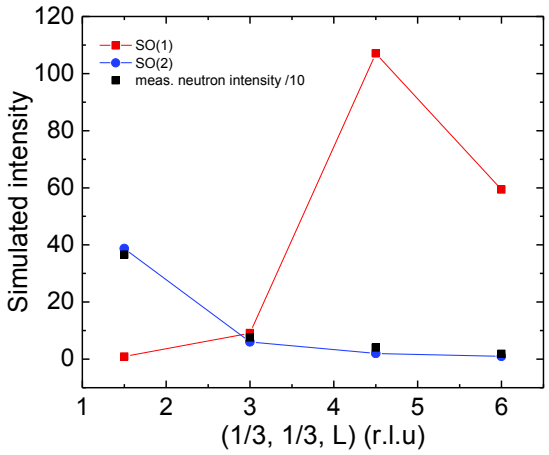

Figure 7.10: Left: the two possible spin configurations when considering either Fe1 or Fe5 ions with spin up, for the high field fM phase. Right: simulated square of the magnetic structure factor (not taking into account magnetic form factor and similar corrections) for SO(1) (red squares) and SO(2) (blue circles), along with the measured neutron intensities (black squares).

The final two possible spin structures in Fig. 7.9 are obtained by; taking either the Fe5 (c) or the Fe1 (d) spin up, each provides the correct spin structure based on this illustration, just for two different domains. Therefore, to find the correct solution, one can simulate the magnetic intensities for a comparison to the already established neutron diffraction, to see if it matches with one of the two possible spin arrangements. The table given in Fig. 7.10 shows the two possible spin orders; SO(1) relating to panel c) of Fig. 7.9 and SO(2) relating to panel d) of Fig. 7.9. The simulated squares of the magnetic structure factor are plotted in Fig. 7.10 (right) for SO(1) (red squares) and SO(2) (blue squares), along with the scaled neutron intensities (black squares). The common scale factor (in this case /10) is needed due variations in the neutron flux and the sample size.

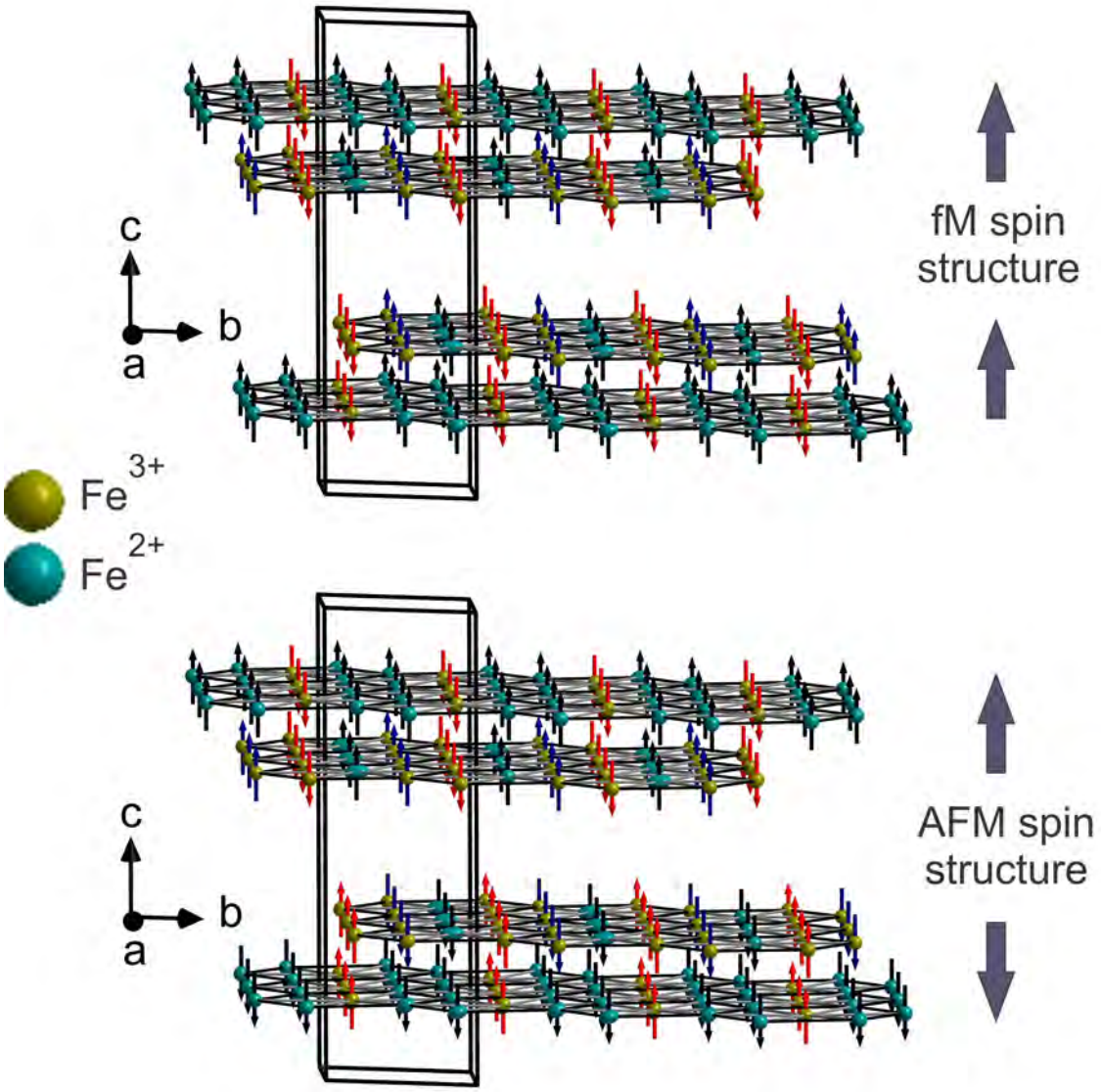

Figure 7.11: The combined spin and CO superstructure in the refined $P\bar{1}$ cell. Top: ferrimagnetic spin structure. Bottom: antiferromagnetic spin structure. The arrows indicate bilayer net magnetization.

However, it is clear that the intensities of SO(2), which takes the Fe1 ion as spin down, clearly has a very different intensity distribution compared to SO(1). Both the measured neutron data (blue squares) and the simulated square of the magnetic structure factor of SO(1) are in very good agreement, indicating that this is the correct spin and charge order arrangement. Therefore, the correct high field fM spin and charge order is that of SO(2) and illustrated in Fig. 7.11 (top), the grey arrows indicate the overall magnetic moment of each bilayer. This does, however, leave the case of the low field spin structure and AFM phase. As it is now clear that the spin structure for the fM phase is described by the proper magnetic space group $P\bar{1}$, from symmetry analysis there is one alternative magnetic space group $P\bar{1}'$. The rule for plotting the AFM structure, from the already established fM phase, is to

maintain all spins in one bilayer, and to invert all other spins in the second bilayer, as depicted in Fig. 7.11 (bottom). This spin arrangement conforms nicely to the proper magnetic space group $P\bar{1}'$ since in this case inversion symmetry inverts the spin direction. The two final structures are now clearly defined by proper magnetic space groups, they are in fact analogous to that observed in $LuFe_2O_4$ by [32], the spin arrangement is the same as shown in Fig. 7.7, but the initial oversight of the lack of intensity at integer positions along c_{hex}, resulted in a refinement in the higher symmetry $C2/m$ space group. Despite $LuFe_2O_4$ maintaining its incommensurate CO structure (but viewed still in a commensurate approximation), both systems crystallographically can be described by the $P\bar{1}$ space group, and for each of the spin structures, proper magnetic space groups; $P\bar{1}$ for the fM phase and $P\bar{1}'$ for the AFM phase, respectively.

The very final point of call, as with the established modes that contribute to the CO as described in Sec. 6.6, it is important to see which modes contribute to the magnetic ordering in these systems. Using the same approach in Sec. 6.6, but instead of normalized valences, normalized spins are used for the matrix calculation. The resulting modes calculated for the fM spin arrangement are; mY1(a,0)=-1 mΣ2(a,0)=2/3, and mΓ2+=1/3. The final modes also calculated for the AFM spin arrangement are: mY1(0,a)=2/3, mΣ2(0,a)=1 and mT1+=-1/3. In terms of the fM phase, the three propagation vectors describing the magnetic order are mY1=($\frac{1}{3}$, $\frac{1}{3}$, $\frac{3}{2}$), mΣ2=($\frac{1}{3}$, $\frac{1}{3}$, 0) and mΓ2+=(0, 0, 0), together providing a match for all reflections seen in the neutron data shown in Fig. 7.4. The mΓ2+=(0, 0, 0) is an essential mode, that allows for a net moment. Similarly, for the AFM phase the corresponding propagation vectors are; mY1=($\frac{1}{3}$, $\frac{1}{3}$, $\frac{3}{2}$), mΣ2=($\frac{1}{3}$, -$\frac{2}{3}$, 0) and mT1+=(0, 0, $\frac{3}{2}$), and relate to all reflections observed in this magnetic phase by [32], where the mΣ2=($\frac{1}{3}$, -$\frac{2}{3}$, 0) is symmetry equivalent to ($\frac{1}{3}$, $\frac{1}{3}$, 0). It was the absence of seeing intensity at (0, 0, $\frac{3}{2}$) type positions in previous refinements by [104] that led to the initial overlook of a secondary AFM phase, and only a contribution of the mΣ2=($\frac{1}{3}$, $\frac{1}{3}$, 0) mode in the fM phase. These results are in good agreement with those published by [32], but now classified in two proper magnetic space groups $P\bar{1}$ (fM phase) and $P\bar{1}'$ (AFM phase). Therefore the final combined spin and charge order is established in the $P\bar{1}$ space group, the final charge order structure is that of anti-polar bilayers which results in an antiferroelectric state.

7.4 Discussion

The final combined spin and charge order of $YbFe_2O_4$ has now been established in the $P\bar{1}$ space group. The former, for the first time is described by two proper magnetic space groups, namely $P\bar{1}$ and $P\bar{1}'$. It was, the correct refinement of the CO structure in $P\bar{1}$, (discussed in detail in Chapter. 6), which led to the correct respective structures for each magnetic phase, contrary to that published by [32] for $LuFe_2O_4$, which saw discrepancies with the observed reflections and the tested 4 possible magnetic space groups from symmetry analysis. From all of the work presented in this thesis, there is a very strong scientific case that both systems exhibit the same crystal and magnetic structure, at least apart from the incommensuration for $LuFe_2O_4$, which persist there for all temperatures. Although $LuFe_2O_4$ does not transition into a commensurate CO phase, intensity at both ($\frac{1}{3}\pm\tau$, $\frac{1}{3}\mp 2\tau$, 15) and ($\pm\tau$, $\pm\tau$, $\frac{3}{2}$) type positions is there, but the $C2/m$ symmetry largely underes-

timates the intensity of integer reflections, which resulted in the higher symmetry monoclinic space group. As highlighted in Chapter 6, the proposition that the magnetic interactions may be a relevant part of the driving force for CO was considered based on the commensurate nature of the magnetic order, and the incommensuration in τ observed for $LuFe_2O_4$ as the temperature starts to reach T_N [106]. This was further emphasized by the observation of a completely commensurate CO phase in $YbFe_2O_4$, where the magnetic correlations in $YbFe_2O_4$ are notably strong compared to $LuFe_2O_4$, seen also in classically deemed off-stoichiometric samples, which, through polarized neutron diffraction, saw 3D peak intensity in such samples. This could provide some explanation as to why $YbFe_2O_4$ enters into a commensurate CO phase. Our experimental findings are in good agreement with a theoretical study by Xiang *et al.* [25] (though on $LuFe_2O_4$), which expresses that exchange energy gain may be one aspect that drives the CO. In part of this study they look at presence of spin-charge coupling with two models, considering the spin ordering in terms of a 1D chain (chains of Fe^{2+} ions alternate with 1D chains of Fe^{3+}) and in a $\sqrt{3} \times \sqrt{3}$ CO state. From two previous electrostatic calculations by [54, 216] it was determined that the 1D chain model is only slightly less stable than the $\sqrt{3} \times \sqrt{3}$ CO case, and exhibits no ferroelectric polarization. For the latter case, their spin and charge configuration for one bilayer is exactly the same as the one established experimentally in this thesis. The same examination of the spin ordering in these two CO regimes by [25] discovered that there is in fact a large difference between the 1D chain and typical $\sqrt{3} \times \sqrt{3}$ CO, where the calculated total spin moments are 0 and 2.33 $\mu_B/f.u.$, respectively. This result is highly evidential of spin-charge coupling in $LuFe_2O_4$. Furthermore, it was predicted that a magnetic field stabilizes the fM $\sqrt{3} \times \sqrt{3}$ CO state due to the Zeeman effect, which is observed in $YbFe_2O_4$, in the low and high field neutron diffraction data. It is more obvious in $YbFe_2O_4$, as a large depreciation of the diffuse component is seen, when a field of H=1.8 T is applied, than in $LuFe_2O_4$ there is still some diffuse order even with H=2.5 T. However, this is not surprising since the magnetic correlations in $YbFe_2O_4$ are stronger along c_{hex}. Lastly, more recent inelastic neutron studies on $LuFe_2O_4$ by [218] also highlighted the presence of spin-charge bilayer superstructure, pertaining to one Fe^{2+} rich monolayer and one Fe^{3+} rich monolayer, which is in agreement with our findings, however they propose a polar CO structure in contrast to our polar bilayers stacked antiferroelectrically. With theoretical grounding as well as the experimental work and analysis provided in this chapter, it is reasonable to state that both systems exhibit spin-charge coupling, where the exchange energy gain in the spin order maybe one of the driving forces for the CO. One important question remains open: Is this a proper antiferroelectric material or just a polar one. The former scenario implies the possibility of flipping of one of the bilayers, by application of a steady and constant electric field to reach a ferroelectric state. This final question and its implications in terms of applications and the future of these systems is discussed in more detail in the following, final chapter.

8 | Summary and outlook

In this thesis, $YbFe_2O_4$ was examined for the first time in a different light, due to the growth of highly stoichiometric single crystals exhibiting 3D incommensurate and 3D commensurate charge order, which had not be observed previously. With a large portion of this thesis dedicated to the refinement of the crystallographic structure, finding a space group that incorporated all superstructure reflections observed, with the correct relative intensities was achieved in the remarkably low-symmetry space group $P\bar{1}$. This space group applies for temperatures below 280 K, with (for some samples) the structure incommensurately modulated at higher temperatures until heating above the main CO transition T_{inCO}=305 K, above which only diffuse 2D CO exists, and is described by the original $R\bar{3}m$ cell. A strong focus was placed on the synthesis of highly stoichiometric crystals of $YbFe_2O_4$, by trial and error using different gas ratios to tune and establish the optimum conditions for producing, what would be classed as samples exhibiting truly intrinsic properties, not smeared by oxygen off-stoichiometry [118, 121, 123]. It was determined, that the optimum gas ratio for growth was that of $CO:CO_2$=1:2.5, where many of the single crystals obtained from this boule exhibited long-range CO as seen in in-house single crystal x-ray diffraction. Of the many samples analyzed, there were three types of CO which can occur in $YbFe_2O_4$ (see Sec. 4.2.3, Fig. 4.7): Type 1 contains only 2D CO correlations, Type 2 samples show the same incommensurate behavior as highly stoichiometric $LuFe_2O_4$ at T_{inCO}=305 K but on further cooling below 280 K, sees a phase transition to a commensurate CO state T_{CCO}, the final Type 3 charge order is commensurate at all temperatures, with an increase of intensity on cooling of each CO domain. Detailed macroscopic measurements were performed on a sample with Type 2 CO, which allowed the successful establishment of the magnetic phase diagram for $YbFe_2O_4$. It was here that many large similarities were observed between the two magnetic phases present in both $YbFe_2O_4$ and $LuFe_2O_4$, each showing only a small region of stabilization of the AFM phase, with the AFM phase in $YbFe_2O_4$ being stable in slightly higher fields. A large contrast was observed in the temperature range ∼260-240 K, here the fM phase is stable in H=0, which means highly stoichiometric $YbFe_2O_4$ exhibits a spontaneous fM, in contrast to $LuFe_2O_4$.

The final refinements in the $P\bar{1}$ space group at 90 K and 200 K elucidated the occurrence of a very subtle magneto-structural transition, proposed below T_{LT} in $LuFe_2O_4$ [104], but a refinement in the $P1$ symmetry at 90 K will resolve any speculation of a symmetry change due to these structural distortions at lower temperature. The bond valence sum analysis analysis at each temperature resulted in polar bilayers stacked antiferroelectrically. This is in contrast to the previous refinement by [48], which resulted in a final cell $C2/m$ and a CO representative of charged bilayers, and to the initially proposed polar bilayers and ferroelectricity by [63]. The refinement in

the higher symmetry $C2/m$ cell [48], was performed in a commensurate approximation, but as we have seen from the refinements performed on $YbFe_2O_4$ in this thesis, substantial intensity lies on both integer and half-integer positions, the former being relatively weak in $LuFe_2O_4$ due to the dis-commensurations of τ. As $YbFe_2O_4$ is nudged to a commensurate CO phase, the temperature dependence viewing $hh\ell$ plane was studied with high energy x-ray diffraction and a MAR imaging plate. By plotting the intensity as a function of temperature of a specific τ incommensuration for example ($\frac{1}{3}\pm\tau$, $\frac{1}{3}\mp 2\tau$, 15), it was clear that the intensity is strong at τ positions, and since the CO in $LuFe_2O_4$ remains incommensurate down to low temperature, the commensurate approximation will not account for the intensity observed at τ satellites. Furthermore, when simulating the intensities observed in $YbFe_2O_4$ below T_{CCO}, in the $C2/m$ space group, a clear underestimation of integer reflections is seen in the model. However, it is likely that had there been no commensurate CO phase in $YbFe_2O_4$, the same issues with integration of integer reflections would most likely result in the same apparent $C2/m$ structure.

Neutron diffraction data, provided a relative intensity distribution of reflections along ($\frac{1}{3}$, $\frac{1}{3}$, ℓ) equal to that observed in $LuFe_2O_4$, and with the newly established cell, both high and low field spin structures are now assigned to proper magnetic space groups; $P\bar{1}$ (fM) and $P\bar{1}'$ (AFM). The final point of call was to look at the combined spin-charge coupling using XMCD data measured on $YbFe_2O_4$, and again the results are analogous to those on $LuFe_2O_4$. The final spin-charge structure was established, using the initial assumption of the crystallographic space group being $P\bar{1}$, the relative magnetic structures from symmetry analysis would conform. From the XMCD result, 1/3 of the Fe^{3+} ions must take spin up, giving a possibility of 3 spin configurations which needed to be tested, to establish the correct final spin-charge structure. Of those three, one presented an automatic expulsion due to one of the Fe layers presenting only spin up, violating the necessary 2:1 ratio of spin up to spin down. The remaining two, from visual representation were possible candidates. The final spin configuration representative of the data collected on $YbFe_2O_4$, was determined by simulating the intensities of some integer and half-integer reflections (in one magnetic domain) for each of the two spin configurations. It was here that one spin structure presented very unrealistic intensities not consistent with the measured neutron diffraction data. The remaining spin structure was in good agreement with the measured data and thus resulted in the final combined spin-charge structure, consistent with x-ray, neutron diffraction and XMCD, and having symmetry of proper magnetic space groups. Spin-charge coupling, also supported by earlier theoretical studies [25] highlights $YbFe_2O_4$ and $LuFe_2O_4$ as true candidates for possible technological applications. More so in the case of $YbFe_2O_4$, which based on the results in this thesis presents stronger magnetic correlations compared to $LuFe_2O_4$. This was first observed in polarized neutron diffraction on an off-stoichiometric sample, which at 200 K exhibited clear 3D peaks as well as a significant diffuse background. The stronger magnetic correlations in $YbFe_2O_4$, may be one aspect which influences the newly observed commensurate CO phase. The question remains, is the CO in $YbFe_2O_4$ the same as $LuFe_2O_4$? there is strong scientific grounding, provided in the previous chapters to indicate that yes, in fact they are essentially the same. But it was the subtle differences in $YbFe_2O_4$, that allowed for the clear and correct picture for both compounds. Therefore, both $YbFe_2O_4$

and $LuFe_2O_4$ present antiferroelectricity, from anti-polar bilayers, but is it a proper antiferroelectic? , i.e. switchable into a polar structure by application of an electric field. This is a key remaining question, which must be elucidated. Switchability of the CO by an electric field along with the spontaneous fM phase, somewhat close to room temperature, would in principle provide all the elements required to be fully functional in electronic devices. However, given that the resistivity is similar as in $LuFe_2O_4$, for which experiments by several groups have excluded the possibility of switching the CO with an electric field [25,176], this is unlikely. Nevertheless, a direct test on $YbFe_2O_4$ should be done. There are still some further unanswered questions remaining, such as what effect Yb has at lower temperatures, the observation of a Schottky anomaly in the specific heat, and broad features in the magnetization below 50 K show distinct ordering of Yb^{3+}. A clear understanding of the magnetic behavior below T_{LT} in $YbFe_2O_4$ is still required, as this was not of primary focus in this work. Spanning out further than the RFe_2O_4 series, a closer look at RFe_3O_7 systems could provide a naturally occurring ferroelectric state due to the nature of the bilayer stacking in the unit cell. In conclusion, three very important results have been achieved , the discovery of a commensurate CO phase in $YbFe_2O_4$ which led to the correct refinement in the $P\bar{1}$ cell, representative also of $LuFe_2O_4$. For the first time mapping the magnetic phase diagram uncovered a spontaneous fM phase not present in $LuFe_2O_4$, and lastly, the combined spin and CO structure representative of both $YbFe_2O_4$ and $LuFe_2O_4$.

9 | Acknowledgements

Just like every Oscar speech ever written, I shall try to give my best Meryl Streep performance. I would like to thank the following people, for all their support, guidance and teaching over the last years. The latter is not only physics specific but in some cases all areas of my life. P.S, if I have forgotten anyone at all I do apologize, it is not a reflection on you, but how frazzled my brain is after writing this detailed list of events, which have transpired over what seems like a millennia. I write my thanks to the following:

Prof. Manuel Angst for being a great supervisor, we shared a large number of beamtimes and conferences together. Our best ideas often came from a stroll outside and a ciggy break. You always allow students to pursue their own interests, which is fantastic as the student from the beginning starts to think independently. I will never forget one of the times we were in Oakridge, Tennessee and it was just the trip from hell. But oh so funny. Thank you for being a great teacher and advisor, but also someone that I felt comfortable to talk to when I needed.

Prof. Thomas Brückel for allowing me the opportunity to conduct my PhD research in this institute. Without this I may not have solved the final structures of $YbFe_2O_4$ and $LuFe_2O_4$.

Dr. Karen Friese always made time when she could to help with any crystallographic questions or data which was not playing ball. Your knowledge of this topic is endless.

Dr. Yixi Su and Dr. Kirill Nemkovski for their helpful assistance at the beamline DNS, for daring to measure a tiny 3.5 mg single crystal, pushing those boundaries saw for the first time 3D magnetic order in $YbFe_2O_4$. Thanks for believing.

Dr. Matthias Frontzek for being a fantastic collaborator and friend. I enjoyed the time we spent at the beamline DMC, and for subbing the pizza. I owe you a pizza I think. I also really enjoyed the opportunity of giving my first seminar talk at the institute.

Dr. Douglas Robinson thank you for the detailed help when measuring at 6-ID-D, the notes you wrote on the Displex system were paramount, and really helped us work more independently on the beamline.

Dr. Songxue Chi in providing a superb user support, and generally making each trip more worthwhile. The beamline is fantastic. The data is still yet to be published but it will make a distinct mark.

Dr. Astrid Schneidewind and Dr.Čermák although I did not get enough time on PANDA, I would have liked more. The data I obtained was not only useful, but I really feel like the organization of user time; set-up, measuring time, problem solving and data analysis was on point. Apparently comparable to NIST, although

I am yet to measure there. The aid you provide the user does hasten the data processing, to a point in which it can be published. This is so often overlooked. I really enjoyed this aspect at PANDA.

Dr. Karel Prokes and Dr. Fabiano Yokaichiya both of you I could ditto to my monologue provided for the PANDA beamline. Fabiano, and your general interest with each users work, made it a pleasure to work with you. I was alone for the week long beamline, but I did not feel it. Thanks for all your help then. Karel, your humor will always bring a smile to my face.

Dr. Ryoichi Kajimoto and Dr. Mitsutaka Nakamura the chance to measure at the beamline 4SEASONS, so early on in my journey as a master student/PhD student really allowed me to grow as a researcher. It was a tough beamline to start with, but your generous, extremely punctual support before, during and after really made a difference. Thank you.

Dr. Thomas Muller and Dr. Markus Wasck I thank you not only for performing a very helpful XMCD measurement together for me. But your friendship to me over the years. We have all helped each other and care about if the other is okay. The laughs and the beers along the way (coke for tom) have been something I will always remember. Good luck in your new endeavors guys and thank you.

Alice klapper, Dr Markus Schmitz, Dr. Johannes Reim, Paul Hering, Dr. Xiao Sun, Dr. Pankaj Thakuria, Tobias Cronert... I decided to make this a little more personal than putting you directly into the JCNS-2 category. Also including Tom and Markus above, I could not have wished to have worked with a better group of PhD students. For both my masters and PhD, the experiences we all had together... P.o.F rehearsal... and the romantic get away some of you may remember in Tutzing, will always leave a warm place in all our hearts. You guys are the best. Thank you for everything.

Dr. Paul Zakalek I reserved a special spot for you, right here. All of the above sentiment applies, but the creation of the peak-finder software and you kindly sparing time to help me with issues of programming, saved me more times than I can count. Thank you so much HBS king.

Jörg Perßon and his guidance with all students when synthesis and crystal growth was needed.

Dr. Arthur Glavic for his creation of the plot program to handle and analyze DNS data.

Barbara and Laura I have to say, I think you both have the hardest jobs in the institute. I will shout from the roof tops gladly to whom will listen, about how many times you have both helped me in a time of crisis. Both with actions and a gentle ear to listen. JCNS-2 is lucky to have both of you keeping things in check.

Frank, Micha, Guido, Robert, Bodo and Berthold I think the whole Forschungszentrum would come to a standstill if none of you turned up to work one day. You are all national treasures, each in your own right. On this account I really am speechless (I know!) because I don't think any of the words would do justice to how much you give to the institute. Robert, I still have your copy of twin peaks... Thank you all from the bottom of my heart, for all the time you gave me to help me get to this point right now. For the last minute sample holders, in which you smiled and 30 mins later handed it to me. All of you have this ability to fix anything, even if its just been set on fire and burned to ash, some how you will fix it. Awesome.

I would also like to thank all the young investigator group members Dr. Pankaj Thakuria, Sabreen Hammouda, Georgi Khazaradze, Dr. Joost de Groot, Dr. Shilpa Adiga. Working with all of you over the years has certainly been a highlight in my life. Good luck to you all. Support from the initiative and networking fund of Helmholtz Association by funding the Helmholtz University Young Investigator Group "Complex Ordering Phenomena in Multifunctional Oxides" is gratefully acknowledged.

I would like to extend my thanks to the whole of the JCNS-2/PGI-4 institute, for allowing me to be part of the family and making the working environment very pleasant.

Lastly, but by far the least, I would like to thank my family and friends for all their support over the last years. Mum and dad, I feel on some level I do not deserve to have such wonderful parents. Thank you for always being by my side, and believing in me when I cannot see the light. I have had best friends in my life time. But none that match up to Shirin, she has been there through the good times but also the bad. I would not be sat here writing this last part of the thesis without you by my side. You never gave up on me, and boy did you come to my rescue a number of times. I will be grateful to you for what you have done for the rest of my life. Thank you. Adi, Jess and Salome, although you came into my life more recently, I can say for the first time, that the duration of a friendship does not always dictate how good the bond is. I am grateful to you all so much. Thanks for caring. To all the people that I loved and cared about, but are no longer here in person, this thesis is for you.

A final note: one lesson I have learned, which I feel is perhaps more profound on a cosmic level, is not what is obtained through qualification or career advancement (these are a given) but the interactions and bonds we form as people, and to other people. I will confess that without a certain small number of people, still believing in me, still giving me the will and energy to carry on, I may have never finished. Or I would have been completely numb by the end. Another important lesson- never assume anyone seems okay, ask them how they are. The chances are you may help more than you know just by a kind few words. We determine who were are, how we act and how we can change the world, no matter how small it may be. It is the help, love and support of people which can make a difference. I was never a fan of group work as a child, as most of the time I had to do the work by myself. However as adults, I feel the mutual collaboration between individuals is what inspires us, regardless of the context, take this away and you are left with a difficult road ahead of you. So pay it forward. Buy a coffee for the person behind you, take some left over food to someone that is hungry, because you never know what happened to this person before they got into that situation. A small gesture is all it takes to change someones day around. Lastly, I shall finish by saying that I am extremely proud of this thesis, the obstacles faced did not deter me, it did not define me, it did change how I view life, and for that I am grateful. I hereby lay to rest, the final interpretation of $YbFe_2O_4$ and $LuFe_2O_4$.

A | Appendix 1

A.1 Further heat capacity analysis

The data shown in Fig. A.1 shows the steps taken to fit the low temperature Schottky anomaly.

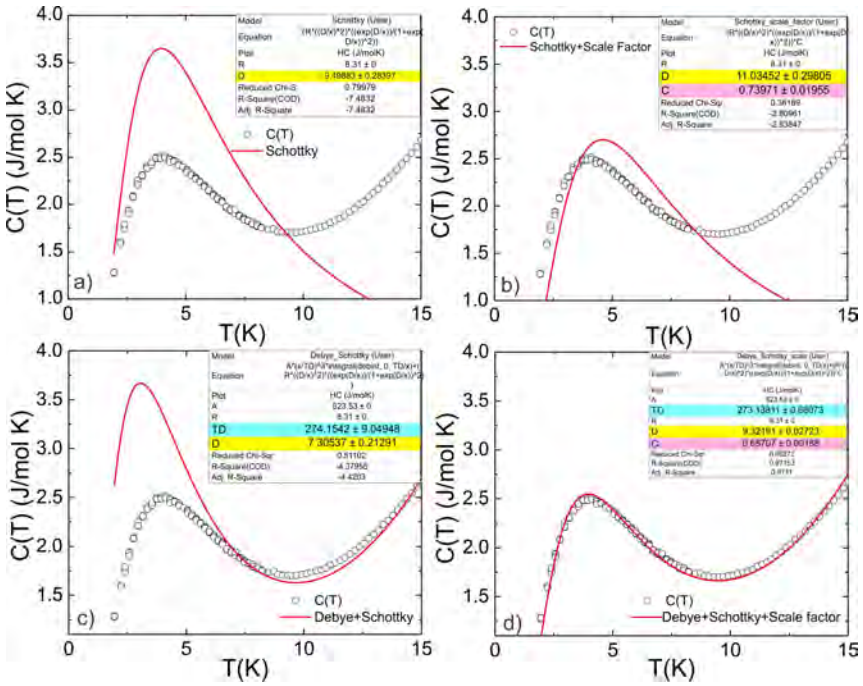

Figure A.1: Low temperature fits of the specific heat capacity for $YbFe_2O_4$: a) Schottky contribution b) Schottky contribution times a scale factor c) Debye approximation plus Schottky contribution and d) Debye approximation plus Schottky contribution times a scale factor. Highlighted rows in tables represent values obtained for energy gap Δ (D) (yellow) in the Schottky contribution, the Scale factor C (pink) and the Debye temperature T_Θ (TD).

A.2 Incommensurate peak intensity of $LuFe_2O_4$

The figure given here, shows the 2D integration of the incommensurate satellites around $(\frac{2}{3}, \frac{2}{3}, \ell)$.

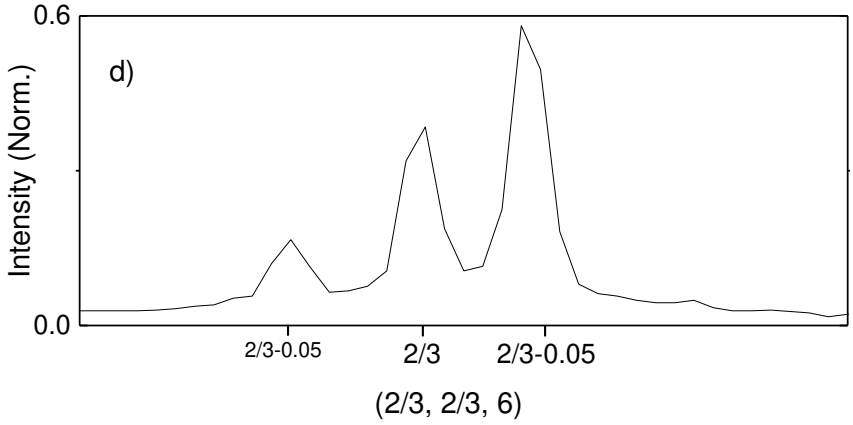

Figure A.2: A 2D line box integration in hh of incommensurate CO region in $LuFe_2O_4$

A.3 Conversion of ADP parameters

The ADP's refined by [75] were given in terms of the anisotropic β factor. In order to compare them with data provide in this work the values were converted using the following relations; given that $B_{11} = B_{22} = B_{33} = B(iso)$ (isotropic) and $B_{23} = B_{31} = B_{12} = 0$:

$$\beta_{11} = B_{11} \times \frac{a^{*2}}{4} \qquad \beta_{22} = B_{22} \times \frac{b^{*2}}{4} \qquad \beta_{33} = B_{33} \times \frac{c^{*2}}{4} \tag{A.1}$$

$$\beta_{23} = B_{12} \times \frac{b^{*}c^{*}}{4} \qquad \beta_{31} = B_{31} \times \frac{c^{*}a^{*}}{4} \qquad \beta_{12} = B_{12} \times \frac{a^{*}b^{*}}{4} \tag{A.2}$$

The three diagonal β_{ii} relations are shown in equation set A.1 and off-diagonal elements β_{ij} respectively, in Eqn's. A.2. From here, a simple substitution of B_{ij} into the following equation gives the converted ADP's from B to U [212, 219, 220]:

$$U = \frac{B}{8\pi^2} \tag{A.3}$$

A.4 Tested monoclinic structures at 200 K

A.4.1 Individual Y1 and Y2 irreducible representations

Before discussing in detail, the final structural solutions included in this appendix, of the different Y1 and Y2 modes, it is necessary to explain some of the difficulties encountered with the refinements. In total, the six possible structures obtained from symmetry analysis of the individual Y1 and Y2 mode were all attempted under the same conditions, initially. However, it became quickly apparent that there was a general trend with the success of the refinement based on the difference in symmetry, more specifically dependent on where the inversion centre lies. All Y2-mode structures were refined with no real difficulty (no initial restrictions required to ease refinement). However, all refinements of the Y1-modes presented some or all of the following issues:

- Negative ADP's (Anisotropic Displacement Parameters)/ negative Isotropic parameters: negative ADP's are often inherent due to bad absorption correction (this was not the case as it has been tested and the correct structural solution for this compound is described later) or simply the space group symmetry is wrong. For refinements which give negative isotropic (Iso) displacement parameters in the beginning is a clear indication that the symmetry is wrong. For all Y1-structures this was the case. When negative ADP's occur with the lighter oxygen atoms, some early restrictions can provide a better stabilization of the refinement, leading to a better outcome and positive Iso. But unfortunately in the case of the work presented here, negative ADP's off much heavier Yb and Fe atoms occurred, a direct result of incorrect symmetry.

- Difficulty in stabilizing the molecular mass: often in terms of the Y1-modes investigated. Which was not the natural selection from the structure solution in the refinement software, but rather a forced CIF of the alternative symmetry. Some of the atoms would be rejected. This can of course be solved by inputting them manually or using the electron density map and Fourier difference. However, the stability of maintaining the correct number of atoms for these refinements remained a difficulty.

- Negative or unreasonable twin components: with the factors already mentioned above, which in some or all cases reside, a knock on effect of these bad refinements led to negative twin components. In the case of the monoclinic structures $C2/m$ and $C2/c$, due to lost symmetry elements going from the high symmetry $R\bar{3}m$, each have three twin components. After refinement typically one of the twin components would result in a negative volume. However, with the $C2$ structure which loses in addition 2-fold roto-inversion symmetry and thus a total of six twin components, in some cases half of the twins gave a negative value.

- Extinction (Giso) (isotropic correction): with the poorer and more unstable refinements the value of Giso would be extremely large, typically in the range of 0.1-0.3 etc for better refinements, the structure solutions obtained from the Y1-mode would result in values as high as circa 20.

The points listed above explain why there is only a $C2$ Y1-mode structure plotted in Fig. A.3. A refinement of the higher symmetry $C2/c$ and $C2/m$ with the inversion centre at the Yb layer was not possible and therefore not included in the detailed discussion. The table shown in A.1 gives an overview of the most important refinement parameters. From this it is clear to see the vast difference in refinement parameter values of each Y-mode. The large values obtained for both the general R-factor and goodness of fit for the $C2/m$ (Y1) and $C2/c$ (Y1) structures were R_{obs}= 71.85 %, 73.68 % and GoF_{obs}=22.30 and 21.72, respectively. The refinement using the slightly lower symmetry $C2/c$ (Y2-mode) with the inversion centre at the Yb layer, gave a final R value of R_{obs}=14.92 %, and GoF_{obs}=9.51. Even with this slight reduction in symmetry the overall refinement parameters were higher than that of the $C2/m$ refinement. The CO arrangement in the $C2/c$ cell obtained from the BVS analysis shown in Fig. A.3 also results in charged bilayers, with majority Fe^{2+} in each iron layer. This is quite different to the comparative $C2/m$ structure previously reported on $LuFe_2O_4$ [26], which also has the inversion centre at the Yb

layer. The final charge order here however gave an antiferroelectric configuration. Comparing the $C2/c$ to the $C2/m$ structure refined on $YbFe_2O_4$, the distinctive difference is rather than having alternate charged layers of Fe^{3+} and Fe^{2+}, the $C2/c$ has charged bilayers with majority Fe^{2+}.

Parameter	Y1-$C2/c$	Y2-$C2/c$	Y1-$C2$	Y2-$C2$
R_{int}/R_{σ} (%)	49.34/2.20	9.94/1.62	7.65/2.74	7.65/2.74
R_{obs}/wR_{obs} (%)	73.68/98.23	14.92/39.0	17.50/40.24	9.45/23.48
$R_{all}/wR2_{all}$ (%)	73.92/98.79	15.10/39.16	18.14/41.92	10.06/24.09
GoF_{obs}/GoF_{all}	21.72/21.30	9.51/9.42	7.09/7.01	4.14/4.03
Uniq. ref (obs/all)	6834/7190	11745/12323	27478/30567	27478/30567
Neg. ADPs	Yb1,2,Fe1,2,O1,2,4,5	No	O atoms(Iso)	O atoms(Iso)
Neg. Twins	2,3 and 4	No	2,3 and 4	2 and 6
Giso	17.41	0.13	0.14	0.11

Table A.1: Refinement parameters obtained for individual Y1 and Y2 mode structure solutions at 200 K.

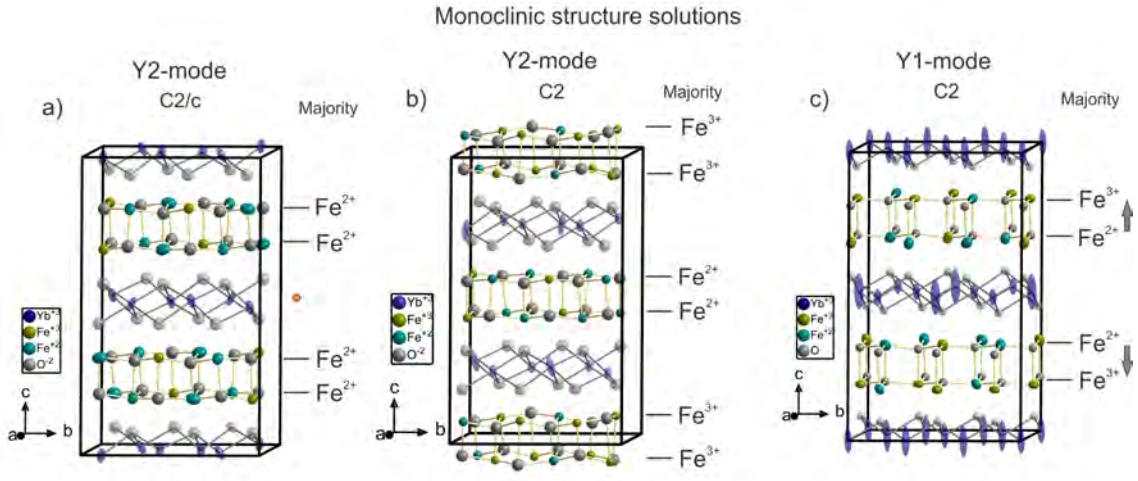

Figure A.3: Structural representations from all successful refinements, using symmetry analysis of the the individual Y1 and Y2 IR's at 200 K. The structures shown in (a) $C2/m$, (b) $C2/c$ and (c) $C2$, come from the Y2-mode IR. The same $C2$ structure shown in (d), was the only successful refinement of a structure solution from a Y1 mode IR. Therefore both (c) and (d) give the two possible settings with either the Fe bilayer or Yb layer at the centre of the unit cell. The overall charge of each iron layer is depicted by a line and respective Fe valence. The orange dot next to the centre of (a) and (b) represents the point of inversion. The arrows used next to the bilayers on the $C2$ (Y1-mode) cell show the polarization direction of each bilayer. In this particular case the iron bilayers are antiferroelectrically stacked. The rest present charged bilayers.

The overall R-value when refining the ADP's of the oxygen atoms was improved marginally to 9.35, from 9.45 %, however the O1 and O12 atoms were non-positive definite. The Y1 mode which gives the $C2$ symmetry with an Yb layer at the centre of the unit cell yielded overall larger refinement parameters of R_{obs}=17.50 % and GoF_{obs}=7.09 %, compared to the Y2-mode with the Fe layer bilayer at the centre, resulting in an R_{obs}=9.45 % and GoF_{obs}=4.14, respectively. The ability to refine each of the $C2$ structures stems from the complete lowering of the symmetry, where not only the 3-fold roto-inversion symmetry is lost going from the $R\bar{3}m$ to $C2/m$, but the 2-fold roto-inversion symmetry is also removed. This results of

course in additional twin components (due to lost symmetry elements), 6 to be precise compared to the higher symmetry candidates. Despite the slightly lower R-value obtained for the $C2$ (Y2-mode), each $C2$ refinement resulted in negative twin components; three twins for the Y1-$C2$ structure (twins 2, 3, and 4) and two respectively for the Y2-$C2$ structure (twins 2 and 6), which in this case were set to zero. Twin component 2 is the (110) 2-fold roto-inversion lost symmetry element (180°) in direct space, lost when going from $C2/c$ to $C2$. Twins 3 and 4 arise from the 120 and 240° rotation around c_{hex}, and twins 5 and 6 is the 2-fold rotation around $[-1, -1, 0]_{hex}$ (240° around c_{hex}). Viewing the CO arrangement from the calculated BVS provides two very different outcomes, the $C2$ structure (Y2-mode) produces alternate charged bilayers, of Fe^{2+} and Fe^{3+} majority. Similar to the $C2/m$ the $C2/c$ presents only Fe^{2+} majority charged bilayers. The $C2$ (Y1-mode) structure presents an antiferroelectrically stacked CO configuration, similar to the alternative $C2/m$ CO refinement on $LuFe_2O_4$ [26, 48], which observed the same stacking when the inversion centre was at the Yb layer. However the solidarity of the refinement of this space group comes into question when a number of the free parameters cannot be stabilized, with the occurrence of negative ADP's of oxygen atoms and negative twin components, this symmetry is most likely the incorrect one. The final refinements of the lowest symmetry $C2$ structure was somewhat successfully completed using the symmetries obtained from both Y1 and Y2-mode representations. As shown in Table. A.2, each of the two refinements were completed only by maintaining the oxygen atoms as isotropic.

Site	$C2/m$ (Y2)	$C2/c$ (Y2)	$C2$ (Y2)	$C2$ (Y1)
Fe1	2.99(3) (3+)	2.91(5) (3+)	2.99(2) (3+)	2.270(14) (3+)
Fe2	2.241(15) (2+)	2.41(3) (2+)	2.41(2) (2+)	2.227(19) (2+)
Fe3	2.52(3) (3+)	2.09(2) (2+)	2.053(15) (2+)	2.280(16) (2+)
Fe4	2.16(2) (2+)		2.68(3) (3+)	2.628(19) (3+)
Fe5			2.69(3) (3+)	2.123(14) (2+)
Fe6			2.19(2) (2+)	2.400(2) (2+)

Table A.2: The calculated BVS of all Fe-sites for each successful refinement. The brackets next to each calculated value is the valence which was used based on the calculated number. The BVS value for the Fe1 site (yellow highlight) was taken as Fe^{3+} to maintain the 2:1 valence ratio.

A.4.2 Monoclinic structures from the combined Y1 and Y2 IR's

In order to view the remaining structures from symmetry analysis a combination of Y1 and Y2 modes have been included in Table. 6.5. For consistency and continuation from the higher symmetry space groups described in the previous section, refinements of the Cc and Cm were performed. The refinement of the higher symmetry Cc structure shown in Fig. A.4 (left) gave a relatively large R_{obs}=14.43 % further complemented by a high value of GoF_{obs}=6.63 (see Table. A.3). These factors aside there are a number of further parameters which eliminate this as a possible structure solution. Heavy restrictions were required in the beginning, before a single refine-

ment cycle: all Fe and O atoms were restricted by fixed coordinates. A randomized seed of 10 was also used to enable stable initial refinement cycles. This particular technique was used on several difficult refinements, one's which were either due to bad space group selection not providing a solution for many of the reflections measured, or low symmetry space groups; can be difficult to stabilize in the beginning based on the number of reflections and free parameters.

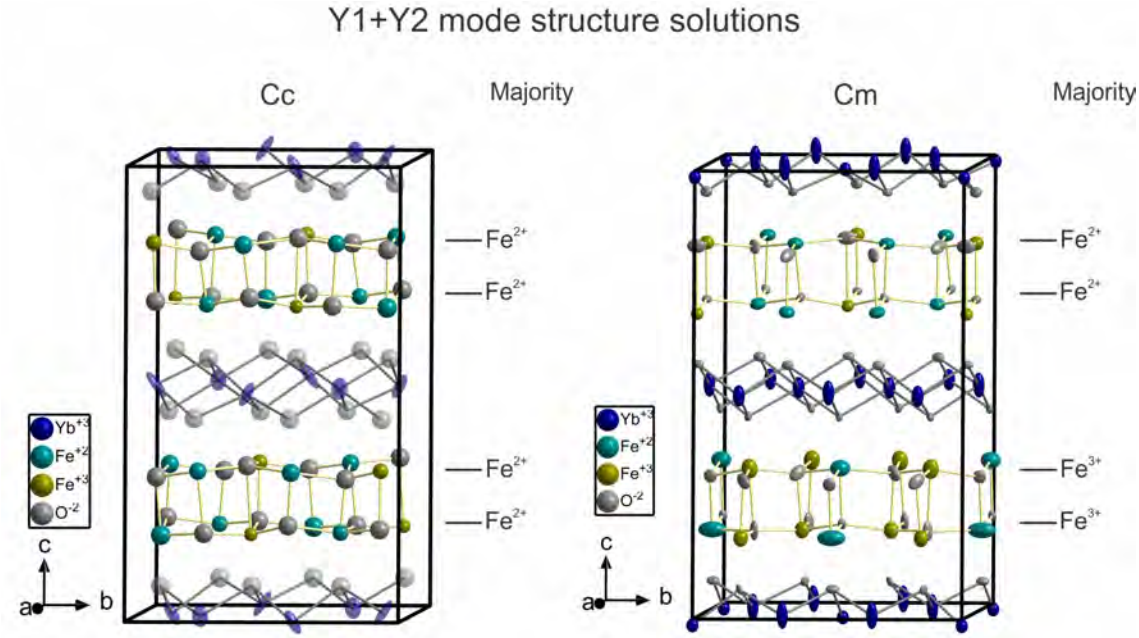

Figure A.4: Structural representations from all successful refinements using symmetry analysis of the combined Y1 and Y2 IR's at 200 K. Left: Cc structure and right: Cm structure. The overall charge of each iron layer is depicted by a line and relative iron valance.

Parameter	Cc (Y1+Y2)	Cm (Y1+Y2)
R_{int}/R_{σ} (%)	7.61/2.73	7.61/2.73
$R_{obs}/wR2_{obs}$ (%)	14.43/36.54	7.57/19.49
$R_{all}/wR2_{all}$ (%)	14.97/36.96	8.06/19.48
GoF_{obs}/GoF_{all}	6.43/6.18	3.44/3.42
Unique ref. obs/all	27566/30586	27606/30628
Negative ADPs	Fe, O set isotropic	No
Negative Twins	Twin 5	Twin2, 4 and 6
Giso	0.16481	0.07326

Table A.3: Refinement parameters obtained for the higher symmetry Cc and Cm structures from combined Y1 and Y2 mode IR's at 200 K.

After the refinement had completed a number of cycles, the 6 relative twin components based on lost symmetry elements were introduced (similar to the lower symmetry refinement of the $C2$ structure, which resulted from two combined order parameters, Y2(a,b;0,0,0,0), using representation analysis) and the isotropic extinction parameter. Restrictions of all atoms were disabled, but all Fe and O atoms

were kept to isotropic. In both cases a number of negative ADP's resulted. This along with a negative twin component and the high R-values, removed this from the list of potential candidate structures. The BVS calculated from the refinement program and given in Table A.3 show a few low and unrealistic values for a rounded approximation of an Fe^{2+} valence, for example the Fe5 atom gave BVS=1.89. When taking into account the BVS values obtained, the final CO structure provides stacked charged layers of majority Fe^{2+}. This particular type of potential CO was seen from the refinement of the higher symmetry $C2/c$ structure, and also resulted in a number of negative ADP's and twin components, but produced a much larger R_{obs} of 73.68 %. Although, the R-value for the refinement in Cc is lower, the poor values calculated for the free parameters are far too substantial to ignore. The second refinement using the slightly lower symmetry Cm structure, which instead of a glide plane along c has a mirror plane parallel to $\overrightarrow{c}$, is also shown in Fig. A.4 (right).

Site	Cc BVS	Cm BVS
Fe1	2.19(4) (2+)	2.015(18) (2+)
Fe2	2.82(5) (3+)	2.391(18) (2+)
Fe3	1.97(3) (2+)	2.51(2) (3+)
Fe4	2.36(3) (2+)	3.01(3) (3+)
Fe5	1.89(3) (2+)	2.82(2) (3+)
Fe6	2.72(4) (3+)	2.79(2) (3+)
Fe7	–	2.075(14) (2+)
Fe8	–	2.149(19) (2+)

Table A.4: BVS of each Fe site from both Cc and Cm refinements at 200 K. The highlighted cell (yellow) indicates a value which was lower than the expected norm.

Refinement stability and a lower R_{obs}=7.57 %, congruent to the more reasonable values obtained for the free refinement parameters indicate that the symmetry of this structure fits better to the reflections measured, compared with that of the Cc structure. The ADP's of each atom were refined successfully giving no non-positive definite error's, however the Yb1 atoms on each corner of the top Yb-O layer have unreasonably small ADP's for such a heavy atom. Moreover, half of the twin components during the refinement stages gave negative values, and as a result set to zero. These factors along with a final GoF_{obs}=3.44 (quite above the ideal value of 1) provides a slim basis for this structure being the correct choice. The BVS calculated from this refinement, given in Table. A.4 were all within reasonable error producing no substantial outliers (values unrealistic extending way beyond the normal value). The CO pattern obtained from the arrangement of Fe valences is one with alternate charged bilayers of majority Fe^{2+} and Fe^{3}, respectively. This same CO pattern was observed in both $C2/m$ and $C2$ Y2 mode IR's shown in Fig. A.3. Although all of the refinements tried and tested for both Y1 and Y2 IR's as well as combined Y1+Y2 produce poor parameter values, not indicative of the final cell choice for $YbFe_2O_4$ and a revised look at $LuFe_2O_4$, it is interesting that the majority of structures in the monoclinic space group conform to the charged bilayers reported previously in $LuFe_2O_4$ [48]. Furthermore, had the extra half integer reflections not been observed in the $YbFe_2O_4$ single crystal diffraction. The previous CO superstructure would still hold.

A.5 Refinement parameters from the $P1$ structure

Site	x	y	z	U11	U22	U33	U12	U13	U23
Yb1	1.3135(3)	0.5976(6)	0.7218(7)	0.00514(10)	0.00573(2)	0.00930(6)	-0.00325(7)	-0.000566(8)	0.000051(4)
Yb2	0.9872(9)	0.2579(9)	0.7303(4)	0.00284(10)	0.00235(8)	0.0244(2)	-0.000615(10)	-0.00247(5)	-0.00137(5)
Yb3	1.6481(15)	-1.0702(13)	0.7270(6)	0.00431(6)	0.00484(6)	0.0133(10)	-0.00241(5)	-0.000622(8)	-0.00105(6)
Yb4	-0.00105(5)	-0.0724(13)	1.2287(5)	0.00339(6)	0.00366(6)	0.0237(13)	-0.00163(5)	-0.00197(9)	-0.000609(3)
Yb5	1.4871(10)	-0.7392(9)	1.2117(3)	0.00415(12)	0.00409(9)	0.00976(14)	-0.00183(9)	-0.00129(9)	0.000212(9)
Yb6	1.8135(10)	-0.4062(9)	0.2388(4)	0.00315(10)	0.00346(9)	0.0125(14)	-0.00151(8)	-0.000053(9)	-0.00115(9)
Fe1	1.4249(4)	-0.4080(3)	-0.4080(11)	0.00568(4)	0.00803(5)	0.00805(3)	-0.00323(4)	-0.00198(4)	-0.000173(3)
Fe2	1.5870(3)	-0.7318(3)	0.9027(8)	0.00629(4)	0.00812(4)	0.00502(3)	-0.00429(4)	0.000163(3)	-0.000499(2)
Fe3	1.2565(4)	-0.0719(4)	0.9071(7)	0.00875(5)	0.0124(5)	0.00407(2)	-0.00549(4)	0.000387(3)	-0.00228(3)
Fe4	0.5402(3)	-0.0727(3)	1.0494(8)	0.00648(4)	0.00619(4)	0.00556(3)	0.00556(4)	-0.000919(3)	-0.000236(3)
Fe5	1.7125(3)	-0.4083(3)	0.5476(10)	0.00476(4)	0.00521(4)	0.00883(3)	-0.00217(3)	-0.000929(3)	-0.000795(3)
Fe6	1.7546(4)	-1.0662(3)	0.4017(10)	0.00510(4)	0.00584(4)	0.00833(3)	-0.00185(3)	-0.000237(3)	-0.00121(3)
Fe7	0.8761(3)	0.2635(3)	1.0504(9)	0.00513(4)	0.00552(4)	0.00595(3)	0.00595(3)	0.000736(3)	-0.00108(3)
Fe8	1.1060(5)	-0.7436(5)	0.4009(8)	0.0123(6)	0.0174(6)	0.00254(2)	-0.00891(5)	0.000061(3)	-0.000208(3)
Fe9	1.0397(4)	-0.0678(3)	0.5456(11)	0.00651(4)	0.00411(4)	0.0122(4)	-0.00223(4)	-0.00181(4)	0.000115(3)
Fe10	1.3776(5)	-0.7357(4)	0.5461(11)	0.01375(6)	0.01142(5)	0.00808(4)	-0.00822(5)	-0.000445(4)	-0.000144(4)
Fe11	0.9173(4)	-0.3979(4)	0.9050(10)	0.00655(4)	0.00951(5)	0.00566(3)	-0.00288(4)	0.000589(3)	-0.00145(3)
Fe12	1.1924(5)	-0.3943(5)	1.0491(11)	0.01277(7)	0.01288(6)	0.00877(4)	-0.00846(6)	-0.000496(4)	-0.000343(4)
O1	1.3305(14)	-0.7348(13)	0.6648(4)	0.00397(15)	0.00484(14)	0.00610(11)	-0.00131(12)	-0.00190(10)	0.00159(9)
O2	0.9945(15)	-0.0583(13)	0.6647(4)	0.00528(16)	0.00450(14)	0.00673(12)	-0.000351(13)	0.000388(11)	-0.000672(10)
O3	1.6748(15)	-0.4050(14)	0.6628(4)	0.00632(17)	0.00758(17)	0.00592(11)	-0.00459(14)	-0.00322(11)	0.00152(10)
O4	0.5093(17)	-0.0957(15)	1.1645(5)	0.00860(2)	0.00544(16)	0.0107(15)	-0.00347(16)	-0.00415(14)	0.000879(13)
O5	1.1462(16)	-0.3870(17)	1.1654(4)	0.00602(18)	0.00976(2)	0.00540(10)	-0.00210(15)	0.000391(11)	0.00080(11)
O6	0.8480(14)	0.2729(15)	1.1652(4)	0.00343(15)	0.00952(2)	0.00686(12)	-0.00253(10)	-0.000378(10)	0.00139(11)
O7	0.9600(19)	-0.3970(17)	0.7871(5)	0.00874(4)	0.01276(3)	0.00793(14)	-0.00594(19)	0.00194(14)	-0.00589(14)
O8	1.2689(16)	-0.4208(15)	0.9272(4)	0.00660(19)	0.00595(17)	0.00927(13)	-0.00256(15)	0.00159(13)	-0.00170(12)
O9	1.2989(2)	-0.0756(17)	0.7864(4)	0.0157(3)	0.00964(2)	0.00636(12)	-0.00945(2)	-0.00250(14)	-0.000088(12)
O10	1.6175(17)	-0.7255(14)	0.7882(5)	0.00957(2)	0.00476(17)	0.0119(17)	-0.00341(15)	0.00316(15)	-0.00593(13)
O11	1.1476(16)	-0.7435(16)	0.2855(4)	0.00608(18)	0.00799(16)	0.00810(13)	-0.00460(16)	0.000065(12)	-0.000872(12)
O12	1.7815(15)	-1.0497(14)	0.2859(4)	0.00574(17)	0.00648(15)	0.00551(10)	-0.00247(13)	-0.000625(10)	-0.000546(10)
O13	1.4533(18)	-0.4151(14)	0.2860(4)	0.01209(2)	0.00728(17)	0.00539(11)	-0.00704(16)	0.00152(12)	-0.00380(11)
O14	1.8971(15)	-0.7375(15)	0.9237(3)	0.01005(4)	0.0101(17)	0.00322(7)	-0.00510(16)	0.000019(9)	-0.00151(9)
O15	0.8540(2)	-0.4052(16)	1.0301(5)	0.01099(6)	0.00625(19)	0.0161(2)	-0.00437(18)	-0.00290(18)	-0.00106(16)
O16	1.0920(18)	-0.0951(16)	0.4127(5)	0.00992(2)	0.00439(15)	0.0136(17)	0.00121(16)	0.00285(16)	0.000340(14)
O17	1.5801(15)	-1.0445(14)	0.9248(3)	0.00693(16)	0.0112(18)	0.00430(8)	-0.00369(14)	0.000249(9)	0.00197(9)
O18	1.4410(16)	-0.7368(15)	0.4198(3)	0.00906(2)	0.0101(18)	0.00444(9)	-0.00460(16)	0.000836(11)	-0.00139(10)
O19	1.7358(2)	-0.3807(3)	0.3959(5)	0.01261(3)	0.01197(3)	0.01117(12)	-0.00615(3)	-0.00202(13)	-0.000984(13)
O20	2.0270(18)	-0.7238(16)	0.5238(5)	0.00677(2)	0.00748(2)	0.01073(17)	-0.000932(16)	-0.00383(14)	0.000059(14)
O21	1.3957(19)	-0.3925(18)	0.5314(6)	0.00909(3)	0.00895(2)	0.02425(3)	-0.00552(18)	-0.00395(2)	-0.00277(2)
O22	1.7285(18)	-0.1054(14)	0.5278(7)	0.00857(3)	0.00239(14)	0.02943(4)	-0.00228(15)	0.00230(2)	-0.00111(17)
O23	1.2122(16)	-0.0482(18)	1.0406(4)	0.00697(18)	0.01332(2)	0.00931(13)	-0.00459(18)	-0.000987(12)	-0.0016(14)
O24	0.5638(17)	0.2414(2)	1.0498(7)	0.00543(18)	0.01093(2)	0.02877(4)	-0.00589(19)	-0.00290(19)	0.00117(3)

Table A.5: Atomic positions and anisotropic displacement parameters of the $P1$ structure refined at 90 K. The additional atomic positions are attributed to the loss of inversion symmetry, which includes a double of each atom type all except two special Wykcoff positions of the Yb1 (Wyck=1c) and Yb4 (Wyck=1h)

a (Å)	b (Å)	c (Å)	$\alpha(°)$	$\beta(°)$	$\gamma(°)$	V (Å^3
5.982(1)	5.986(2)	16.877(1)	86.556(9)	83.1680(1)	59.962(5)	519.5(5)

Table A.6: Lattice parameters for $P1$ structure at 90 K.

A.6 Hysteretic response of the (1, 0, -1) reflection

A measurement of integrated intensity as a function of applied field for the (1 0 -1) structural reflection, measured at 200 K, is shown in Fig. A.5 (top). Plotted along with the complimentary M vs H data (black squares). The statistic were too poor for this reflection, indicated by the large error bars and no relation to the M vs H data is seen. For a clear example of the hysterestic trend of the magnetic intensity at structural reflections, comparable data on $LuFe_2O_4$ is shown in Fig. A.5 (bottom).

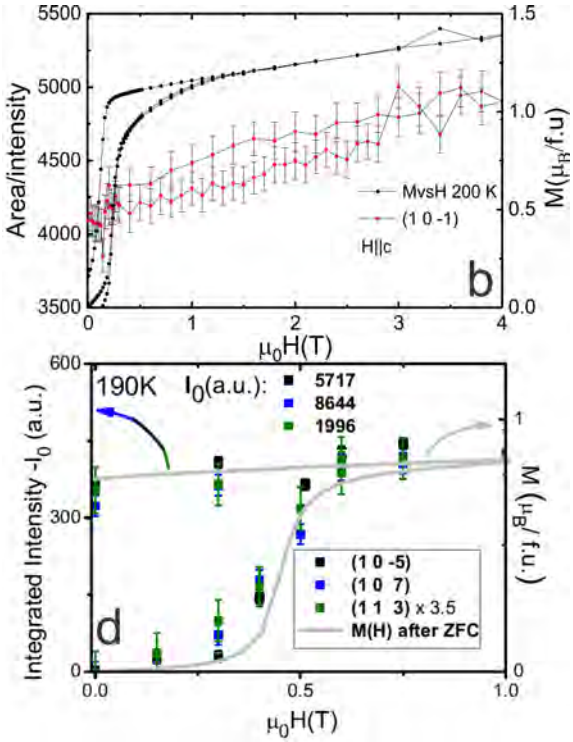

Figure A.5: Top: the integrated intensity as a function of field for the (1 0 -1) reflection (red squares) measured at 200 K, plotted with complementary M vs H (black curve). Bottom: similar data on $LuFe_2O_4$, at several structural reflections measured at 190 K, figure taken from [32] and adapted.

Bibliography

[1] E. Dagotto. Complexity in strongly correlated electronic systems. *Science*, 309(5732):257–262, 2005.

[2] A. P. Ramirez. Colossal magnetoresistance. *J. Phys.: Condens. Matter*, 9(39):8171, 1997.

[3] P. S. Wang and H. J. Xiang. Room-temperature ferrimagnet with frustrated antiferroelectricity: Promising candidate toward multiple-state memory. *Phys. Rev. X*, 4(1), 2014.

[4] A. Urushibara, Y. Moritomo, T. Arima, A. Asamitsu, Gt Kido, and Y. Tokura. Insulator-metal transition and giant magnetoresistance in $La_{1-x}Sr_xMnO$. *Phys. Rev. B*, 51(20):14103, 1995.

[5] S. P. Poole, H. A. Farach, R. J. Creswick, and R. Prozorov. *Superconductivity*. Academic Press, New York, 2nd edition, 2007.

[6] J. Bardeen, L. N. Cooper, and J. R. Schrieffer. Theory of Superconductivity. *Phys. Rev.*, 108:1175–1204, 1957.

[7] N. A. Spaldin, S-W. Cheong, and R. Ramesh. Multiferroics: past, present, and future. *Phys. Today*, 63(10):38–43, 2010.

[8] N. A. Spaldin. *Magnetic materials: fundamentals and applications*. Cambridge University Press, 2010.

[9] S-W. Cheong and M. Mostovoy. Multiferroics: a magnetic twist for ferroelectricity. *Nat. Mater.*, 6(1):13–20, 2007.

[10] M. Fiebig and N. A. Spaldin. Current trends of the magnetoelectric effect. *Eur. Phys. J. B*, 71(3):293–297, 2009.

[11] M. Fiebig. Revival of the magnetoelectric effect. *J. Phys. D: Appl. Phys.*, 38(8):R123, 2005.

[12] W. Eerenstein, N. D. Mathur, and J. F. Scott. Multiferroic and magnetoelectric materials. *Nature*, 442(7104):759–765, 2006.

[13] Y. Sun, Y. LiQin, and C. JunZhuang. Multiferroics and magnetoelectric effects in charge ordered compounds. *Sci. China Phys. Mech.*, 56(1):222–231, 2013.

[14] T. Jia, Z. Cheng, H. Zhao, and H. Kimura. Domain switching in single-phase multiferroics. *Appl. Phys. Rev.*, 5(2):021102, 2018.

[15] H. J. Zhao, W. Ren, Y. Yang, J. Íñiguez, X. M. Chen, and L. Bellaiche. Near room-temperature multiferroic materials with tunable ferromagnetic and electrical properties. *Nat. Commun.*, 5, 2014.

[16] M. Bibes and A. Barthélémy. Towards a magnetoelectric memory. *Nat. Mater.*, 7:425, 2008.

[17] S. Blundell and D. Thouless. *Magnetism in condensed matter*, volume 18. Oxford university press New York, 2001.

[18] J. van den Brink and D. I. Khomskii. Multiferroicity due to charge ordering. *J. Phys. Condens. Matter*, 20(43):434217, 2008.

[19] L. Landau and E. Lifshitz. Lehrbuch der theoretische physik akademie-verlag. *Akademie-Verlag Berlin*, 10, 1987.

[20] K. Binder. Theory of first-order phase transitions. *Rep. Prog. Phys.*, 50(7):783, 1987.

[21] V. Pokrovsky. Landau and theory of phase transitions. In *APS March Meeting Abstracts*, 2009.

[22] H. T. C. Stoof, K. B Gubbels, and D. Dickerscheid. *Ultracold quantum fields*. Springer, 2009.

[23] E. A. DiMarzio. A classification of the kinds of order parameters. *Ann. N.Y. Acad. Sci.*, 279(1):86–87, 1976.

[24] M. T. Dove. *Structure and dynamics: an atomic view of materials*, volume 1. Oxford University Press, 2003.

[25] H. J. Xiang, E. J. Kan, Su-Huai Wei, M-H. Whangbo, and Jinlong Yang. Origin of the ising ferrimagnetism and spin-charge coupling in $LuFe_2O_4$. *Phys. Rev. B*, 80(13):132408, 2009.

[26] J. de Groot. *Charge, spin and orbital order in the candidate multiferroic material $LuFe_2O_4$*. PhD thesis, RWTH Aachen, 2012.

[27] R. A. M^c Kinnon. Studies of new multiferroics. Master's thesis, University of Warwick, 2011.

[28] T. Nagamiya. Helical spin ordering: 1 theory of helical spin configurations. In *Solid State Physics*, volume 20, pages 305–411. Elsevier, 1968.

[29] I. Sosnowska, T. P. Neumaier, and E. Steichele. Spiral magnetic ordering in bismuth ferrite. *J. Phys. C: Solid State Phys.*, 15(23):4835, 1982.

[30] C. P. Bean and J. D. Livingston. Superparamagnetism. *J. Appl. Phys.*, 30(4):S120–S129, 1959.

[31] Y-R. Lee, T. T. Wang, T. M. Rvachov, J-H. Choi, W. Ketterle, and M.-S. Heo. Pauli paramagnetism of an ideal fermi gas. *Phys. Rev. A*, 87(4):043629, 2013.

[32] J. de Groot, K. Marty, M. D. Lumsden, A. D. Christianson, S. E. Nagler, S. Adiga, W. J. H. Borghols, K. Schmalzl, Z. Yamani, S. R. Bland, R. de Souza, U. Staub, W. Schweika, Y. Su, and M. Angst. Competing ferri- and antiferromagnetic phases in geometrically frustrated $LuFe_2O_4$. *Phys. Rev. Lett.*, 108(3):037206, 2012.

[33] M. Angst. Ferroelectricity from iron valence ordering in rare earth ferrites? *Phys. Status Solidi RRL*, 7(6):383–400, 2013.

[34] G. Toulouse. *Theory of the frustration effect in spin glasses: I*, volume 9. World Scientific Publishing Company, 1987.

[35] G. H. Wannier. Antiferromagnetism. the triangular ising net. *Phys. Rev.*, 79(2):357, 1950.

[36] Y. Yamada, S. Nohdo, and N. Ikeda. Incommensurate charge ordering in charge-frustrated $LuFe_2O_4$ system. *J. Phys. Soc. Jpn.*, 66(12):3733–3736, 1997.

[37] S. F. Edwards and F. Tanaka. The ground state of a spin glass. *J. Phys. F: Met. Phys.*, 10(11):2471, 1980.

[38] M. Palassini and A. P. Young. Nature of the spin glass state. *Phys. Rev. Lett.*, 85:3017–3020, 2000.

[39] J. Snyder, B. G. Ueland, J. S. Slusky, H. Karunadasa, R. J. Cava, and P. Schiffer. Low-temperature spin freezing in the $Dy_2Ti_2O_7$ spin ice. *Phys. Rev. B*, 69:064414, 2004.

[40] C. H. Booth, J. S. Gardner, G. H. Kwei, R. H. Heffner, F. Bridges, and M. A. Subramanian. Local lattice disorder in the geometrically frustrated spin-glass pyrochlore $Y_2Mo_2O_7$. *Phys. Rev. B*, 62:R755–R758, 2000.

[41] V. V. Brazhkin. Metastable phases, phase transformations, and phase diagrams in physics and chemistry. *Phys. Usp.*, 49(7):719, 2006.

[42] X. S. Xu, M. Angst, T. V. Brinzari, R. P. Hermann, J. L. Musfeldt, A. D. Christianson, D. Mandrus, B. C. Sales, S. McGill, J. . W. Kim, and Z. Islam. Charge order, dynamics, and magnetostructural transition in multiferroic $LuFe_2O_4$. *Phys. Rev. Lett.*, 101(22):227602, 2008.

[43] H. L. Williamson, T Mueller, M Angst, and G Balakrishnan. Growth of $YbFe_2O_4$ single crystals exhibiting long-range charge order via the optical floating zone method. *J. Cryst. Growth*, 2017.

[44] M. Naka and S. Ishihara. Magnetoelectric effect in organic molecular solids. *Sci. Rep.*, 6:20781, 2016.

[45] M. Coey. Condensed-matter physics: Charge-ordering in oxides. *Nature*, 430(6996):155–157, 2004.

[46] Y. Sun, L. Yan, and C. JunZhuang. Multiferroics and magnetoelectric effects in charge ordered compounds. *Sci. China Phys. Mech.*, 56(1):222–231, 2012.

[47] W. Pan, Q. Zhang, A. Bhalla, and L. E. Cross. Field-forced antiferroelectric-to-ferroelectric switching in modified lead zirconate titanate stannate ceramics. *J. Am. Ceram. Soc.*, 72(4):571–578.

[48] J. de Groot, T. Mueller, R. A. Rosenberg, D. J. Keavney, Z. Islam, J. W. Kim, and M. Angst. Charge order in $LuFe_2O_4$: An unlikely route to ferroelectricity. *Phys. Rev. Lett.*, 108(18):187601, 2012.

[49] P. D. Hatton, S. B. Wilkins, T. A. W. Beale, T. Johal, D. Prabhakaran, and A. T. Boothroyd. Direct observation of orbital ordering in layered manganites. *J. Supercond.*, 18(5-6):687, 2005.

[50] H. A. Jahn and E. Teller. Stability of polyatomic molecules in degenerate electronic states. i. orbital degeneracy. *Proc. R. Soc. London, Ser. A*, 161:220–235, 1937.

[51] P. D. Hatton, S. B. Wilkins, T. A. W. Beale, T. K. Johal, D. Prabhakaran, and A. T. Boothroyd. Resonant soft X-ray scattering—a new probe of charge, spin and orbital ordering in the manganites. *J. Magn. Magn. Mater.*, 290-291:891 – 897, 2005.

[52] Y. Tokura and N. Nagaosa. Orbital physics in transition-metal oxides. *Science*, 288(5465):462–468, 2000.

[53] K. I. Kugel and D. I. Khomskiĭ. The Jahn-Teller effect and magnetism: transition metal compounds. *Phys.-Uspekhi*, 25(4):231, 1982.

[54] H. J. Xiang and M-H. Whangbo. Charge order and the origin of giant magnetocapacitance in $LuFe_2O_4$. *Phys. Rev. Lett.*, 98(24):246403, 2007.

[55] A. Nagano, M. Naka, J. Nasu, and S. Ishihara. Electric polarization, magnetoelectric effect, and orbital state of a layered iron oxide with frustrated geometry. *Phys. Rev. Lett.*, 99:217202, 2007.

[56] J. Nasu, A. Nagano, M. Naka, and S. Ishihara. Doubly degenerate orbital system in honeycomb lattice: Implication of orbital state in layered iron oxide. *Phys. Rev. B*, 78(2):024416, 2008.

[57] H. L Williamson. Magnetic and charge order in $LuFe_2O_4$ and $YbFe_2O_4$ multiferroics. Master's thesis, University of Warwick, 2012.

[58] N. A. Hill. Why are there so few magnetic ferroelectrics? *J. Phys. Chem. B*, 104(29):6694–6709, 2000.

[59] L. M. Volkova and D. V. Marinin. Magnetoelectric ordering of $BiFeO_3$ from the perspective of crystal chemistry. *J. Supercond. Novel Magn.*, 24(7):2161, 2011.

[60] T Katsufuji, S Mori, M Masaki, Y Moritomo, N Yamamoto, and H Takagi. Dielectric and magnetic anomalies and spin frustration in hexagonal $RMnO_3$ (R= Y, Yb, and Lu). *Phys. Rev. B*, 64(10):104419, 2001.

[61] I. D. Brown. *Bond Valences*, chapter Bond Valence Theory, pages 11–58. Springer Berlin Heidelberg, Berlin, Heidelberg, 2014.

[62] M. Angst, P. Khalifah, R. P. Hermann, H. J. Xiang, M.-H. Whangbo, V. Varadarajan, J. W. Brill, B. C. Sales, and D. Mandrus. Charge order superstructure with integer iron valence in Fe_2OBO_3. *Physical review letters*, 99(8):086403, 2007.

[63] N Ikeda, H Ohsumi, K Ohwada, K Ishii, T Inami, K Kakurai, Y Murakami, K Yoshii, S Mori, Y Horibe, and H Kito. Ferroelectricity from iron valence ordering in the charge-frustrated system $LuFe_2O_4$. *Nature*, 436(7054):1136–1138, 2005.

[64] J. Iida, M. Tanaka, H. Kito, and J. Akimitsu. Successive phase-transitions in nearly stoichiometric $ErFe_2O_4$. *J. Phys. Soc. Jpn.*, 59(11):4190–4191, 1990.

[65] B. B. Van Aken, T. T. M. Palstra, A. Filippetti, and N. A. Spaldin. The origin of ferroelectricity in magnetoelectric $YMnO_3$. *Nat. Mater.*, 3:164, 2004.

[66] C. J. Fennie and K. M. Rabe. Ferroelectric transition in $YMnO_3$ from first principles. *Phys. Rev. B*, 72:100103, 2005.

[67] I Dzyaloshinsky. A thermodynamic theory of "weak" ferromagnetism of antiferromagnetics. *J. Phys. Chem. Solids*, 4(4):241–255, 1958.

[68] Y Noda, Y Fukuda, H Kimura, I Kagomiya, S Matumoto, K Kohn, T Shobu, and N Ikeda. Review and prospect of ferroelectricity and magnetism in YMn_2O_5. *J. Korean Phys. Soc.*, 42(SUPPL.), 2003.

[69] A. Chauhan, S. Patel, R. Vaish, and C. Bowen. Anti-ferroelectric ceramics for high energy density capacitors. *Materials*, 8(12):8009–8031, 2015.

[70] G. Shirane. Ferroelectricity and antiferroelectricity in ceramic $PbZrO_3$ containing Ba or Sr. *Phys. Rev.*, 86(2):219–227, 1952.

[71] G. Shirane, E. Sawaguchi, and Y. Takagi. Dielectric properties of lead zirconate. *Phys. Rev.*, 84(3):476–481, 1951.

[72] X. Hao, J. Zhai, L. B. Kong, and Z. Xu. A comprehensive review on the progress of lead zirconate-based antiferroelectric materials. *Prog. Mater Sci.*, 63:1 – 57, 2014.

[73] N. Kimizuka, A. Takenaka, Y. Sasada, and T. Katsura. A series of new compounds $A^{3+}Fe_2O_4$ A = Ho, Er, Tm, Yb, and Lu. *Solid State Commun.*, 15(8):1321–1323, 1974.

[74] J. Iida, S. Takekawa, and N. Kimizuka. Single-crystal growth of $LuFe_2O_4$, $LuFeCoO_4$ and $YbFeMgO_4$ by the floating zone method. *J. Cryst. Growth*, 102(3):398–400, 1990.

[75] Kato, K., Kawada, I., Kimizuka, N., Katsura, and T. Crystal-structure of $YbFe_2O_4$. *Z. Kristallogr.*, 141(3-4):314–320, 1975.

[76] I. Shindo, N. Kimizuka, and S. Kimura. Growth of YFe_2O_4 single crystals by floating zone method. *Mater. Res. Bull.*, 11(6):637 – 643, 1976.

[77] K. Oka, M. Azuma, N. Hayashi, S. Muranaka, Y. Narumi, K. Kindo, S. Ayukawa, M. Kato, Y. Koike, Y. Shimakawa, and M. Takano. Charge and magnetic orderings in the triangular-lattice antiferromagnet $InFe_2O_4$. *J. Phys. Soc. Jpn.*, 77(6):064803, 2008.

[78] N. Kimizuka and T. Katsura. Standard free-energy of formation of $YbFe_2O_4$, $Yb_2Fe_3O_7$, $YbFeO_3$, and $Yb_3Fe_5O_{12}$ at 1200°C. *J. Solid State Chem.*, 15(2):151–157, 1975.

[79] T. Sekine and T. Katsura. Phase equilibria in the system Fe-Fe_2O_3-Lu_2O_3 at 1200°C. *J. Solid State Chem.*, 17:49 – 54, 1976.

[80] Y Nakagawa, M Inazumi, N Kimizuka, and K Siratori. Low-temperature phase transitions and magnetic properties of YFe_2O_4. *J. Phys. Soc. Jpn.*, 47(4):1369–1370, 1979.

[81] M. Kishi, S. Miura, Y. Nakagawa, N. Kimizuka, I. Shindo, and K. Siratori. Magnetization of $YbFe_2O_{4+x}$. *J. Phys. Soc. Jpn.*, 51(9):2801–2805, 1982.

[82] J. Iida, Y. Nakagawa, and N. Kimizuka. Field heating effect anomalous thermomagnetization curves observed in hexagonal $LuFe_2O_4$. *J. Phys. Soc. Jpn.*, 55(5):1434–1437, 1986.

[83] J. Iida, Y. Nakagawa, S. Takekawa, and N. Kimizuka. High-field magnetization of single-crystal $LuFe_2O_4$. *J. Phys. Soc. Jpn.*, 56(10):3746–3747, 1987.

[84] J. Iida, S. Kakugawa, G. Kido, Y. Nakagawa, S. Takekawa, and N. Kimizuka. High-field magnetization of single-crystals YFe_2O_4, $YbFe_2O_4$ and $LuFe_2O_4$. *Physica B: Condensed Matter*, 155(1-3):307–310, 1989.

[85] M. Isobe, N. Kimizuka, J. Iida, and S. Takekawa. Structures of $LuFeCoO_4$ and $LuFe_2O_4$. *Acta Crystallogr. C*, 46:1917–1918, 1990.

[86] J. Iida, Y. Nakagawa, S. Funahashi, S. Takekawa, and N. Kimizuka. Two-dimensional magnetic order in hexagonal $LuFe_2O_4$. *Journal de Physique*, 49(C-8):1497–1498, 1988.

[87] J. Iida, M. Tanaka, Y. Nakagawa, S. Funahashi, N. Kimizuka, and S. Takekawa. Magnetization and spin correlation of 2-dimensional triangular antiferromagnet $LuFe_2O_4$. *J. Phys. Soc. Jpn.*, 62(5):1723–1735, 1993.

[88] N. Ikeda, M. Tanaka, H. Kito, S. Sasaki, and Y. Yamada. Synchrotron observation of the charge ordering and spontaneous polarization in $LuFe_2O_4$. *Ferroelectrics*, 222(1-4), 1999.

[89] M. Tanaka, K. Siratori, and N. Kimizuka. Mössbauer study of RFe_2O_4. *J. Phys. Soc. Jpn.*, 53(2):760–772, 1984.

[90] Tadashi Sugihara, Kiiti Siratori, Isamu Shindo, and Takashi Katsura. Parasitic ferrimagnetism of YFe_2O_4. *J. Phys. Soc. Jpn.*, 45(4):1191–1198, 1978.

[91] S. Funahashi, J. Akimitsu, K. Siratori, N. Kimizuka, M. Tanaka, and H. Fujishita. Two-dimensional spin correlation in YFe_2O_4. *J. Phys. Soc. Jpn.*, 53(8):2688–2696, 1984.

[92] S. Funahashi, Y. Morii, and H. R. Child. Two-dimensional neutron diffraction of YFe_2O_4 and $CoCr_2O_4$. *J. Appl. Phys.*, 61(8):4114–4116, 1987.

[93] T Matsumoto, M. Nobuo, J Iida, M Tanaka, and K Siratori. Magnetic properties of the two dimensional antiferromagnets RFe_2O_4 R=Y, Er at high pressure. *J. Phys. Soc. Jpn.*, 61(8):2916–2920, 1992.

[94] J. Akimitsu, Y. Inada, K. Siratori, I. Shindo, and N. Kimizuka. Two-dimensional spin ordering in YFe_2O_4. *Solid State Commun.*, 32(11):1065 – 1068, 1979.

[95] Y. Matsui. Extra electron reflections observed in YFe_2O_4, $YbFe_2O_2$, $Yb_2Fe_3O_7$ and $Yb_3Fe_4O_{10}$. *J. Appl. Crystallogr.*, 13:395–397, 1980.

[96] N. Kimizuka and T. Mohri. Spinel, $YbFe_2O_4$, and $Yb_2Fe_3O_7$ types of structures for compounds in the In_2O_3 and Sc_2O_3-A_2O_3-BO Systems [A:Fe, Ga, or Al; B: Mg, Mn, Fe, Ni, Cu, or Zn] at temperatures over 1000°C. *J. Solid State Chem.*, 60(3):382–384, 1985.

[97] M. Tanaka, H. Iwasaki, K. Siratori, and I. Shindo. Mössbauer study on the magnetic-structure of $YbFe_2O_4$ - a two-dimensional antiferromagnet on a triangular lattice. *J. Phys. Soc. Jpn.*, 58(4):1433–1440, 1989.

[98] N. Ikeda, Y. Yamada, S. Nohdo, T. Inami, and S. Katano. Incommensurate charge ordering in mixed valence system $LuFe_2O_4$. *Physica B: Condensed Matter*, 241:820–822, 1997.

[99] H. Schmid. Multi-ferroic magnetoelectrics. *Ferroelectrics*, 162(1):317–338, 1994.

[100] N. Ikeda, S. Nohdo, Y. Yamada, E. Takahashi, and K. Kohn. Charge ordering of $LuFe_2O_4$ observed by an anomalous X-ray dispersion. *J. Korean Phys. Soc.*, 32:S165–S168, 1998.

[101] Y. Yamada and N. Ikeda. Valence fluctuation and polarization fluctuation in $LuFe_2O_4$. *J. Korean Phys. Soc.*, 32:S1–S4, 1998.

[102] Y. Yamada, K. Kitsuda, S. Nohdo, and N. Ikeda. Charge and spin ordering process in the mixed-valence system $LuFe_2O_4$: Charge ordering. *Phys. Rev. B*, 62(18):12167–12174, 2000.

[103] N. Ikeda, H. Ohsumi, M. Mizumaki, S. Mori, Y. Horibe, and K. Kishimoto. Frustration and ordering of iron ions on triangular iron mixed valence system RFe_2O_4. *J. Magn. Magn. Mater.*, 272-276(0):E1037 – E1039, 2004.

[104] A. D. Christianson, M. D. Lumsden, M. Angst, Z. Yamani, W. Tian, R. Jin, E. A. Payzant, S. E. Nagler, B. C. Sales, and D. Mandrus. Three-dimensional magnetic correlations in multiferroic LuF_2O_4. *Phys. Rev. Lett.*, 100(10):107601, 2008.

[105] J. S. Wen, G. Y. Xu, G. D. Gu, and S. M. Shapiro. Robust charge and magnetic orders under electric field and current in multiferroic $LuFe_2O_4$. *Phys. Rev. B*, 81(14):144121, 2010.

[106] M. Angst, R. P. Hermann, A. D. Christianson, M. D. Lumsden, C. Lee, M. . H. Whangbo, J. . W. Kim, P. J. Ryan, S. E. Nagler, W. Tian, R. Jin, B. C. Sales, and D. Mandrus. Charge order in $LuFe_2O_4$: Antiferroelectric ground state and coupling to magnetism. *Phys. Rev. Lett.*, 101(22):227601, 2008.

[107] A. M. Mulders, S. M. Lawrence, U. Staub, M. Garcia-Fernandez, V. Scagnoli, C. Mazzoli, E. Pomjakushina, K. Conder, and Y. Wang. Direct observation of charge order and an orbital glass state in multiferroic $LuFe_2O_4$. *Phys. Rev. Lett.*, 103(7):077602, 2009.

[108] M. Tanaka. Mössbauer study of RFe_2O_4 family - a 2-dimensional antiferromagnet on a triangular lattice. *Nucl. Instrum. Methods Phys. Res. B*, 76(1-4), 1993.

[109] J. Wen, G. Xu, G. Gu, and S. M. Shapiro. Magnetic-field control of charge structures in the magnetically disordered phase of multiferroic $LuFe_2O_4$. *Phys. Rev. B*, 80(2):020403, 2009.

[110] T. Mueller, J de Groot, J. Strempfer, and M. Angst. Stoichiometric $YFe_2O_{4-\delta}$ single crystals grown by the optical floating zone method. *J. Cryst. Growth*, 428:40 – 45, 2015.

[111] T. Müller. *Order and disorder in the charge and spin structures of* $YFe_2O_{4-\delta}$ *and* $Ni_{0.42}Mn_{0.58}TiO_3$. PhD thesis, RWTH Aachen, 2017.

[112] T. Funk, A. Deb, S. J. George, H. Wang, and S. P. Cramer. X-ray magnetic circular dichroism—a high energy probe of magnetic properties. *Coord. Chem. Rev.*, 249(1):3–30, 2005.

[113] Jonathan C. Lang. X-ray magnetic circular dichroism. *Characterization of Materials*, 2002.

[114] C. Z. Kapusta, P. Fischer, and G. Schütz. Magnetic X-ray absorption spectroscopy. *J Alloys Compd*, 286(1):37–46, 1999.

[115] K. T. Ko, H. J. Noh, J. Y. Kim, B. G. Park, J. H. Park, A. Tanaka, S. B. Kim, C. L. Zhang, and S. W. Cheong. Electronic origin of giant magnetic anisotropy in multiferroic $LuFe_2O_4$. *Phys. Rev. Lett.*, 103(20):207202, 2009.

[116] K. Kuepper, M. Raekers, C. Taubitz, M. Prinz, C. Derks, M. Neumann, A. V. Postnikov, F. M. F. de Groot, C. Piamonteze, D. Prabhakaran, and S. J. Blundell. Charge order, enhanced orbital moment, and absence of magnetic frustration in layered multiferroic $LuFe_2O_4$. *Phys. Rev. B*, 80(22):220409, 2009.

[117] J. Blasco, S. Lafuerza, J. García, and G. Subías. Structural properties in RFe_2O_4 compounds (R= Tm, Yb, and Lu). *Phys. Rev. B*, 90(9):094119, 2014.

[118] K. Yoshii, N. Ikeda, Y. Matsuo, Y. Horibe, and S. Mori. Magnetic and dielectric properties of RFe_2O_4, $RFeMO_4$, and $RGaCuO_4$ R=Yb and Lu, M=Co and Cu. *Phys. Rev.B*, 76(2):024423, 2007.

[119] K. Yoshii, D. Matsumura, H. Saitoh, T. Kambe, M. Fukunaga, Y. Muraoka, N. Ikeda, and S. Mori. Current-induced enhancement of magnetic anisotropy in spin-charge-coupled multiferroic $YbFe_2O_4$. *J. Phys. Soc. Jpn.*, 83(6):063708, 2014.

[120] Y. Murakami, N. Abe, T. Arima, and D. Shindo. Charge-ordered domain structure in $YbFe_2O_4$ observed by energy-filtered transmission electron microscopy. *Phys. Rev. B*, 76(2):024109, July 2007.

[121] A. J. Hearmon, D Prabhakaran, H Nowell, F Fabrizi, M. J. Gutmann, and P. G. R. Helical scattering signatures of strain and electronic textures in $YbFe_2O_4$ from three-dimensional reciprocal-space imaging. *Phys. Rev. B*, 85(1):014115, 2012.

[122] C. R. Serrao, J. R. Sahu, K. Ramesha, and C. N. R. Rao. Magnetoelectric effect in rare earth ferrites, $LnFe_2O_4$. *J. Appl. Phys.*, 104(1):016102, 2008.

[123] Y. Sun, Y. Liu, F. Ye, S. Chi, Y. Ren, T. Zou, F. Wang, and L. Yan. A magnetoelectric multiglass state in multiferroic $YbFe_2O_4$. *J. Appl. Phys.*, 111(7):07D902, 2012.

[124] K. Yoshii, N. Ikeda, T. Michiuchi, Y. Yokota, Y. Okajima, Y. Yoneda, Y. Matsuo, Y. Horibe, and S. Mori. Magnetic and dielectric properties of $YbFe_{2-x}Mn_xO_4$ (0 <= x <= 1). *J. Solid State Chem.*, 182(7):1611–1618, 2009.

[125] C-H. Li, F. Wang, Y. Liu, X-Q. Zhang, Z-H. Cheng, and Y. Sun. Electrical control of magnetization in charge-ordered multiferroic $LuFe_2O_4$. *Phys. Rev. B*, 79(17):172412, 2009.

[126] F. Wang, C. H. Li, T. Zou, Y. Liu, and Y. Sun. Electrically driven magnetic relaxation in multiferroic $LuFe_2O_4$. *J. Phys. Condens. Matter*, 22(49):496001, 2010.

[127] K. Yoshii, N. Ikeda, Y. Nishihata, D. Maeda, R. Fukuyama, T. Nagata, J. Kano, T. Kambe, Y. Horibe, and S. Mori. Exchange bias in multiferroic RFe_2O_4 R = Y, Er, Tm, Yb, Lu, and In. *J. Phys. Soc. Jpn.*, 81(3):033704, 2012.

[128] H. X. Yang, H. F. Tian, Z. Wang, Y. B. Qin, C. Ma, J. Q. Li, Z. Y. Cheng, R. Yu, and J. Zhu. Effect of oxygen stoichiometry in $LuFe_2O_{4-\delta}$ and its microstructure observed by aberration corrected transmission electron microscopy. *J. Phys. Condens. Matter*, 24(43):435901, 2012.

[129] T. Maruyama, Y. Murakami, D. Shindo, N. Abe, and T. Arima. Observations of charge-ordered and magnetic domains in $LuFe_2O_4$ using transmission electron microscopy. *Phys. Rev. B*, 86(5):054202, 2012.

[130] K. Matsumoto, T. Koyama, S. Mori, K. Yoshii, T. Kambe, and N. Ikeda. Doping effect on charge ordered structure in mn-doped $YbFe_2O_4$. *3rd International Congress On Ceramics (icc3): Advances In Electro Ceramics*, 18, 2011.

[131] Y. Liu, T. Zou, F. Wang, X-Q. Zhang, Z-H. Cheng, and Y. Sun. Anisotropic giant dielectric tunability in electronic ferroelectric $YbFe_2O_4$. *Physica B: Condensed Matter*, 405(16):3391–3394, 2010.

[132] F. Wang, T. Zou, Y. Liu, L. . Q. Yan, and Y. Sun. Extrinsic and intrinsic nonlinear current-voltage characteristics in charge ordered oxides. *J. Appl. Phys.*, 111(3):033703, 2012.

[133] S. Nicoud, M. Huvé, O. Hernandez, A. Pautrat, M. Duttine, A. Wattiaux, C. Colin, H. Kabbour, and O. Mentré. Comprehensive study of oxygen storage in $YbFe_2O_{4+x}$ ($x \leq 0.5$): Unprecedented coexistence of FeO_n polyhedra in one single phase. *J. Am. Chem. Soc.*, 139(47):17031–17043, 2017.

[134] T. Duffar. *Crystal Growth Processes Based on Capillarity: Czochralski, Floating Zone, Shaping and Crucible Techniques*. Wiley, 2010.

[135] C. Guguschev, J. Götze, and M. Göbbels. Cathodoluminescence microscopy and spectroscopy of synthetic ruby crystals grown by the optical floating zone technique. *Am. Mineral.*, 95(4):449–455, 2010.

[136] B. D. Josephson. Possible new effects in superconductive tunnelling. *Physics Letters*, 1(7):251–253, jul 1962.

[137] J. Clarke and A. I. Braginski. *The SQUID Handbook: Applications of SQUIDs and SQUID Systems*. John Wiley & Sons, 2006.

[138] Juliano Toniolo, Antonio S. Takimi, Mônica J. Andrade, Renato Bonadiman, and Carlos P. Bergmann. Synthesis by the solution combustion process and magnetic properties of iron oxide Fe_3O_4 and α-Fe_2O_3 particles. *J. Mater. Sci.*, 42(13):4785–4791, 2007.

[139] D. Martien. *Introduction to AC Susceptibility*. Quantum Design, Corporate Headquarters, 11578 Sorrento Valley road, San Diego, CA, USA.

[140] M. Bałanda. AC susceptibility studies of phase transitions and magnetic relaxation: Conventional, molecular and low-dimensional magnets. *Acta Phys. Pol. A*, 124(6):964–976, 2013.

[141] J. Als-Nielsen D. McMorrow. *Elements of Modern X-Ray Physics*. John Wiley and Sons Ltd, 2011.

[142] K. Prokeš and F. Yokaichiya. Chapter 2 - elastic neutron diffraction on magnetic materials. volume 25 of *Handbook of Magnetic Materials*, pages 67 – 143. Elsevier, 2016.

[143] D. S. Sivia. *Elementary scattering theory: for X-ray and neutron users*. Oxford University Press, 2011.

[144] K. Hasegawa. Introduction to single crystal X-ray analysis. *The Rigaku Journal*, 28(1):14–18, 2012.

[145] J. Greensite. Scattering theory. In *An Introduction to Quantum Theory*, 2053-2563, pages 22–1 to 22–32. IOP Publishing, 2017.

[146] S. W. Lovesey and S. P. Collins. *X-ray scattering and absorption by magnetic materials*. Number 1. Oxford University Press, 1996.

[147] Steven R. Spurgeon. Experimental neutron scattering, by b.t.m. willis and c.j. carlile. *Contemporary Physics*, 55(3):250–251, 2014.

[148] C. Kittel. *Introduction to Solid State Physics, 6th edition*. Wiley, New York, 1986.

[149] P. J. Brown. Magnetic form factors. *IUCr*, C:Chap. 4.4, pp. 454–461, 2006.

[150] T. Brückel and W. Schweika. Polarized neutron scattering. *Lectures of the 1st Summer School held at the Forschungszentrum Jülich from*, 10, 2002.

[151] T. Chatterji. Chapter 1 - magnetic neutron scattering. In T. Chatterji, editor, *Neutron Scattering from Magnetic Materials*, pages 1 – 24. Elsevier Science, Amsterdam, 2006.

[152] Y. Zhu, editor. *Modern Techniques for Characterizing Magnetic Materials*. Springer US, 1 edition, 2005.

[153] M. Blume. Polarization effects in slow neutron scattering ii. spin-orbit scattering and interference. *Phys. Rev.*, 133(5A):A1366, 1964.

[154] M. Blume. Polarization effects in the magnetic elastic scattering of slow neutrons. *Phys. Rev.*, 130(5):1670, 1963.

[155] S. V. Maleev, V. G. Bar'yakhtar, and R. A. Suris. The scattering of slow neutrons by complex magnetic structures. *Soviet Phys.-Solid State (English Transl.)*, 4, 1963.

[156] H. X. Yang, H. F. Tian, Y. Zhang, Y. B. Qin, L. J. Zeng, C. Ma, H. L. Shi, and J. B. Lu. Phase separation and ferroelectric ordering in charge-frustrated $LuFe_2O_{4-\delta}$. *Solid State Commun.*, 150(31-32):1467–1472, 2010.

[157] Agilent Technologies XRD Products. *Supernova X-ray Diffractomter System User Manual*, 1.9 edition, Sept 2014.

[158] K. Mullaney, R. Correia, S/ E. Staines, S. W. James, and R. P. Tatam. Monitoring techniques for the manufacture of tapered optical fibers. *Appl. Opt.*, 54(28):8531, 2015.

[159] C.C. Enz and G.C. Temes. Circuit techniques for reducing the effects of op-amp imperfections: autozeroing, correlated double sampling, and chopper stabilization. *Proceedings of the IEEE*, 84(11):1584–1614, 1996.

[160] W. Clegg, A. J. Blake, M. Cole, J, S. O. Evans, J, P. Main, S. Parsons, and D. J. Watkin. *Crystal Structure Analysis*. Oxford University Press (OUP), jun 2009.

[161] P/ Müller. Practical suggestions for better crystal structures. *Crystallogr. Rev.*, 15(1):57–83, 2009.

[162] Cryogenic nitrogen jets for x-ray crystallography. Oxford Instruments Superconductivity Limited, 2003. All rights reserved., 2003.

[163] *Rigaku Oxford Diffraction, (2015), CrysAlisPro Software system, version number 1.171.37.35, Rigaku Corporation, Oxford, UK.*

[164] Heinz Maier-Leibnitz Zentrum *et al.* Dns: Diffuse scattering neutron time-of-flight spectrometer. *JLSRF*, 1(A27), 2015.

[165] R. Allemand, J. Bourdel, E. Roudaut, P. Convert, K. Ibel, J. Jacobe, J.P. Cotton, and B. Farnoux. Position-sensitive detectors (P.S.D.) for neutron diffraction. *Nucl. Instrum. Methods*, 126(1):29 – 42, 1975.

[166] L. Palatinus and G. Chapuis. SUPERFLIP–a computer program for the solution of crystal structures by charge flipping in arbitrary dimensions. *J. Appl. Crystallogr.*, 40(4):786–790, 2007.

[167] M. C. Burla, R. Caliandro, B. Carrozzini, G. L. Cascarano, C. Cuocci, C. Giacovazzo, M. Mallamo, A. Mazzone, G. Polidori, et al. Crystal structure determination and refinement via SIR2014. *J. Appl. Crystallogr.*, 48(1):306–309, 2015.

[168] G. Oszlányi and A. Süto. *Ab initio* structure solution by charge flipping. II. Use of weak reflections. *Acta Cryst. A*, 61(1):147–152, 2005.

[169] P. Muller, R. Herbst-Irmer, A. Spek, T. Schneider, and M. Sawaya. *Crystal Structure Refinement: A Crystallographer's Guide to SHELXL*. International Union of Crystallography Texts on Crystallography. OUP Oxford, 2006.

[170] F. L. Hirshfeld and D. Rabinovich. Treating weak reflexions in least-squares calculations. *Acta Crysta. Sect. A*, 29(5):510–513, 1973.

[171] L. Arnberg, S. Hovmöller, and S. Westman. On the significance of 'non-significant' reflexions. *Acta Cryst. A*, 35(3):497–499, 1979.

[172] G. S. Pawley. TheR-factor ratio test in crystallography: an approximation. *Acta Cryst. Sect. A*, 26(6):691–692, nov 1970.

[173] I. D. Brown and D. Altermatt. Bond-valence parameters obtained from a systematic analysis of the inorganic crystal structure database. *Acta Crystallogr., Sect. B: Struct. Sci*, 41(4):244–247, 1985.

[174] N. E. Brese and M. O'keeffe. Bond-valence parameters for solids. *Acta Crystallogr., Sect. B: Struct. Sci*, 47(2):192–197, 1991.

[175] T. F George. *Computational studies of new materials II: from ultrafast processes and nanostructures to optoelectronics, energy storage and nanomedicine*. World Scientific, 2011.

[176] S. Lafuerza, G. Subias, J. Blasco, J. Garcia, G. Nisbet, K. Conder, and E. Pomjakushina. Determination of the charge-ordered phases in $LuFe_2O_4$. *Epl*, 107(4):47002, 2014.

[177] W. Liu and H. H. Thorp. Bond valence sum analysis of metal-ligand bond lengths in metalloenzymes and model complexes. 2. refined distances and other enzymes. *Inorg. Chem.*, 32(19):4102–4105, 1993.

[178] O. C. Gagné and F. C. Hawthorne. Comprehensive derivation of bond-valence parameters for ion pairs involving oxygen. *Acta Crysta. B*, 71:562–78, 2015.

[179] S. M Kanowitz and G. J. Palenik. Bond valence sums in coordination chemistry using oxidation-state-independent R_0 values. a simple method for calculating the oxidation state of iron in Fe-O complexes. *Inorg. Chem.*, 37(8):2086–2088, 1998.

[180] S. Kimura and K. Kitamura. Floating zone crystal growth and phase equilibria: A review. *J. Am. Ceram. Soc.*, 75(6):1440–1446, 1992.

[181] W. N. Klaus-Werner Benz. *Introduction to Crystal Growth and Characterization*. Wiley VCH Verlag GmbH, 2014.

[182] F. Wang, J. Kim, G. D. Gu, Y. Lee, S. Bae, and Y-J Kim. Oxygen stoichiometry and magnetic properties of $LuFe_2O_{4+\delta}$. *J. Appl. Phys.*, 113(6):063909, 2013.

[183] Li C-H, Y. Liu, F. Wang, X. Luo, Sun Y-P, Zhang X-Q, Cheng Z-H, and Y. Sun. Photoinduced magnetization change in multiferroic $YbFe_2O_4$. *Chin. Phys. Lett.*, 26(12):127501, 2009.

[184] D. Feng and G. Jin. *Introduction to condensed matter physics*, volume 1. World Scientific, 2005.

[185] W. Schweika. XYZ-polarisation analysis of diffuse magnetic neutron scattering from single crystals. In *J. Phys. Conf. Ser.*, volume 211, page 012026. IOP Publishing, 2010.

[186] Y. Matsuo, S. Mori, A. Hirata, K. Yoshii, and N. Ikeda. Doping effect on charge ordered structure in RFe_2O_4 R=Lu and Yb. *International Conference On Magnetism*, 200, 2010.

[187] K. Fujiwara, M. Miyajima, M. Fukunaga, J. Kano, H. Kobayashi, and N. Ikeda. Iron vacancy effect on the magnetization of $YbFe_2O_4$. *Trans. Mater. Res. Soc. Jpn.*, 41(1):139–142, 2016.

[188] Y. Sun, J-Z Cong, Y-S Chai, L-Q Yan, Y-L Zhao, S-G Wang, Wei Ning, and Y-H Zhang. Giant exchange bias in a single-phase magnet with two magnetic sublattices. *Appl. Phys. Lett.*, 102(17):172406, 2013.

[189] Y. Zhang, H. X. Yang, Y. Q. Guo, C. Ma, H. F. Tian, J. L. Luo, and J. Q. Li. Structure, charge ordering and physical properties of $LuFe_2O_4$. *Phys. Rev. B*, 76(18):184105, 2007.

[190] F Wang, J Kim, Y. . J. Kim, and G. D. Gu. Spin-glass behavior in $LuFe_2O_{4+\delta}$. *Phys. Rev. B*, 80(2):024419, 2009.

[191] A. Ruff, S. Krohns, F. Schrettle, V. Tsurkan, P. Lunkenheimer, and A. Loidl. Absence of polar order in $LuFe_2O_4$. *Eur. Phys. J. B*, 85(8):30296–6, 2012.

[192] N. Hasegawa, T. Mitsumura, M. Takesada, A. Onodera, J. Kano, and N. Ikeda. Specific heat study of multiferroic $LuFe_2O_4$ single crystal. *Ferroelectrics*, 462(1):145–150, 2014.

[193] N. W. Ashcroft and N. D. Mermin. *Solid State Physics*. Holt-Saunders, 1976.

[194] K. Kumar, A. K. Pramanik, A. Banerjee, P. Chaddah, S. B. Roy, S. Park, C. L. Zhang, and S-W. Cheong. Relating supercooling and glass-like arrest of kinetics for phase separated systems: Doped $CeFe_2$ and (La, Pr, Ca) MnO_3. *Phys. Rev. B*, 73(18):184435, 2006.

[195] G. K. White T. H. K. Barron. *Heat Capacity and Thermal Expansion at Low Temperatures*. Springer, 1999.

[196] M. De Souza, Ricardo Paupitz, A. Seridonio, and R. E. Lagos. Specific heat anomalies in solids described by a multilevel model. *Braz. J. Phys.*, 46(2):206–212, 2016.

[197] C. M. N. Kumar, Y. Xiao, H. S. Nair, J. Voigt, B. Schmitz, T. Chatterji, N. H. Jalarvo, and T. Brückel. Hyperfine and crystal field interactions in multiferroic $hocro_3$. *J. Phys.: Condens. Matter*, 28(47):476001, 2016.

[198] M. Falkowski, M. Reiffers, M. Zapotoková, A. Kowalczyk, T. Tolinski, and E. Gazo. Heat capacity studies of ndni4si compound. *Acta Physica Polonica A*, 115(1):126, 2009.

[199] M. T. Hutchings and W. P. Wolf. Crystal field for Yb^{3+} in garnets. *J. Chem. Phys.*, 41(3):617–626, 1964.

[200] F Rivera-López, P Babu, Ch Basavapoornima, CK Jayasankar, and V Lavín. Efficient $Nd^{3+} \rightarrow Yb^{3+}$ energy transfer processes in high phonon energy phosphate glasses for 1.0 μm Yb^{3+} laser. *Journal of Applied Physics*, 109(12):123514, 2011.

[201] S. Park, Y. Horibe, Y. J. Choi, C. L. Zhang, S. . W. Cheong, and W. Wu. Pancakelike ising domains and charge-ordered superlattice domains in $LuFe_2O_4$. *Phys. Rev. B*, 79(18):180401, 2009.

[202] A. Rais, A. M. Gismelseed, and I. A. Al-Omari. On the magnetic compensation effect of lithium-chromium ferrites $Li_{0.5}Cr_xFe_{2.5-x}O_4$ ($0 \leq x \leq 1.55$). *physica status solidi (b)*, 242(14):2949–2955, 2005.

[203] E. W. Gorter and J. A. Schulkes. Reversal of spontaneous magnetization as a function of temperature in LiFeCr spinels. *Phys. Rev.*, 90(3):487, 1953.

[204] M. Inazumi, Y. Nakagawa, M. Tanaka, N. Kimizuka, and K. Siratori. Magnetizations and mössbauer spectra of YFe_2O_{4-x}. *J. Phys. Soc. Jpn.*, 50(2):438–444, 1981.

[205] R. H. Blessing. Outlier Treatment in Data Merging. *J. Appl. Crystallogr.*, 30(4):421–426, 1997.

[206] Brian H Toby. R factors in rietveld analysis: How good is good enough? *Powder diffraction*, 21(1):67–70, 2006.

[207] R. Herbst-Irmer and G. M. Sheldrick. Refinement of obverse/reverse twins. *Acta Crystallogr., Sect. B: Struct. Sci*, 58(3):477–481, 2002.

[208] W. J. A. M. Peterse and J. H. Palm. The anisotropic temperature factor of atoms in special positions. *Acta Crystallogr.*, 20(1):147–150, 1966.

[209] ISOTROPY software suite.

[210] B. J. Campbell, H. T. Stokes, D. E. Tanner, and D. M. Hatch. ISODISPLACE: a web-based tool for exploring structural distortions. *J. Appl. Crystallogr.*, 39(4):607–614, 2006.

[211] H. Arnold. Transformations of the coordinate system (unit-cell transformations). In *International Tables for Crystallography Volume A: Space-group symmetry*, pages 78–85. Springer, 2006.

[212] R. W. Grosse-Kunstleve and P. D. Adams. On the handling of atomic anisotropic displacement parameters. *J. Appl. Crystallogr.*, 35(4):477–480, 2002.

[213] D. Watkin. Structure refinement: some background theory and practical strategies. *J. Appl. Crystallogr.*, 41(3):491–522, 2008.

[214] R. E. Marsh. Centrosymmetric or noncentrosymmetric? *Acta Crysta. B*, 42(2):193–198, 1986.

[215] E. Kroumova, J. M. Perez-Mato, and M. I. Aroyo. WYCKSPLIT: a computer program for determination of the relations of Wyckoff positions for a group-subgroup pair. *J. Appl. Crystallogr.*, 31(4):646, 1998.

[216] Makoto Naka, Aya Nagano, and Sumio Ishihara. Magnetodielectric phenomena in a charge- and spin-frustrated system of layered iron oxide. *Phys. Rev. B*, 77(22):224441, 2008.

[217] A. B. Harris and T. Yildirim. Erratum: Charge and spin ordering in the mixed-valence compound $LuFe_2O_4$. *Phys. Rev. B*, 82(34417):029902, 2010.

[218] S. M. Gaw, H. J. Lewtas, D. F. McMorrow, J. Kulda, R. A. Ewings, T. G. Perring, R. A. McKinnon, G. Balakrishnan, D. Prabhakaran, and A. T. Boothroyd. Magnetic excitation spectrum of $LuFe_2O_4$ measured with inelastic neutron scattering, June 2014.

[219] M. J. Kronenburg. Atomic displacement parameters and anisotropic thermal ellipsoid lengths and angles. *Acta Crysta. A*, 60(3):250–256, 2004.

[220] WF Kuhs. Atomic displacement parameters. In *IuCr. D*, pages 228–242. Springer, 2006.